

**LITHIUM ELECTRONIC ENVIRONMENTS IN
RECHARGEABLE BATTERY ELECTRODES**

Thesis by
Adrian Hightower

In Partial Fulfillment of the Requirements
for the Degree of
Doctor of Philosophy

California Institute of Technology
Pasadena, California

2001
(Defended July 14, 2000)

For My Family

©2001

Adrian Hightower

All Rights Reserved

Acknowledgments

This work was made possible by the generous support of a great number of people. I would like to thank the following people for making this journey a rewarding one.

- Dr. Brent Fultz, my thesis advisor, who has provided steadfast support and guidance during my graduate career;
- Dr. Ratnakumar Bugga, who taught me all I know on batteries, fuel cells and accomplishing tasks at the Jet Propulsion Laboratory;
- Dr. Channing Ahn and Carol Garland, who patiently shared their art of Electron Microscopy;
- Dr. Peter Rez, for his invaluable expertise in Electron Energy Loss Spectroscopy and unfailing sense of humor;
- Dr. Charles Witham, Peter Bogdanoff, Stephen Glade, Claudine Chen, Sven Bossuyt, Yun Ye, Jason Graetz and my fellow graduate students who work as hard as they play;
- Pam Albertson, Elena Escot, and the entire staff of the Caltech Material Science Department;
- Eddie Grado, Frank Vargas, Cheryl Hawthorne, Sue Borrego, Michelle Medley and the Caltech Office of Minority Student Affairs;
- My family: Mom, Dad, Erica, Stephanie, Jeffery, Sheila, Natalie, Sarah, Jonathan, and my beloved Michelle.

This work has been supported by the U. S. Dept. of Energy grant DE-FG03-94ER14493.

Abstract

This work investigates the electronic environments of lithium in the electrodes of rechargeable batteries. The use of electron energy-loss spectroscopy (EELS) in conjunction with transmission electron microscopy (TEM) is a novel approach, which when coupled with conventional electrochemical experiments, yield a thorough picture of the electrode interior.

Relatively few EELS experiments have been performed on lithium compounds owing to their reactivity. Experimental techniques were established to minimize sample contamination and control electron beam damage to studied compounds. Lithium hydroxide was found to be the most common product of beam damaged lithium alloys. Under an intense electron beam, halogen atoms desorbed by radiolysis in lithium halides. EELS spectra from a number of standard lithium compounds were obtained in order to identify the variety of spectra encountered in lithium rechargeable battery electrodes. Lithium alloys all displayed characteristically broad Li K-edge spectra, consistent with transitions to continuum states. Transitions to bound states were observed in the Li K and oxygen K-edge spectra of lithium oxides. Lithium halides were distinguished by their systematic chemical shift proportional to the anion electronegativity. Good agreement was found with measured lithium halide spectra and electron structure calculations using a self-consistent multiscattering code.

The specific electrode environments of LiC_6 , LiCoO_2 , and Li-SnO were investigated. Contrary to published XPS predictions, lithium in intercalated graphite was determined to be in more metallic than ionic. We present the first experimental evidence of charge compensation by oxygen ions in deintercalated LiCoO_2 . Mössbauer studies on cycled Li-SnO reveal severely defective structures on an atomic scale.

Metal hydride systems are presented in the appendices of this thesis. The mechanical alloying of immiscible Fe and Mg powders resulted in single-phase bcc alloys of less than 20 at% Mg. Kinetic studies on $\text{LaNi}_{5-x}\text{Sn}_x$ alloys proved that the mass transfer of hydrogen through these alloys was not hindered with increasing Sn substitutions for Ni. Collaborations with Energizer© found $\text{LaNi}_{4.7}\text{Sn}_{0.3}$ alloys to possess limited utility in rechargeable nickel-metal-hydride sealed-cell batteries.

Table of Contents

Title page	i
Copyright page	ii
Acknowledgments	iii
Abstract	iv
Table of Contents	v
List of Tables and Figures	xi
1 Introduction	1
1.1 Components of a Battery	1
1.2 References	7
2 Techniques and Instrumentation	8
2.1 Battery Electrochemistry	8
2.1.1 Thermodynamics	8
2.1.2 Kinetics	9
2.1.3 Reversibility	11
2.2 Mössbauer Spectrometry	14
2.2.1 Recoil Free Fraction	18
2.2.2 Hyperfine Parameters	19
2.2.2.1 Isomer Shift, IS	19
2.2.2.2 Electric Quadrupole Hyperfine Interactions, QS	21
2.2.2.3 Magnetic Dipole Hyperfine Interactions	23
2.3 Electron Energy Loss Spectroscopy	25
2.3.1 Kinematics	25
2.3.2 Data Acquisition and Analysis	31

2.3.3	Energy Resolution	37
2.3.4	Energy Loss Spectrum	39
2.3.4.1	Zero-Loss Peak	39
2.3.4.2	Low-Loss Spectra	40
2.3.4.2.1	Plasmons	40
2.3.4.2.2	Single-Electron Excitations	41
2.3.4.2.3	Excitons	43
2.3.4.3	Core-Loss Spectra	44
2.3.5	XPS and EELS	46
2.4	References	47
3	Lithium EELS Spectra	49
3.1	Near Edge Structure	49
3.2	Beam Damage	50
3.2.1	Electron Specimen Interactions	50
3.2.2	Radiation Damage of Metallic Lithium	54
3.2.3	Radiation Damage of Lithium Fluoride	57
3.3	Metallic Lithium and Alloys	63
3.4	Lithium Oxides	68
3.5	Lithium Halides	73
3.6	Electron Structure Calculations	77
3.7	References	82
4	Specific Electrode Environments	85
4.1	Electron Energy Loss Spectrometry on Lithiated Graphite	85

4.1.1	Introduction	85
4.1.2	Experimental	86
4.1.3	X-ray Diffraction Results	87
4.1.4	TEM Micrographs	87
4.1.5	Carbon K-edge	90
4.1.6	Lithium K-edge	90
4.1.7	Comparison to XPS Results	93
4.1.8	Discussion	93
4.1.9	Conclusion	93
4.1.10	References	96
4.2	EELS Analysis of LiCoO ₂	98
4.2.1	Introduction	98
4.2.2	Experimental	100
4.2.3	Electrochemical Results	102
4.2.4	X-Ray Diffractometry	105
4.2.5	EELS Analysis	105
4.2.5.1	Li K-edge and Cobalt M ₂₃ edge	107
4.2.5.2	Oxygen K-edge	107
4.2.5.3	Cobalt L ₂₃ Edges	112
4.2.6	Cycled Cathodes	112
4.2.6.1	TEM Micrographs of Cycled Cathodes	114
4.2.6.2	EELS Spectra of Cycled Cathodes	116
4.2.7	Discussion	121

4.2.8	Conclusions	123
4.2.9	References	126
4.3	^{119}Sn Mössbauer Spectrometry of the Li-SnO Anode	128
4.3.1	Introduction	128
4.3.2	Experimental	129
4.3.3	Electrochemical Results	133
4.3.4	X-Ray Diffractometry and TEM Results	133
4.3.5	Mössbauer Spectrometry Results	139
4.3.5.1	Mössbauer Spectra of Control Samples	139
4.3.5.2	Mössbauer Spectra of Anode Materials	143
4.3.5.3	Recoil-Free Fractions: Standards	145
4.3.5.4	Recoil-Free Fractions: Anode Materials	147
4.3.6	Oxidation in Ambient Air	150
4.3.7	Thermodynamics of Anode Reactions and Oxidation	153
4.3.8	Conclusions	158
4.3.9	Acknowledgments	160
4.3.10	References	162
Appendix A Mechanical Alloying of Fe and Mg		166
A.1	Introduction	166
A.2	Experimental	167
A.3	Results	169
A.3.1	X-ray Diffractometry	169
A.3.2	Density	172

A.3.3 Mössbauer Spectrometry	172
A.3.4 Rotating Magnetometry	177
A.4 Discussion	177
A.4.1 Chemical Distributions in bcc Alloys	177
A.4.2 Limits of Solubility	183
A.5 Conclusion	185
A.6 References	187
Appendix B Kinetics of H diffusion in LaNi_{5-x}Sn_x Alloys	189
B.1 Introduction	189
B.2 Experimental	191
B.3 Results	193
B.3.1 Steady State Measurements	193
B.3.1.1 Potentiodynamic Polarization	193
B.3.1.2 Discharge Characteristics	193
B.3.2 Transient Measurements	196
B.3.2.1 Chronoamperometry	196
B.3.2.2 Chronocoulometry	198
B.4 Temperature Studies	200
B.5 Conclusion	206
B.7 References	208
Appendix C Performance of LaNi_{4.7}Sn_{0.3} Electrodes in Sealed Cells	210

C.1 Introduction	210
C.2 Experimental	211
C.3 Results and Discussion	213
C.3.1 Isotherms	213
C.3.2 Self Discharge	215
C.3.3 Rate Measurements	215
C.3.4 Pressure Measurements	217
C.3.5 Cycle Life	217
C.3.6 AC Impedance	223
C.4 Conclusions	223
C.5 References	225

List of Tables and Figures

Chapter 1		
Figure 1.1	Diagram of a lithium ion cell.	2
Table 1.1	Anode materials	3
Table 1.2	Cathode materials	4
Table 1.3	Characteristics of organic solvents	6
Chapter 2		
Figure 2.1	Cathodic and anodic currents versus polarization, η	12
Figure 2.2	Atom recoil, decay lineshape, lines separated by recoil	15
Figure 2.3	Elements that may be studied using Mössbauer spectroscopy	16
Figure 2.4	Mössbauer effect absorption and Doppler-derived energy	17
Figure 2.5	Mössbauer spectra with quadrupole and magnetic splitting	20
Figure 2.6	Nuclear quadrupole moment with nearby charges	22
Table 2.1	Relative Mössbauer peak intensities for ^{57}Fe	23
Figure 2.7	Kinematics of inelastically scattered electron	26
Figure 2.8	Bethe surface for K-shell ionization	30
Figure 2.9	Inner-shell ionization and associated nomenclature	32
Figure 2.10	Schematic of EELS spectrometer	33
Figure 2.11	Collection-angle geometry in image mode	35
Figure 2.12	Collection angle geometry in diffraction mode	36
Figure 2.13	Instrument response for EELS detector	38
Table 2.2	Characteristics of EELS processes	38

Figure 2.14	Aluminum volume plasmons	42
Figure 2.15	Electron energy levels and energy-loss spectrum	45
Chapter 3		
Figure 3.1	Knock-on displacement energy of atomic species	52
Figure 3.2	EELS spectra of beamed damaged metallic lithium	55
Table 3.1	Thermodynamic constants for select Li compounds	56
Figure 3.3	Radiolytic displacement sequence for alkali halides	58
Figure 3.4	EELS spectra of beamed damaged lithium fluoride	59
Figure 3.5	Micrograph of beamed damaged lithium fluoride	58
Figure 3.6	Micrograph of beam damaged lithium tin	61
Figure 3.7	EELS low-loss spectra of lithium alloys	64
Figure 3.8	Lithium K-edges of lithium alloys	65
Figure 3.9	Aluminum L ₂₃ edge	67
Figure 3.10	EELS low-loss spectra of lithium oxides	69
Figure 3.11	Lithium K-edges of lithium oxides	70
Figure 3.12	Oxygen K-edges of lithium alloys	72
Figure 3.13	EELS low-loss spectra of lithium halides	74
Figure 3.14	Lithium K-edges of lithium halides	75
Figure 3.15	Chemical shift versus anion electronegativity	76
Figure 3.16	Simulated lithium K-edges for LiF	78
Figure 3.16	Simulated lithium K-edges for LiCl	79
Figure 3.17	Simulated lithium K-edges for LiBr	80

Chapter 4

Figure 4.1	XRD pattern of KS44 graphite and lithiated graphite	88
Figure 4.2	Micrograph of lithiated graphite	89
Figure 4.3	Carbon K-edge for KS44 graphite and lithiated graphite	91
Figure 4.4	Lithium K-edge of metallic Li, LiF, and lithiated graphite	92
Figure 4.5	Initial charge-discharge curves of lithiated KS44 graphite	94
Figure 4.6	Layered ABCABC stacking of LiCoO ₂	99
Figure 4.7	Initial cycles of LiCoO ₂ cell	103
Figure 4.8	Electrochemical discharge curves of LiCoO ₂	104
Figure 4.9	XRD patterns of discharged LiCoO ₂	106
Figure 4.10	Co M ₂₃ and Li K edge of cobalt oxide standards	108
Figure 4.11	Oxygen K-edge of cobalt oxide standards	109
Table 4.1	Occupation numbers of CoO	111
Table 4.2	Occupation numbers of LiCoO ₂	111
Figure 4.12	Cobalt L ₂₃ edges of cobalt oxide standards	113
Figure 4.13	TEM micrographs of discharged cathodes	115
Figure 4.14	Li K-edge and cobalt M ₂₃ edges of discharged cathodes	117
Figure 4.15	Oxygen K-edges of discharged cathodes	118
Figure 4.16	Cobalt L ₂₃ edges of discharged cathodes	119
Figure 4.17	Simulated oxygen K-edge in LiCoO ₂	122
Table 4.3	Normalized areas of oxygen K-edge peaks	125
Table 4.4	Normalized areas of cobalt L-edge peaks	125

Figure 4.18	Electrochemical discharge curves for lithium-tin anode	134
Figure 4.19	Cycle life of lithium-tin anode	135
Figure 4.20	XRD pattern of lithium–tin alloy and anodes	137
Figure 4.21	TEM micrograph of cycled lithium-tin anode	138
Figure 4.22	Mössbauer spectra of tin standards and cycled lithium-tin anodes	140
Figure 4.23	XRD patterns of oxidized $\text{Li}_{2,3}\text{SnO}$ anode	151
Figure 4.24	XRD patterns of oxidized Li_5SnO anode	152
Figure 4.25	Deconvoluted Mössbauer spectra of oxidized $\text{Li}_{2,3}\text{SnO}$ anode	154
Figure 4.26	Deconvoluted Mössbauer spectra of oxidized Li_5SnO anode	155
Figure 4.27	Deconvoluted Mössbauer spectra of oxidized $\text{Li}_{22}\text{Sn}_5$	156
Table 4.5	Relative spectral areas in Li_5SnO	161
Table 4.6	Relative spectral areas in $\text{Li}_{2,3}\text{SnO}$	161
Appendix A		
Figure A.1	XRD patterns of Fe-Mg alloys	170
Figure A.2	XRD pattern of annealed $\text{Fe}_{85}\text{Mg}_{15}$	171
Figure A.3	Lattice parameters of hcp and bcc phases	173
Figure A.4	Fractions of hcp and bcc phases from XRD	174
Figure A.5	Density measurements of as-milled alloys	175
Figure A.6	Mössbauer spectra of as-milled Fe-Mg alloys	176
Figure A.7	Hyperfine magnetic field distributions	178
Figure A.8	Calculated nearest neighbor ratio	179
Figure A.9	Saturation magnetization for Fe-Mg alloys	180

Appendix B

Figure B.1	Potentiodynamic polarization curves for $\text{LaNi}_{5-x}\text{Sn}_x$ alloys	194
Figure B.2	Diffusion limiting currents of $\text{LaNi}_{5-x}\text{Sn}_x$ alloys	195
Figure B.3	Discharge curves of $\text{LaNi}_{5-x}\text{Sn}_x$ alloys	197
Figure B.4	Analysis of chronoamperometric curves of $\text{LaNi}_{5-x}\text{Sn}_x$ alloys	199
Figure B.5	Analysis of chronocouometric response of $\text{LaNi}_{5-x}\text{Sn}_x$ alloys	201
Figure B.6	Variation of hydrogen diffusion coefficient	202
Figure B.7	Chronoamperometric response of $\text{LaNi}_{4.8}\text{Sn}_{0.2}$ at various T	203
Figure B.8	Chronocoulmetric response of $\text{LaNi}_{4.8}\text{Sn}_{0.2}$ at various T	204
Figure B.9	Arrhenius plot of $\text{LaNi}_{4.8}\text{Sn}_{0.2}$ diffusion coefficients	205
Table B.1	Determination of Diffusion coefficients	207

Appendix C

Figure C.1	Gas phase desorption isotherms of anode materials	214
Figure C.2	Self discharge curves at 23°C and 45°C	216
Figure C.3	Electrochemical capacities of AA cells	218
Figure C.4	Fractions of H_2 gas evolved during charging	219
Figure C.5	Cycle life of sealed cell measured at JPL	220
Figure C.6	Cycle life of sealed cell measured at Energizer	221
Figure C.7	Cell internal resistance vs. cycle number	222

Chapter 1 Introduction

1.1 Components of a Battery

The fundamental components of an electrochemical cell are the anode, cathode, electrolyte, and external load to complete the circuit. The anode is the electrode where molecules or ions from the electrolyte are oxidized upon spontaneous reaction (discharge). The electrons from the oxidized species of the anode move as current through the wires of the external load. Upon discharge, ions or molecules are reduced at the cathode by reacting with electrons from the external load. The electrolyte provides the media for ionic current with positive ions moving toward the cathode and negative ions moving toward the anode upon discharge (Figure 1.1). For low currents, the cell voltage is the difference in electrochemical potential between the cathode and the anode [1]. For higher currents, a voltage drop across the cell may also be important [2].

Anodes of rechargeable lithium battery systems are generally composites of a lithium alloy, a conducting diluent (carbon black), and a polymer binder (polyvinylidene fluoride). Anode materials are chosen for their high chemical potential for lithium (low voltage) relative to the cathode environment. These materials, including metallic lithium, are extremely reactive owing to their high chemical potential of lithium. Lithiated anode materials react quickly with moisture from the air to form lithium hydroxide and lithium oxides. Table 1 lists some common lithium anode materials.

For rechargeable batteries, critical characteristics of electrode materials are capacity, chemical potential, cycle life, and kinetics. As a general rule, electrodes materials with larger capacities have smaller cycle life and vice versa. The design of

secondary lithium ion batteries has been the history of optimizing and compromising these characteristics [3]. Good kinetics implies efficient charge transfer and mass transfer reactions at and through the various interfaces in the cell and in the material. Cycle life is the number of times an electrode can be charged and discharged before a substantial loss of capacity occurs. Cycle life is generally dependent on the structural and chemical stability of the electrode.

Table 1.1 Anode Materials

Material	Voltage range vs. lithium, V	Theoretical specific capacity, Ah/g
Li metal	0.0	3.86
LiAl	0.3	0.8
Li-tin oxide amorphous	0.1-1.2	0.65
LiC ₆ (doped coke or graphite)	0.0-0.5	0.370
Li _{0.5} C ₆ (coke)	0.0-1.3	0.185
LiWO ₂	0.3-1.4	0.12
LiMoO ₂	0.8-1.4	0.199
LiTiS ₂	1.5-2.7	0.226

Although metallic lithium has the best energy density and voltage, its practical use as an anode material is limited by its dangerously fast kinetics, which lead to heterogeneous plating of lithium on the anode during charging. This leads to the formation of dendrites, which eventually short the battery, possibly leading to dangerous run away reactions. Except for the smallest cells, the formation of dendrites inhibits the cycle life of metallic lithium anodes to tens of cycles.

Lithiated graphite (LiC₆) is currently the most popular anode material in lithium ion systems. This work details how lithium ions intercalate between graphite planes where they are reduced to neutral atoms. The preferential intercalation of lithium between the graphite planes allows for rapid mass transfer through the graphite phase.

The chemical potential of lithium in graphite is very similar to that of lithium in its metallic form owing to limited charge transfer from Li to the surrounding carbon. Strong covalent bonding between the graphite layers provides a stable lattice to promote a cycle life on the order of thousands of cycles.

The cathode of most lithium ion batteries is a composite of a lithium transition metal oxide (Table 1.2), a conducting diluent, and a polymer binder. Lithium cobalt oxide is the most widely used cathode material in lithium ion systems. LiCoO_2 has an ordered rock-salt structure with lithium and cobalt planes alternating between close-packed oxygen layers. As with graphite, the layered structure of LiCoO_2 allows for rapid diffusion in the lithium plane. A model of strict charge transfer views LiCoO_2 as being composed of Li^+ , Co^{+3} , and O^{2-} ions. Conventional wisdom views the lithium deintercalation accompanied with a change in cobalt valence from Co^{+3} to Co^{+4} . Thus oxygen atoms remain unchanged as O^{2-} ions. This work refutes this model and suggests significant charge compensation by oxygen atoms with lithium deintercalation. The high cost of cobalt has stimulated interest in alternative cathode materials, most notably manganese oxides.

Table 1.2 Cathode Materials

Material	Voltage range vs. lithium, V	Theoretical specific capacity, Ah/g
LiCoO_2	3.73-4.0	0.5
LiMn_2O_4	3.9-4.1	0.15
$\text{Li}_2\text{Mn}_2\text{O}_4$	2.6-2.7	0.75
LiVO_2	2.9-3.0	0.226
LiNiO_2	3.5-3.7	4.5

Electrolytes of rechargeable lithium systems are combinations of a lithium salt and an organic solvent with less than 50 ppm of water. An electrolyte needs to be highly conductive over a large temperature range as well as electrochemically stable over a wide range in voltage (0 to 4.1 V vs Li/Li+). Typical salts in lithium ion systems include LiAsF₆, LiBF₆, LiClO₄ and LiPF₆, chosen for economic and environmental reasons. The organic molecules used in electrolytes decompose on the surface of an electrode forming a solid-electrolyte interphase (SEI) [4, 5]. For lithium ion systems, the SEI is composed of reduced electrolyte products and reduced electrode material. Common lithium compounds of the SEI are lithium carbonate (Li₂CO₃), lithium oxide (Li₂O), lithium hydroxide (LiOH), lithium alkoxides, lithium fluoride (LiF), and electrolyte salt reduction products yet to be characterized [1]. The SEI can have the beneficial role of protecting the electrode from decomposing and stable SEI's do not consume further lithium, minimizing irreversible capacity.

Blends of carbonates are currently used as electrolyte solvents (Table 1.3). These blends optimize the benefits and offset the deficiencies of each carbonate. For example, the rapid kinetics of propylene carbonate (PC) are hampered by its destructive effects on anode surfaces. Ethylene forms a passivating SEI on the electrode, thus enhancing the battery's cycle life. Blending EC and PC in a 1:1 ratio has proved a very successful electrolyte. Much work has been done to formulate electrolyte blends to lower the operating temperature of lithium ion batteries to less than 0°C [6].

Table 1.3 Characteristics of Organic Solvents*.

Characteristic	γ BL	THF	1,2-DME	PC	EC	DMC	DEC	DEE	Dioxolane
Structural formula									
Boiling temperature, °C	202–204	65–67	85	240	248	91	126	121	78
Melting temperature, °C	–43	–109	–58	–49	–39–40	4.6	–43	–74	–95
Density, g/cm ³	1.13	0.887	0.866	1.198	1.322	1.071	0.98	0.842	1.060
Solution conductivity, S/cm	1.1×10^{-8}	2.1×10^{-7}	3.2×10^{-8}	2.1×10^{-9}	$<10^{-7}$	$<10^{-7}$	$<10^{-7}$	$<10^{-7}$	$<10^{-7}$
Viscosity at 25°C, cP	1.75	0.48	0.455	2.5	1.86	0.59	0.75	0.65	0.58
Dielectric constant at 20°C	39	7.75	7.20	64.4	89.6 (at 40°C)	3.12	2.82	5.1	6.79
Molecular weight	86.09	72.10	90.12	102.0	88.1	90.08	118.13	118.18	74.1
H ₂ O content, ppm	<10	<10	<10	<10	<10	<10	<10	<10	<10
Electrolytic conductivity at 20°C, 1M LiAsF ₆ , mS/cm	10.62	12.87	19.40	5.28	6.97	11.00 (1.9 mol)	5.00 (1.5 mol)	~10.00†	~11.20†

* γ BL = γ -butyrolactone; THF = tetrahydrofuran; 1,2-DME = 1,2-dimethoxyethane; PC = propylene carbonate; EC = ethylene carbonate; DMC = dimethyl carbonate; DEC = diethyl carbonate; DEE = diethoxyethane.

† Estimation based on Walden's rule.

1.2 References

- [1] J.O.M Bockris and S. U. M. Khan, *Surface Electrochemistry : A Molecular Level Approach*, (Penum Press, New York, 1993).
- [2] A. J. Bard and L. R. Faulkner, *Electrochemical Methods: Fundamentals and Applications*, (John Wiley & Sons, New York 1980).
- [3] D Linden, *Handbook of Batteries*, (McGraw-Hill. New York, 1976).
- [4] D. T. Sawyer, A. Sobkowiak, J. L. Roberts Jr, *Electrochemistry for Chemists*, (John Wiley & Sons, New York, 1995).
- [5] G. Prentice, *Electrochemical Engineering Principles*, Prentice-Hall, New Jersey, 1991).
- [6] M. C. Smart, B. V. Ratnakumar* and S. Surampudi, Y. Wang, X. Zhang and S. G. Greenbaum, A. Hightower, C. C. Ahn and B. Fultz, *J. Electrochem. Soc.* **146**, 11 (1999).

Chapter 2 Techniques and Instrumentation

2.1 Battery Electrochemistry

Batteries, fuels cells, and corrosion process all convert the energy of chemical reactions into electrical energy and thus adhere to the same laws of kinetics and thermodynamics. The interconversion of chemical and electrical energy is accomplished by an ionic current flow through an electrolyte. This electrolyte must lie between two chemical potentials in electrical contact with each other.

2.1.1 Thermodynamics of a Battery

A battery can be thought of as an engine that derives work from a gradient in chemical potential. From the First law of thermodynamics we can derive the relationship between the work done by the battery and the Gibbs free energy of a reaction.

$$\Delta U = q - w \quad (2.1)$$

Here ΔU is the change in Internal Energy, q is the heat added to system, and w is the work done by the system. We can further define the heat added as $q = T\Delta S$ and the work done by the battery as the sum of the mechanical work, $w_p = p\Delta V$ and electrochemical work w_e , $w = w_p + w_e$. Thus we have the internal energy defined as

$$\Delta U = T\Delta S - p\Delta V - w_e \quad (2.2)$$

Comparing this to the change in Gibbs Free energy,

$$\Delta G = \Delta U - T\Delta S + p\Delta V \quad (2.3)$$

we find that the change in Gibbs free energy is equal to the negative of the electrochemical work.

$$\Delta G = -w_e = -nF\Delta E \quad (2.4)$$

The work done by the battery upon spontaneous discharge acts to lower the Free energy of the system by a value proportional to the number of electrons transferred, n , the Faraday constant, F , and the difference in electrochemical potential across cell, ΔE .

Conversely, electrochemical work must be done on a battery to charge it. For practical applications, this fundamental analysis must be expanded upon and applied to the various reacting species within the battery. We now build upon these relations and expound on the kinetics of electrochemical cells.

2.1.2 Kinetics

The kinetics of electrodes are best understood in the relationship between the flow of current and driving electrochemical potential. We start with an electrode reaction involving a number, n , of electrons, e , an oxidized species, O , and its reduced state, R .



For a galvanic cell, electrochemical convention defines the electrode at higher electrochemical potential (lower free energy) as the cathode, while the one at lower electrochemical potential (higher free energy) is the anode. Cathodic current results from the reduction of electrode species. Anodic currents oxidize electrode species. Both cathodic and anodic reactions occur simultaneously with electron-transfer rate constants k_c and k_a defined by Arrhenius relations.

$$k_c = A_c e^{-\frac{\Delta G_c}{RT}} \quad (2.6)$$

$$k_a = A_a e^{-\frac{\Delta G_a}{RT}} \quad (2.7)$$

These rate constants have units of $(\text{sec})^{-1}$ while the standard free energies of activation, ΔG_a and ΔG_c , are the sum of a charge-dependent and charge-independent components.

We assume Faraday's law governs the processes, i.e., the amount of electrochemical reaction is proportional to the number of electrons transferred. The charge dependent component of ΔG_a and ΔG_c , can be expanded in terms of a potential difference across the electrode-solution interface, ΔE , and Faradays constant, F . Only a fraction of ΔE is effective in accelerating the reaction rate and is represented by the symmetry parameter α , $0 < \alpha < 1$.

$$\Delta G_c = (\Delta G_{co})_{\Delta E=0} + (\Delta G_c)_{\Delta E} = (\Delta G_{co})_{\Delta E=0} + \alpha n F \Delta E \quad (2.8)$$

$$\Delta G_a = (\Delta G_{ao})_{\Delta E=0} + (\Delta G_a)_{\Delta E} = (\Delta G_{ao})_{\Delta E=0} - (1 - \alpha) n F \Delta E \quad (2.9)$$

Free energies of activation can be expanded into their Arrhenius relations.

Building charge-independent terms and rate constants, A_c , and A_a , into k_{co} and k_{ao} yields the following relations.

$$k_c = k_{co} e^{\frac{\alpha n F \Delta E}{RT}} \quad (2.10)$$

$$k_a = k_{ao} e^{\frac{(1-\alpha) n F \Delta E}{RT}} \quad (2.11)$$

The rate of electron transfer at the electrode interface is a product of these electron transfer rate constants and the concentration of the reacting species, C_O and C_R . The amount of reacting species depends on mass transfer mechanisms at the electrode-electrolyte interface. Diffusion, convection (stirring), and migration (movement of ions in an electric field) are the primary mass transport mechanisms. Thus we can define the net current, j_{net} , at an electrode as a function of the above electron transfer rate constants, C_O , C_R , F , and n .

$$j_{net} = j_c - j_a \quad (2.12)$$

$$j_{net} = nF(k_c C_O - k_a C_R) \quad (2.13)$$

$$j_{net} = nF \left(C_O k_{co} e^{\frac{\alpha n F \Delta E}{RT}} - C_R k_{ao} e^{\frac{(1-\alpha) n F \Delta E}{RT}} \right) \quad (2.14)$$

Of particular interest is the condition when the net current flow across the electrode-solution interface is zero, $C_O=C_R$, $k_a=k_c$, and $\Delta E = \Delta E_{eq}$. Under these conditions of equilibrium potential difference ΔE_{eq} , the current densities represent the equilibrium exchange current density, j_o . The activation overpotential, η , is the difference between ΔE and ΔE_{eq} .

$$\eta = \Delta E - \Delta E_{eq} \quad (2.15)$$

$$j_o = j_c = nFC_O k_{co} e^{\frac{\alpha n F \Delta E_c}{RT}} = j_a = nFC_R k_{ao} e^{\frac{(1-\alpha) n F \Delta E_c}{RT}} \quad (2.16)$$

Finally, substituting j_o and η into Equation 2.12 yields the Butler-Volmer equation.

$$j_{net} = j_o \left(e^{\frac{\alpha n F \eta}{RT}} - e^{\frac{(1-\alpha) n F \eta}{RT}} \right) \quad (2.17)$$

Note that Equation 2.17 assumes equal concentration of the oxidizing species and the reduced species (Figure 2.1). More thorough forms of the Butler-Volmer equation allow for a concentration dependent term [1].

2.1.3 Reversibility

From the Butler-Volmer relation we see that the reversibility of a reaction is only dependent on the free energies of activation. The exchange current is a practical measure of the reversibility of the process. Large exchange currents for a given reaction imply facile activation energies in both directions. Primary batteries have other processes that occur at lower activation energy than the reverse reaction. This is true for the zinc (Zn)

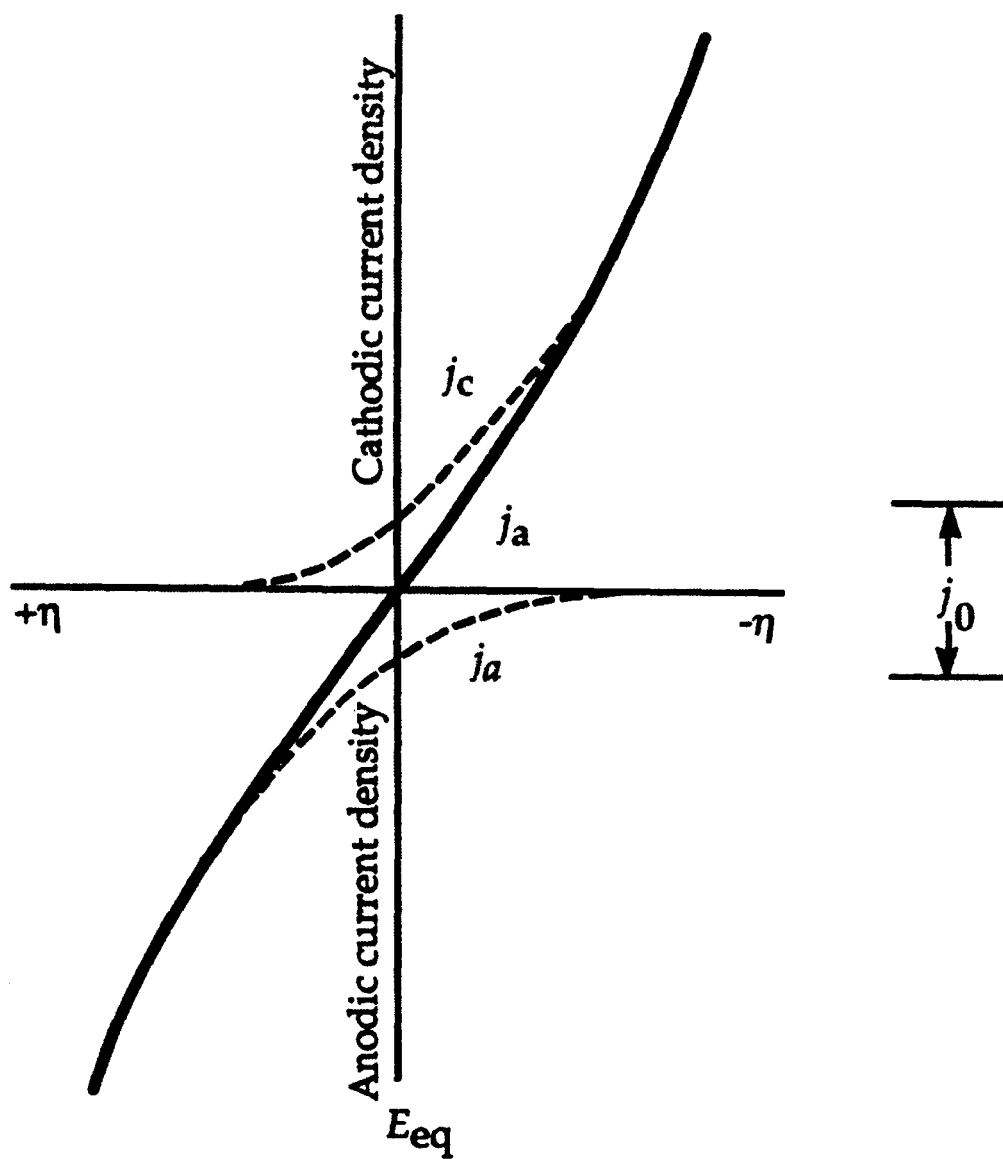


Figure 2.1. Cathodic and anodic components of current as a function of electrode polarization, η [1]

anode of the most popular primary battery design. When the primary cell is discharged, an anodic current flows across the Zn electrode.



If one attempts to recharge the anode by applying an opposing voltage larger than the cell voltage, a cathodic current is observed in the production of hydrogen gas, H₂.



Standard sealed primary cells are not designed to withstand the pressure from this gas build up. Extreme cases result in cell case rupture and subsequent ignition of the evolved H₂ [2].

2.2 Mössbauer Spectrometry

Mössbauer Spectroscopy involves the recoilless resonant absorption and emission of gamma rays to determine the chemical state of atoms in a lattice. It is named for Rudolf L. Mössbauer who was awarded the 1961 Nobel Prize in Physics for his Ph.D. thesis work.

Aspects of the Mössbauer effect are described in Figure 2.2. The energy of a gamma ray photon, E_0 , is the difference in energy between a nuclear excited state, E_e and the ground state, E_g [3]. The atom can recoil with energy, E_R during this emission process. Subsequently the energy of the emitted gamma ray is $E_\gamma = E_0 - E_R$ (Figure 2.2a). The energy linewidth, Γ of this process is proportional to bandwidth of excited states, ΔE (Figure 2.2b).

The resonant process Mössbauer Spectroscopy implies that the emitted and absorbed photon must have equivalent energies precise to $\Gamma = 10^{-6} - 10^{-9}$ eV. Such energy overlap only occurs if individual atoms are not significantly displaced from their lattice sites by emission or absorption of gamma rays. These recoilless processes are only possible for solids in which the entire matrix recoils as a unit. Since the mass of the entire matrix exceeds that of atoms by several orders of magnitude, the recoil energy, E_R is much less than Γ . Figure 2.2c describes the separation of Mössbauer lines by nucleus recoil. The stringent requirement of the resonant recoilless process limits the types of materials that can be studied. Figure 2.3 shows elements that may be studied with Mössbauer Spectroscopy [4].

Mössbauer spectra are typically generated by varying the energy of the gamma ray source. The source is mounted onto a precision velocity transducer that induces an appropriate Doppler shift. When the energy of source gamma rays equal nuclear resonant energies, absorption of the gamma ray will result. The transducer typically scans a small

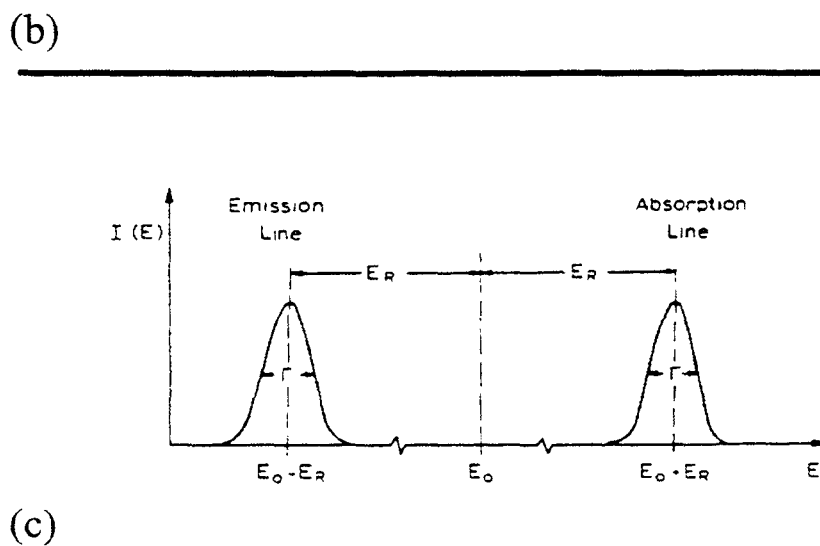
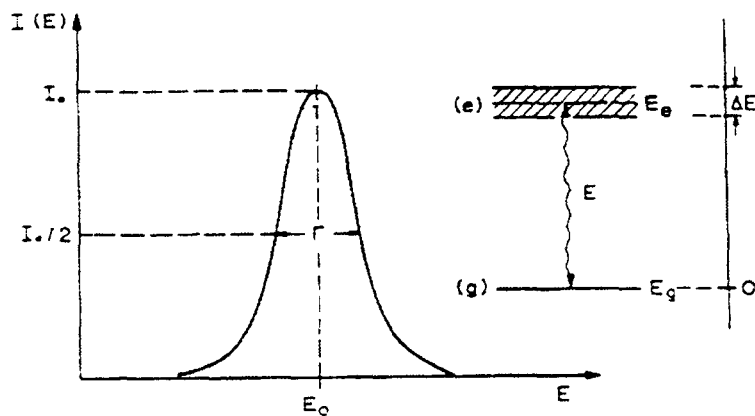
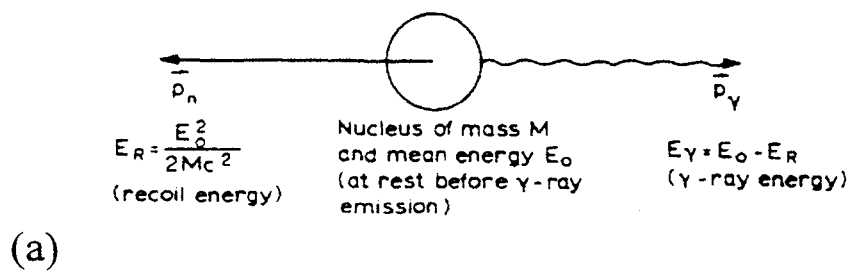


Figure 2.2. Recoil of the nucleus during emission. (b) The Mössbauer line shape from the decay of the nuclear excited state. (c) Separation of the Mössbauer lines by the recoil of the nucleus. The Mössbauer effect is only possible in the absence of this recoil [3].

Elements that Can Be Studied with Mössbauer Spectroscopy

K	Ca	Sc	Ti	V	Cr	Mn	Fe	Co	Ni	Cu	Zn	Ga	Ge	As	Se	Br	Kr
Rb	Sr	Y	Zr	Nb	Mo	Tc	Ru	Rh	Pd	Ag	Cd	In	Sb	Sn	Te	I	Xe
Cs	Ba	La	Hf	Ta	W	Re	Os	Ir	Pt	Au	Hg	Tl	Pb	Bi	Po	At	Rn
Fr	Ra	Ac															
			Ce	Pr	Nd	Pm	Sm	Eu	Gd	Tb	Dy	Ho	Er	Tm	Yb	Lu	
			Th	Pa	U	Np	Pu	Am	Cm	Bk	Cf	Es	Fm	Md	No	Lw	

☒ EASY TO STUDY , EXTENSIVE RESEARCH

▨ MORE DIFFICULT TO STUDY , SOME RESEARCH

☐ VERY DIFFICULT OR LIMITED RESULTS

Figure 2.3. Elements that may be studied by Mössbauer spectroscopy [4].

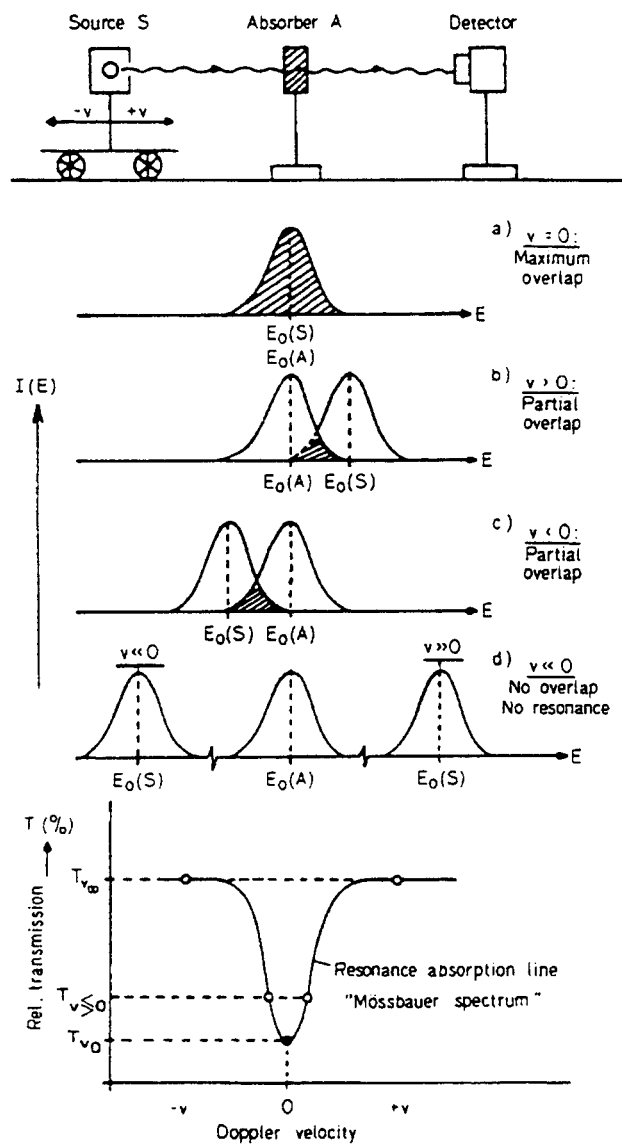


Figure 2.4. Mössbauer effect absorption as a function of the Doppler-derived energy ($E_R=0$ is assumed) [3].

velocity range on the order of millimeters per second. Figure 2.4 illustrates the experiment.

The chemical, crystallographic, and magnetic environment of the absorber influence its nuclear states and thus its Mössbauer spectra. The overall intensity (recoil-free fraction, f) and the line energies (hyperfine parameters) are the two most common pieces of information derived from the Mössbauer spectra.

2.2.1 Recoil Free Fraction, f

The percentage of emissions with no photon response is characterized by the recoil free fraction, f . This factor determines the overall intensity of the resonance spectrum. The recoil free fraction can be predicted using the Debye model [3]

$$f = e^{-2M} \quad (2.20)$$

with

$$M = \frac{6E_R}{k_b \theta_D} \left[\frac{1}{4} + \left(\frac{T}{\theta_D} \right)^2 \int_0^{\frac{\theta_D}{T}} \frac{\zeta d\zeta}{e^\zeta - 1} \right] \quad (2.21)$$

Here, T is temperature, k_b is Boltzman's constant, θ_D is the Debye temperature, and E_R is the recoil energy defined in Fig. 2.1. This temperature-dependent form of f , also known as the Lamb-Mössbauer factor, is comparable to the Debye-Waller factor in X-ray scattering. The main difference being that lattice vibrations are short relative to an X-ray scattering process but long compared to the lifetime of the Mössbauer excited state. The Lamb-Mössbauer factor reduces to:

$$f = \exp \left(-\frac{E_R}{k_b \theta_D} \left\{ \frac{3}{2} + \frac{\pi^2 T^2}{\theta_D^2} \right\} \right) \quad T \ll \theta_D \quad (2.22)$$

and

$$f = \exp\left(-\frac{6E_R T}{k_b \theta_D^2}\right) \quad T \geq \theta_D \quad (2.23)$$

The recoil free fraction is influenced by same factors that determine the vibrational response of a lattice. These include E_R , T , and stiffness of the atom in the lattice, represented by θ_D . The recoil free fraction is higher at lower temperatures and with less energetic photons.

2.2.2 Hyperfine Parameters

Electronic effects on the nucleus determine the absorption peak energies of Mössbauer spectra. These effects are isomer shifts (IS), electric quadrupole hyperfine interactions (QS), and magnetic dipole hyperfine interactions (MD). A summary of these interactions is displayed in Figure 2.5.

2.2.2.1 Isomer Shift, IS

Isomer shifts are caused by interactions of nuclear charge with electron density inside the nucleus. Electrons must have finite probability of being inside the nucleus (s-electrons) to directly influence the isomer shift, though other electrons (p-, d-, and f-) indirectly influence these shifts. This electronic interaction with the nucleus can be interpreted to give unequivocal information about the valence of the absorbing atom. The isomer shift is:

$$IS = const \cdot \left(\frac{\Delta R}{R}\right) \left[|\psi(0)|_A^2 - |\psi(0)|_S^2 \right] \quad (2.24)$$

with

R = the radii of assumed spherical atomic nuclei,

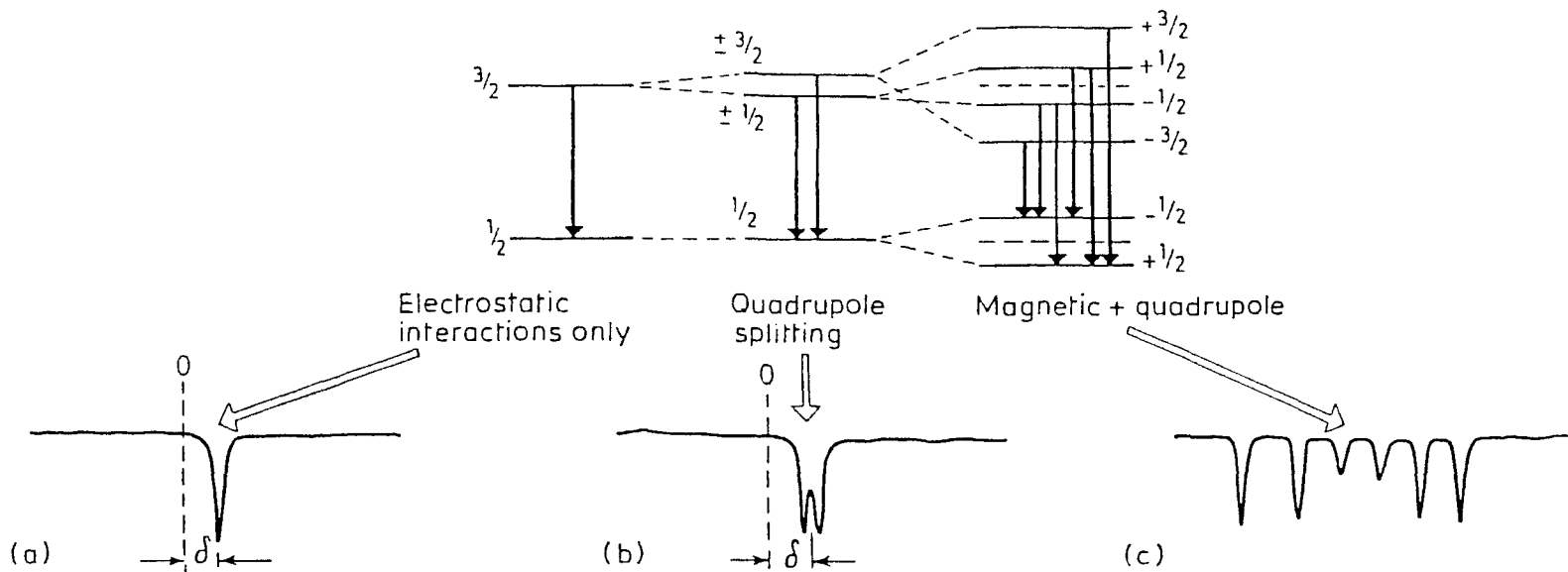


Figure 2.5. Changes in nuclear energy caused by quadrupole and magnetic splitting with the resulting Mössbauer spectra [5].

$|\psi(0)|^2$ = the probability density of the s-electron at the nucleus

$\Delta R = R_e - R_g$ (e = excited, g = ground)

A and S subscripts -> absorber and source

2.2.2.2 Electric Quadrupole Hyperfine Interactions, QS

A nucleus with a spin greater than 1/2 will have an electric quadrupole moment that will interact with an electric field gradient. An electric field will split the degenerate energy levels of a nucleus with spin 3/2 level into two distinct degenerate levels $\pm 3/2$ and $\pm 1/2$. This allows for two absorption levels and thus a splitting of peaks in Mössbauer spectra. The energy linewidth, QS, of this splitting is:

$$QS = \frac{1}{2} e V_{zz} Q \left(1 + \frac{1}{3} \chi^2 \right)^{\frac{1}{2}} \quad (2.25)$$

with

$$\chi = \frac{(V_{xx} - V_{yy})}{V_{zz}}. \quad (2.26)$$

Here e is electron charge, Q is the nuclear quadrupole moment, V_{ii} are the electric field gradients along the given direction ($i = x, y, z$), and χ is an asymmetry parameter, which describes the difference in electric field gradient in the x and y direction. Non-uniform electron density within an atom can cause these field gradients. Thus quadrupole splitting is greatly influenced by the bonding of the absorbing atom. An oversimplified model of this effect is shown in Figure 2.6.

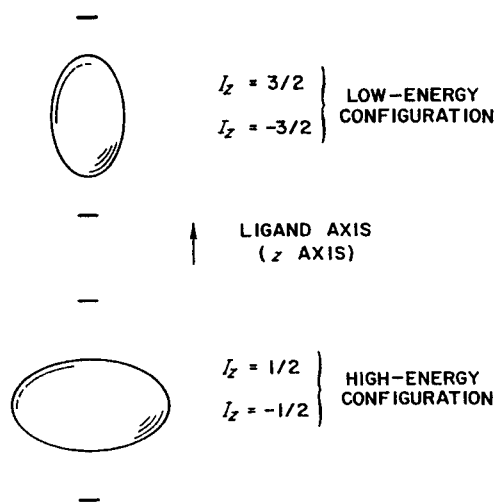


Figure 2.6. Coupling of the nuclear quadrupole moment with nearby charges. The oversimplified drawing depicts the $I_z=3/2$ and $I_z=1/2$ sins exactly along and perpendicular to the z-axis; the correct mechanical solution is more complex [4].

2.2.2.3 Magnetic Dipole Hyperfine Interactions

Magnetic dipole hyperfine interactions, also known as the nuclear Zeeman effect, arise from interactions of the nuclear magnetic moment with a magnetic field at the nucleus. The magnetic moment of a nucleus is related to its angular momentum. The angular momentum or nuclear spin I , is the sum of the orbital, L and spin, S angular momentum, $I = L + S$. The magnetic field splits degenerate energy levels into $2I+1$ equally spaced, non-degenerate energy levels. Splitting of the excited state, $I_e=3/2$, and ground state, $I_g=1/2$, creates eight possible energy transitions. From these eight transitions, only six are allowed by selection rules: $\Delta I=1$; $\Delta m=0, \pm 1$. The probabilities of these six transitions and thus their corresponding peak intensities can be calculated by squaring the corresponding Clebsch-Gordon coefficients (Table 2.1 [6]).

Table 2.1 Relative Mössbauer peak intensities for ^{57}Fe assuming no thickness effects.

Absorption Peaks	Normalized Intensities
3 and 4	1
1 and 6	3
2 and 5	varies from 0 to 4 depending on the moment projection on the magnetic field; isotropic average of 2.

An absorbing atom influenced by the nuclear Zeeman effect will yield a distinct sextet of peaks dependent on the magnetic field at its nucleus (hyperfine magnetic field, HMF). When there are multiple magnetic environments for an absorbing element, the Mössbauer spectra is a sum of superimposed sextet peaks. The values of the hyperfine magnetic fields, HMG, can be extracted from spectra using the method of La Caër and Dubois [7].

The HMF is generated by 1) the orbital angular momentum of 4f and 5f electrons, 2) densities of spin-up and spin-down electrons at the nucleus (polarization of local s-electrons),

3) externally applied fields, or 4) any combination of the above. In the case of iron, the magnetic polarization model [8] explains the chemical origins of perturbations in the HMF. The HMF perturbation, ΔH , is the sum of perturbations caused by local environments, H_L , and those caused by nonlocal environments, H_{NL} . With ^{57}Fe , H_L arises from the polarization of s-electrons by unpaired 3d-electrons at the same atom. H_L is directly proportional to the change of the local magnetic moment at the ^{57}Fe atom. Neighboring atoms can affect the bonding nature of the ^{57}Fe 3d-electrons and thus influence H_L .

The second component, H_{NL} , arises from polarization of nonlocal 4s-electrons at the ^{57}Fe nucleus. These perturbations are due to changes in the magnetic moments of neighboring lattice sites. H_N is dependent on whether neighboring sites are occupied by solute atoms or by other ^{57}Fe atoms whose moments may be perturbed by nearby solute atoms.

2.3 Electron Energy Loss Spectrometry

Electron Energy Loss Spectroscopy (EELS) measures the energy distribution of electrons inelastically scattered by a specimen. A typical EELS experiment utilizes a transmission electron microscope (TEM) to direct an electron beam through a magnetic prism. The magnetic prism spatially separates electrons by energy. The energy distribution of the scattered electrons gives valuable information on the valence, bonding, and coordination of elements of the specimen. EELS is not affected by the fluorescence yield limitation that restricts light elements X-ray analysis. The sensitivity of EELS to light elements makes it a preferred technique for analysis of Li chemical environments.

2.3.1 Kinematics

The interaction of a fast moving electron with an atom is illustrated in Figure 2.7. The difference between the initial and final wave vectors, k_0 and k_1 respectively, [9] is given by

$$\mathbf{q} = \mathbf{k}_0 - \mathbf{k}_1 \quad (2.27)$$

We assume the scattering is symmetric in the azimuthal angle to describe the scattering process in terms of the scalar wave numbers. Conservation of energy reveals the relationship between the energy loss of a scattering event and the scalar wave numbers of the electron.

$$E = [(m_0c^2)^2 + (\hbar k_0c)^2]^{\frac{1}{2}} - [(m_0c^2)^2 + (\hbar k_1c)^2]^{\frac{1}{2}} \quad (2.28)$$

which simplifies to

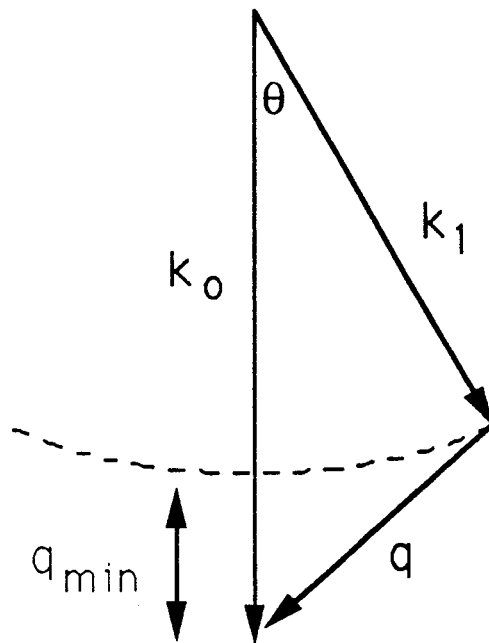


Figure 2.7. Kinematics of an electron inelastically scattered by an atom.

$$\left(\frac{E}{R}\right) \left[\gamma - \frac{E}{2m_o c^2} \right] = (k_o a_o)^2 - (k_1 a_o)^2 \quad (2.29)$$

where $\gamma = (1 - v^2/c^2)^{-1/2}$, m_o is the rest mass of an electron, a_o is the Bohr radius, and $R = 13.6$ eV is the Ryberg energy. Equation 2.29 is independent of the scattering angle θ , implying that all scattered wave vectors of the same magnitude correspond to inelastic events of the same energy.

The law of cosines is applied to the vector triangle defined by the conservation of momentum (Figure 2.7).

$$q^2 = k_o^2 + k_1^2 - 2k_o k_1 \cos \theta \quad (2.30)$$

Substituting Equations 2.3.4 into 2.3.5 gives

$$(q a_o)^2 = \frac{2E_o \gamma^2}{R} \left[1 - \left(1 - \frac{E}{E_o \gamma} + \frac{E^2}{2E_o \gamma^2 m_o c^2} \right)^{\frac{1}{2}} \cos \theta \right] - \frac{E \gamma}{R} + \frac{E^2}{2R m_o c^2} \quad (2.31)$$

We are now interested in the case for $\theta = 0$, corresponding to $q = q_{\min} = k_o - k_1$. From the binomial expansion of the square root term, we find terms up to the second order in E cancel, leaving

$$(q a_o)_{\min}^2 = \frac{E^2}{4R E_o} + \frac{E^3}{(8\gamma^3 R E_o^2)} + \dots \quad (2.32)$$

For nearly all collisions, $\gamma^{-3} E/E_o \ll 1$ holds true and thus only the E^2 terms are important.

We can then express q_{\min} as

$$q_{\min} \cong k_o \theta_E \quad (2.33)$$

$\theta_E = E/(2\gamma E_o)$ is the characteristic or most probable scattering semiangle. θ_E can be thought of as the classical scattering angle in “billiard-ball” collisions.

The excitations of core electrons show distinct profiles that give insight to the coordination and valence state of the excited electrons. The intensity of inner-shell transitions, $I(E, \beta)$, can be expanded in terms of N , the number of atoms per unit area in the sample illuminated by the incident electron beam, $I_i(\beta)$, the total number of electrons collected by the spectrometer, and $d\sigma/dE$ the energy differential cross section per atom.

$$I(E, \beta) = NI_i(\beta) \frac{d\sigma}{dE}(E, \beta) \quad (2.34)$$

The energy differential cross section is obtained by integrating the double differential cross section $d\sigma^2/dEdq$ obtained from Fermi's Golden Rule of scattering theory. Under the first Born approximation, which assumes only single scattering events within each atom, $d\sigma/dE$ is given by

$$\frac{d\sigma}{dE} = \frac{8\pi R}{E_o} \rho(E) \sum_l \int_{q_{\min}}^{q_{\max}} \frac{1}{q^3} \left| \langle \epsilon l | e^{i\mathbf{q}\cdot\mathbf{r}} | n_0 l_0 \rangle \right|^2 dq \quad (2.35)$$

where \mathbf{r} is the position vector of the incident electron. The matrix element is evaluated over the coordinates of all atomic electrons and summed over all degenerate energy states. Lastly, ψ_1 is a continuum wave functions such that the square of the matrix has units of inverse energy. The continuum wave function is normalized by the energy, $E^{0.25}$, which gives an inverse square root dependence. This means. The energy differential cross section can further be expressed in terms of df/dE , the general oscillator strength (GOS).

$$\frac{d\sigma}{dE} = \frac{4\pi a_o^2}{(E/R)(E_o/R)} \rho(E) \sum_l \int \frac{df(q, E)}{dE} d[\ln(qa_o)^2] \quad (2.36)$$

with

$$\frac{df(q, E)}{dE} = \frac{E}{R(qa_o)^2} \left| \langle \epsilon | e^{iq \cdot r} | n_o l_o \rangle \right|^2 \quad (2.37)$$

The GOS for the excitation of a 1s electron (K-shell ionization) can be expressed on a two-dimensional plot known as a Bethe surface (Figure 2.8). This plot clearly demonstrates that maximum intensity occurs just above the inner-shell binding energy E_K , and at $\theta=0$, $q=q_{min}=k_o\theta_E$. This regime corresponds to the *dipole region* of scattering and, in terms of a particle model, represents “soft” collisions with relatively large impact parameters. At a large energy loss, the intensity is concentrated in a region known as the *Bethe Ridge* where q satisfies

$$(qa_o)^2 = \frac{E}{R} + \frac{E^2}{(2m_o c^2 R)} \quad (2.38)$$

The equivalent scattering angle, $\theta_c=(2\theta_E)^{1/2}$, is known as the *cut-off angle*, above which scattering intensity falls to zero. These “hard” collisions have small impact parameters and primarily involve the electrostatic field of a single inner-shell.

Evaluation of Equation 2.36 yields an approximate behavior of

$$\frac{d\sigma}{dE} \propto E^{-s} . \quad (2.39)$$

Here, s is constant over a limited energy range. The value for s tends to decrease as β , E and the thickness of the sample increase. For inner-shell scattering, s is 4.5 for small angles and 2.5 for large angles.

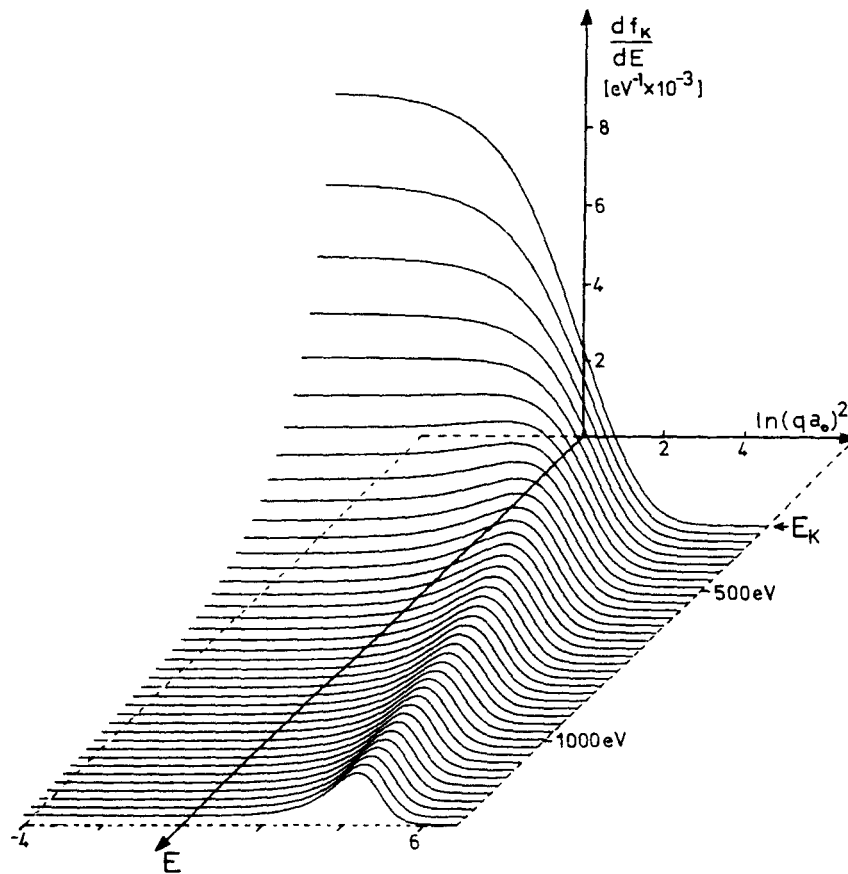


Figure 2.8. Bethe surface for K-shell ionization of carbon, calculated from a hydrogenic model [9].

Ionization energies of electrons from the K, L, M, N, and O (quantum numbers $n=1-5$ respectively) can be approximated by

$$E_n = \frac{-R(Z - \epsilon_n)^2}{n^2} \quad (2.40)$$

Here $R= 13.6$ eV is the ionization energy of hydrogen and $Z-\epsilon_n$ is the effective atomic number decreased by screening [10]. The observed “core edges” are referred to by nomenclature similar to that of X-ray spectroscopy. Core K, L, M, N, and O edges [11] refer to excitations of K, L, M, N, and O shell electrons (Figure 2.9).

The above expressions assume that the incident electrons undergo one inelastic scattering event. In practice EELS spectra are dominated by *plural* scattering (>1 scattering event) and *multiple* scattering (>20 scattering events). Quantitative analysis of EELS spectra usually requires data processing techniques to remove plural and multiple scattering contributions. The Fourier-log method [12] deconvolutes the entire energy loss spectrum and must be used to determine core edge losses at less than 100 eV. The Fourier-ratio method [13] provides convenient deconvolution for high-energy core edges.

2.3.2 Data Acquisition and Analysis

EELS spectra were acquired at room temperature using a Gatan 666 parallel detection magnetic prism spectrometer attached to a Philips EM 420 transmission electron microscope. A schematic drawing of a parallel EELS spectrometer is shown in Figure 2.10. Measurements were performed with 100 keV electrons at a collection angle of either 11 or 50 mrad. The TEM beam current was approximately 7 nA.

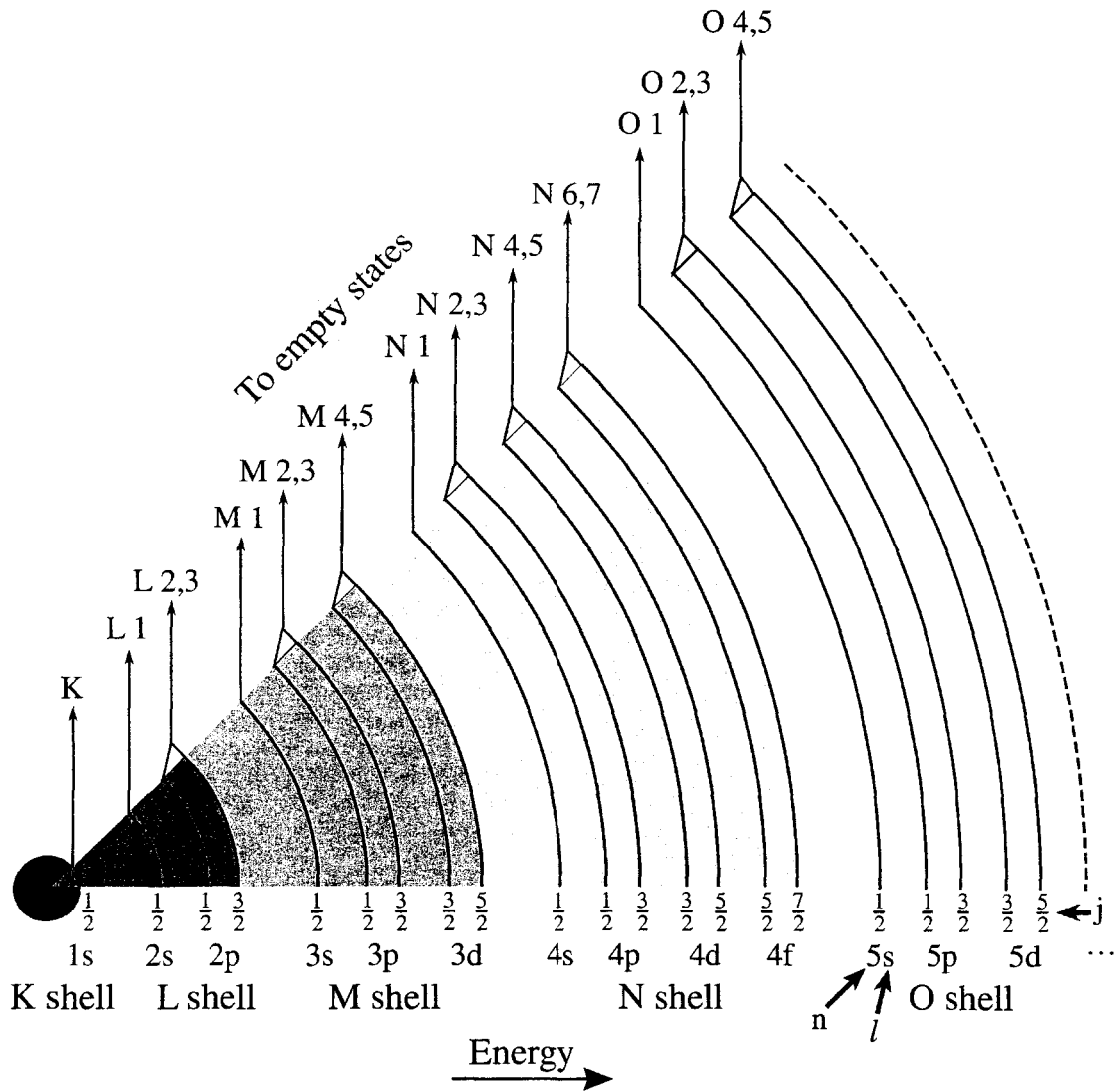


Figure 2.9. Possible inner-shell ionization edges and their associated nomenclature [11].

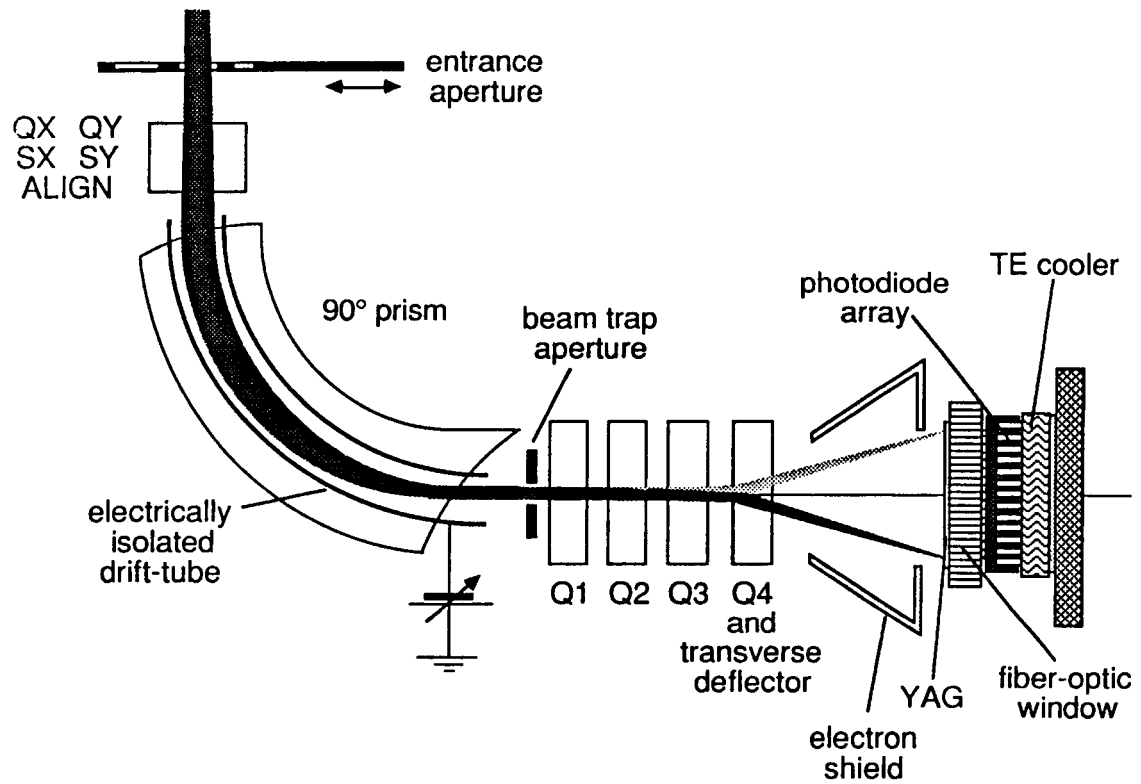


Figure 2.10. Gatan model 666 parallel-recording spectrometer. **Q** and **S** represent quadrupole and sextupole electron lenses respectively [18].

The spectrum signal to noise ratio and sample spatial resolution can be optimized by operating the TEM in either image or diffraction mode. “Coupling” refers to the object for the spectrometer at the projector crossover. We adopt the microscopists’ terminology referring to “image mode” as the case when the specimen image is projected onto the view screen and the back focal plane of the objective lens contains the Fourier transform of the image or diffraction pattern (diffraction coupling, Figure 2.11). “Diffraction mode” refers to the case when the diffraction pattern is projected on the screen (image coupling). In this case, the collection angle, β , is determined by the width of the spectrometer aperture and the camera length (Figure 2.12). 120 mm is the shortest camera length on the Philips EM 420 and the largest collection aperture is 5 mm. Thus the maximum obtainable collection angle in diffraction mode is 21 mrad, while the collection angles in excess of 100 mrad can easily be obtained in image mode. Spectra are generally acquired at the same β since detailed intensity variations in the spectrum depend on the range of electron scattering angles gathered by the spectrometer.

The magnetic prism bends the electron beam via the Lorentz Force, $\mathbf{F} = -e \mathbf{v} \times \mathbf{B}$, with $-e$ being the charge of an electron, \mathbf{v} its velocity, and \mathbf{B} the magnetic field. For \mathbf{v} perpendicular to \mathbf{B} , the electron adopts a circular trajectory of radius R . Equating the Lorentz force with the centripetal force, $F = mv^2/R$, we see $R = mv/eB$. Thus, electrons of lower kinetic energies or lower velocities undergo larger deflection. If the detector is positioned to accept electrons that traverse roughly one-fourth of the circular orbit, the spectrometer is called a 90°-prism spectrometer. The electron beam is extremely sensitive to external magnetic fields. These fields disrupt beam trajectory and influence spectra resolution. The moving of metal chairs, fields from computer monitors,

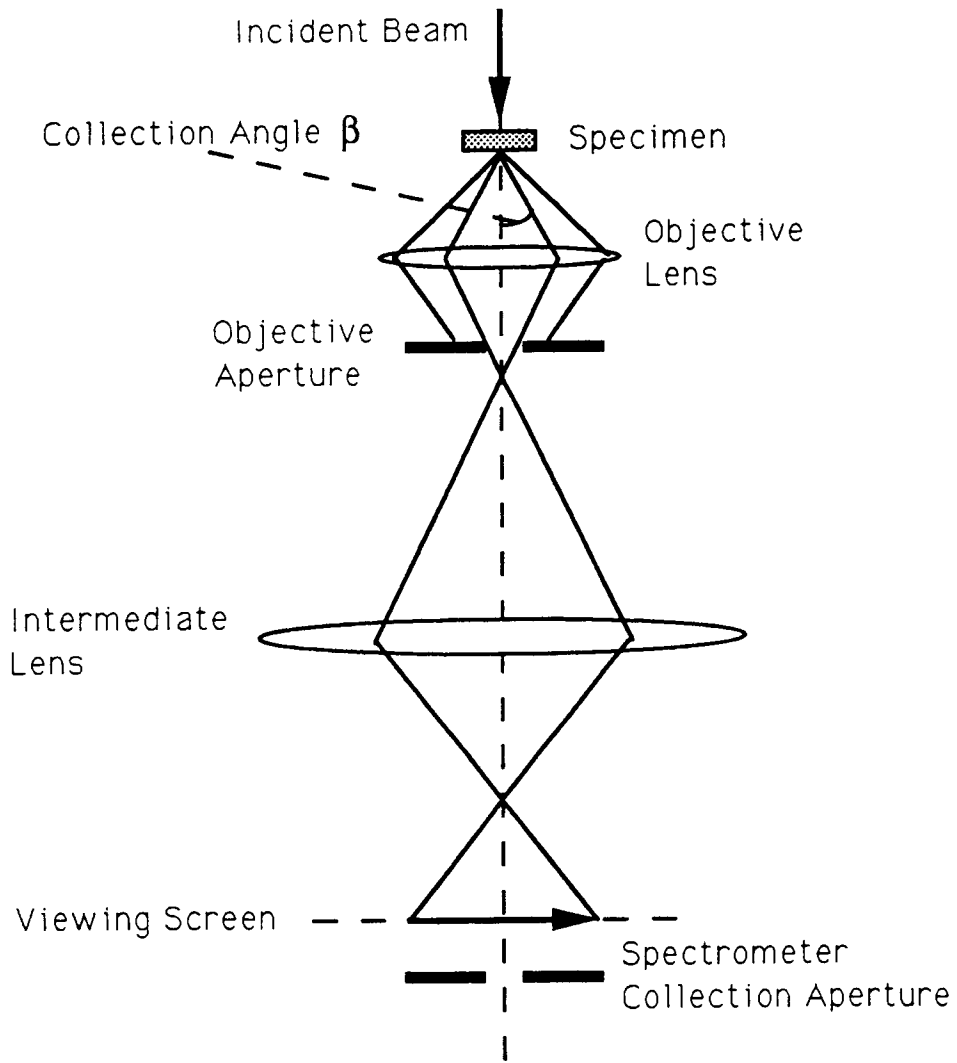


Figure 2.11. Collection-angle geometry for energy loss spectra collected in a transmission electron microscope in image mode [19].

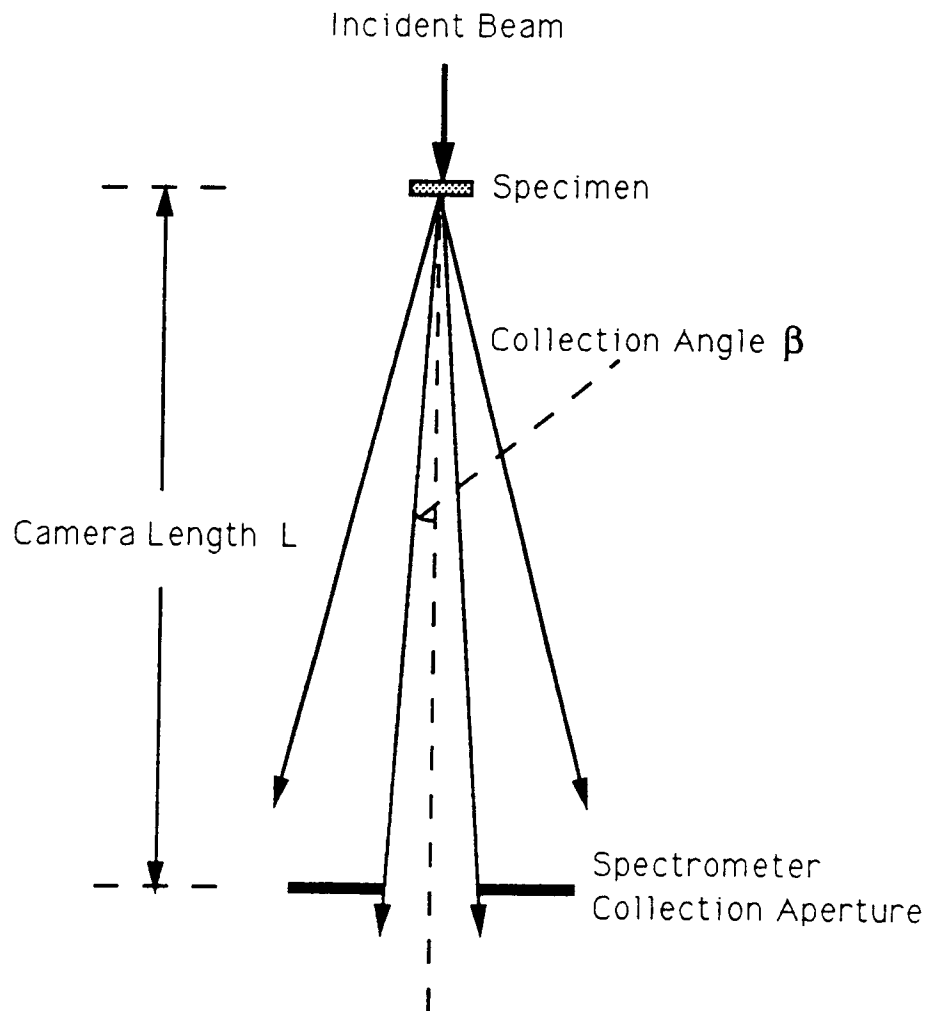


Figure 2.12. Collection-angle geometry for energy loss spectra acquired in diffraction mode [19].

and the opening of metal doors can all cause measured spectra to drift or broaden. Care was taken to ensure consistent experimental conditions.

The Gatan 666 parallel detector is a single crystal yttrium-aluminum garnet (YAG) scintillator, fiber-optically coupled to a linear photodiode array of 1024 channels. Each channel is made up of a 25 μm wide diode. A thermoelectric cooler attached to the photodiode array regulates scintillator temperature, thus minimizing thermal noise contributions.

Parallel detectors have high detective quantum efficiency but add noise to the raw data and suffer non-uniform response across the array [14]. A number of steps were taken to ensure accurate spectra were acquired from the detector. Thermal and electronic noise components were measured by a detector dark count obtained from the array in the absence of illumination. A detector dark count was measured for each spectrum under identical acquisition times. Two techniques were employed to address the non-uniform channel to channel gain of the detector array. First, an instrument response was recorded by uniformly illuminating the detector. Subsequent spectra were normalized by this instrument response (Figure 2.13). Secondly, multiple scans of a feature were taken by shifting the spectra across the array. These separate scans were subsequently aligned and summed.

2.3.3 Energy Resolution

The energy distribution in the incident electron beam is dictated by electrostatic interactions between electrons at the filament crossover (Boersch effect). The resolution of typical electron sources are 2.5 eV with Tungsten, 1.5 eV with LaB_6 , and 0.5 eV with

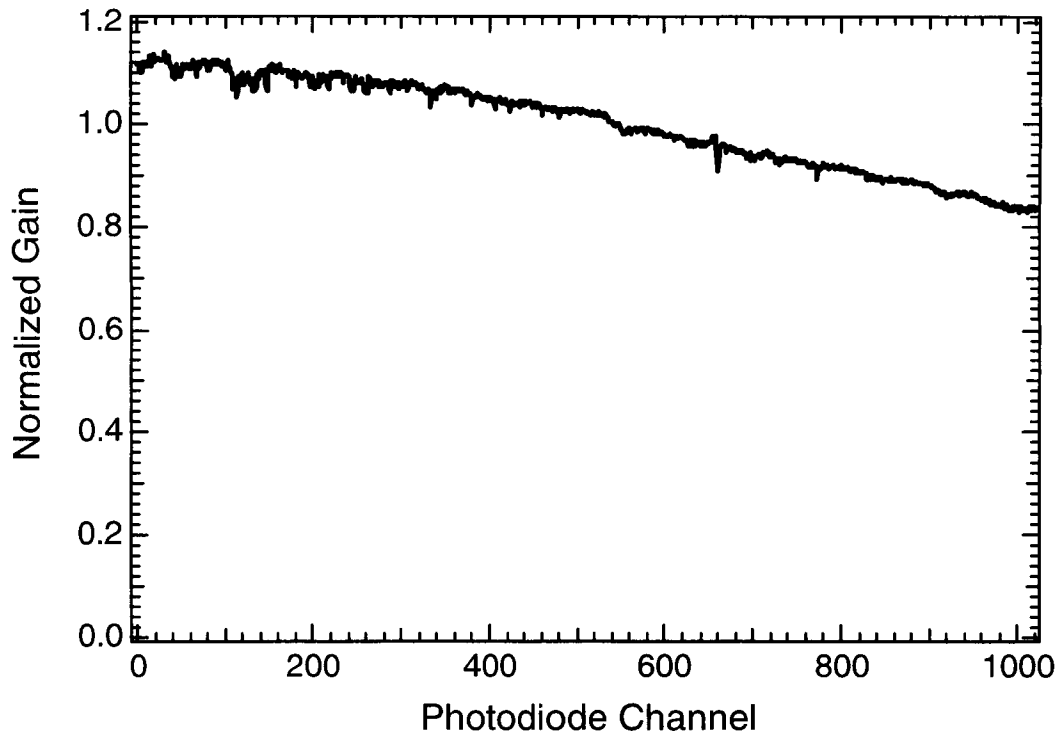


Figure 2.13. Instrument response of linear photodiode array.

cold Field Emission Guns. Energy resolution decreases slightly as the energy loss increases. This is never more than 1.5 times the zero-loss peak up to about 1000 eV energy loss. Energy resolution also degrades as electron voltage increases, with the full width half maximum tripling from 100keV to 400keV. Lastly, resolution degrades with larger spectrometer entrance apertures due to contributions from off-axis beams.

Optimum energy resolution is achieved with small projector crossover and a small (1 mm or 2 mm) entrance aperture. The energy resolution of our Gatan 666 spectrometer is 1.2 eV with a dispersion of 0.2 eV/channel and 2.5 eV at 0.5 eV/channel, as measured from the shape of the zero-loss peak in the EELS spectra.

2.3.4 Energy Loss Spectrum

An EELS spectrum is a measure of the elastic and inelastic scattering processes of the transmitted electrons. The important inelastic interactions, in order of energy loss, are phonon excitations, inter- and intra-band transitions, plasmon excitations, and inner-shell ionization. Values for the energy loss and scattering semiangle, θ_E , are summarized in Table 2.2. θ_E is the most probable scattering semiangle for a given energy loss.

Table 2.2 Characteristics of EELS Processes

Process	Energy loss (eV)	θ_E (mrads)
Phonons	~0.02	5 - 15
Inter/intra-band transitions	5 - 25	5 - 10
Plasmons	~5 - 25	<~ 0.1
Inner-shell ionization	~10 - 1000	1 - 5

2.3.4.1 Zero-Loss Peak

The zero-loss or elastic peak is made up of unscattered electrons, elastically scattered electrons, and electrons which excite phonons. These electrons lose negligible

energy relative to EELS measurements upon passing through a sample. The full width half maximum of the zero-loss peak is a few eV and is dependent on the energy distribution of the incident electron beam. The intensity of the zero-loss peak can damage the scintillator and saturate the photodiode array. Care must be taken to minimize the area of the detector exposed to the zero-loss peak.

2.3.4.2 Low-Loss Spectra

The low-loss region of an EELS spectrum is typically defined as the region from 0 eV – 50 eV. Spectral features in this region are associated with interactions of the incident electrons with valence electrons. The principle mechanisms that influence the low-loss spectrum are plasmon interactions, single-electron excitations and excitons. Although calculating the intensity of the low-loss region is technically feasible, the potential results do not yet justify the labor to do so. Spectra from the low-loss region are best identified by comparison to compiled EELS spectra. The EELS Atlas by Ahn and Krivanek is an excellent resource [15].

2.3.4.2.1 Plasmons

Valence electrons can be excited to collectively oscillate with modes determined by the sample's plasma frequency, ω_p . These oscillations of valence electrons, known as *plasmons*, are longitudinal waves of charge density propagating through the sample. The plasmon energy is proportional to the root of the free-electron density, n .

$$E_p = \hbar\omega_p = \hbar\left(\frac{ne^2}{\epsilon_0 m}\right)^{\frac{1}{2}} \quad (2.41)$$

For h , planks constant, ϵ_0 , the permittivity of free space, ω_p , the plasmon frequency, e and m are the electron charge and mass. Free electron densities for metals range from 10^{22} to 10^{23} cm^{-3} , giving plasmon energies $\sim 10\text{eV}$ [16].

For 100 keV incident electrons, the typical mean-free paths for plasmon excitations is $l_p, \approx 100 \text{ nm}$ and scattering angles are typically $< 0.1 \text{ mrad}$. Therefore incident electrons interacting with plasmons are strongly forward scattered. Multiple plasmon collision events may occur depending on sample thickness. Figure 2.14 displays plasmons of a thick Al sample. It is speculated that plasmons can be carried by one atom at a time explaining their occurrence in insulating materials [9]. Unfortunately, all metals and alloys have similar plasmon energies, although with careful observation it is possible to observe changes in composition from small shifts in the plasmon peaks.

Above a critical wave vector, $q_c = \omega_p/v_F$, a plasmon can transfer all its energy to a single electron, which can then lose energy through an interband transition. This transfer in energy takes place when the plasmon phase velocity is comparable to the Fermi velocity, v_F . The transfer of energy to single-electron transitions is the dominant mechanism of plasmon damping.

2.3.4.2.2 Single –Electron Excitations

In addition to plasmon excitations (a collective electron response), incident electrons can transfer energy to a single atomic electron within the specimen. If sufficient energy is transferred, the atomic electron can undergo inter or intra-band transitions. These single-electron interactions (i.e., the creation of electron-hole pairs)

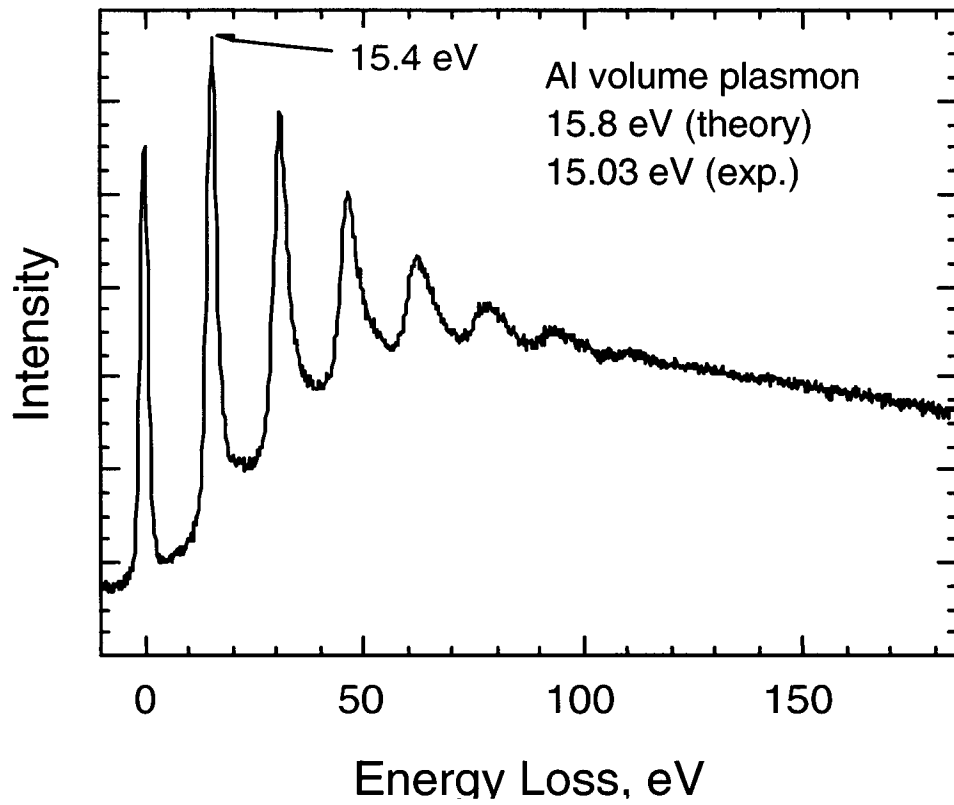


Figure 2.14. Aluminum volume plasmons.

can add fine structure to the energy-loss spectrum and broaden (possibly shift) plasmon peaks [17].

2.3.4.2.1 Excitons

In semiconductors and insulators, electrons can be excited from the valence band to a series of states lying below the bottom of the conduction band. Such an excitation creates a bound conduction-band electron and a valence-band hole. This bound electron-hole pair is called an *exciton*. The resulting energy loss, E_x , is dependent on the band gap energy, E_g , and the exciton binding energy E_b (n is an integer).

$$E_x = E_g - E_b/n^2 \quad (2.42)$$

An exciton can move through the crystal and transport energy, though remains electrically neutral.

The ability to detect excitons by EELS depends greatly on binding energy. In weakly bound excitons, the radius of the “orbiting” electron is larger than the interatomic spacing. These are known as *Mott-Wannier* excitons and have binding energies, $E_b < 1$ eV. These are commonly found in high-permittivity semiconductors (e.g. Cu_2O , CdS) and generally not observed in EELS. *Frenkel* excitons are tightly bound and the hole is usually on the same atom as the electron. These excitons are common in molecular crystals and alkali halides ($E_b \bullet$ several electron volts). In alkali halides, energy-loss peaks due to exciton transitions are observed below the “plasmon” resonance peak (Section 3.5).

2.3.4.3 Core-Loss Spectra

Spectral features above 50 eV are associated with ionization of atoms by excitation of their core electrons into higher unoccupied energy states (Figure 2.15). The relaxation of the atom to its initial state may produce a characteristic X-ray or Auger electron.

Relative to plasmon excitations, the ionization cross sections of core transitions and their mean-free paths are small. As follows, core edges intensities are small compared to plasmon peaks and become smaller with increasing energy loss (Equation 2.39). The characteristic scattering angles, θ_E , of core transitions is much larger than those of plasmons (Table 2.2) and thus, for thick samples, it is common to observe plasmon signatures superimposed on the near edge structure of a core loss.

The shapes of ionization edges contain information about the valence and coordination of the excited atom. The shape of the region within 50 eV from the onset energy, termed the energy loss near edge structure (ELNES), is greatly influenced by the nature of the lowest unoccupied states (Section 2.3.1). There are no simple relationships between specific edge types and shapes, although near edge structures can be classified into various categories: saw-tooth, delayed edge, whitelines, plasmon-like, and sharp maximum / delayed continuum [10]. Small intensity oscillations can sometimes be detected at energies extending beyond 50 eV above the onset energy. These oscillations arise from the constructive and destructive interference of backscattered electrons. These oscillations are called extended energy-loss fine structure (EXELFS) and are analogous to extended X-ray absorption fine structure (EXAFS) in X-ray Spectra.

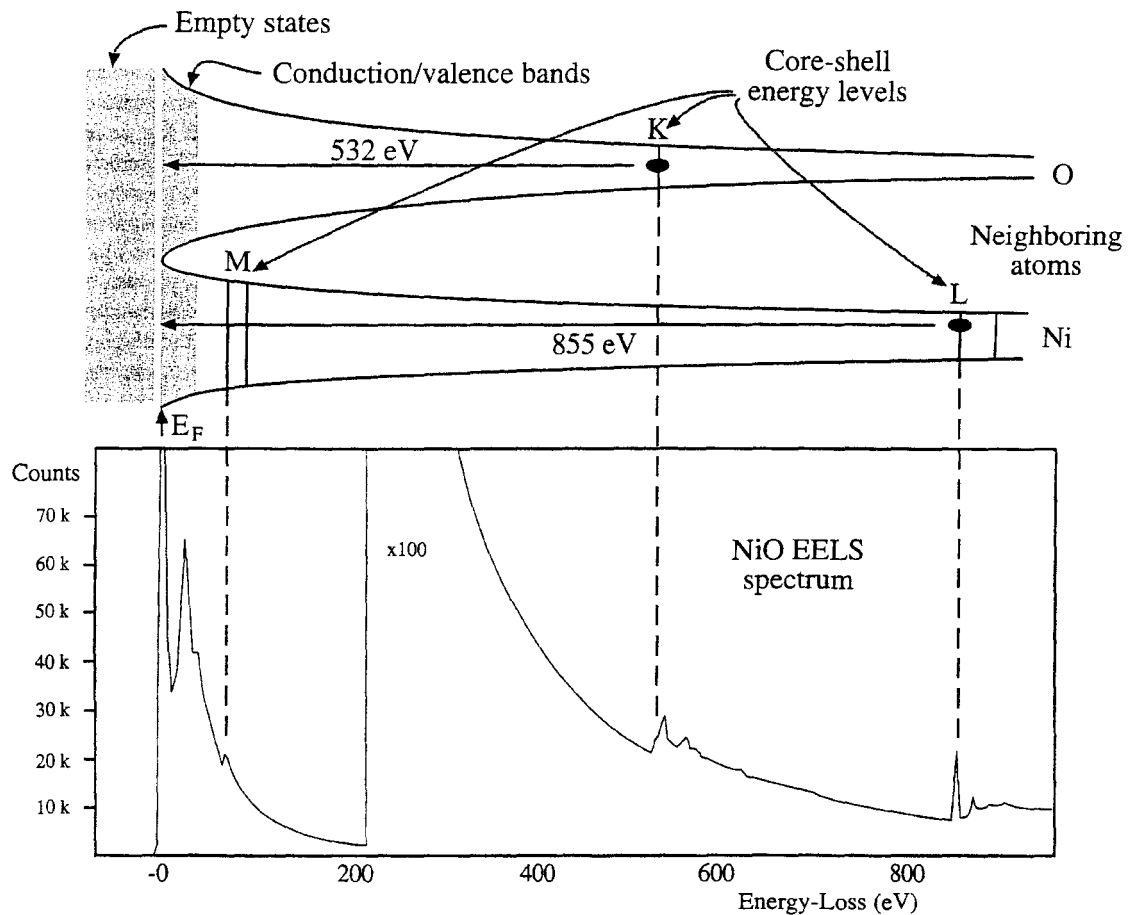


Figure 2.15. The correspondence between the energy levels of electrons surrounding Ni and O atoms and the energy loss spectrum. The zero-loss peak is above the Fermi energy E_F , the plasmon peak is at the energy level of the conduction/valence bands, and the critical ionization energy required to eject specific K-, L-, and M- shell electrons is shown.

Ionization-loss electrons, like plasmon-loss electrons, are strongly forward scattering (Table 2.2). The angular distribution of ionization-loss electrons is generally confined to < 15 mrad, which is well within the spectrometer collection angle.

2.3.5 XPS and EELS

X-ray photoelectron spectroscopy (XPS) data provide information on core-binding energies by measuring the energy spectrum of ejected photo-electrons. Differences in the EELS and XPS spectra are a consequence of the different electrons these methods detect. XPS utilizes photons ($\text{Al K}\alpha = 1486.6$ eV) to excite bound electrons into the vacuum level. The energy of an ejected electron, E , is given by $E = \hbar\omega - E_b - \phi$ where ω is the frequency of the incident photon, E_b is the electron binding energy and ϕ the work function of the specimen. Thus, in terms of the transition matrix (Equation 2.37), the final state of the excited electron, ψ_1 , is within the vacuum level. In contrast, EELS measures the difference between energy of initial and final states where the final states, ψ_1 , include the lowest unoccupied states of the excited electron. The mean free path of photo-electrons is on the order of 1 nm. Thus XPS measurements provide analysis of the top few atomic layers. EELS measures the bulk properties by measuring the energy lost by an electron transmitted through 50 – 100 nm of material.

2.4 References

- [1] D. T. Sawyer, A. Sobkowiak, J. L. Roberts Jr, *Electrochemistry for Chemists*, (John Wiley & Sons, New York, 1995).
- [2] D Linden, *Handbook of Batteries*, (McGraw-Hill. New York, 1976).
- [3] P. Gütlich, R. Link, and A. Trautwein, *Mössbauer Spectroscopy and Transition Metal Chemistry* (Springer-Verlag, New York, 1978).
- [4] R. L. Cohen, *Applications of Mössbauer Spectroscopy* (Academic Press, New York, 1976) Volume I.
- [5] P. E. J. Flewitt and R. K. Wild, *Physical Methods for Materials Characterization*, (Institute of Physics Publishing, London, 1994).
- [6] T. Stephens, *Chemical Environment Selectivity in Mössbauer Diffraction*, Thesis, (California Institute of Technology, Pasadena 1996).
- [7] G. Le Caër and J. M. Dubois, *J. Phys. E : Sci. Instrum.* **12**, 1083 (1979).
- [8] B. T. Fultz, *Mössbauer Spectroscopy Applied to Magnetism and Materials Science*, edited G. J. Long and F. Grandjean (Plenum Press, New York, 1993), Chap. 1.
- [9] R.F. Egerton, *Electron Energy-Loss Spectroscopy in the Electron Microscope*, Plenum Press, New York, 1986.
- [10] L. Reimer, *Transmission Electron Microscopy*, Springer-Verlag, New York. (1997).
- [11] D. B. Williams and C. B. Carter. *Transmission electron Microscopy; Spectrometry IV*, (Plenum Press, New York, 1996).
- [12] R. E. Burge and D. L. Misell, *Phil. Mag.* **18**, 261 (1968).
- [13] R. F. Egerton and M. J. Whelan, *Phil. Mag.* **30**, 739 (1974).

- [14] R.F. Egerton, *Transmission Electron Energy Loss Spectrometry in Materials Science*, the Minerals, Metals, and Materials Society, Pennsylvania, 1992.
- [15] C. C. Ahn and O. L. Krivanek,, *EELS Atlas*, Gatan Inc, Warrendale, PA (1983).
- [16] Raether, Heinz, *Exciton of Plasmons Interband Transitions by Electrons*, Springer-Verlag, New York, 1980.
- [17] W. Y. Liang and S. L. Cundy, *Phil. Mag.* **19**, 1031 (1969).
- [18] M. M. Disko, C. C. Ahn, and B. Fultz, *Transmission Electron Energy Loss Spectroscopy in Materials Science*, (TMS, Warrendale, 1992).
- [19] D. H. Pearson, *Measurements of White Lines in Transition Metals and Alloys using Electron Energy Loss Spectroscopy*, Thesis, (California Institute of Technology, Pasadena 1991).

Chapter 3 Lithium EELS Spectra

To interpret local chemical environment effects in EELS spectra of Li materials, it is important to investigate a systematic series of Li systems to establish standards and trends. In this section we discuss the near edge structure of EELS spectrum before exploring various Li systems.

3.1 Near Edge Structure

The electron energy loss near-edge structure (ELNES) of a core excitation can give insight to the structural and electronic properties of the excited atom. ELNES essentially probes the local symmetry -projected unoccupied density of states (DOS) at a particular atomic site. EELS fingerprints arise when the local DOS available to the excited electron is dominated by the interaction of the central atom with neighboring atoms. Thus ELNES is sensitive to the valence and coordination of the excited species. After studying a number of reference compounds with known structural and chemical properties, it is possible to identify unknown phases in complex microstructures.

The valence of the central atoms greatly affects the edge onset energy of an excited electron. Shifts in core binding energies from the effective charge of a central atom have been well characterized by XPS. The final state energies of the excited electron also shift with the effective charge of the central atom. The chemical shift of an edge energy onset, measured by EELS, is the combination of these effects. The chemical shifts of lithium compounds are especially prominent due to the large electronegativity of lithium leading to substantial band gap energies in insulating samples.

Relaxation effects play an important role in the ELNES of lithium compounds.

When a core hole is created by an inner-shell excitation, the surrounding electron orbitals are pulled inward. The screening by the surrounding orbitals reduces the magnitude of the measured binding energy by an amount equal to the “relaxation energy”. Leapman et al. [1] found that a difference in relaxation energy between a metal and its compounds has a significant effect on the measured chemical shift. Lithium, with its small atomic number ($Z=3$), should be particularly susceptible to relaxation effects.

3.2 Beam Damage

3.2.1 Electron Specimen Interactions

The reactivity of reduced Li and its susceptibility to radiation damage under an electron beam present a formidable challenge to EELS analysis of Li samples. The nature of the radiation damage depends greatly on the microstructure of the sample. The dominant effect of radiation damage on crystalline microstructures is atomic displacement (knock-on damage) resulting in vacancy / interstitial pairs known as Frenkel defects.

Thin samples of metallic Li and LiF were prepared by thermal evaporation onto amorphous holey carbon TEM grids. A large glove bag was placed over the evaporator to minimize atmospheric exposure during transfers. The evaporating chamber was back-filled with Ar where the samples were immersed in Fluorinert® FC-43 gettered with Li chips.

The calculations of threshold energy for knock-on damage suggest a significant number of inelastic collisions result in atomic Li displacement. In an elastic collision of a

stationary particle of mass M and an incident particle of mass $m \ll M$ and velocity v , conservation of energy and momentum dictate the maximum energy transferred to the stationary particle, T'_{max} , is

$$T'_{max} = \frac{2(\gamma_2 mv^2)(\gamma_2 mv^2 + 2mc^2)}{Mc^2} . \quad (3.1)$$

Here c is the speed of light. The energy required to displace an atom, T_d , is related to the details of inter-atomic bonding. Average atomic displacement energies estimated from sublimation energies were found to be 6.1 eV for Li and 31.2 eV for carbon in graphite [2]. Rearranging Equation 3.1, one can calculate the threshold incident electron energy, U_{th} in MeV, which transfers energy, $T'_{max} = T_d$ in eV, to an atom of atomic weight A . Figure 3.1 displays the values of U_{th} plotted versus T_d [3].

$$U_{th} = \frac{\sqrt{(14.4 + 0.186 \cdot A \cdot T_d)}}{20} - 0.511 \quad (3.2)$$

Assuming elastic collisions, U_{th} for incident electrons are calculated to be 19 keV for Li and 150 keV for carbon in graphite. The dependence of U_{th} on the atomic weight, A , indicates we need primarily be concerned with knock-on damage to Li atoms as opposed to other elements present in our compounds (the exception being Li halides described below).

To ensure beam damage was not resulting from sample heating, we calculated the rise in temperature of the sample. The rise in specimen temperature can be derived from the radial form of the radial form of the differential equation for heat conduction

$$\frac{1}{r} \frac{\partial}{\partial r} \left[r \frac{\delta T}{\delta r} \right] + \frac{1}{\kappa_e} j \left(\frac{dU}{dz} \right) = 0 \quad (3.3)$$

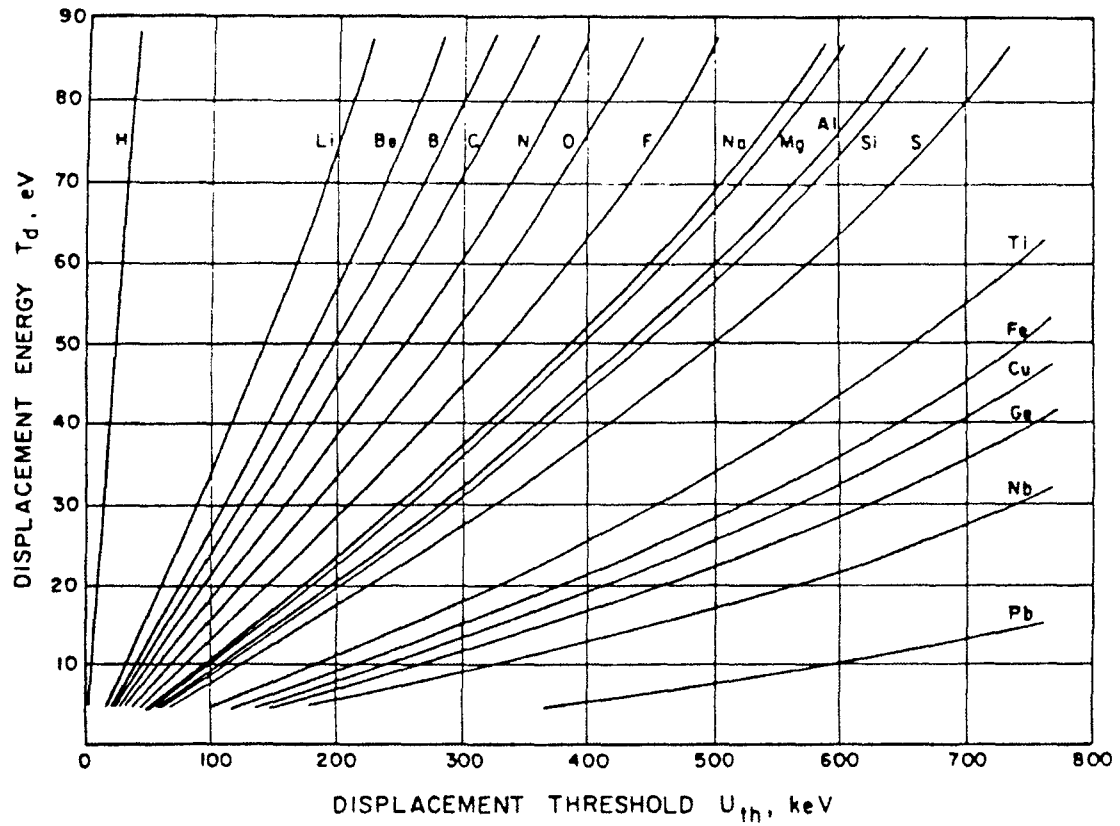


Figure 3.1. Knock-on displacement energy of atomic species [3].

for the appropriate boundary conditions. Here dU/dZ is the average rate of energy loss, κ is the specimen thermal conductivity, j is the beam current, and e is the charge of an electron. The average rate of energy loss to electronic processes in a solid of density N given determined from the Thomson-Widdington law [3]

$$-\frac{dU}{dz} \cong 4\pi a^2 R^2 N Z \frac{1}{\frac{1}{2} m_e v^2} \ln \frac{\frac{1}{2} m_e v^2}{T_{\min}} \quad (3.4)$$

where a is the Bohr radius, R is the Ryberg constant and Z is the atomic number. T_{\min} is the minimum energy transferable to an atom constrained in a solid (phonon $\sim 10^{-2}$ eV).

For a specimen of uniform thickness, thermally anchored to a good conducting medium at the periphery $r = s$, the maximum temperature rise at the center of an irradiated area of radius b is

$$T_{\max} = j \frac{(dU/dZ)}{2\pi\kappa e} \cdot \left(\frac{1}{2} + \ln\left(\frac{s}{b}\right) \right) \quad (3.4)$$

Assuming a range in sample thickness of 400 nm to 1000 nm, $b = 400$ nm, $s = 20$ μ m, $j = 7$ nA, a rise in sample temperature of 0.5°K to 1.0°K is calculated from irradiation of 100 keV electrons.

Metallic Li samples appeared to “boil” during TEM observations at 200 keV. This was determined to be a consequence of knock-on damage since the calculated temperature rise was negligible. Thus, the majority of radiation damage is a result of the direct transfer of momentum from incident electrons to the Li nucleus. 100 keV was chosen as a reasonable compromise between knock-on damage and instrument performance.

3.2.2 Radiation Damage of Metallic Lithium

Beam damage of metallic Li was studied at 100 keV by concentrating the electron beam onto a thin area of the Li sample. Figure 3.2 presents a time sequence of EELS spectra for this exposed region. Over a few minutes, the area of the low-loss region was significantly reduced, resulting in the suppression of Li plasmons at 7.5 eV and 15eV. This is consistent with sample thinning as Li atoms are liberated from the sample under the electron beam. Under TEM image mode, the specimen was observed to undergo physical shrinkage, especially under a focused incident beam. Over slightly longer time periods Li plasmon peaks evolved into distinct profiles commonly associated with oxidized Li, primarily LiOH [4]. Under a concentrated electron beam, the broad profile of the Li K-edge evolves to two sharp peaks at 59.5 eV and 64.5 eV, similar to peaks observed in samples exposed to atmosphere [4]. Exposure to the intense electron beam can remove metallic Li, exposing preexisting LiOH or stimulate Li reactions with moisture and oxygen present in the microscope, leading to the formation of LiOH [5].

The possibility of excited lithium reacting with the amorphous carbon substrate has been ruled out in light of beam damage experiments performed on SiO₂ substrates. Radiation damage of metallic Li on SiO₂ substrate show identical results as those performed on amorphous carbon substrate. The Li K-edge in LiC₆ and other reactive Li alloys (LiAl, Li₂₂Sn₅, Li₂₂Si₅) all show the same peaks at 59.5 eV and 64.5 eV when exposed to the atmosphere.

The majority of the observed LiOH is inherent to our specimen and not formed in situ during exposure to the focused electron beam. The region displayed in Figure 3.2 loses 26% of its low-loss intensity during exposure to the electron beam.

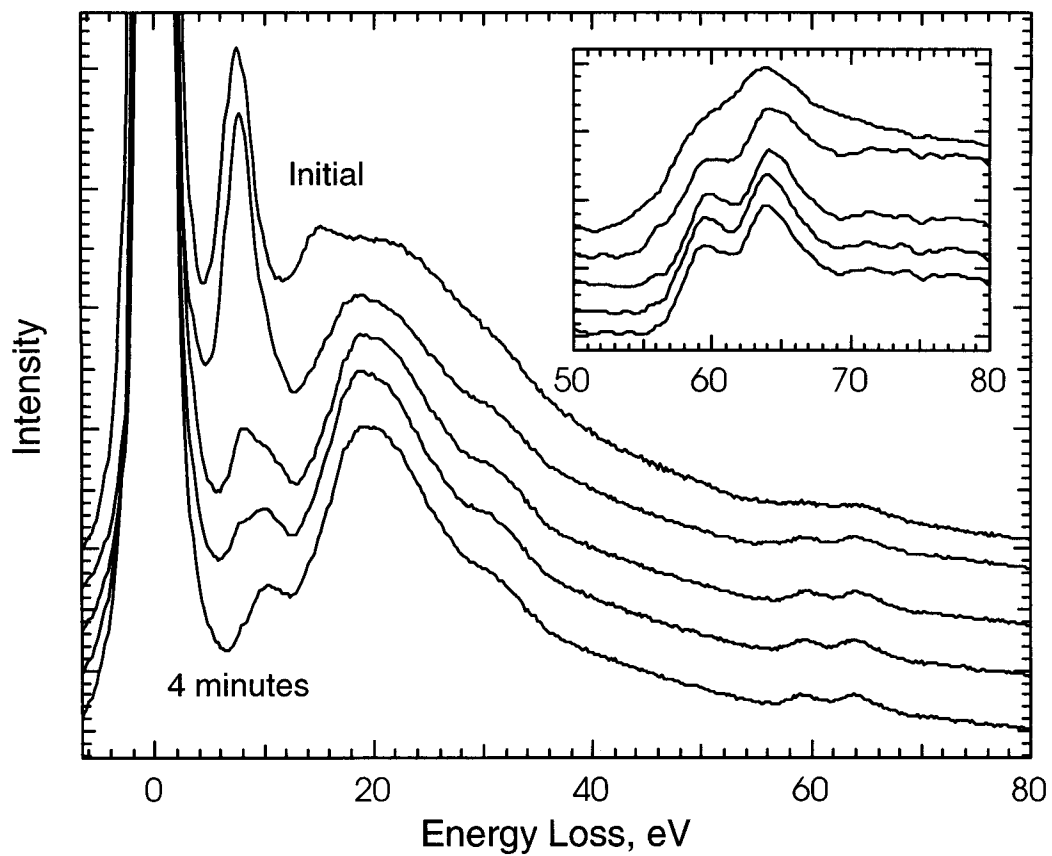


Figure 3.2. EELS spectra of metallic lithium exposed to focused 100 keV electron beam.

This reduction in spectral intensity is consistent with thinning of the specimen. If LiOH were growing in situ, we would expect the low-loss intensity to increase as the region's thickness increased relative to the plasmon mean free path.

There is some degree of moisture present in the TEM chamber. When metallic Li is exposed to an H₂O partial pressure in the TEM vacuum of 10⁻⁸ Torr, one finds a prevalence of Li oxides rather than Li hydroxides [6]. However, it is possible that rate of LiOH growth is enhanced by the focused electron beam.

Table 3.1 Thermodynamic constants for select lithium compounds [7].

Material	ΔG° (kcal/mol)	ΔH° (kcal/mol)	ΔS° (kcal/mol)
H ₂ O	-54.6	-57.8	45.1
Li ₂ O	-134.3	-143.1	9.06
LiOH	-105.1	-116.6	10.23
LiH	-16.4	-21.7	4.79
Li ₂ O ₂	-136.5	-151.2	13.5
Li ₂ CO ₂	-37.1	-47.5	9
Li ₂ C ₂	-13.4	-14.2	14
LiCl	-91.79	-97.58	14.17

Although from Table 3.1 we find Li₂O is more thermodynamically stable, hydroxylation of the oxide dominates in the presence of H₂O. Zavadil and Armstrong [6] propose the following reaction pathways for metallic Li exposure to H₂O.



The lack of spectroscopic evidence of LiH suggest further hydrolysis and reaction with metallic Li:



3.2.3 Radiation Damage of Lithium Fluoride

Electron irradiation of alkali halides simulates desorption of halogen atoms through the mechanism of radiolysis. This leads to the aggregation of the alkali metal and the formation of color centers [8,9]. Figure 3.3 displays the energy –to-momentum conversion sequence for the radiolysis of alkali halides. In the case of LiF, this results in an F_2^- molecular ion, called an H center, on a single anion site and the exciton electron at the anion vacancy, known as an F center. The H-F centres constitute Frenkel defects.

Numerous low-energy electron energy loss spectroscopy (LEELS) studies on LiF correlate peaks at 2.1eV with point defect (F centers) excitations [10]. These defects are produced along with a large flux of secondary electrons which induce F centers to coalesce into F_2^- centers. EELS spectra of beam damaged LiF show a strong temperature dependence, most likely attributed to surface relaxation and restoration processes [11]. Correspondingly, metallic Li clusters are smaller at lower temperatures as agglomeration of metallic islands is suppressed.

Figure 3.4 displays EELS spectra of LiF under a concentrated electron beam. The low-loss spectrum of Figure 3.4a clearly shows a decrease in the characteristic LiF 22 eV bulk plasmon and the evolution of a 7 eV bulk plasmon of metallic Li. The intensity of the 7eV plasmon decreases as Li atoms are liberated from the sample with further irradiation. The area under the LiF spectra decreases with exposure consistent with thinning of the LiF sample. Figure 3.4b expands the region around the Li K-edge. The distinct peaks at 62 eV and 70 eV evolve into a broad Li K-edge consistent with metallic Li. We expect the bold spectra of Figure 3.4 to represent the specimen before much of

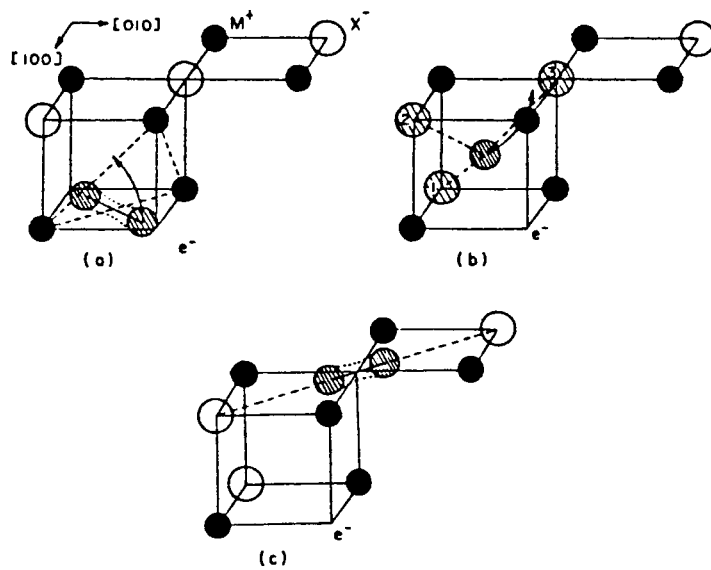


Figure 3.3. Radiolytic displacement sequence for rock-salt structure alkali halides.

Cations M^+ are black, anions X^- are white and molecular ions X_2^- are shaded.

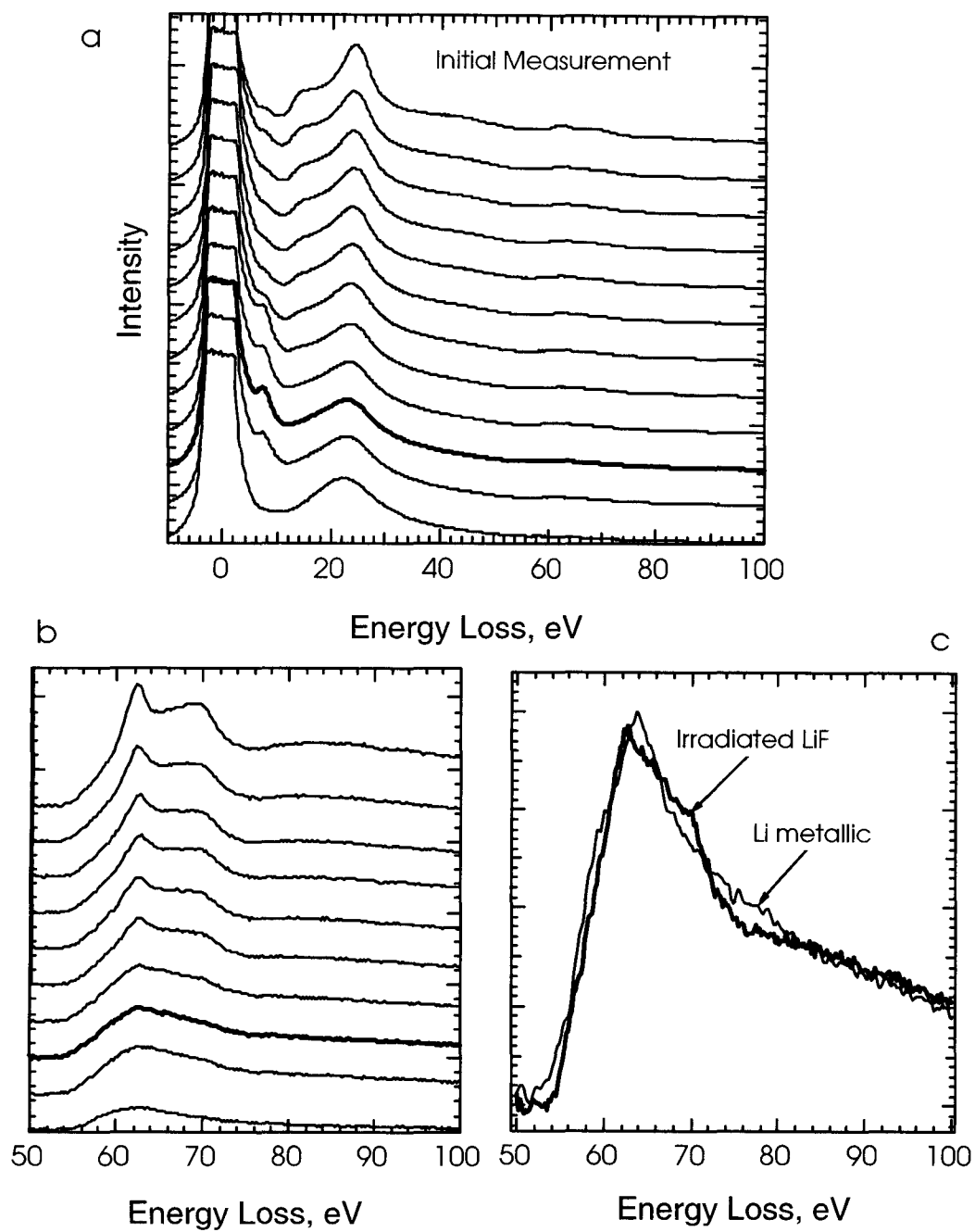


Figure 3.4. Evaporated LiF irradiated by 100 keV electrons for four minutes.

the created metallic Li was lost to knock-on damage. Figure 3.4c compares the Li K-edge EELS spectra of beam damaged LiF with that of a metallic Li specimen.

Figure 3.5 displays a dark field / bright field pair of the damaged area. The diffraction pattern contains distinct rings from fcc LiF and broader bands from bcc Li metal. The dark field / bright field pair was taken using the overlapping (220) ring of LiF and (211) ring of Li metal. Particles of LiF range from 30 nm to 1 μ m, while particles of Li average 10 nm. The round and broad features of the Li K-edge are consistent with those of small particles (Figure 3.4b).

A thorough understanding of radiation damage and its effects is essential for obtaining accurate EELS measurements of lithium compounds. In addition to the displacement of Li and halide atoms, changes in the valence of transition metals valence can be induced by radiation damage [12]. These changes in valence can affect the near edge structure of measured EELS spectra. Specifically with lithium metal oxides, changes in the transition metal valence can affect the O K-edge in addition to the core edges of the metal. (Section 3.4). Enough beam damage studies were performed in the course of this work to give confidence in our ability to understand and control the radiation damage (Figure 3.6).

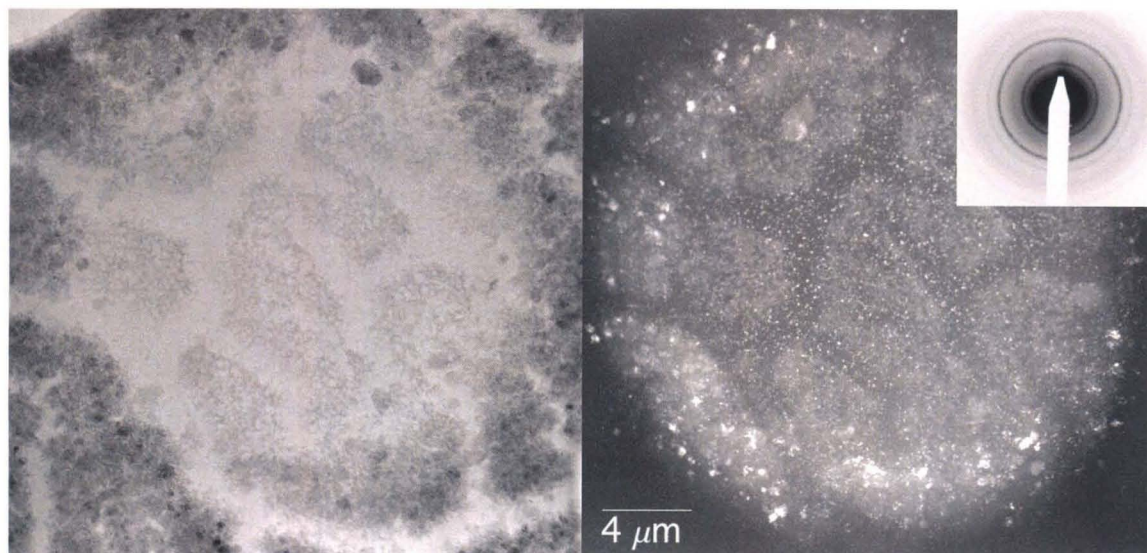


Figure 3.5. TEM bright and dark field micrographs of evaporated LiF irradiated by 100 keV electrons. Larger LiF particles (30-1 μ m) are imaged from the fcc (220) ring while metallic Li particles (10nm) are imaged from the bcc (221) ring.

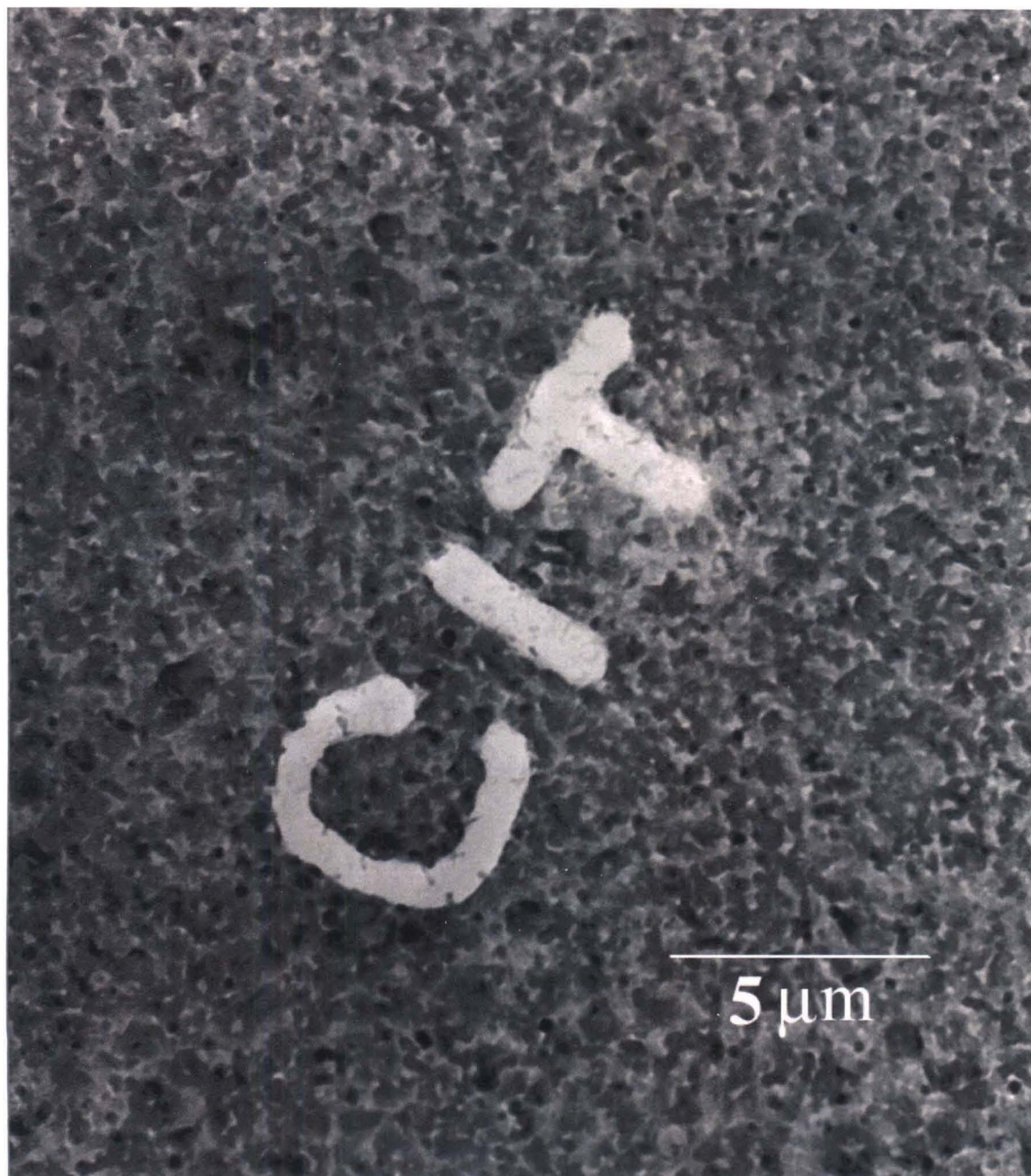


Figure 3.6. TEM bright field micrograph of evaporated $\text{Li}_{22}\text{Sn}_5$ irradiated by a focused beam of 200 keV electrons.

3.3 Metallic Lithium and Alloys

The low-loss spectrum of a lithium alloy is typically dominated by bulk plasmons. Figure 3.7 shows the profiles of metallic Li, LiAl, and $\text{Li}_{22}\text{Sn}_5$ with plasmon peaks at 7 eV, 15 eV, and 7 eV respectively. The plasmon-loss energy is proportional to the square root of the free electron density. The low-loss spectra may contain multiple plasmon peaks depending on thickness. Buried among the bulk plasmons are the Al L_{23} edge at 70 eV, a Sn N_{45} edge at 27 eV, and Li K-edges around 55 eV. The bulk plasmons shown in Figure 3.7 overwhelm the other useful edges. Thus, to study the core transitions, one must use thinner specimens or deconvolute the spectra of thicker samples.

The Li K edges of the tested Li alloys have broad profiles characteristic of transitions to continuum states. The edges shift relative to metallic Li, consistent with their respective Fermi Energies. Figure 3.8 displays background-subtracted Li K-edges of metallic Lithium, LiAl, and $\text{Li}_{22}\text{Sn}_5$.

The background-subtracted Li K-edge displayed in Figure 3.8 is comparable to those reported by Liu and Williams [13]. From optical density of states calculations of the Li K edge, Bross [14] predicts a sharp peak at 56.3 eV and two broader secondary peaks at 58.4 and 61.4 eV. These peaks are most likely attributed to Van Hove singularities (where $\nabla E(\mathbf{k})=0$ in the energy band structure). Multiple scattering, phonon broadening at room temperature and the finite energy resolution of the spectrometer limit our ability to observe the features proposed by Bross.

The large atomic ratio of Li in the $\text{Li}_{22}\text{Sn}_5$ alloy has made this alloy attractive as an anode material. This alloy has a voltage of 0.1 V vs. lithium and a large theoretical capacity, 791 mAh/g, but suffers from poor cycle life attributed to mechanical failure

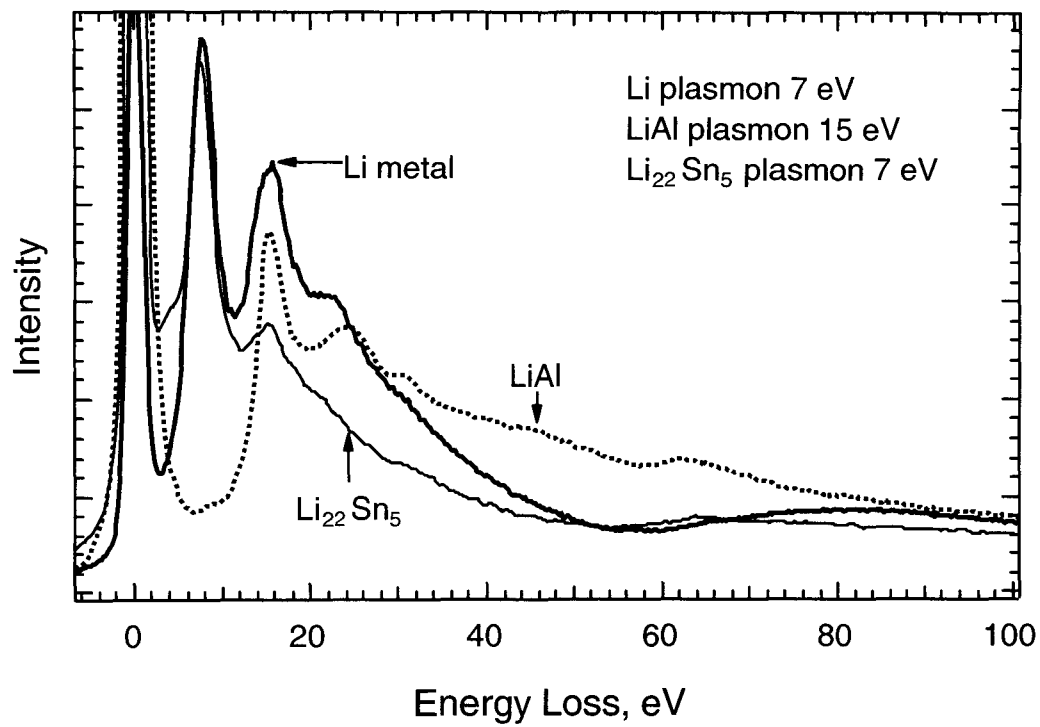


Figure 3.7. The low-loss spectra of metallic Li, LiAl, and $\text{Li}_{22}\text{Sn}_5$.

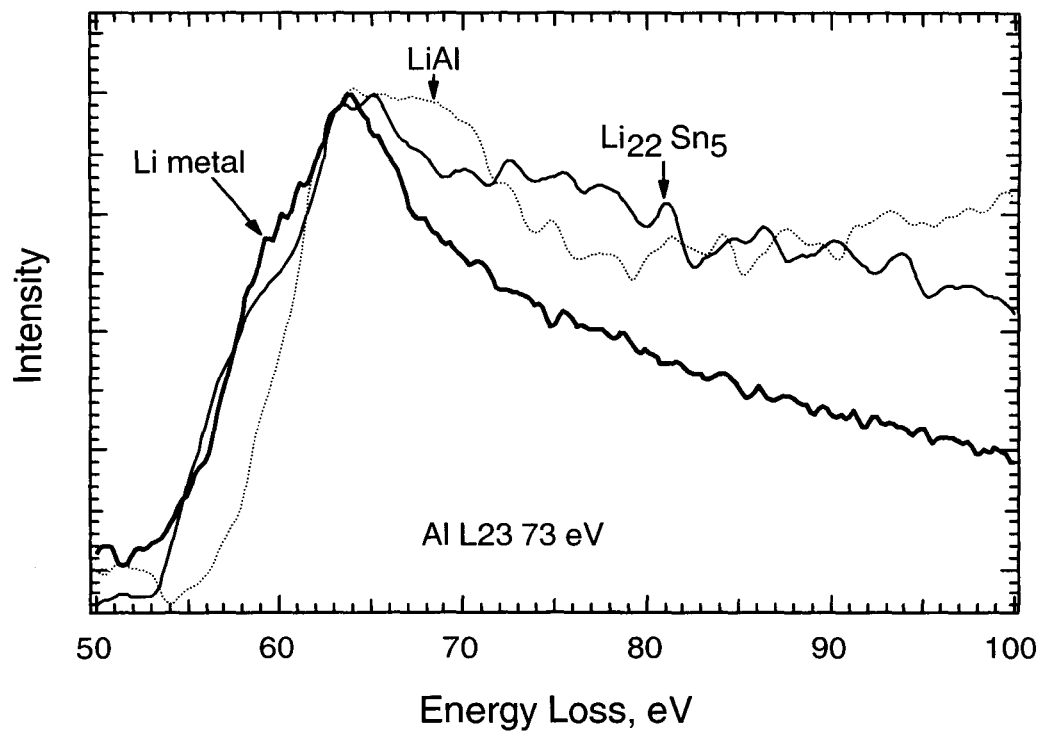


Figure 3.8. Lithium K-edges of metallic Li, LiAl, and Li₂₂Sn₅.

(Section 4.2). The crystal unit cell of the $\text{Li}_{22}\text{Sn}_5$ phase contains 432 atoms with 16 distinct Li environments and four Sn environments. Around each Li atom, 66-85% of its nearest neighbors will be other Li atoms. It is therefore not surprising that the Li K-edge experiences a minimal chemical shift, <0.2 eV. This lack of chemical shift is also consistent with the electrochemical potential relative to metallic lithium.

The B32 Zintl phase of LiAl holds great promise as an anode material. This ordered body-centered cubic (bcc) phase has relatively fast kinetics, a voltage of 0.3 V vs. lithium, and a theoretical specific capacity of 800 mAh/g. However, poor cycle life attributed to a face-centered cubic (fcc) phase transition limits its utility.

We attribute the chemical shift of the LiAl Li K-edge to the nature of the Zintl phase. This class of compounds consists of an electropositive, cation component and an anionic component of moderate electronegativity. Nevertheless, these Zintl compounds are not salt-like, but have metallic properties including luster and electronic conductivity. The profile of the Li K-edge of LiAl is clearly metallic and does not show the sharp features one expects with transitions to bound states. It is reasonable to believe Li 2p states are pulled further from Li nucleus by the anionic Al neighbors. Thus, in a core excitation, the Li 1s electron is excited a higher energy state in LiAl than Li metal. This could explain 2.2 eV chemical shift observed in the LiAl Li K-edge. We define the chemical shift as the difference in edge onset taken at half the peak maximum (59 eV).

The L_{23} edge of Al displays a delayed maxima 10-15 eV from the threshold (Figure 3.9). This is due to the centrifugal potential barrier when 2p electrons are excited to final states with $l>2$. The L_{23} edge of Al has a profile similar to metallic Al rather than Al_2O_3 .

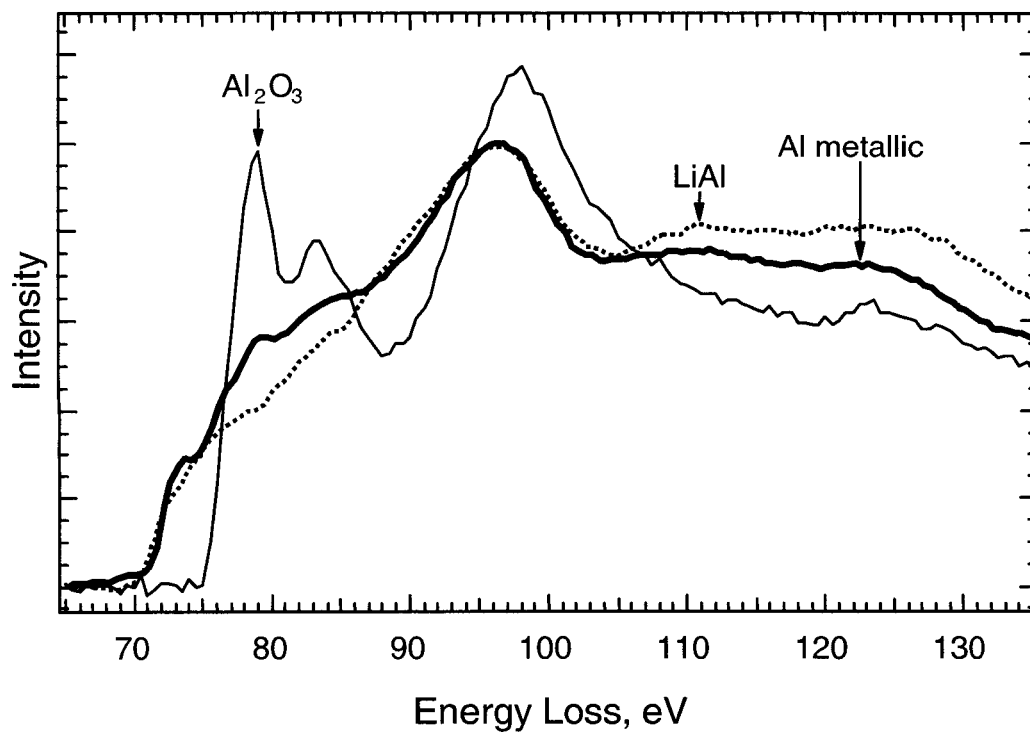


Figure 3.9. Aluminum L₂₃ edges of metallic Al, LiAl, and Al₂O₃.

This is similar to the minor modification of the carbon K-edge by Li intercalation (Section 4.1.4). We speculate that Li in a metallic state does not significantly reconfigure the lowest energy states of the solute atoms.

3.4 Lithium Oxides

EELS studies on lithium oxides are important for several reasons. From Section 3.2 on radiation damage we see that it is important to know the lithium oxide spectra radiation damage of specimens. Additionally, there are numerous opportunities for contamination during sample preparation. Above all, the removal of moisture from sample environments is the most important step for the successful specimen preparation [15]. A number of lithium oxides were studied in order to recognize contaminants and understand the electronic states of lithium in transition metal oxides.

Lithium hydroxide, LiOH, is the end product of lithium exposure to moisture. This holds true, to varying extents, for the majority of lithium compounds. Figure 3.10 displays the low-loss spectra of LiOH, Li₂CO₃, and LiNiO₂. The distinct peaks at 11 eV, 18.5 eV and 30 eV of the LiOH low-loss spectra are easily discerned in beam damaged samples. The peak at 18 eV was found to correspond to the (101) ring of the TEM diffraction pattern. This interpretation is consistent with early LiOH EELS spectra by Fellenger [13]. The background subtracted Li K-edge of LiOH displayed in Figure 3.11 show peaks at 59.5 eV and 64.5 eV. These sharp features can be understood qualitatively by considering the consequence of the Li/LiOH phase transition. Energy bands narrow as metallic Li evolves into insulating LiOH. The narrow bands correspond to a sharper density of states profile and thus more well defined final states. Additionally, the Li K-

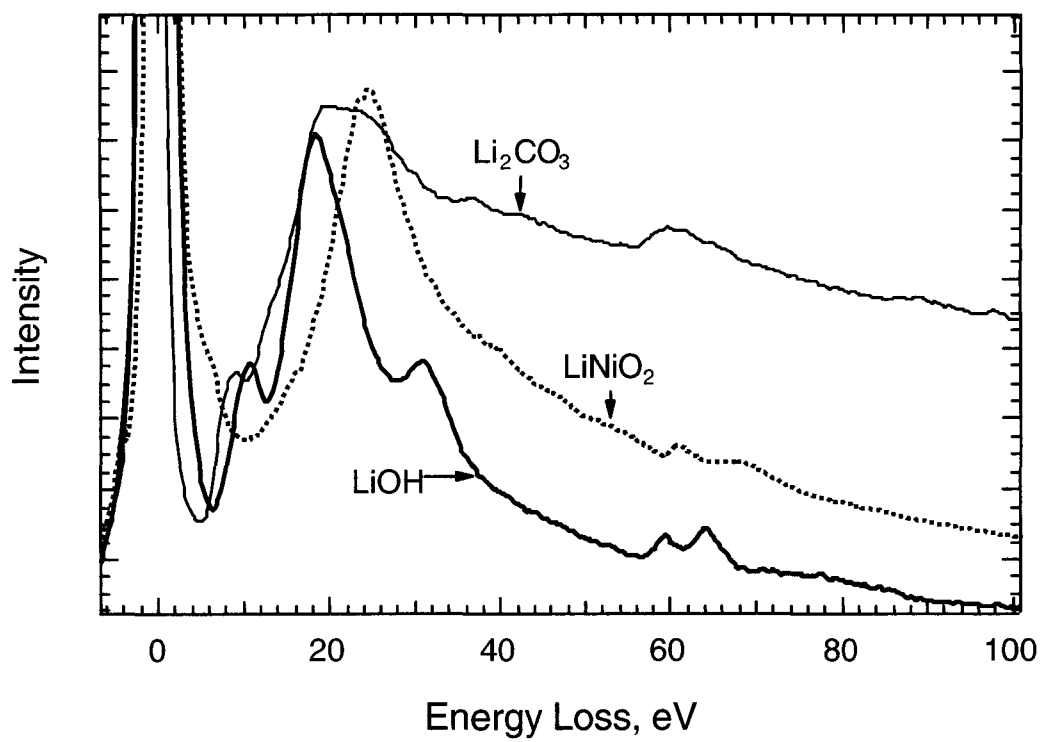


Figure 3.10. Low-loss spectra of lithium carbonate (Li_2CO_3), lithium hydroxide (LiOH), and lithium nickel oxide (LiNiO_2).

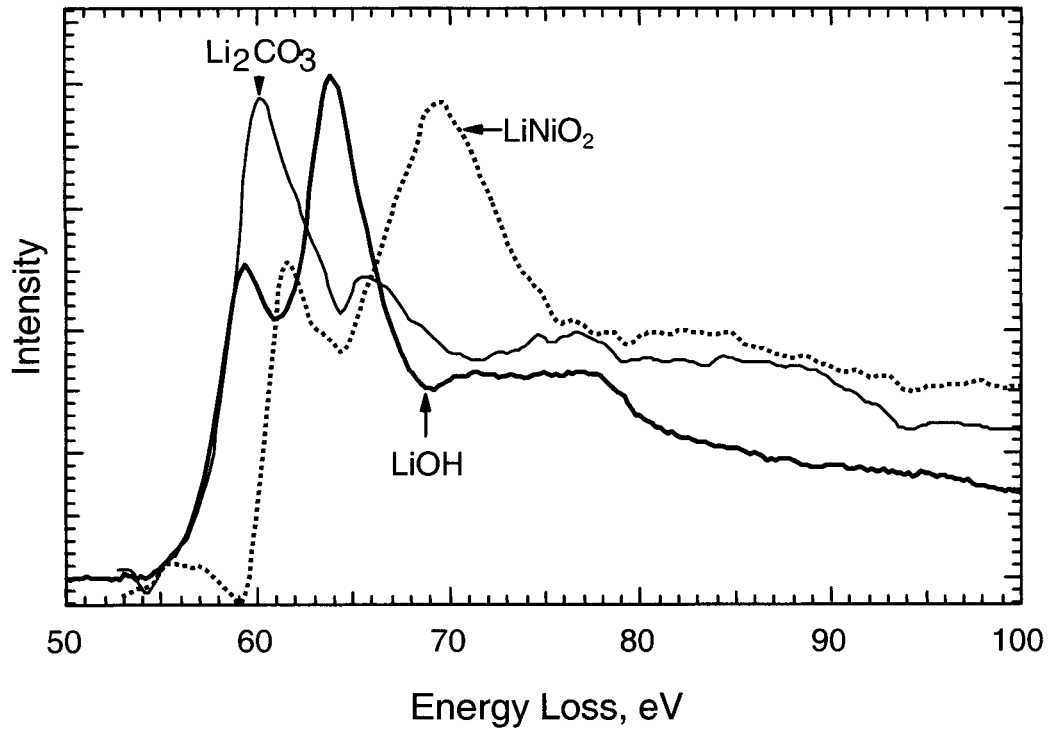


Figure 3.11. Lithium K-edges of lithium carbonate (Li_2CO_3), lithium hydroxide (LiOH), and lithium nickel oxide (LiNiO_2).

edge of the insulator is less susceptible to broadening from secondary plasmon scattering. Liu et al. [15] associates the LiOH peak seen at 68 eV to the density of states around the second N_1 symmetry point in the N direction in the Li Brillouin zone [16].

Lithium nickel oxide, LiNiO_2 , has been studied as a viable cathode material. It has the same layered structure as LiCoO_2 (Figure 4.5) but is unstable with lithium deintercalation due to Jahn-Teller distortion [17]. In this CuPt tetragonal distorted phase (Section 4.2.1), six oxygen atoms are octahedrally coordinated to a central lithium atom. The low-loss spectrum of LiNiO_2 displays a plasmon at 9.5 eV, typical of transition metal oxides. The background subtracted Li K-edge shown in Figure 3.11 has distinct peaks at 61.5 eV and 69.5 eV similar to those seen in LiF (Figures 3.4b, 3.14). The chemical shift and distinct profile of the LiNiO_2 Li K-edge is attributed to the difference in electronegativity between Li and its oxygen first nearest neighbors. Structural effects must also play a role in this Li K-edge profile. Taftø and Zhu [18] have found metal K-ELNES to exhibit a more prominent peak at the edge in the case of octahedral as opposed to tetrahedral oxygen.

Similarly, first nearest neighbor anions greatly determine the measured oxygen K-edges (Figure 3.12). The oxygen K-edge of LiOH has a doublet peak very similar to the one seen in the Li K-edge. We speculate these peaks represent the same bound states associated with the excitation of Li 1s electrons. Thus, there is likely significant hybridization between the unfilled Li 2p and the oxygen 2p atomic orbitals.

The oxygen K-edge of LiNiO_2 has an additional prepeak at 529 eV associated with transitions to oxygen 2p states hybridized with Ni 3d states [19]. This type of hybridization shifts spectral weight to the lowest-energy states in a number of third row

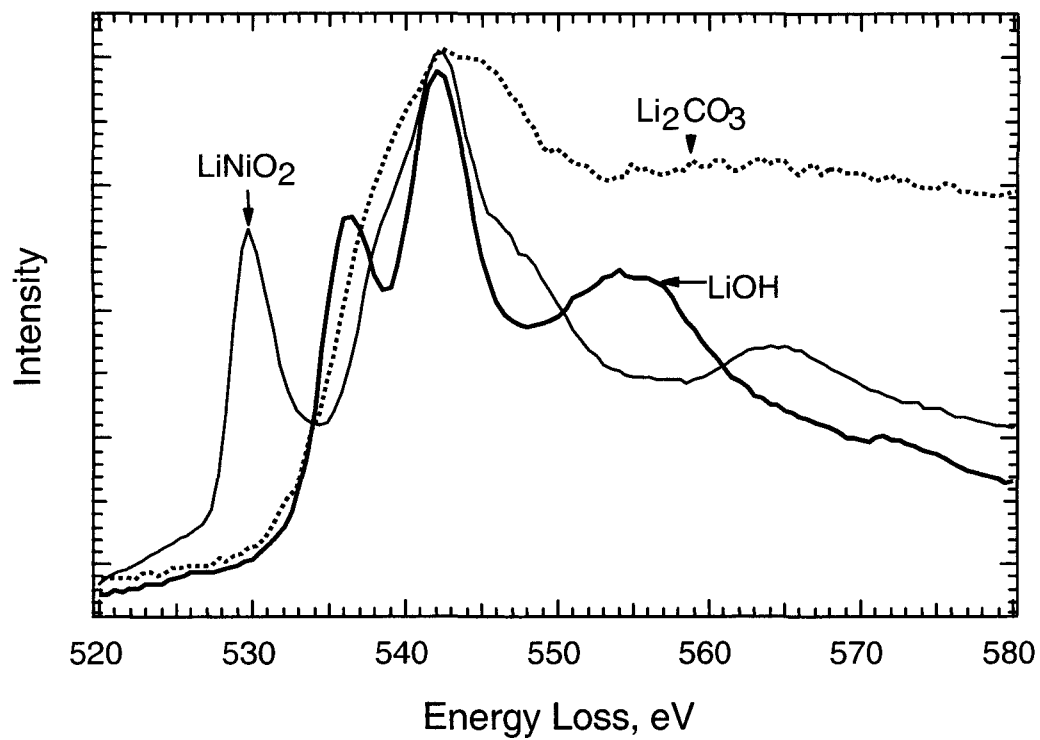


Figure 3.12. Oxygen K-edges of lithium carbonate (Li_2CO_3), lithium hydroxide (LiOH), and lithium nickel oxide (LiNiO_2).

transition metal oxides [20]. The prepeak intensity is dependent on the degree of hybridization with unoccupied 3d states and thus decreases as the number of electrons in 3d band increases [21]. The structure above 535 eV is associated with transitions to higher energy bands of Ni 4s, 4p and oxygen 3p character.

3.5 Lithium Halides

Lithium halides can be found as components of the solid electrolyte interphase (Section 1.1). The rock salt structures and ionic bonds of the lithium halides produce large chemical shifts in the measured Li K-edges. The low-loss region of LiF displays considerable fine structure between 17 eV - 20 eV due to excitons (Figure 3.13). Figure 3.14 displays the Li K-edges of evaporated lithium halides and a crushed LiNiO₂ sample. All of these materials have Li atoms coordinated by octahedrally anions. The strongly electronegative anions form a potential “cage” for electron scattering.

Large chemical shifts in the Li K-edge are observed in EELS spectra of lithium halides. Relative to metallic lithium, the lowest unoccupied electronic states of Li ions shift to higher energies as Li 2p orbitals are “pulled” toward the anion neighbors. The band gaps of the LiF, LiCl and LiBr are 14.5 eV, 9.4 eV, and 7.6 eV respectively [22]. The edge thresholds in many ionic insulators correspond to excitations to bound exciton states within the band gap. Thus the measured chemical shift is reduced by an amount equal to the exciton binding energy. Figure 3.15 displays a linear relation of anion electronegativity with the measured chemical shift. In the case of the lithium halides and the LiNiO₂ samples, the chemical shift was taken to be the difference between the maximum of the initial transition peak and the onset of the metallic Li K-edge at 54 eV.

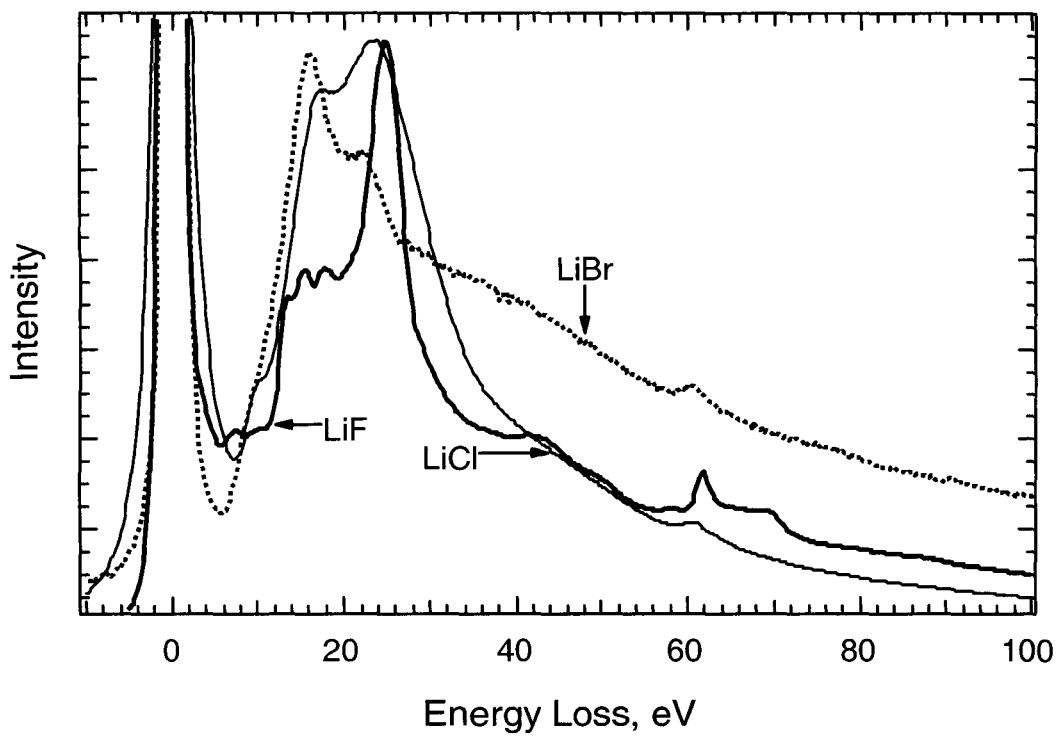


Figure 3.13. Low-loss spectra of evaporated LiF, LiCl, and LiBr.

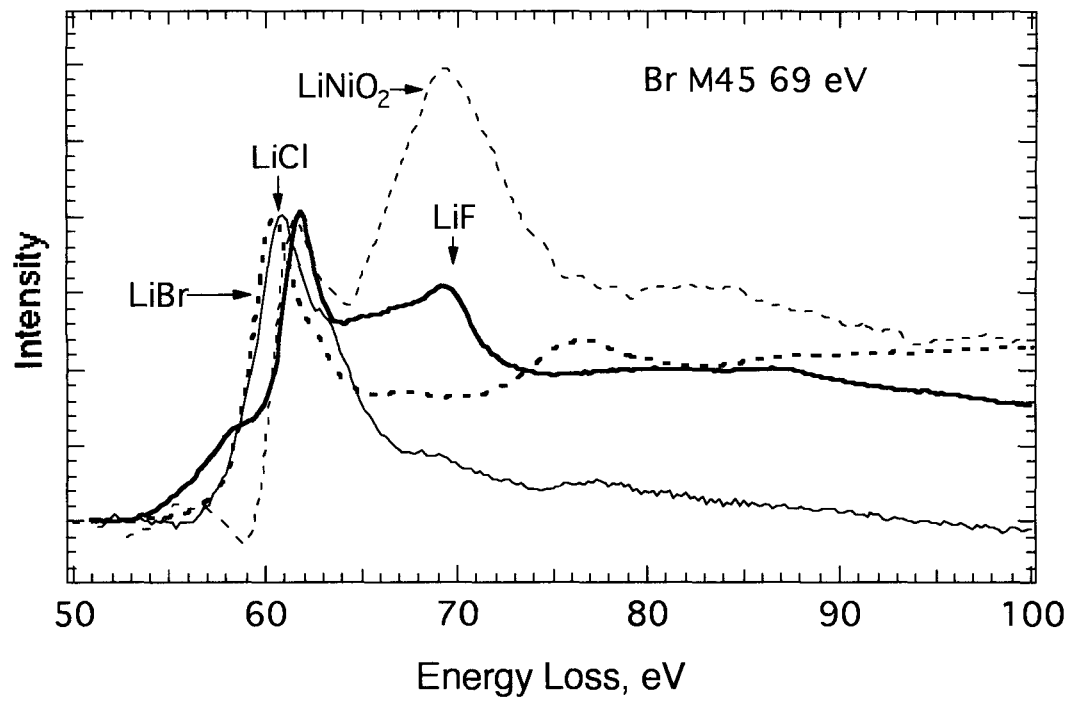


Figure 3.14. Lithium K-edges of LiF, LiCl, LiBr, and LiNiO₂.

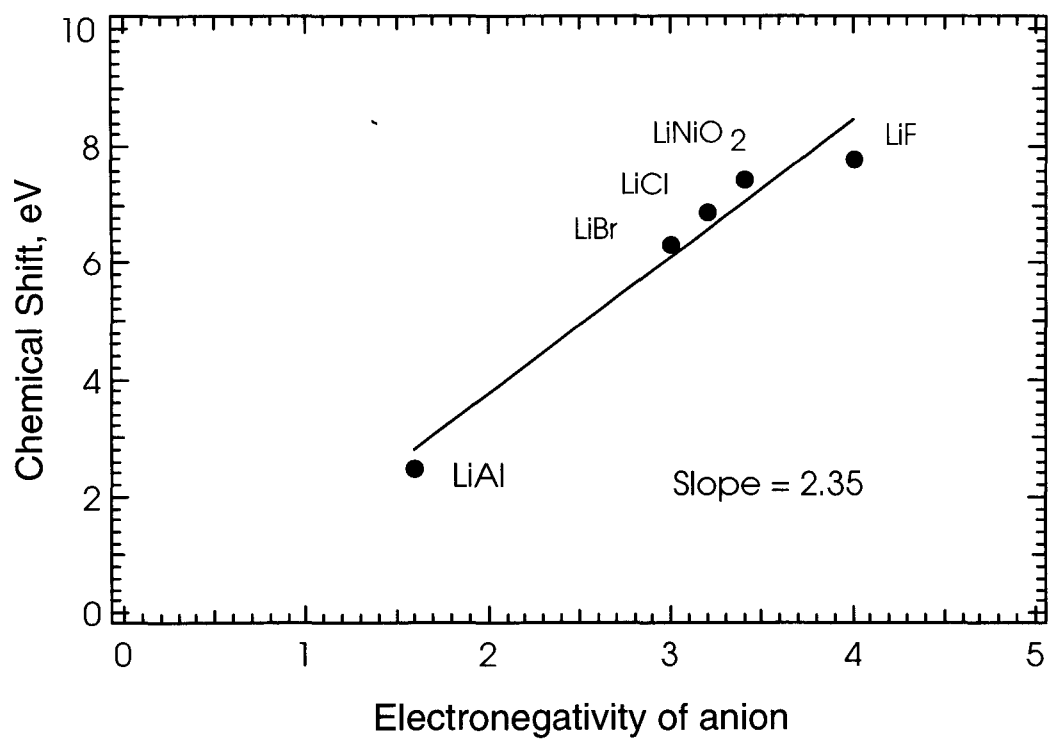


Figure 3.15. Measured chemical shift of the the Li K-edge versus the anion electronegativity.

The chemical shifts are calculated to be 7.8 eV, 7.4 eV, 6.9 eV and 6.3 eV for LiF, LiNiO₂, LiCl, and LiBr respectively. The chemical shift of LiAl is taken from the difference in Li K-edge onsets at half the peak maximum. Although LiAl is an ordered bcc phase, polar nature of the Zintl phase justifies its use in this plot.

3.6 Electron Structure Calculations

The near edge structures of the lithium halides and LiOH were calculated using the self-consistent FEFF8 code of Rehr et al. [23]. This method is similar to Korringa-Kohn-Rostocker (KKR) band structure calculations but additionally allows for variance in the number of nearest neighbor shells (cluster size). These central atom approximations allowed for the core hole potential to be accurately modeled [24, 25]. It is thus possible to distinguish the contribution of specific scattering paths to the near edge structure. Cluster sizes of six coordination shells were employed to determine the near edge structure. Previous work on MgO has shown that six to seven shells are enough to obtain the near edge structure of these materials [26]. Figure 3.16-3.18 shows the measured and calculated Li K-edges for various Li halides. All of the simulated Li K-edges predict initial peaks at lower values than those measured. The calculated FEFF8 spectra shown in Figure 3.16-3.18 have been shifted to match measured spectra (LiF - 3.8 eV, LiCl - 2.8 eV, and LiBr - 2.5 eV). The difference between the measured and calculated edge onset is most likely an underestimation of the respective band gaps of the Li halides (LiF - 14.78 eV, LiCl - 9.4 eV, LiBr - 7.6 eV) [22]. The LiBr Li K-edge is influenced by a Br M₂₃ edge at 69 eV. M₂₃ edges have massive delayed maximum which

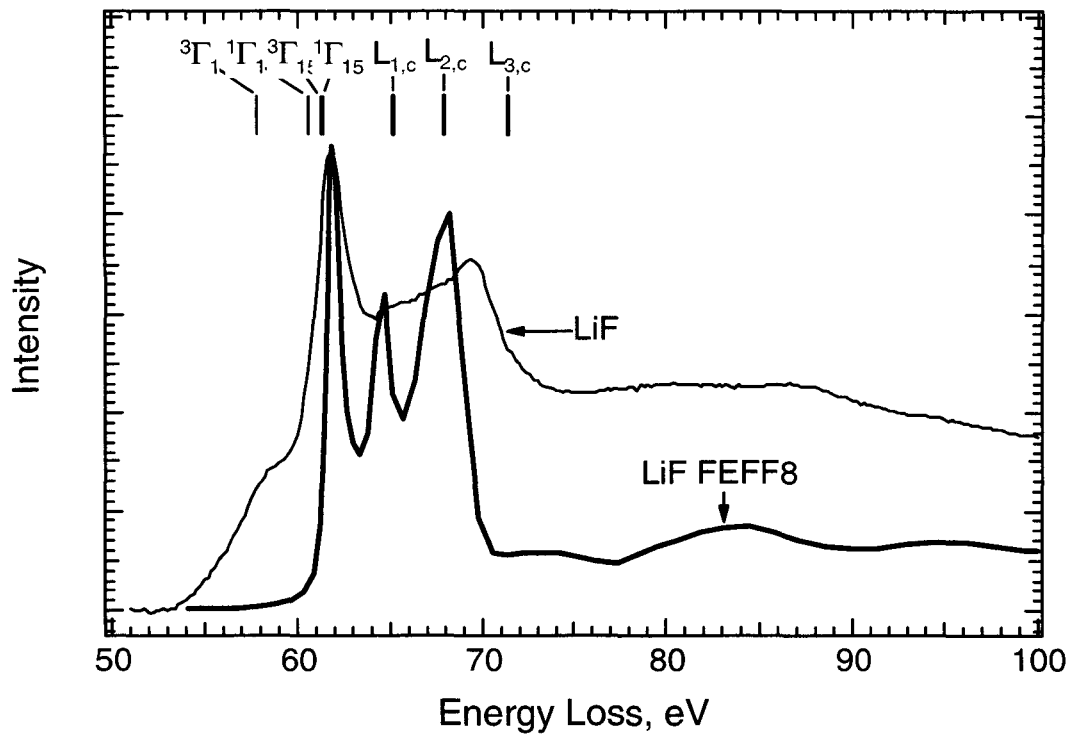


Figure 3.16. Lithium K-edges of evaporated LiF and calculated with multiple scattering FEFF8 code.

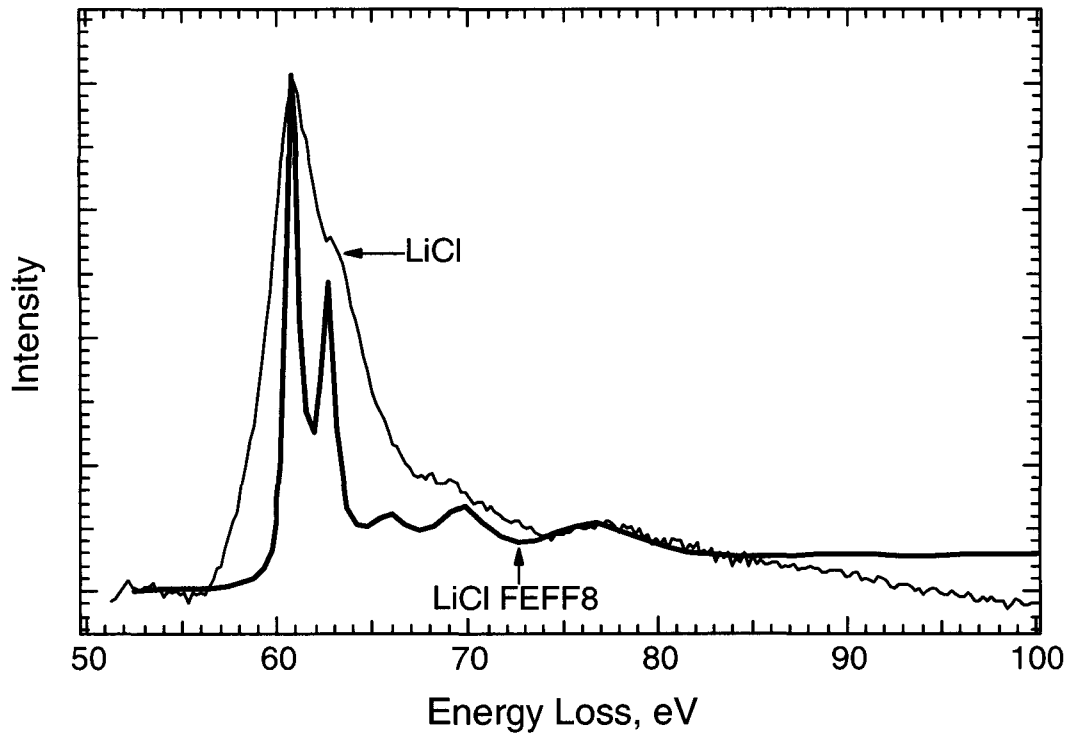


Figure 3.17. Lithium K-edges of evaporated LiCl and calculated with multiple scattering FEFF8 code.

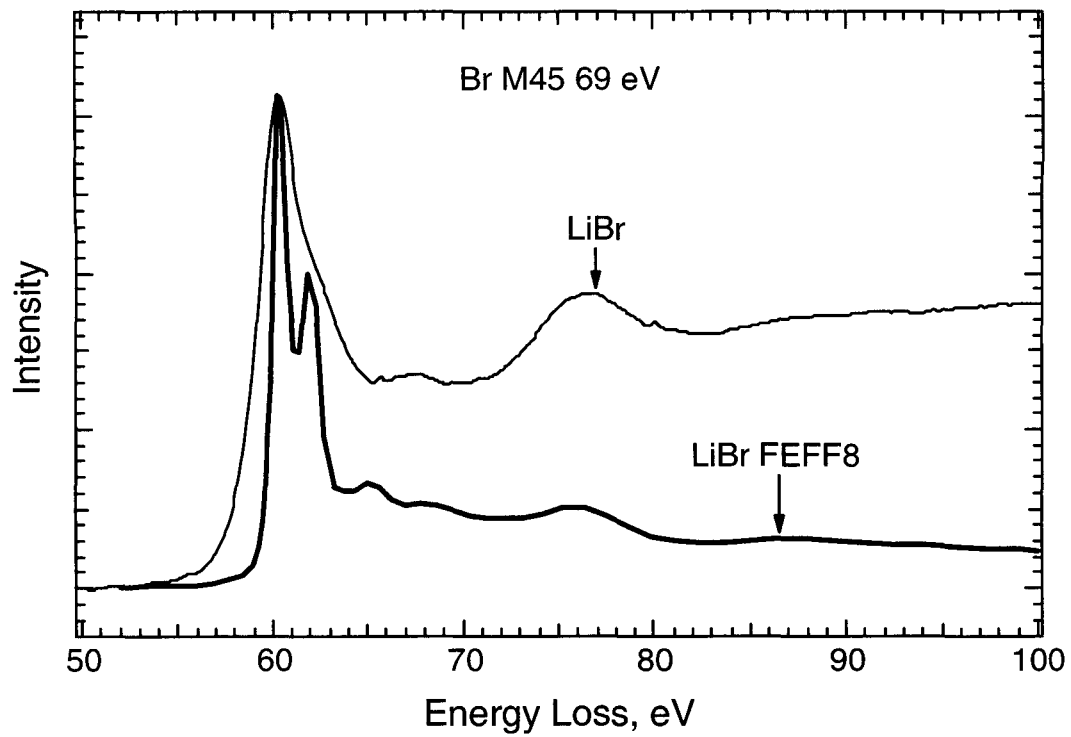


Figure 3.18. Lithium K-edges of evaporated LiBr and calculated with multiple scattering FEFF8 code.

accounts for the slow rise in intensity. The M_{23} edge probably washes out the small peak at around 78 eV.

A great deal of work has been done to characterize the features of the Li K-edge of LiF. Self-consistent local density calculations by Zunger and Freeman [27] accurately predict interband transition to states having ~93% Li 2p character, $L_{1,c}$, $L_{2,c}$, and $L_{3,c}$. (Figure 3.16). The methods used by Zunger and Freeman ignore the possibility of multiplet structure in the excitons formed upon exciting the Li K-shell. Bandgaps are commonly underestimated by local density approximations. Using a LiF_6^{-5} cluster with a self-consistent unrestricted Hartree-Fock method, Kunz et. al. [28] calculate fine splitting in the region from 58 eV to 62 eV. Using the Boukaert-Smaluckowski-Wigner (BSW) notation common to energy-band theory, the $^1\Gamma_1$ and $^3\Gamma_1$ state represent the $^{1,3}S$ states of the free Li ion. The $^1\Gamma_{15}$ and $^3\Gamma_{15}$ state represent the $^{1,3}P$ states of the free Li ion. The 3.6 eV splitting of $^1\Gamma_1$ - $^3\Gamma_1$ is speculated to arise from constraining of Li^+ excited states by the electrophobic F ions [29]. In the case of the 1.0 eV splitting of $^1\Gamma_{15}$ - $^3\Gamma_{15}$ is speculated to arise from the orientation of the Li p-like orbitals between and parallel to bonding with the neighboring fluorines. [28]. The transition from the Li K-shell to a $1s2s$ (3S) state is not dipole allowed. The peak at 58 eV has also been observed in XPS observations [30].

3.7 References

- [1] R. D. Leapman, L. A. Grunes, and P. L. Fejes, *Phys. Rev. B* **26**, 614 (1982).
- [2] S. Ono, K. Hojou, and K. Kanaya, *Proc. Fifth Int. Conf. on High Voltage Electron Microscopy*, (Jap. Soc. Electron Microscopy, Kyoto, 1977), p. 481.
- [3] L. W. Hobbs, *Quantitative Electron Microscopy, Proc. of the 25th Scottish Universities Summer School in Physics*, edited by J. N. Chapman and A. J. Craven (SUSSP Publications, Edinburgh, 1983), p. 413.
- [4] D. R. Liu and D. B. Williams, *Phil. Mag. B* **53**, 123 (1986).
- [5] K. R. Zavadil and N. R. Armstrong, *Surface Science*, **230**, 47 (1990).
- [6] K. R. Zavadil and N. R. Armstrong, *Surface Science*, **230**, 47 (1990).
- [7] W. A. Hart and O. F. Beurnel, *Comprehensive Inorganic Chemistry*, Vol. 1, J. C. Bailar, H. J. Emeleus, R. Nyholm and A. F. Trotman-Dickenson (Pergamon, Oxford, 1973), p. 331.
- [8] D. G. Lord and T. E. Gallon, *Solid State Commun.*, **36**, 606 (1973).
- [9] L. S. Cota, Araiza, and B. D. Powell, *Surf Sci.* **51**, 504 (1975).
- [10] Y. Tadami, K. Saiki, and A. Koma, *Solid State Commun.* **70**, 261 (1988).
- [11] F. Golek, and W. J. Sobolewski, *Solid State Commun.*, **110**, 143 (1999).
- [12] L. A. J Garvie and A. J. Craven, *Ultramicroscopy.* **54**, 83 (1994).

metallic Li references

- [13] H. Fellenger, *Z. Phys.* **196**, 311 (1961).
- [14] H. Bross, *Proceeding from the International Symposium on X-ray Spectra and Electronic Structure of Materials*, Vol. 2, edited by A. Faessler, G. Wiech, Munich, p. 1 (1973).

- [15] D. R. Liu, H. E. Rommal, and D. B. Williams, *J. of Electron Microscopy Technique*, **4**, 381 (1986).
- [16] H. Bross and G. Bohn, *Z. Phys.B* **20**, 261 (1975).
- [17] I. Nakai, K Takahashi, Y. Shiraishi, T. Nakagome, F. Nishikawa, *J. of Solid State Chemistry*, **140**, 145 (1998).
- [18] J. Taftø and J. Zhu, *Ultramicroscopy*, **9**, 349 (1982).
- [19] P. Kuiper, G. Kruizinga, J. Ghijsen, and G. A. Sawatzky, *Phys. Rev. Lett.* **62**, 221 (1989).
- [20] G. van der Laan, J. Zaanen, and G. A. Sawatzky, *Phys. Rev.* **23**, 4253 (1986).
- [21] G. van der Laan, C. Weestra, C. Haas, and G. A. Sawatzky, *Phys. Rev.* **23**, 4369 (1981).
- [22] Landolt-Bornstein: Numerical Data and Functional Relations in science and Technology, New Series Vol. 23, subvolume a, edited by O. Madelung , New York, p. 160 (1984).
- [23] J. J. Rehr, S. I. Zabinsky, and R. C. Albers, *Phys. Rev. Lett.*, **69**, 3397 (1992).
- [24] R. Brydson, D. D. Vvedensky, W. Engel, H. Sauer, B. G. Williams, E. Zeitler and J. M. Thomas, *J. Phys. Chem.* **92**, 962 (1988).
- [25] R. Brydson, J. Bruley, and J. M. Thomas, *Chem. Phys. Letts.* **149**, 343 (1988).
- [26] L. A. J. Garvie, A. J. Craven, *American Mineralogist*, **79**, 411 (1994).
- [27] A. Zunger and A. J. Freeman, *Phys. Rev. B* **16**, 2901 (1977).
- [28] A. B. Kunz, J. C. Boisvert, and T. O. Woodruff, *Phys. Rev. B* **30**, 2158 (1984).
- [29] T. Aberg and J. L. Dehmer, *J. Phys. C* **6**, 1450 (1973).

[30] J. P. Scott, S. L. Hulbert, F. C. Brown, B. Bunker, T. C. Chiang, T. Miller, and K. H. Tan, Phys. Rev. B **30**, 2163 (1984).

Chapter 4 Specific Electrode Environments

4.1 Electron Energy Loss Spectrometry on Lithiated Graphite

4.1.1 Introduction

Lithiated graphite is the standard anode material in Li – ion rechargeable batteries [1]. Highly crystallized graphite can intercalate one Li atoms to a composition of LiC_6 . This is equivalent to specific charge of 372 Ah kg^{-1} [2], although in practice graphite anodes have specific capacities of $320 - 360 \text{ Ah kg}^{-1}$. Graphite anodes have high voltages of 3-4V versus the cathode, but the difference in electrochemical potential between metallic lithium and lithiated graphite is small, about 0.01 V. The intercalation of Li into highly crystallized graphite changes the hexagonal planes stacking sequence of the hexagonal planes from an ABABAB to AAAAAA [3]. This change in stacking sequence and the high chemical potential of Li in graphite suggest that better understanding interesting of the LiC_6 interlayer states would facilitate improvements to Li- ion electrochemical cells.

The results of numerous studies on the band structure of lithium intercalated graphite demonstrate the difficulty in determining the degree of hybridization between Li atomic orbitals and graphite interlayer states. Early theoretical calculations of the LiC_6 band structure began with the notion of complete charge transfer of Li valence electrons to the graphite π bands [4,5]. This evolved into an elegant theory of alkali-intercalated graphite interlayer states as interacting nonorthogonal hybrid states of Li 2s and graphite interlayer states [6,7]. This gives credence to X-ray photoelectron spectroscopy (XPS) results by Momose et al. [8] and others [9] claiming Li to be intercalated into graphite as

ionic Li^+ . Early experimental work by Grunes et al. [10] using Electron Energy Loss Spectroscopy (EELS) demonstrated distortions of the graphite band structure upon intercalation of alkali metals. Hartwigsen et al. [11] used a density functional theory, local density approximation to determine the degree of charge transfer from Li to the intercalant host lattice to be $0.5e$ for LiC_6 and $0.4e$ for LiC_8 . Further experiments using inelastic X-ray scattering spectroscopy (IXSS) by Schülke [12] were able to correlate features of LiC_6 spectra to band structure calculations by Holzwarth et al. [13].

We report transmission EELS measurements of the Li K-edge in intercalated graphite and in metallic Li. We show the Li K-edge for Li in graphite resembles neutral metallic Li rather than of Li^+ .

4.1.2 Experimental

LiC_6 samples were prepared by electrochemical methods [14]. Anodes were constructed from KS 44 graphite using 6 wt% polyvinylidene fluoride (PVDF) as a binder. A ternary mixture of alkyl carbonates, i.e., 1:1:1 of ethylene carbonate (EC), diethylene carbonate (DEC), and dimethyl carbonate (DMC) with 1 M LiPF_6 was used as the electrolyte. Carbon half-cells were subjected to 40 electrochemical charge-discharge cycles. The carbon electrodes were left in a charged state before being washed in DMC and vacuum dried.

X-ray diffractometry was performed with an INEL powder diffractometer using $\text{Mo K}\alpha$ radiation ($\lambda = 0.7092 \text{ \AA}$). The LiC_6 samples were crushed with a mortar and pestle in an Argon-filled glove box. Anode materials were sealed under Ar with paraffin wax in Pyrex capillary tubes. Detection limits were determined primarily by the statistical quality of the data,

estimated to be about 1%. The powdered anode material was placed onto holey carbon TEM grids. The TEM grids were immersed in Li gettered Flourinert® FC-43 before insertion into the microscope, where Flourinert evaporated. EELS spectra were acquired at room temperature using a Gatan 666 parallel detection magnetic prism spectrometer attached to a Philips EM 420 transmission electron microscope. Energy resolution of the spectrometer was about 1.2 eV with a dispersion of 0.2 eV per channel. Measurements were performed with 100 keV electrons at a collection angle of 50 mrad. Image coupling was employed to determine LiC₆ spectra. The TEM beam current was approximately 7 nA.

4.1.3 X-ray Diffraction Results

X-ray diffractometry confirmed the presence of LiC₆ and LiC₁₂ phases in the graphite anode materials [15,16]. These results were consistent with color of lithiated graphite, which depends on the predominance of LiC₆ (green/gold) or LiC₁₂ (blue/black) [17]. Diffraction peaks were broader for LiC₆ than for the unlithiated KS44 graphite samples.

4.1.4 TEM Micrographs

The transmission electron micrographs show a heterogeneous distribution of phases in the graphite samples. The microstructure of the cycled materials ranged from sheet-like graphite regions to dense polycrystals. As measured from dark field and bright field images (Figure 4.2), the sheet-like regions were on the order of 100 nm. Moiré fringes were found in some of these regions indicating random orientation of overlapping graphite regimes. The crystallites in the polycrystalline regions were very small and of

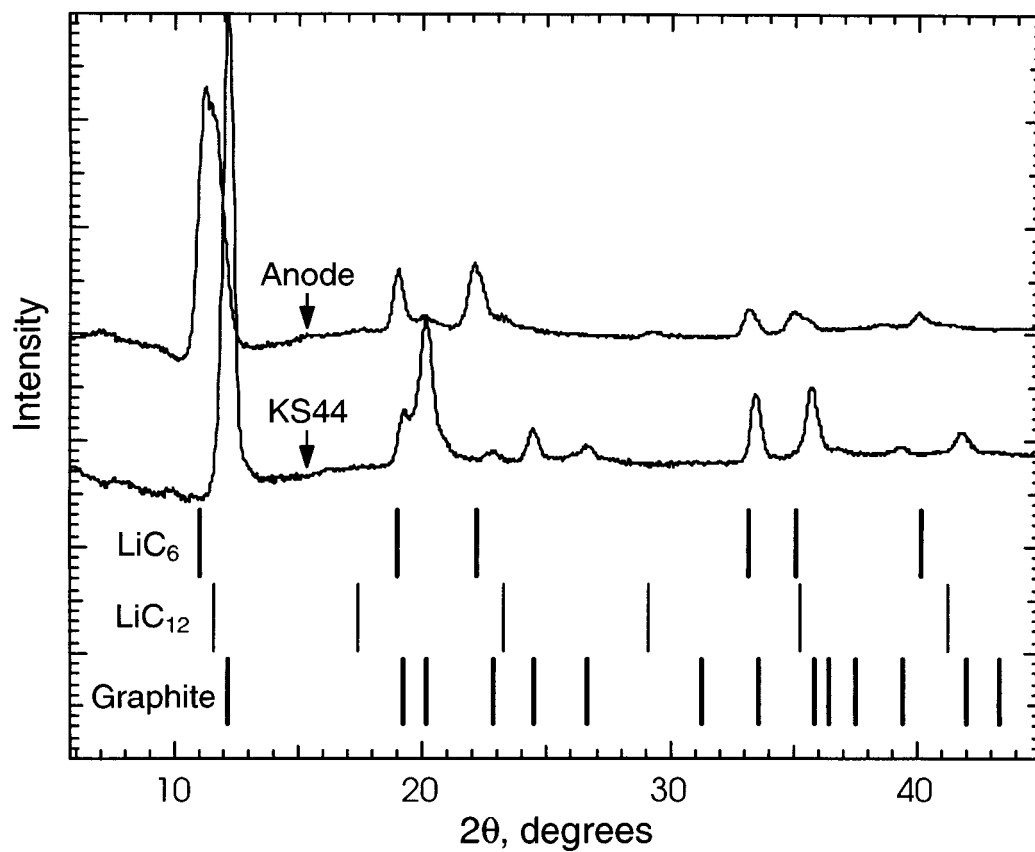


Figure 4.1. X-ray pattern of KS44 and electrochemically lithiated graphite displaying LiC_6 and LiC_{12} phases.

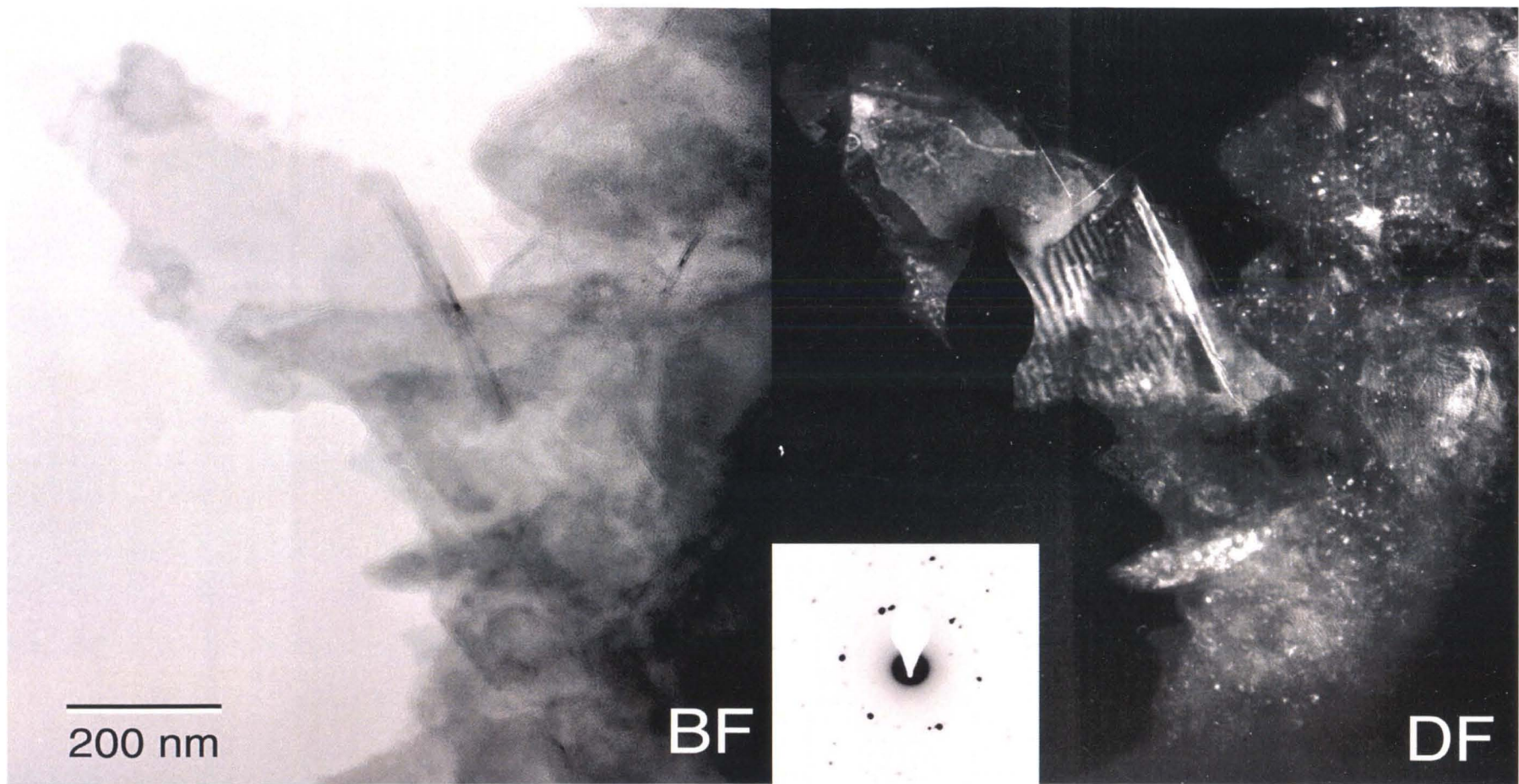


Figure 4.2. Bright and dark field TEM micrographs of cycled LiC_6 .

the order of 10 nm. These polycrystalline regions could be areas of low strained, organized carbon surrounded by highly buckled or tetrahedrally bonded carbon [15].

Electron Energy Loss Spectrometry determined the presence of intercalated lithium in both polycrystalline and sheet-like regions. Figure 4.2 shows bright field / dark field TEM micrographs of a region containing polycrystalline and sheet like graphite. The characteristic Li K-edge at 52 eV is seen in both the sheet-like and polycrystalline regions. Regions showing similar morphology and thickness were found to be without the 52 eV peak. These are assumed to be lithium deficient regions.

4.1.5 Carbon K-edge

Figure 4.3 presents the carbon K edges of LiC_6 and KS 44 graphite. A peak at 301 eV is found in LiC_6 but not observed in the graphitic carbon. Disko [18] and others [19] have demonstrated the sensitivity of the carbon K-edge to the direction of the momentum transfer vector \mathbf{q} . We therefore do not expect the intensity of the $1s \rightarrow \pi^*$ peak to be reliable, since it is not an average over many crystal orientations. Nevertheless, the onset energy of the carbon K-edge onset energy and the location of the $1s \rightarrow \pi^*$ peak are essentially the same for graphitic carbon and LiC_6 .

4.1.6 Lithium K-edge

Figure 4.4 displays the Li K-edge obtained from intercalated LiC_6 , LiF, and metallic Li. We identify the onset of the Li K edge in the metallic sample at 55 eV, consistent with results of Liu and Williams [20]. The broad profile of the metallic Li K-edge is consistent with the promotion of core electrons into a continuum of free electron

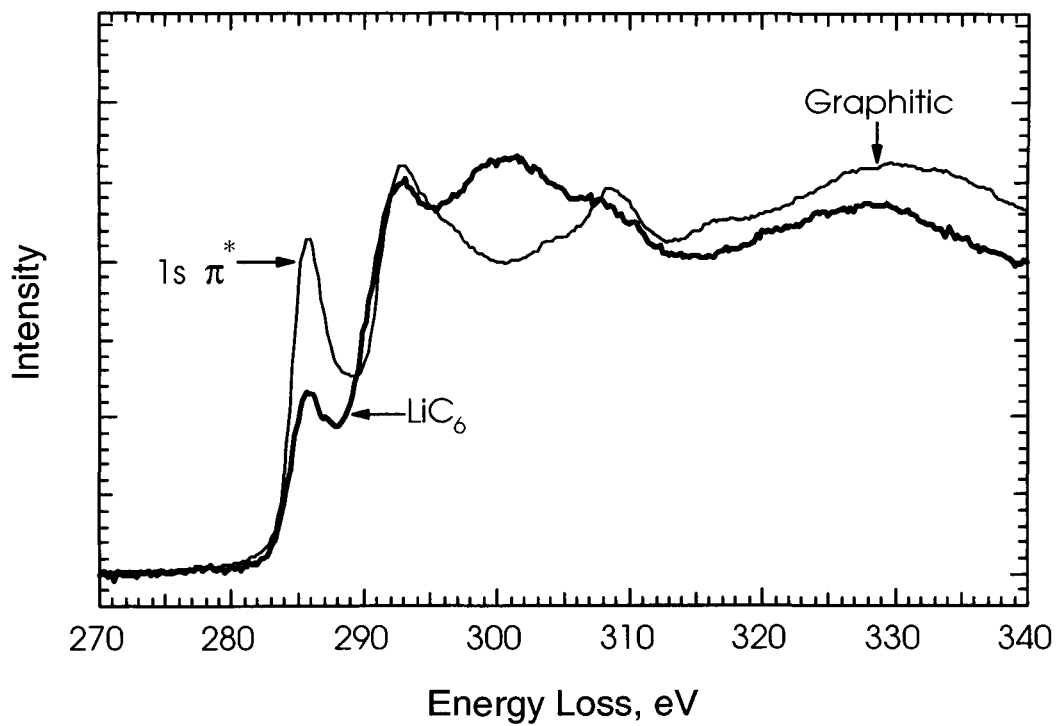


Figure 4.3. Carbon K-edge for LiC₆ and KS44 normalized by the area 50 eV after the edge onset.

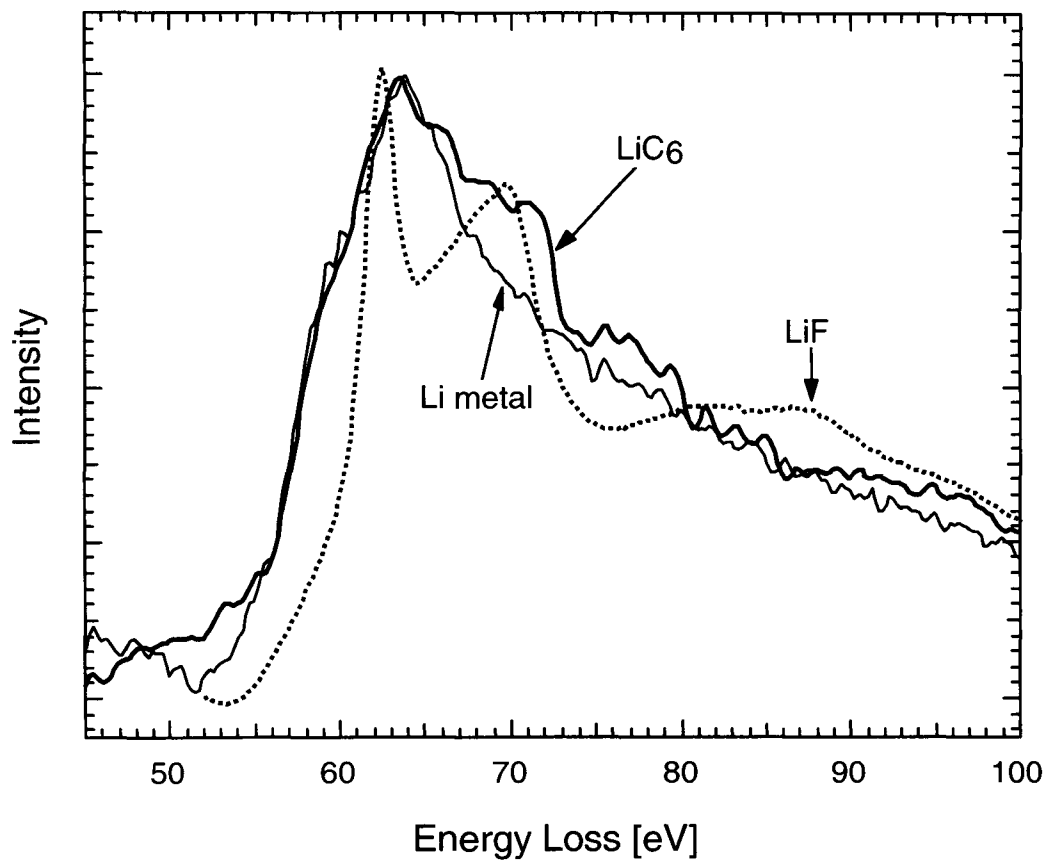


Figure 4.4. Li K-edge of metallic Li, LiC₆, and LiF. The pre-edge background of the raw data was fit to an exponential and subtracted from the data.

states. The Li K-edge onset of LiC_6 is shifted by only 0.2 eV from the K-edge of metallic Li and has a similarly broad profile. Our observed Li K-edge for LiC_6 lacks the peaks at 59 eV and 63 eV previously observed by Grunes et al.[10]. These peaks evidently originate from oxidized Li as they are found in samples exposed to atmosphere, or after long times in the microscope (Figure 3.2). The Li K-edge of LiF, similar to that reported by Chen et al.[21], shows a strong of chemical shift and sharp features of well-defined unoccupied states. Such large differences are expected with the large electron transfer from Li to F.

4.1.7 Comparison to XPS

Our EELS spectra of the Li K-edge indicate that Li in LiC_6 has a local electronic structure more similar to Li metal than Li^+ , contrary to previous XPS studies. Extensive XPS results confirm a Li K-edge chemical shift of about 3 eV in LiC_6 with respect to metallic Li [8,9], easily resolved from the 1.3 eV chemical shift of Li_2O [22]. The mean free path of photoelectrons measured by XPS is on the order of 1 nm. Thus, assuming that the surface Li remains unreacted, we expect XPS to be more sensitive to Li surface states.

4.1.8 Discussion

The similarities of Li K-edges in LiC_6 and metallic Li are consistent with observed electrochemical potentials. This imposes significant safety concerns on the commercial use of lithium ion batteries. Measurements of electrochemical potentials in half-cells (Figure 4.5) show LiC_6 to be less than 0.01 V above Li metal [15]. The similar

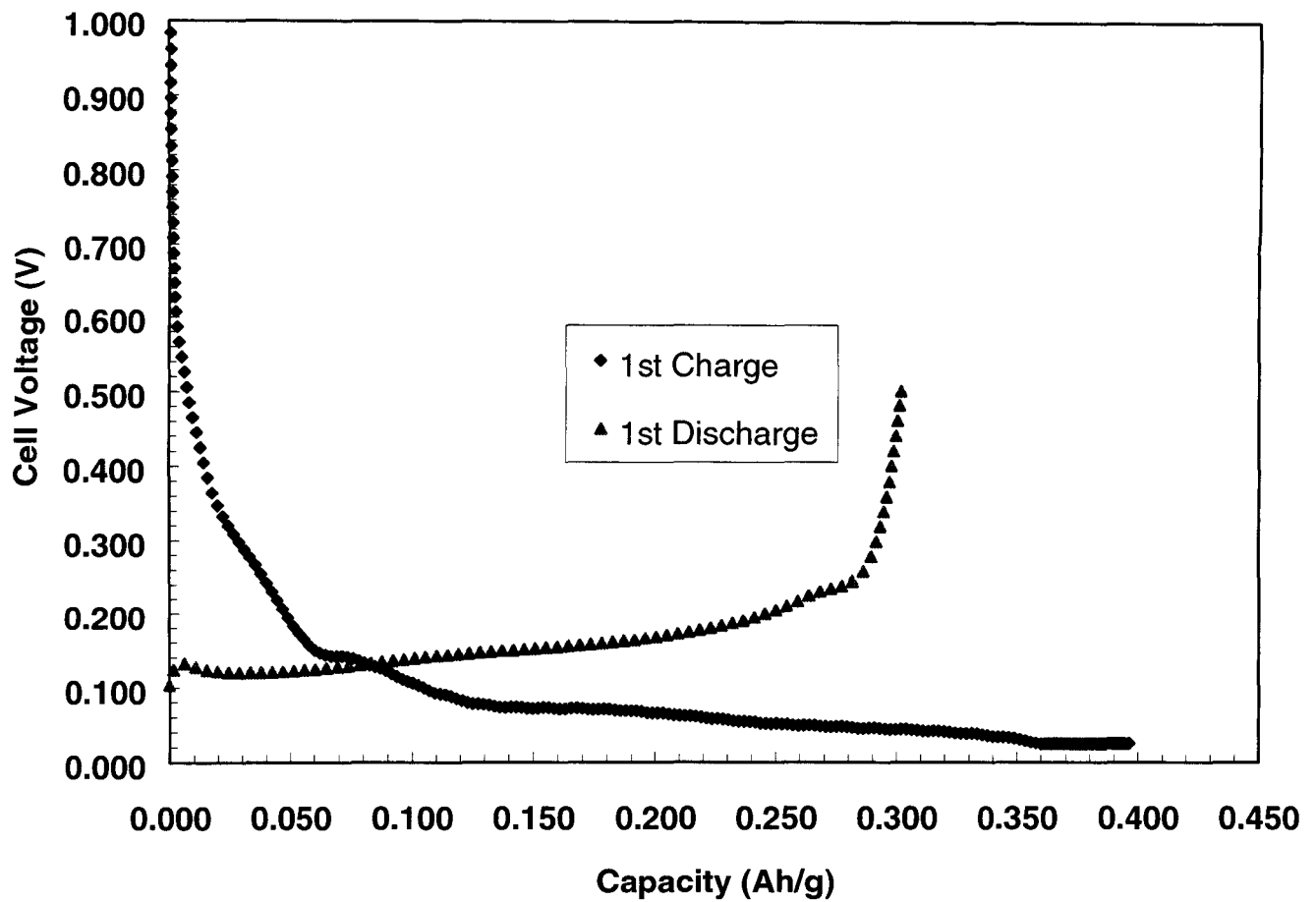


Figure 4.5. Initial charge and discharge curves of lithiated KS44 graphite.

chemical potentials of Li in LiC_6 and metallic Li suggest similar environments for valence electrons. Electrochemical potentials and EELS Li K-edge profiles both suggest limited charge transfer from Li to surrounding carbon. The observed carbon K edge is little affected by intercalated Li, but effects should be diminished by the 6:1 ratio of C to Li, and could diminish further if there were a loss of Li from the TEM sample. The shape of the Li K-edge, on the other hand, would be unaffected by any possible loss of Li.

4.1.9 Conclusions

We report results from transmission EELS studies on lithium intercalated and discuss beam damage under conditions of observation. Detailed results on the C and Li K-edges of LiC_6 are presented. The carbon K-edge in LiC_6 shows an energy onset of 285 eV, unchanged from the edge onset found in graphite. The near edge structure of the LiC_6 carbon K-edge has a peak at 301 eV not found in graphite. Nevertheless, the Li K edge energy onset was found to be indistinguishable in LiC_6 and metallic Li. These EELS findings contradict the shifted Li K edges found for LiC_6 by XPS. We suggest that XPS spectra are modified by the proximity of Li to the surface of the material.

4.1.10 References

- 1) A. Hérold, Bull Soc. Chim. France, **187**, 999, (1955).
- 2) M. S. Dresselhaus and G. Dresselhaus, Adv. Phys., **30**, 139 (1980).
- 3) J. R. Dahn, A. K. Sleight, H. Shi, B. M. Weydanz, J. N. Reimers, Q. Zhong, and U. von Sacken,

in *Lithium Batteries : New Materials, Developments and Perspectives*, edited by G. Pistoia (WEditor, Amsterdam, 1994), p. 1.
- 4) N. A. W. Holzwarth, S. G. Louie, S. Rabii, Phys. Rev. B, **26**, 5382, (1982).
- 5) J. J Ritsko, Phys. Rev. B, **25**, 6452, (1982).
- 6) N. A. W. Holzwarth, S. G. Louie, and S. Rabii, Phys. Rev. B, **30**, 2219, (1984).
- 7) M. Posternak, A. Baldereschi, AJ Freeman, Wimmer , Phys Rev. Letters, **50**, 761 (1983).
- 8) H. Momose, H. Honbo, S. Takeuchi, K. Nishimura, T. Horiba, Y. Muranaka, Y. Kozono, H. Miyadera, Journal Power Sources, **68**, 208, (1997).
- 9) G. K. Wertheim, P.M.Th.M. Vanattekum, and S. Basu, Solid State Communications, **33**, 1127, (1979).
- 10) L. A. Grunes, I. P. Gates, J. J. Ritsko, E. J. Mle, D. P. DiVincenzo, M. E. Preil, and J. E. Fische, Phys. Rev. B, **28**, 6681, (1983).
- 11) C. Hartwigsen, W. Witschel, E. Spohr, Phys. Rev. B, **55**, 8, 4953 , (1997
- 12) W. Shülke, A. Berthold, A. Kaprolat, H. J. Guntherodt, Phys. Rev. Letters, **60**, 2217, (1988).
- 13) N. A. W. Holzwarth, S. G. Louie, and S. Rabii, Phys. Rev. B, **28**, 1013, (1983).

14) Smart M C, Ratnakumar B V, Surampudi S, Wang Y, Zhang X, Greenbaum S G.

Hightower

A, Ahn C C and Fultz B Journal Electrochemical Society **146**, 11, (1999).

15) J. R. Dahn, Phys. Rev. B, **44**, 9170 (1991)

16) M. Morita, T. Ichimura, M. Ishikawa and Y. Matsuda, J. Electrochem. Soc., **143**, L26 (1996).

17) Basu, G. K. Wertheim, S. B. Diczenco, in *Lithium: Current Applications in Science, Medicine an Technology*, R. O. Bach, (ed.), John Wiley & Sons, New York (1985).

18) M. M. Disko, *Analytical Electron Microscopy 1981*, edited by R. H. Geiss (San Francisco Press, Inc., San Francisco, CA, 1981), p. 218.

19) W. Schülke, K. – J. Gabriel, A. Berthold, and H. Schulte-Schrepping, Solid State Communications, **79**, 657, (1991).

20) D. R. Liu and D. B. Williams, Phil. Mag. B, **53**, 123, (1986).

21) T-C. Chen, M. Qian, and T. G. Stoebe, Journal Physics Condensed Matter, **11**, 341, (1999).

22) K. R. Zavadil and N. R. Armstrong, Surcae Science, **230**, 47, (1990).

4.2 EELS Analysis of LiCoO₂

4.2.1 Introduction

Currently, all large manufacturers of rechargeable lithium ion batteries use LiCoO₂ as the cathode material. The success of cobalt in cathode materials stems from its excellent stability under electrochemical cycling. Although other transition metal oxides involving nickel or manganese offer economic advantages, their limited cycle life has reduced their practicality.

LiCoO₂ belongs to a class of lithium metal oxides, LiMO₂ (M = V, Cr, Co, and Ni) that have a rhombohedral symmetry corresponding to the R-3m space group (Figure 4.6A). Lithium and cobalt order along the (111) plane form alternating cation planes sandwiched between oxygen planes [1]. The (111) ordering distorts the lattice to hexagonal symmetry. This form of LiCoO₂ belongs to the $\bar{R}3m$ space group with lattice constants $a \approx 2.816 \text{ \AA}$ and $c \approx 14.08 \text{ \AA}$ [2] (Figure 4.6B). This layered crystal structure is typically referred to as the LiCoO₂ “layered” phase. The fully discharged state of the cathode corresponds to LiCoO₂. With charging of the battery, lithium is deintercalated from these planes, leaving vacancies behind. Over charging leaves CoO₂, which is particularly susceptible to cobalt dissolution into the electrolyte [3] or oxygen loss [4].

It is commonly agreed that the transition metals in LiMO₂ cathodes change their valence to accept the charge of the intercalated Li atom. However, the degree to which transition metal ions change their valence and thus the amount of charge compensated oxygen atoms, is open for debate. In the strict ionic charge transfer model, LiCoO₂ ions have integral charges of Li⁺, Co³⁺, and O²⁺. For each lithium atom deintercalated a

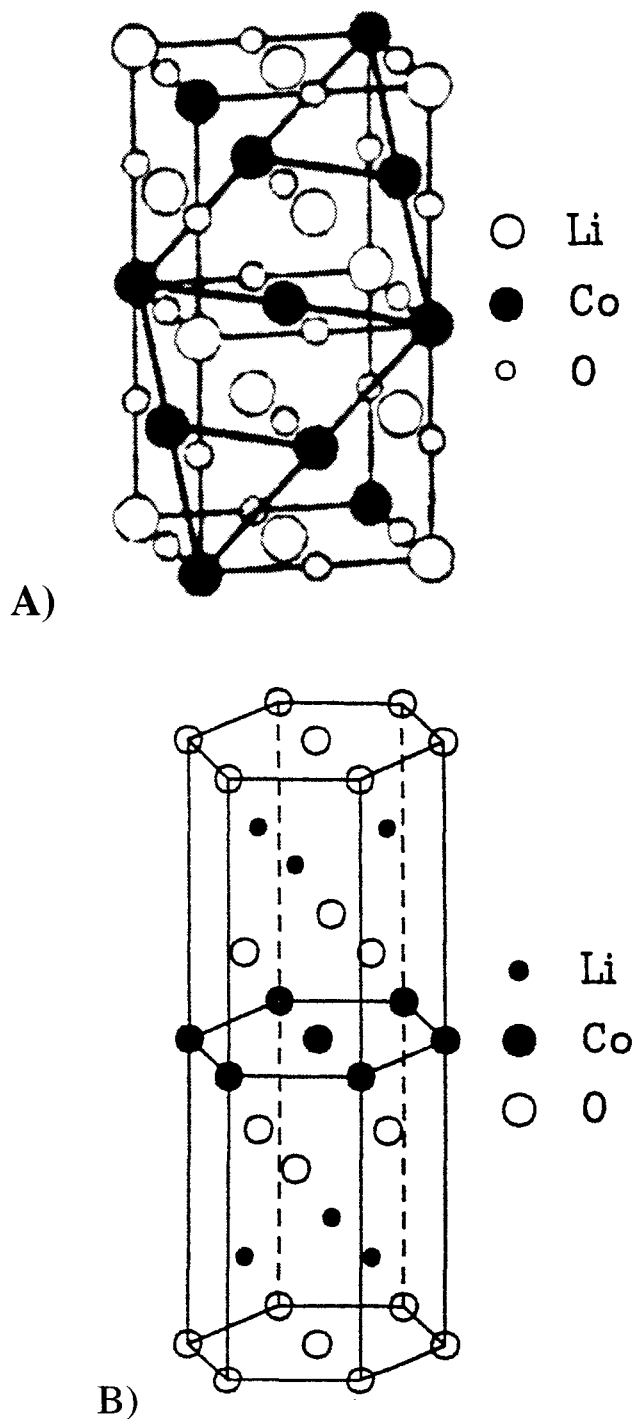


Figure 4.6. A) Schematic diagram of CuPt, ordered rocksalt structure of LiCoO_2 . Lithium and Co cations order along the (111) planes [24]. B) An equivalent depiction empathizing the O-Li-O-Co-O-Li-O layers in LiCoO_2 showing $\dots\text{ABCABC}\dots$ stacking [2]. The c axis of the $R\bar{3}m$ space group is perpendicular to the Li, Co, and O planes.

cobalt atom would arise with a formal charge of Co^{4+} . Thus in the strict ionic formalism, oxygen atoms play only a minor role in lithium deintercalation but retain a constant charge of O^{2-} . This is a gross simplification and there is substantial evidence that the bonding within LiCoO_2 has significant covalent character. This evidence arises from comparison of calculated and experimentally observed ligand-field effects [5-8].

There is anecdotal evidence suggesting oxygen atoms play a greater role in charge compensation than previously suspected. The chemical potential of Li in the cathode changes when substitutions for oxygen and cobalt are made. The cathode voltage depends significantly on the transition metal involved (Table 1.2). However, greater changes in voltage can be observed with anion substitutions. In the case of LiCoO_2 the voltage drops considerably when oxide is substituted for sulfur (2.04 Volts) or selenium (1.46 Volts) [9]. The fact that the voltage of the cathode is more influenced by anion substitution brings the conventional role of the transition metal into question.

My work investigates the electronic states of cobalt and oxygen in cycled cathodes by EELS spectroscopy. The first experimental evidence of charge accommodation by oxygen atoms with lithium intercalation is presented here.

4.2.2 Experimental

The half-cell studies were conducted in three-electrode, O-ring-sealed, glass cells containing spiral rolls of LiCoO_2 , lithium counter electrodes and lithium reference electrodes separated by two layers of porous polypropylene (Celgard 2500). The LiCoO_2 cathodes used for these studies were fabricated with 6 wt% polyvinylidene fluoride (PVDF) binder and 10% Swanigan Carbon Black conductive diluent. The carbonate-

based solvent ethylene carbonate (EC), dimethyl carbonate (DMC) and 1,2-dimethoxyethane carbonate (DME) (1:1:1), containing 1 M LiPF₆ salt, was purchased from Mitsubishi Chemicals (battery grade) with less than 50 ppm of water.

Electrochemical measurements were made using an EG&G Potentiostat/Galvanostat interfaced with an IBM PC, using EG&G Softcorr 352 software. Electrochemical charge-discharge measurements and cycling were performed with a battery cycler manufactured by Arbin Instruments, College Station, TX. The cycling tests were done at current densities of 0.25 mA/cm² for Li intercalation and de-intercalation to the cut-off potentials of 2.5 and 4.0 V vs. Li, respectively. Cells were held at open circuit voltage for 15 minutes between the charge-discharge steps.

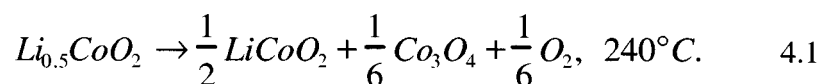
The electrodes underwent 5 charge-discharge cycles and a final charge before the analytical measurements. The LiCoO₂ electrodes were washed repeatedly in (DMC) and dried in an argon-filled glove box. X-ray diffractometry (XRD) was performed on cycled LiCoO₂ with an INEL CPS-120 powder diffractometer using Mo K α radiation ($\lambda=0.7092$ Å). The anode materials were sealed in Pyrex capillary tubes under Ar, using paraffin wax. Detection limits were determined primarily by the statistical quality of the data, and estimated to be about 3%.

Transmission Electron Microscopy (TEM) was performed with a Philips EM 420 instrument. TEM samples were mixed with FlourinertTM and crushed with a mortar and pestle, in an Argon-filled glove box. The powdered mixture of anode material was placed on a holey carbon microscope grid. Electron Energy Loss Spectroscopy (EELS) was performed on the TEM samples using a Gatan 666 parallel detection magnetic prism spectrometer attached to the Philips EM420 TEM. Energy resolution of the spectrometer

was approximately 2.0 eV, with a dispersion of 0.5 eV per channel. EELS measurements were performed with diffraction coupling using 100 keV electrons and a spectrometer collection angle of 11 mrad. The TEM beam current was approximately 7 nA.

4.2.3 Electrochemical

A large capacity fade is observed in the cells during the formation cycles (Figure 4.7), although the reversible capacity was close to what one would expect (~ 120 mAh/g). We attribute the irreversible capacity loss to the build up of a SEI and decomposition of LiCoO₂. Dahn et al. [10] has reported the following reaction upon heating:



The possibility of cobalt extraction from the cathode, and subsequent deposition on the anode, was dismissed as cells were not subjected to the high voltages associated with this process (4.5 V) [11]. The stresses induced by cycling promote cation disorder and microcracking of LiCoO₂ particles [12]. This is consistent with the broadened peaks observed by XRD (Section 4.2.4) and the morphologies observed by TEM (Section 4.2.6.1).

The electrochemical discharge curves of Figure 4.8 have continuous profiles consistent with those of layered LiCoO₂ [2], as opposed to the two step profile of the spinel LiCoO₂ [13-15]. The observed changes in slope of the discharge curves are consistent with documented two-phase regions [2, 11, 16].

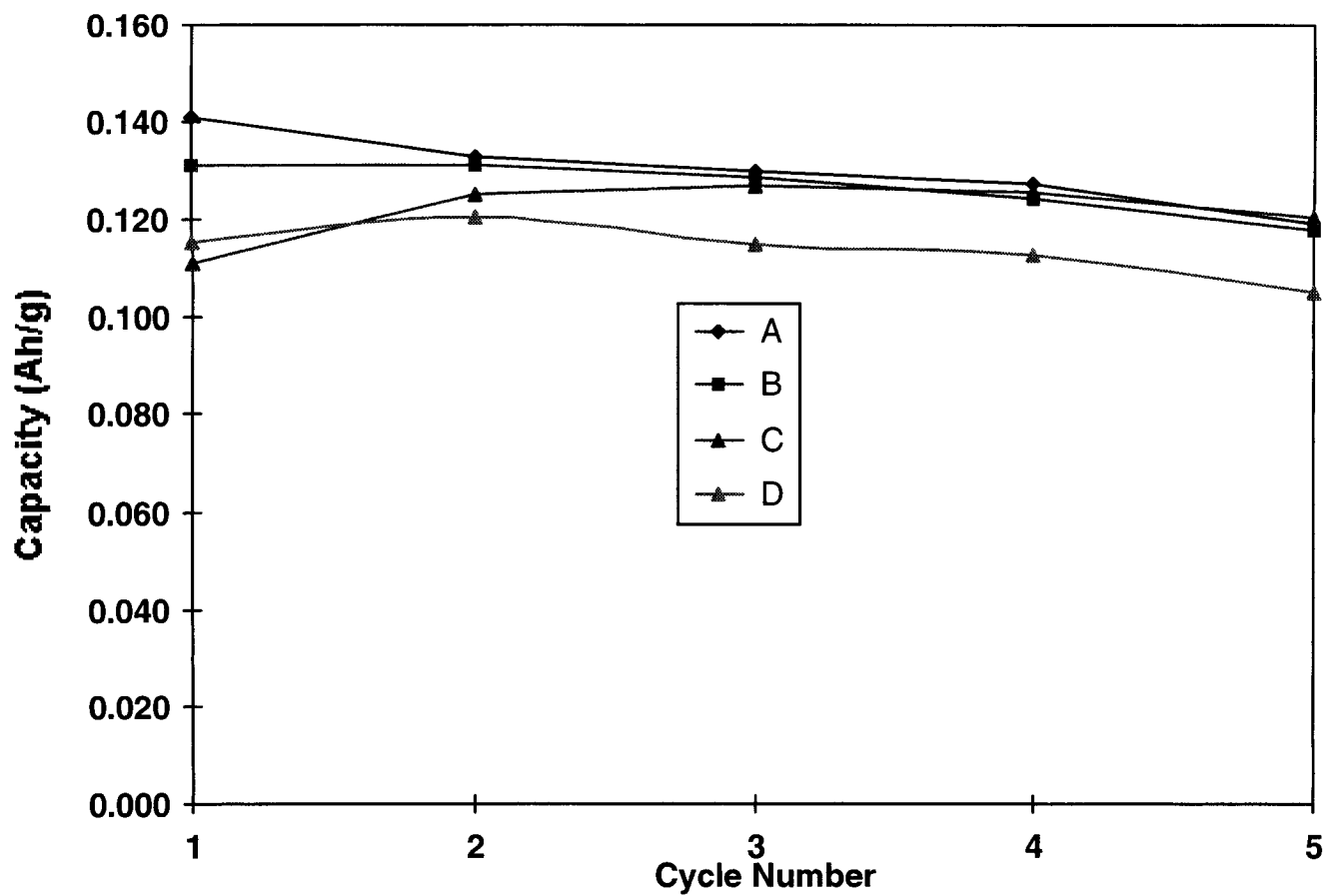


Figure 4.7. Initial cycles of cells discharged to LiCoO_2 (A), $\text{Li}_{0.62}\text{CoO}_2$ (B), $\text{Li}_{0.75}\text{CoO}_2$ (C), and $\text{Li}_{0.62}\text{CoO}_2$ (D).

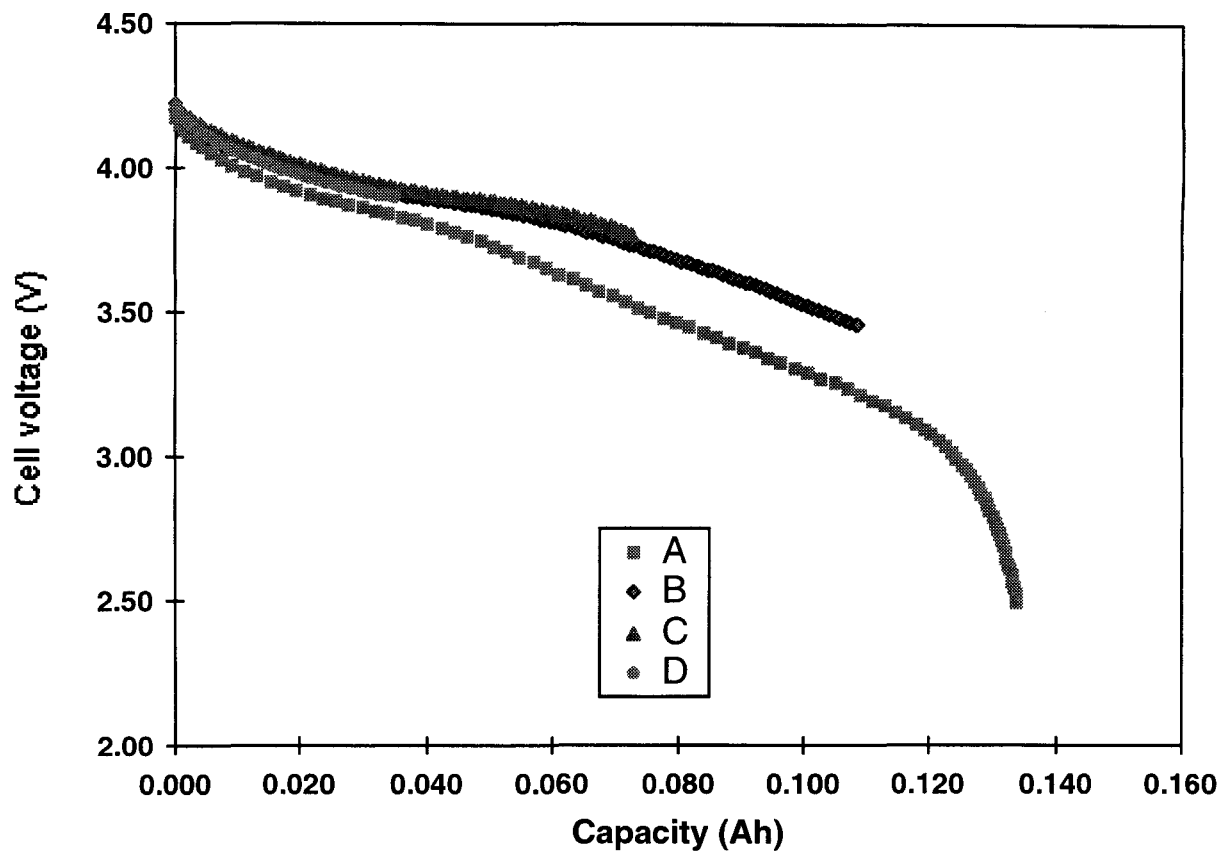


Figure 4.8. Cells discharged to LiCoO₂ (A), Li_{0.62}CoO₂ (B), Li_{0.75}CoO₂ (C), and Li_{0.62}CoO₂ (D).

4.2.4 X-Ray Diffractometry

Figure 4.9 displays XRD patterns of cathodes discharged to various states of charge. The results confirm the lithium concentrations derived from the discharge curves (Figure 4.8) and suggest microstructural damage from cycling as discussed below.

Lithium extraction leads to a decrease of interatomic distance within the *ab* plane and an increase in interplanar distance between the *ab* planes [15,16]. This phenomenon is clearly seen by the decrease in (003) Bragg angle in Figure 4.9. The increase in interplanar distance is attributed to electrostatic repulsion between the layers of oxygen atoms sandwiching the lithium planes. Upon Li deintercalation, the (003) peak is known to disappear near $x=0.93$, as a new peak grows. This defines a first order phase transition, $0.75 < x < 0.93$, to a monoclinic phase which differs by lattice parameter and Li concentration [2]. The measured XRD peaks are broadened due to small grain sizes and nonuniform strain distribution..

4.2.5 EELS Analysis

A number of cobalt oxide standards were investigated and compared with cycled cathodes. CoO has a rocksalt crystal structure with the Co^{+2} ions octahedrally coordinated by O atoms. Co_3O_4 is a spinel with two thirds of the cobalt atoms occupying octahedral interstices (Co^{+3}), the rest tetrahedral ones (Co^{+2}). Bremsstrahlung isochromat spectroscopy (BIS) has shown cobalt in LiCoO_2 to be trivalent with a low-spin ground state configuration, six electrons in the t_{2g} orbitals (d_{xy} , d_{yz} , d_{zx}) and zero electrons in the e_g orbitals ($d_{x^2-y^2}$, d_{z^2})[17].

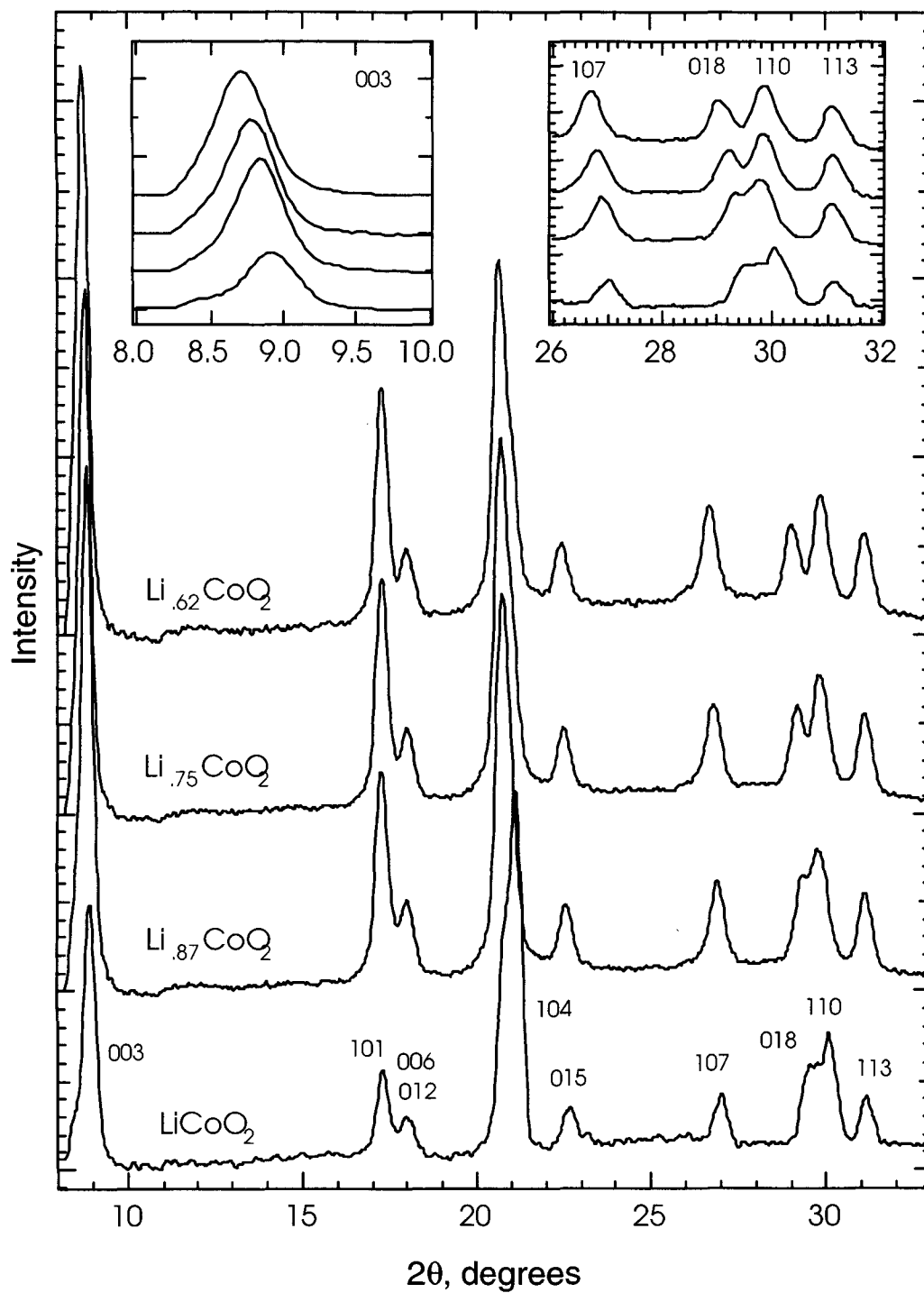


Figure 4.9. X-ray patterns of cycled LiCoO_2 .

4.2.5.1 Cobalt M_{23} , Li K-edge

Figure 4.10 displays the background-subtracted Li K and Cobalt M_{23} edges of CoO, Co_3O_4 , and $LiCoO_2$. The cobalt M_{23} edge onset begins at 60 eV and is evidently affected by the valence and the coordination of cobalt atoms. The plasmon-like profile of the cobalt M_{23} transition is characterized as a *major delayed* edge and displays limited fine structure [18]. The CoO edge corresponds with the expected profile while the edge of Co_3O_4 is broader and shows more structure. The broad peak at 74 eV is most likely attributed to the +3 formal charge on two thirds of the cobalt atoms.

The Cobalt M_{23} edge washes over much detail of the Li K-edge in $LiCoO_2$ spectra. It is clear that the near edge structure of the $LiCoO_2$ edge is more similar to that of Co_3O_4 than CoO. Again the distinct peak at 75 eV is attributed to the Co^{+3} formal charge. The most notable distinction of the $LiCoO_2$ spectra is the peak at 61.5 eV. This peak is most likely the contribution of the Li K-edge. It is prudent to compare the spectra to the Li K-edge of $LiNiO_2$. $LiNiO_2$ has the same crystal structure as $LiCoO_2$ but is not influenced by other overlapping edges (Figure 3.11). The sharp peak at 61 eV of the $LiNiO_2$ Li K-edges matches well with the observed peak in the $LiCoO_2$ spectra. Similar to $LiNiO_2$, the Li K-edge chemical shift is due to the six electronegative oxygen neighbors.

4.2.5.2 Oxygen K-edge

Figure 4.11 displays the oxygen K-edges of some standard samples. Previous investigations on the EELS spectra of transition-metal oxides and full multiple-scattering calculations have identified the origins of four distinct peaks in the oxygen K-edge [19].

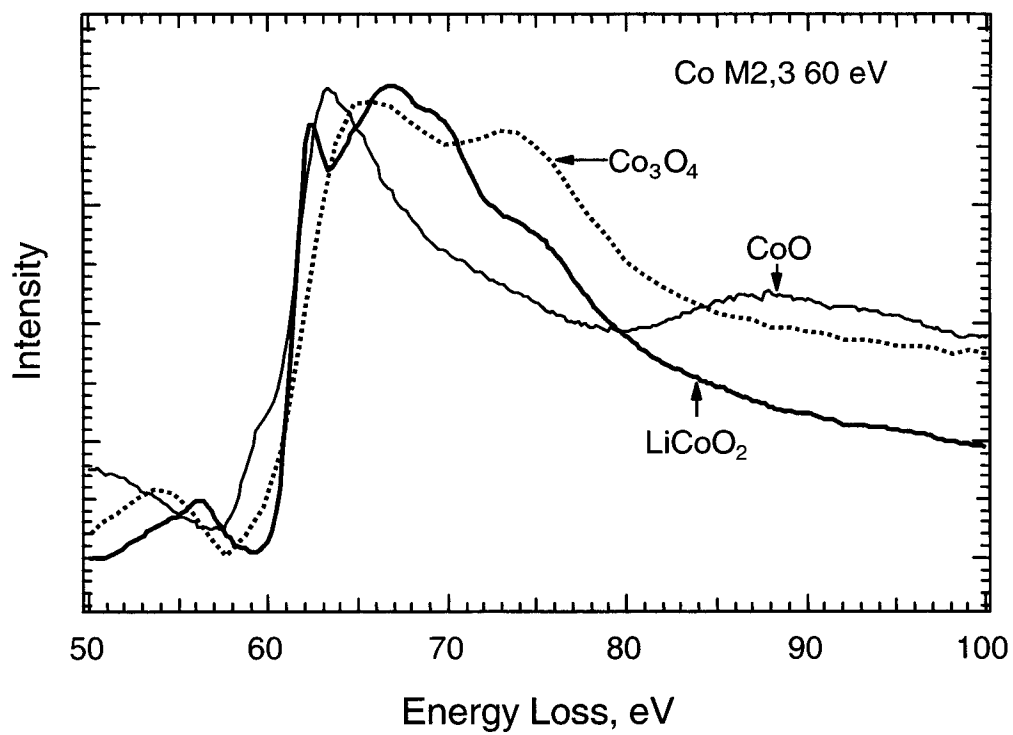


Figure 4.10. Li K and cobalt M₂₃ edge of CoO, Co₃O₄, and LiCoO₂ standards.

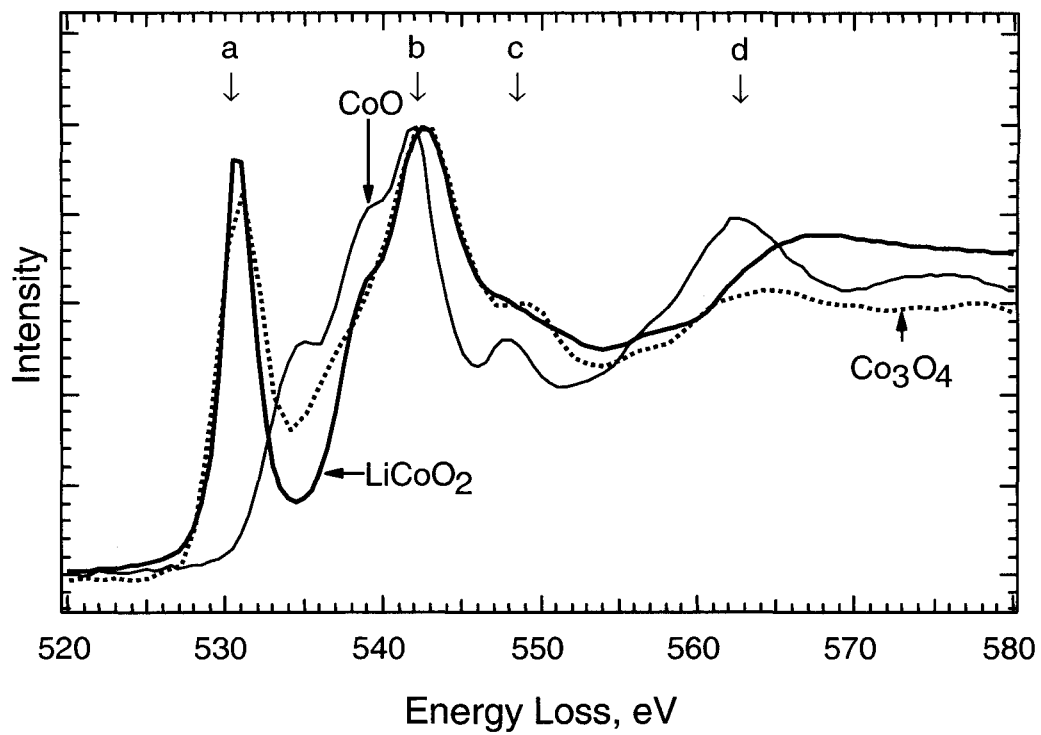


Figure 4.11. Oxygen K-edge of CoO, Co₃O₄, and LiCoO₂ standards.

Labeled *a* in Figure 4.11, the near edge structure at the threshold is attributed to transitions to oxygen states *p* hybridized with cobalt 3*d* states [17, 20]. Peak *b* reflects transitions to oxygen 2*p* states in the cobalt 4*sp* band [21]. The structure of peak *b* is a function of intrashell multiple scattering within the first oxygen coordination shell. Features in the oxygen K-edge of MgO were found to arise by a similar mechanism [22]. Peak *c* arises from intershell multiple scattering from outer-lying oxygen coordination shells. Peak *d* is primarily the result of single-scattering events from the first oxygen coordination shell, and hence is the onset of the extended energy-loss fine structure (EXELFS) region. Defining *R* as the first-neighbor oxygen-oxygen distance, the energy position of peak *d* follows a linear dependence with $1/R^2$ [19].

There are a number of similarities between the spectra of Co₃O₄ and LiCoO₂ while the spectrum of CoO is significantly different. All three spectra agree with published X-ray absorption spectroscopy results [17]. In the CoO spectrum, peak *a* (530 eV) is replaced by a peak at 535 eV (Figure 4.11). Structurally, one might expect comparable oxygen K-edge spectra from the CoO and LiCoO₂ in which oxygen atoms occupy nearly comparable lattice sites. In this case however, it is the difference in oxygen bonding which determines the near edge structure of the oxygen K-edge.

The near-edge structure at onset of the oxygen K-edge is determined by the occupancy of oxygen 2*p* states. In the purely ionic model, oxygen would have an electronic configuration of $1s^2 2s^2 2p^6$, and thus no available states for 1*s* electrons to be promoted into. Covalency increases the number of available oxygen 2*p* states, and thus is measured by the intensity at the threshold of the EELS oxygen K-edge. We therefore conclude that there are oxygen 2*p* states in LiCoO₂ and Co₃O₄, which are filled in CoO.

This is supported by Hamiltonian cluster calculations of LiCoO_2 and CoO [17]. A CoO_6 cluster in octahedral symmetry was employed to determine the occupancy of cobalt 3d states hybridized oxygen 2p states. Hybridization arises with charge transfer from oxygen to cobalt. This leaves holes in the oxygen p band represented by the \underline{L} states. Tables 4.1 and 4.2 display the occupation number of ground state and ionized state. The first ionization state of CoO represents those resulting from doping with Li while the first ionization state of LiCoO_2 can be associated with lithium deintercalation. States with significantly more \underline{L} character are found in the ground state of LiCoO_2 compared to CoO . This increased \underline{L} character in LiCoO_2 bonds is consistent with the larger density of unoccupied oxygen 2p states measured by the EELS oxygen K-edges.

Table 4.1 Occupation numbers of ground state and for electron removal for CoO [17].

GS		Removal	
d^7	0.79	d^6	0.19
$d^8 \underline{L}$	0.20	$d^7 \underline{L}$	0.62
$d^9 \underline{L}^2$	0.01	$d^8 \underline{L}^2$	0.18
		$d^9 \underline{L}^3$	0.01

Table 4.2 Occupation number of ground state and for electron removal for LiCoO_2 [17].

GS		Removal	
d^6	0.47	d^5	0.17
$d^7 \underline{L}$	0.44	$d^6 \underline{L}$	0.51
$d^8 \underline{L}^2$	0.09	$d^7 \underline{L}^2$	0.29
$d^9 \underline{L}^3$	0.00	$d^8 \underline{L}^3$	0.03

We conclude that there is significant hybridization with the Co^{3+} ions and their oxygen nearest neighbors. Thus O 2p states available to O 1s electrons during core

excitations in LiCoO_2 and Co_3O_4 are occupied in CoO . The oxygen K-edge pre-peak is observed in a large number of transitional metal oxides including Sc_2O_3 , TiO_2 , Ti_2O_3 , VO_2 , V_2O_3 , MnO_2 , Fe_2O_3 , Fe_3O_4 , and CuO [19-21].

4.2.5.3 Cobalt L_{23} edge

Figure 4.12 shows the Cobalt L_{23} edges of some standard oxides. From calculated X-ray absorption spectra, one expects multiplet structure in the measured L edges. Limits to EELS resolution result in the broadened peaks, although the breadth and shift of the CoO L_3 peak is consistent with calculations using atomic multiplet theory and cubic crystal field approximations [23]. With Co^{+3} and Co^{+2} atoms contributing to the Co_3O_4 spectrum, it is not surprising to observe peak intensities weighted toward lower energies in Co_3O_4 relative to LiCoO_2 . The L_2 edge of Co_3O_4 and LiCoO_2 is more intense than that of CoO . This could be attributed to the larger number of available cobalt 3d states in Co^{+3} compared to Co^{+2} .

4.2.6 Cycled Cathodes

Cathodes were cycled under relatively passive conditions though they still incurred a significant amount of electrochemical cycling-induced damage. Particles displayed varying degrees of damage suggesting differences in depths of discharge on a local scale.

Significant microstructural damage can occur with delithiation. The observed crystal structure of LiCoO_2 is CuPt structure with ABC stacking order. Recently, Klein et al. [1] succeeded in electrochemically delithiating LiCoO_2 to form CoO_2 , which was

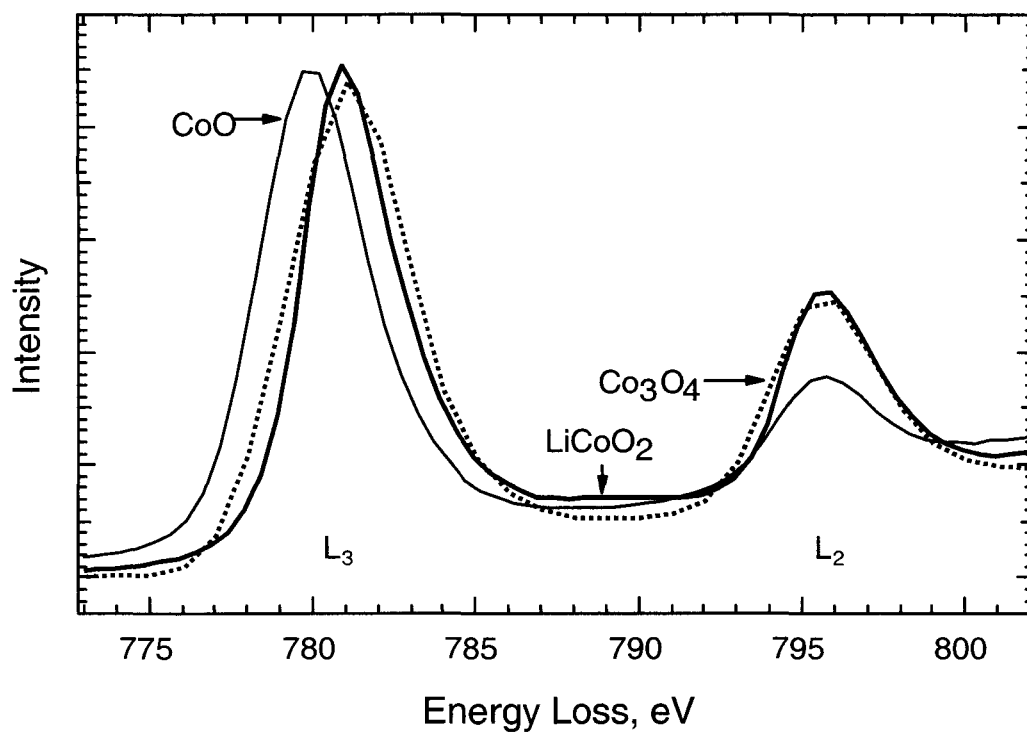


Figure 4.12. Co L₂₃ edge of CoO, Co₃O₄, and LiCoO₂ standards.

found to have a CdI_2 structure with AAA stacking. First-principal total energy calculations confirm these stacking orders as the lowest energy configurations for these systems [24]. It is reasonable that the first order phase transformation to a monoclinic phase [2] and the accompanied changes in stacking order can cause significant microstructural damage.

4.2.6.1 TEM Micrographs of Cycled Cathodes

Figure 4.13 displays two characteristic microstructures observed in the cycled electrodes. The cathode material was composed of polycrystalline regions, with grains on the order of tens of nanometers, and highly crystalline regions with grains on the order of hundreds of nanometers. The size and population of nanocrystals is consistent with the peak broadening observed in XRD analysis (Section 4.2.4).

The (101) diffraction spots, displaying hexagonal symmetry, are the most prominent features of the crystalline LiCoO_2 diffraction pattern (top of Figure 4.13). In addition, the inner two spots are from (003) planes. The spot highlighted by the arrow in Figure 4.13 is from the (220) planes of the Co_3O_4 spinel phase. The Co_3O_4 is a MgAl_2O_4 type spinel with lattice parameter $a = 8.08 \text{ \AA}$ and is distinct from the LiCoO_2 synthesized at lower temperatures (LT- LiCoO_2) [18]. The (220) spinel diffraction spots, displaying hexagonal symmetry, have been observed in a number of cycled cells.

We attribute the elliptical shape of the strong diffraction spots to a contribution from the spinel phase. With the exception of the (220), all of the low order spinel diffractions overlap with those allowed in LiCoO_2 [25]. These spots may have contributions from LiCoO_2 (101) and the spinel (311) diffractions, which virtually

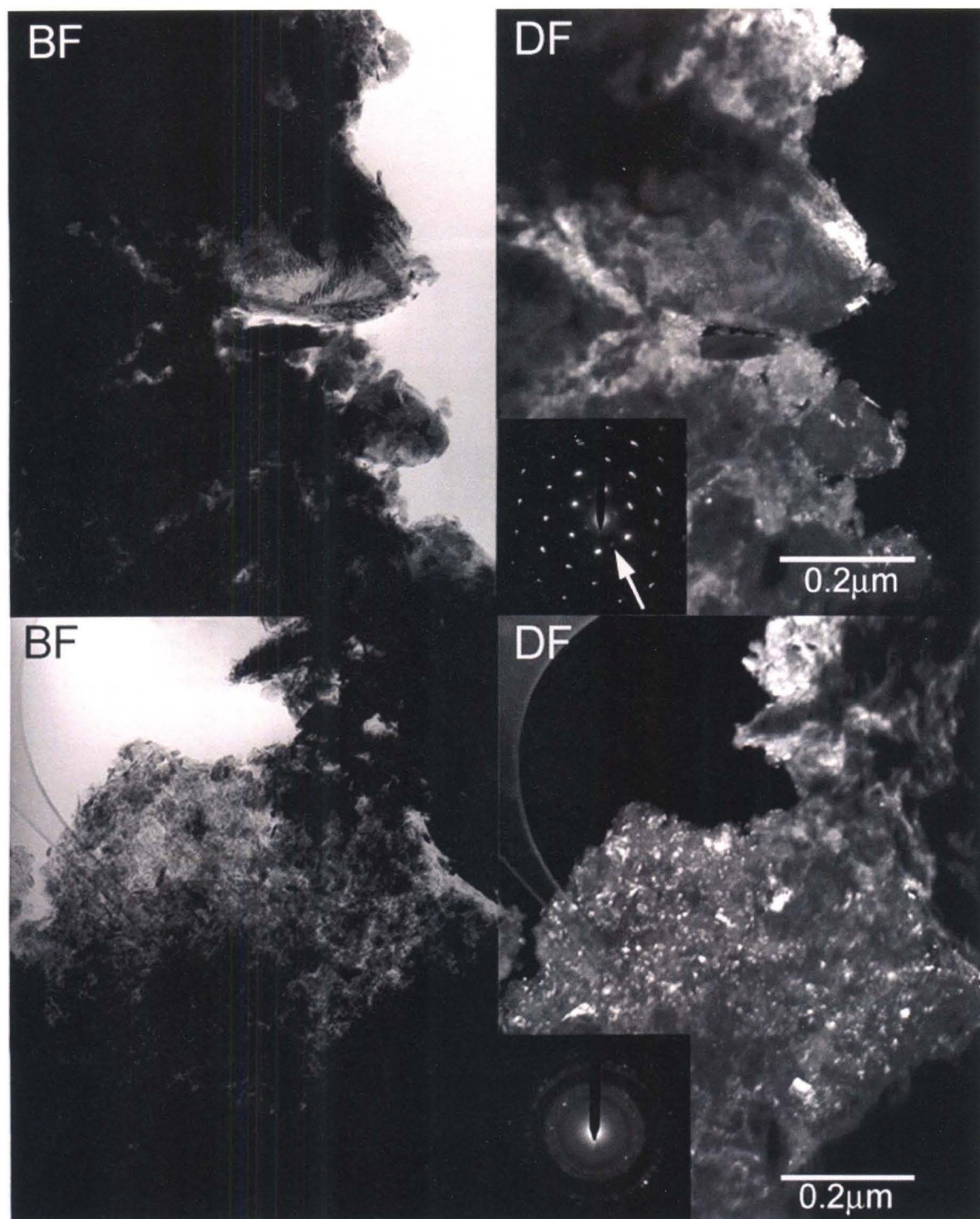


Figure 4.13. Bright field / dark field TEM micrographs of characteristic microstructures of cycled LiCoO_2 cathodes.

overlap. X-ray data of the cycled cathodes do not exhibit a spinel (220) peak, which suggests that the spinel crystallites are limited to a surface layer. The actual Co_3O_4 phase most likely contains numerous defects and cation substitutions. The presence of a Co_3O_4 phase is best explained through the reaction described by Dahn (Section 4.2.3). As Li leaves the cathode, oxygen is evolved and in extreme cases the ordered rocksalt of LiCoO_2 collapses into a spinel of Co_3O_4 (Equation 4.1). This transition is more likely to occur on the surface where the cathode is exposed to the electrolyte.

These results are consistent with those of Wang, et al. [25] who also observe evidence of electrochemical cycling-induced disorder. They found that the electron diffraction patterns of cycled cathodes of LiCoO_2 and LiAlCoO_2 exhibit a new family of (220) reflections indicative of the cubic spinel phase. They also report that this evolution in microstructure is undetectable by X-ray diffraction.

4.2.6.2 EELS Spectra of Cycled Cathodes

Figures 4.14 – 4.16 display background-subtracted EELS spectra of cycled LiCoO_2 at various states of charge. The overall features are similar to those observed in the measured standards with some broadening attributed to a microstructure damaged by electrochemical cycling. Large thin areas (roughly $0.36 \mu\text{m}^2$) were illuminated for EELS analysis to maximize signal-to-noise ratios. The regions used to acquire spectra contained a majority of polycrystalline material along with some large grains. This made it difficult to obtain EELS spectra with good signal to noise ratio. Spectra were deconvoluted using the Fourier-log method (Section 2.3.1) to correct for thickness affects.

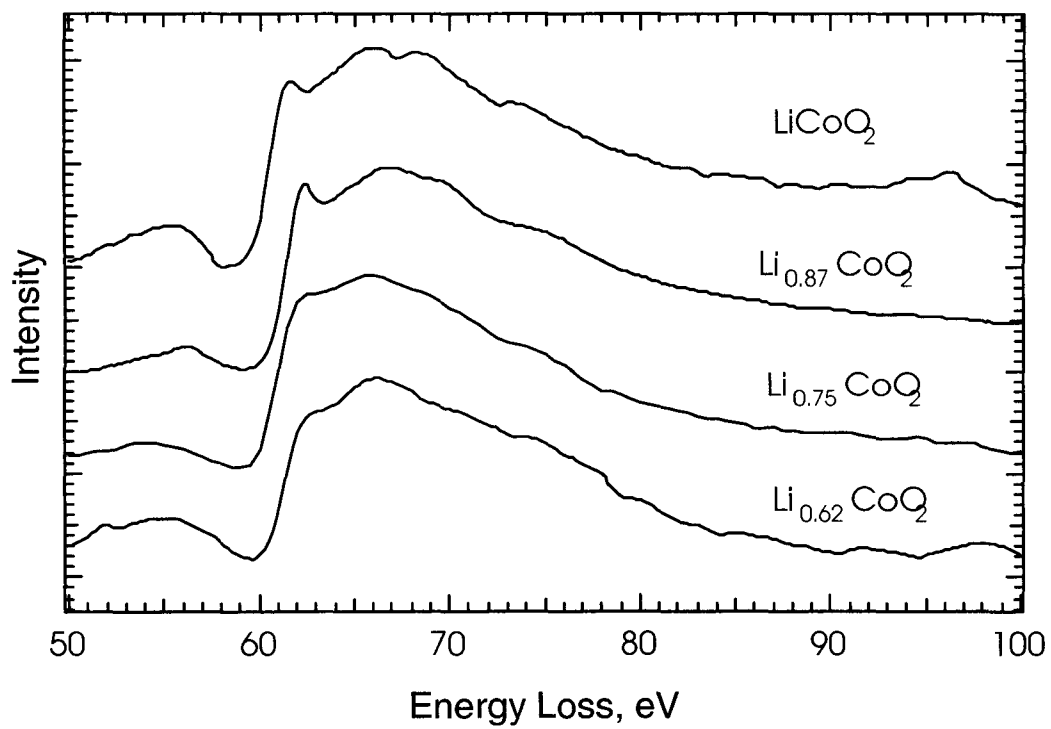


Figure 4.14. Li K and cobalt M_{23} edges of cycled LiCoO_2 .

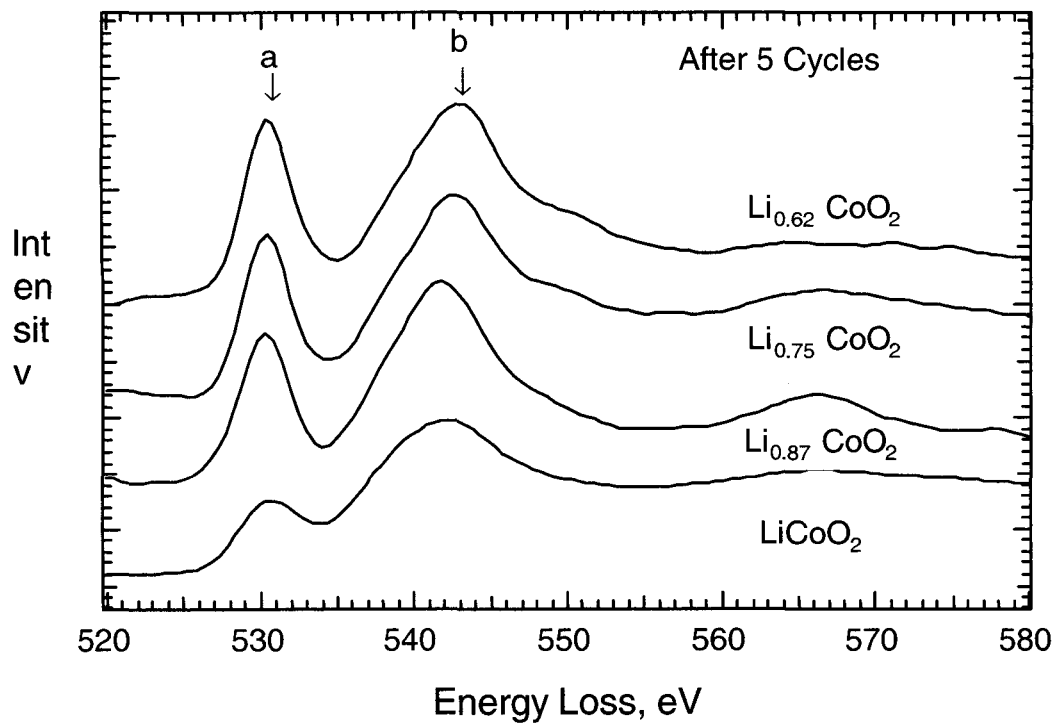


Figure 4.15. O K-edges of cycled LiCoO_2 .

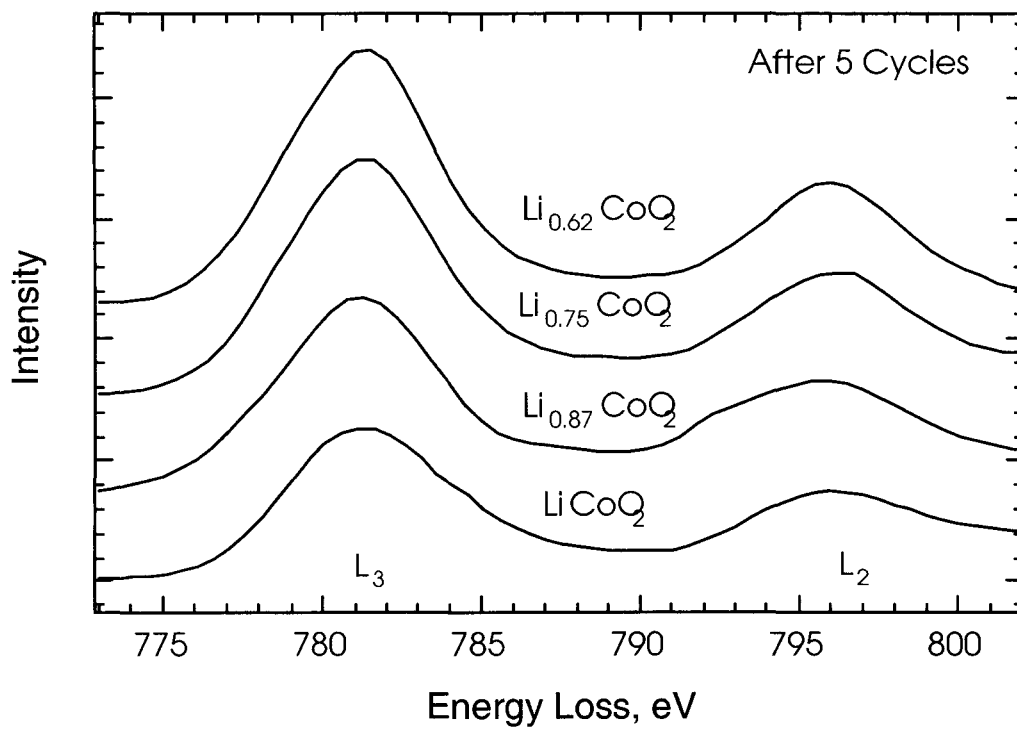


Figure 4.16. Cobalt L₂₃ edges of cycled LiCoO₂.

The region containing the cobalt M_{23} edge (broad onset at 60eV) and Li K-edge (61 eV) is shown in Figure 4.14. From LiNiO_2 spectra (Section 3.4) and spectra from the cobalt oxide standards (4.2.5.1), we conclude the sharp peak at 61 eV is the Li K-edge contribution. It is therefore not surprising to observe this peak to diminish with reduced Li concentration (Figure 4.14).

There is a striking difference in the oxygen K-edge of the cycled LiCoO_2 (Figure 4.15) from that observed in the LiCoO_2 standard (Section 4.2.5.2). Most notably the fine structure of the oxygen K-edge is lost to broadening and the pre-peak at 530 eV (peak *a*) is reduced in all the cycled samples. There may also be a small shift to higher energies of the peak at 540 eV (peak *b*). The most plausible explanation is that there is significant contribution to the spectra from oxygen atoms not associated with the pristine LiCoO_2 phase. The polycrystalline regions are not observed in the LiCoO_2 starting material and are most likely the result of cycling damage. Oxygen atoms in these regions likely occupy a variety of different microstructural sites. These sites could include cobalt deficient regions, regions of the SEI, or sites at grain boundaries. Oxygen atoms in these regions could contribute to the intensity oxygen K-edge spectra above the 532 eV but not to the pre-peak at 530 eV associated the oxygen 2p peaks hybridized with cobalt 3d states. These issues aside, the intensity of the oxygen K-edge pre-peak increases with delithiation.

Figure 4.16 displays the cobalt L_{23} edges for the cycled LiCoO_2 . A small increase in peak intensity can be observed, particularly in the L_3 peak, as lithium is deintercalated. This can be attributed to the increase of unfilled 3d states as cobalt ions increase their valence state to accommodate the absence of lithium charge.

4.2.7 Discussion

Though it is difficult to decouple structural and chemical effects, we speculate that reduced lithium concentration increases the number of available oxygen 2p states. The presence of lithium vacancies requires charge rearrangement around the neighboring cobalt and oxygen atoms. It has traditionally been accepted that in lithium metal oxides (LiMO_2) the valence of the transition metal compensates for the charge on the intercalated Li. The theoretical boundaries for Li concentration in an electrode of Li_xCoO_2 are $0 \leq x \leq 1$. Using a simple ionic charge transfer model, the fully lithiated material has ions with charges of Li^+ , Co^{3+} , and O^{2-} . In the CoO_2 end member the ions have charges of Co^{4+} and O^{2-} . This simple model incorrectly leads to the conclusion that the oxygen valence is virtually unaffected by Li intercalation.

An increase in the number of oxygen 2p states, deduced from the intensity of peak *a*, implies charge transfer from the oxygen to cobalt. Thus the oxygen loses a significant amount of charge as lithium deintercalates.

From another perspective, as lithium intercalates into the cathode, charge accumulates around oxygen atoms, to shift energy bands downward and lower the electronic energy. This could explain the shift in the peak at 540 eV (peak *b*) of the oxygen K-edge to lower energies (Figure 4.15). This peak is associated with transition to oxygen 2p states associated with the conduction band. A lowering of these bands with lithium intercalation would explain the observed shift of this peak to lower energies. The above argument is consistent with the model of oxygen charge compensation proposed by Ceder et al. [9, 26]. Simulations using the soft pseudopotential method [27] in the local spin density approximation (LDA) demonstrate that oxygen atoms of the

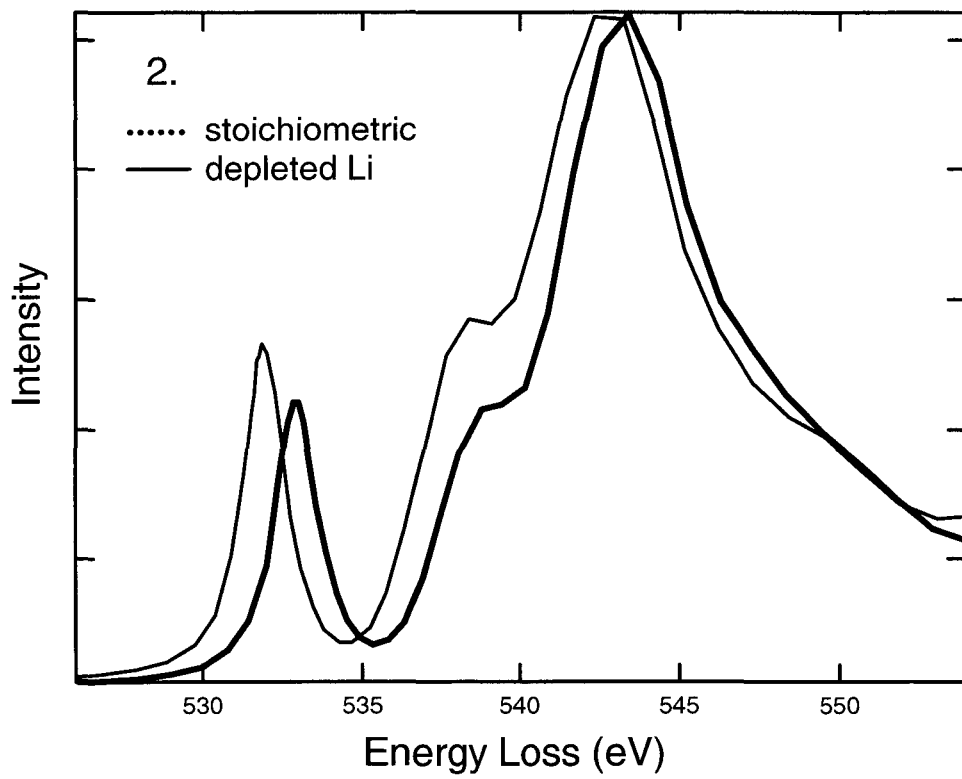


Figure 4.17 Simulation of oxygen K-edge in LiCoO_2 .

cathode accommodate charge with Li intercalation. Although there was significant charge rearrangement around the cobalt atoms, little net charge gain was observed. Bonding within the lattice was found to become increasingly covalent with lithium deintercalation. There is a metal-insulator transition that accompanies this two-phase region [28].

This behavior is supported by calculated energy loss spectra using the ab initio multiple scattering program FEFF8. Figure 4.17 shows a plot of simulated oxygen *K*-edges for stoichiometric ($x = 1.0$) and depleted ($x = 0.66$) Li_xCoO_2 . These simulated edges were convoluted with a gaussian function and normalized to the main peak at 544 eV to more closely represent the experimental data. These calculations show a decrease in the pre-peak of the oxygen *K*-edge with Li intercalation. This decrease indicates a change in the covalent bonding between the Li and O atoms. This simulation predicts a positive 1 eV shift of the pre-peak with increasing Li concentration, which is not observed in the experimental data.

4.2.8 Conclusions

The results of EELS studies of electrochemically cycled LiCoO_2 are presented. EELS measures the O 2p component of the unoccupied states. The energy of these unoccupied states depends on Co – O hybridization. EELS measurements of LiCoO_2 standards reveal a prepeak in the oxygen *K*-edge at 530 eV. For a given composition and phase, the intensity of this prepeak is a measure of covalency in LiCoO_2 . The intensity of the prepeak increase with reduced lithium concentration ($0.67 < x < 1$) in Li_xCoO_2 . Thus the unoccupied O_{2p} states are filled with Li additions. These findings

support the model for oxygen compensation of lithium charge in lithium transition metal oxides. Significant microstructural damage to LiCoO_2 from electrochemical cycling was observed by TEM.

Table 4.3. Normalized areas of oxygen K-edge peaks from Figure 4.15.

X of LiXCoO₂	Peak A	Peak B	Peak A / Peak B
0.62	0.30	0.66	0.45
0.75	0.20	0.53	0.38
0.87	0.23	0.67	0.33
1.00	0.04	0.44	0.08

Errors represent uncertainties in the fitting procedure, which arise in the case of strongly overlapping sub-spectral components.

Table 4.4. Table 4.3. Normalized areas of cobalt L-edge peaks from Figure 4.16.

X of Li_xCoO₂	L₂	L₃	L₂ / L₃
0.62	0.11	0.33	0.34
0.75	0.07	0.25	0.27
0.87	0.08	0.26	0.31
1.00	0.05	0.20	0.23

4.2.9 References

- [1] G. G. Amatucci, J. M. Tarascon, and L. C. Klein, *J. Electrochem. Soc.* **143**, 1114 (1996).
- [2] J N. Reimers and J. R. Dahn, *J. Electrochem. Soc.* **139**, 2091 (1992).
- [3] G. G. Amatucci et al., *J. of Power Sources*, **69**, 11 (1997).
- [4] Y. Gao and J. R. Dahn, *Solid State Ionics*, **84**, 33 (1996).
- [5] S. Sugano, Y. Tanabe, and H. Kitamura, in *Multiplets of Transition Metal Ions in Crystals* (Academic, New York, 1970).
- [6] J. Owens and J. H. M. Thronley, *Rep. Prog. Phys.* **29**, 675 (1966).
- [7] M. Tsukada, *J. Phys. Soc. Jpn.* **49**, 1183 (1980).
- [8] M. Tsukada, H. Adachi, and C. Satoko, *Prog. Surf. Sci.* **14**, 113 (1983).
- [9] G. Cedar t al., *Nature*, 392, 694 (1998).
- [10] J. R Dahn. E. W. Fuller, M. Obrovac, and U. von Sacken, *Solid State Ionics*, **69**, 265 (1994).
- [11] G. G. Amatucci, J. M. Tarascon, and L. C. Klein, *Solid State Ionics*, **83**, 167 (1996).
- [12] H. Wang, Y.-I. Jang, B. Huang, D.R.. Sadoway, Y. -M. Chiang, *J. Pow. Sour.* 81-82, 594 (1999).
- [13] A. Van der Ven and G. Ceder, *Phys. Rev. B* **59**, 742 (1999).
- [14] Zachau-Christiansen et al., *Solid State Ionics, Diffusion & Reactions*, **40/41**, 580 (1990).
- [15] M. M. Thackeray, *Prog. Solid State Chem.* **25**, 1 (1997).
- [16] T. Ohzuku and A. Ueda, *J. Electrochem. Soc.* **141**, 2972 (1994).
- [17] J. van Elp et al., *Phys. Rev. B* **44**, 6090 (1991).

- [18] C. C. Ahn and O. L. Krivanek,, EELS Atlas, Gatan Inc, Warrendale, PA (1983).
- [19] H. Kurata, E. Lefevre, C. Colliex, and R. Brydson, *Phys. Rev. B* **47**, 13763 (1993).
- [20] P. A. van Aken, B Liebscher, V. J. Styrsa, *Phys. Chem. Minerals*, **25**, 494 (1998).
- [21] F. M. F. de Groot, M Grioni, J. C. Fuggle, J. Ghijsen, and G. A. Sawatzky, *Phys. Rev. B* **40**, 5715 (1989).
- [22] P. Rez, X. Weng, and H. Ma, *Microsc. Microanal. Microstruct*, **2**, 143 (1991).
- [23] F. M. F. de Groot, J. C. Fuggle, B. . Thole, G. A. Sawatzky, and H. Petersen, *Phys. Rev. B*, **42**, 5759 (1990).
- [24] C. Wolverton and Alex Zunger, , *Phys. Rev. B*, **57**, 2242 (1998).
- [25] H. F. Wang, Y. I. Jang, B.Y. Huang, D.R. Sadoway, Y.M. Chiang, *Journal of Power Sources*, **82**, 594 (1999).
- [26] M. K. Aydinol, A. F. Kohan, and G. Cedar, *Phys. Rev. B* **56**, 1354 (1997).
- [27] G. Kresse and J. Furthmuler, *Comput. Mat. Sci.* **6**, 15 (1996).
- [28] H. Tukamoto and A. R. West, *J. Electrochem. Soc.***144**, 9 (1997).

4.3 ^{119}Sn Mössbauer Spectrometry of Li-SnO Anode Materials for Li-Ion Cells

4.3.1 Introduction

There is widespread scientific and technical interest in the high specific energy of Li-ion cells for secondary batteries. This high specific energy density is derived from the high cell voltage, typically 4 V (versus 1.3 V for a typical Ni-MH secondary battery). The Li densities in the cathode and anode materials are modest, however, and it is hoped that higher capacities of these electrodes will lead to further increases in the specific energies of Li-ion cells. Anode and cathode materials are now subjects of numerous investigations [1-3]. Huggins performed some early work on alloy anodes [4,5]. Recently, Ioda, et al., of Fujifilm Celltec Co., Ltd., announced a new class of anode material comprising a composite Sn oxide glass [6,7]. These Sn oxide glasses have a reversible capacity of approximately twice that of carbon materials, but unfortunately exhibit a large irreversible capacity and capacity fade after tens of charge-discharge cycles.

Early evidence suggested that the Li inserted in the Sn oxide glass material was ionic [7], but Courtney et al., McKinnon and Dahn have provided convincing evidence for the formation of metallic Sn and Sn-Li alloys during Li insertion [8-10]. The general picture is that Li reduces the Sn oxides to metallic Sn and lithium oxides. Mao, et al. [11,12], has performed further studies on the mechanism of Li insertion in tin oxides and alloys with ^{119}Sn Mössbauer spectrometry measurements using a sealed cell. With increasing Li concentration in the anode material, a series of Li-Sn phases were observed by XRD [13], including $\text{Li}_{22}\text{Sn}_5$, which represents an increase in volume over that of pure $\beta\text{-Sn}$ by a factor of 3.6. Courtney and Dahn argued that since the increase in

specific volume induces large local stresses, the cycle life of the electrode is poor when the Sn-rich regions in the electrode are large [8-13]. The role of microstructure on the cycle life of Sn oxide anodes remains poorly understood, however.

Although the Fujifilm Celltec material has not yet been used for products in the marketplace, its promise has prompted a number of investigations into other Sn and Sn oxide materials that can be used as anodes in Li-ion cells [9-18]. Huang et al. [14] has studied the insertion of Li into SnO, showing again that the Li served to reduce the Sn, and a Li-Sn alloy was formed at higher Li concentrations. Here we report results of ^{119}Sn Mössbauer spectrometry measurements at 11 K and 300 K on partially - and fully-charged Li-SnO anode materials. We present detailed measurements of the recoil-free fractions (RFF.) of the anode materials, and we show that the RFF's of the Sn oxide in the anode is anomalous, indicative of atomic-scale heterogeneities in the distribution of Sn atoms. Similar results are reported for the β -Sn in the anode material, although the contribution from the β -Sn is not definitively resolved from the $\text{Li}_{22}\text{Sn}_5$. We also present results from a study on the deterioration of Li-charged anode materials and Li-Sn alloys during long-term atmospheric exposure. During atmospheric exposure, the selective oxidation of Li causes β -Sn to separate quickly from the Li-Sn alloy, and the β -Sn then oxidizes over longer times. The hyperfine parameters of the Mössbauer spectra indicate that in the early stages of oxidation, the Sn is in small or defective oxides with Sn^{4+} , but a little Sn^{2+} was observed at later times.

4.3.2 Experimental

Electrode and Sample Preparation. — Commercial SnO powder was purchased from Cerac Chemical. The SnO electrodes were fabricated on copper foil substrates using 6 wt % polyvinylidene fluoride (PVDF) binder with 10% carbon black as a conductive diluent. These electrodes were used in half-cells with Li metal as the anode and an electrolyte of 1M LiPF₆ dissolved in 30 % ethylene carbonate (EC) and 70% dimethylene carbonate (DMC). Selected amounts of Li, varying from 0 to 6.4 mole per mole of SnO, were titrated into SnO or extracted from Li_xSnO using galvanostatic measurements at a current density of 0.020 mA cm⁻². Here we define “x” in Li_xSnO as the molar ratio of Li to the initial SnO. Figure 4.18 shows the initial charge and discharge curves, with labels indicating the approximate state of the samples used for Mössbauer spectrometry measurements. In what follows, these samples will be designated Li_{2.3}SnO and Li₅SnO. Similar electrodes and cells were used in measurements of cycle life using an automatic battery cycler made by Arbin Corp., College Station, TX. Cycle life measurements were performed on sealed full-cells with LiCoO₂ cathodes. The voltage range was controlled to be between 3.0 and 4.1 V with a charging current density of 0.2 mA/cm² and a discharging current density of 0.4 mA/cm². Cycle life measurements were also performed on a half-cell using a Li counter electrode. The half-cell cycle life measurements used the same current densities for charging and discharging, but had a voltage range between 0 and 1 V.

To characterize the Li-SnO electrode materials by X-ray diffractometry (XRD), transmission electron microscopy, and Mössbauer spectrometry, after 5 cycles the electrodes were removed from the half-cell and washed in DMC. The electrodes were vacuum dried and the powders were scraped. All operations were performed in a glove

box with a pure and dry argon atmosphere. Samples for XRD were sealed in pyrex capillary tubes under Ar atmosphere. TEM samples were prepared by crushing anode material with a mortar and pestle under Fluorinert FC-43 by 3M. Copper backed, amorphous carbon grids were then dipped into the anode/fluorinert suspension and inserted into the microscope. For Mössbauer spectrometry, the anode powder was mixed with a small amount of dehydrated boron nitride powders to ensure an overall thickness homogeneity. The samples were pressed into pellets that were encapsulated in altuglass sample holders and sealed with an altuglass glue. The samples comprised typically 50 mg of anode material. To study oxidation behavior, powdered samples were also stored in ambient laboratory air. Although the XRD and Mössbauer spectrometry samples were exposed to ambient conditions on different continents, equivalent atmospherics were sought by inoculating the Pasadena air with vapors from a bottle of Chateau le Barradis 1996.

^{119}Sn Mössbauer spectra were obtained at room temperature (denoted “RT”, nominally 300 K) and at 11 K in transmission geometry with a spectrometer operated in the conventional constant acceleration mode. A $\text{Ba}^{119}\text{SnO}_3$ radiation source with a strength of ~ 10 mCi was used. Typical acquisition times were 12 h or 24 h. All ^{119}Sn isomer shifts are referenced to BaSnO_3 at RT. The velocity scale was calibrated with a metallic body-centered (bcc) iron sample and source of ^{57}Co in Rh. Spectra of commercially available powders of SnO_2 , BaSnO_3 , and a $12\ \mu\text{m}$ foil of metallic β -Sn were also measured for use as calibration standards. Spectra of mixtures of known

amounts of commercial powders of SnO_2 , $\text{Li}_{22}\text{Sn}_5$, and $\beta\text{-Sn}$ were also measured at 300 K and 11 K.

All spectra were recorded with adequate counting statistics to permit a deconvolution of the natural linewidth from the spectrum. This deconvolution was useful for revealing the presence of different chemical environments of Sn atoms. The deconvolution utilized a conventional constrained Hesse-Rübatsch method [19]. The use of a model-independent histogram method for such an experimental purpose is new to the best of our knowledge. Since a simple Lorentzian lineshape is deconvoluted from the experimental spectra, in practice the deconvolution procedure is much the same as using the constrained Hesse-Rübatsch method for determining an isomer shift distribution. The calculation of hyperfine parameter distributions from spectra has been the subject of a number of studies and recent reviews [19-22]. Mathematically, this class of "inverse problems" is ill-posed. Small changes in spectra may lead to large changes in the resulting distributions. Regularization methods are therefore required when working with real experimental data, and regularization impairs the deconvolution procedure.^d

Nevertheless, the deconvolution provides a significant and welcome improvement in resolution. For Sn spectra, the FWHM of the deconvoluted Lorentz line was chosen here as a typical minimum FWHM of a single Sn spectral line, that is $\Gamma=0.82$ mm/s. As another consequence of the regularization procedure, small oscillations appear above the flat zero background of the deconvoluted spectra. These oscillations are artifacts of the deconvolution procedure. Although the smoothing parameter must be small to avoid

^d Regularization conditions are set by the smoothing parameter of the constrained Hesse-Rübatsch method [19]. For example, when a Lorentzian line with a full-width-at-half-maximum (FWHM) $\Gamma_L = 0.22$ mm/s is removed from a calibration spectrum of metallic bcc iron (with a good signal-to-noise ratio) whose inner

distorting excessively the main contributions, it must be large enough to avoid the oscillations that are driven by counting statistics.^c All spectra were calculated with the same fitting conditions. The deconvoluted spectra are normalized to unity.

4.3.3 Electrochemical Results

Figure 4.18 shows the cell voltage vs. Li capacity for the first coulometric titration of the SnO electrode. The large irreversible capacity of about one-third the initial capacity (1240 mAh/g) was typical of cells of Sn oxide anode materials [12-18]. This irreversible capacity for the first cycle is probably caused by several factors including the consumption of Li atoms during the reduction of the SnO, the reduction of the electrolyte with the formation of a solid-electrolyte interphase, and perhaps the formation of kinetically inaccessible Li. With $x > 6.2$, the cell voltage of 0 V indicates that there is an electroplating of Li on the electrode.

Cycle life results are presented in Figure 4.19. The impressively high initial capacity declines markedly after several cycles, but the deterioration slows considerably after five cycles. After about 30 cycles the capacity was approximately 300 mAh/g in both the half-cell and full-cell cycling tests. These results are typical of those reported on other Sn oxide anodes [10-18].

4.3.4 X-Ray Diffractometry and TEM Results

lines have a FWHM $\Gamma_M = 0.24$ mm/s, a line well approximated by a Gaussian line of FWHM $\Gamma_G = 0.13$ mm/s remains. This is much wider than the Lorentzian function of FWHM = 0.02 mm/s that is predicted.^c Such oscillations can have only a weak effect on the integral results presented in Tables 4.3 and 4.4, however.

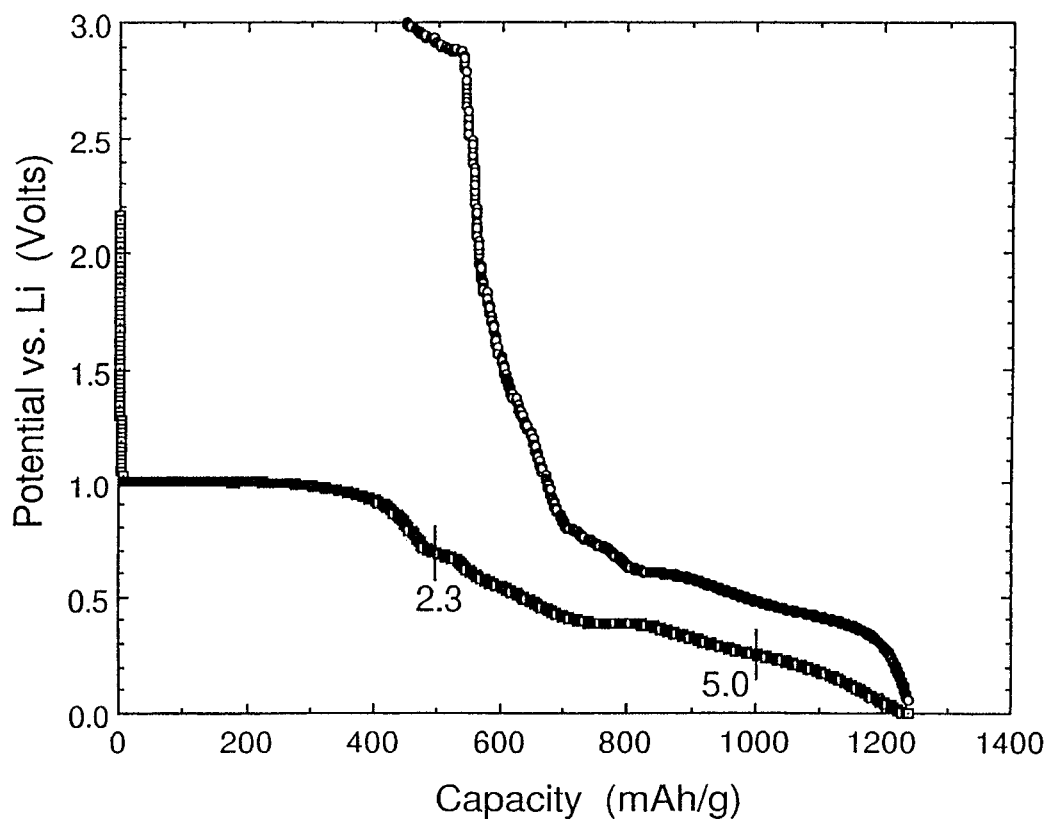


Figure 4.18. First pair of electrochemical charge and discharge curves on SnO anode at 0.02 mA/cm^2 . Anodes for further analysis were obtained from samples charged initially to $x=2.3$ and $x=5$, as marked approximately on the figure.

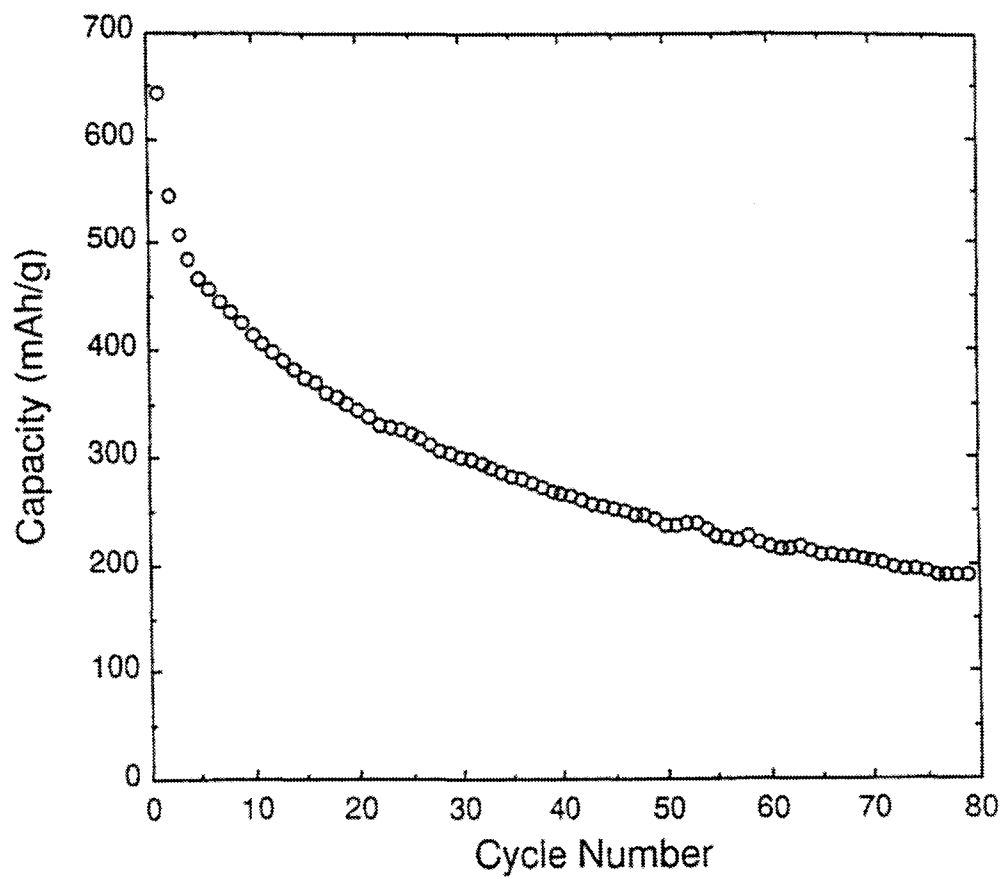


Figure 4.19. Capacity fade data on full cell of SnO anode with LiCoO₂ cathode with 0.43 mA/cm².

X-ray diffractometry was performed with Mo K α radiation ($\lambda = 0.07107$ nm) using an Inel CPS120 powder diffractometer with a position sensitive detector. The electrodes were composed initially of powdered SnO. Nevertheless, upon the first electrochemical titration of Li to $x=5$ in Li_xSnO , XRD showed a distinct diffraction pattern from $\text{Li}_{22}\text{Sn}_5$ alone (see Figure 4.20). The electrode material charged to $x=2.3$ showed a mixture of β -Sn and $\text{Li}_{22}\text{Sn}_5$, but no SnO. Evidently the SnO is quickly reduced during Li insertion. When more Li is inserted, the β -Sn forms an alloy with Li metal. XRD shows this alloy to be $\text{Li}_{22}\text{Sn}_5$ both for low and high Li insertions, but the diffraction peaks from $\text{Li}_{22}\text{Sn}_5$ are broader for the electrode material charged to $x=2.3$. Figure 4.20 also shows a significant broadening of the X-ray peaks from the β -Sn in the anode material, indicative of crystallite sizes of 10 nm or so. There was no evidence for oxides of either Sn or Li in any XRD patterns. From the large amounts of Sn^{4+} observed by Mössbauer spectrometry, we would expect a significant amount of diffraction from Sn oxides. The absence of diffraction peaks from Sn oxide indicates that it is probably amorphous, and its broad diffraction pattern was lost when stripping the diffraction pattern of the glass capillary from the measured data. Although we would expect only weak X-ray scattering from Li oxides, perhaps near the limit of detectability, we also suspect that the Li oxides may be amorphous or present as small particles with broadened diffraction peaks.

Transmission electron microscopy was performed with a Philips EM430 transmission electron microscope operated at 200 keV. A bright field transmission electron micrograph of the Li_5SnO material is presented in Figure 4.21. The electron beam damage to the specimen proved to be quick, substantial, and recognizable as a change in the shapes of the regions being examined. The image in Fig. 4.20 was acquired

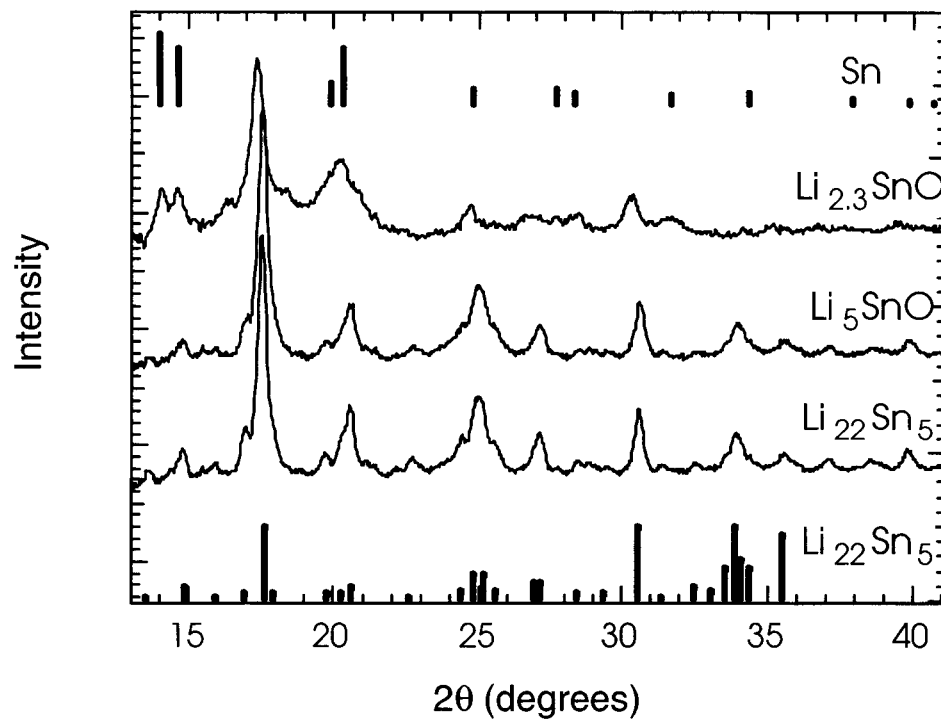


Figure 4.20. X-ray diffraction patterns of $\text{Li}_{22}\text{Sn}_5$ alloy, and Sn oxide materials, Li_xSnO , charged initially to $x=2.3$ and $x=5$.

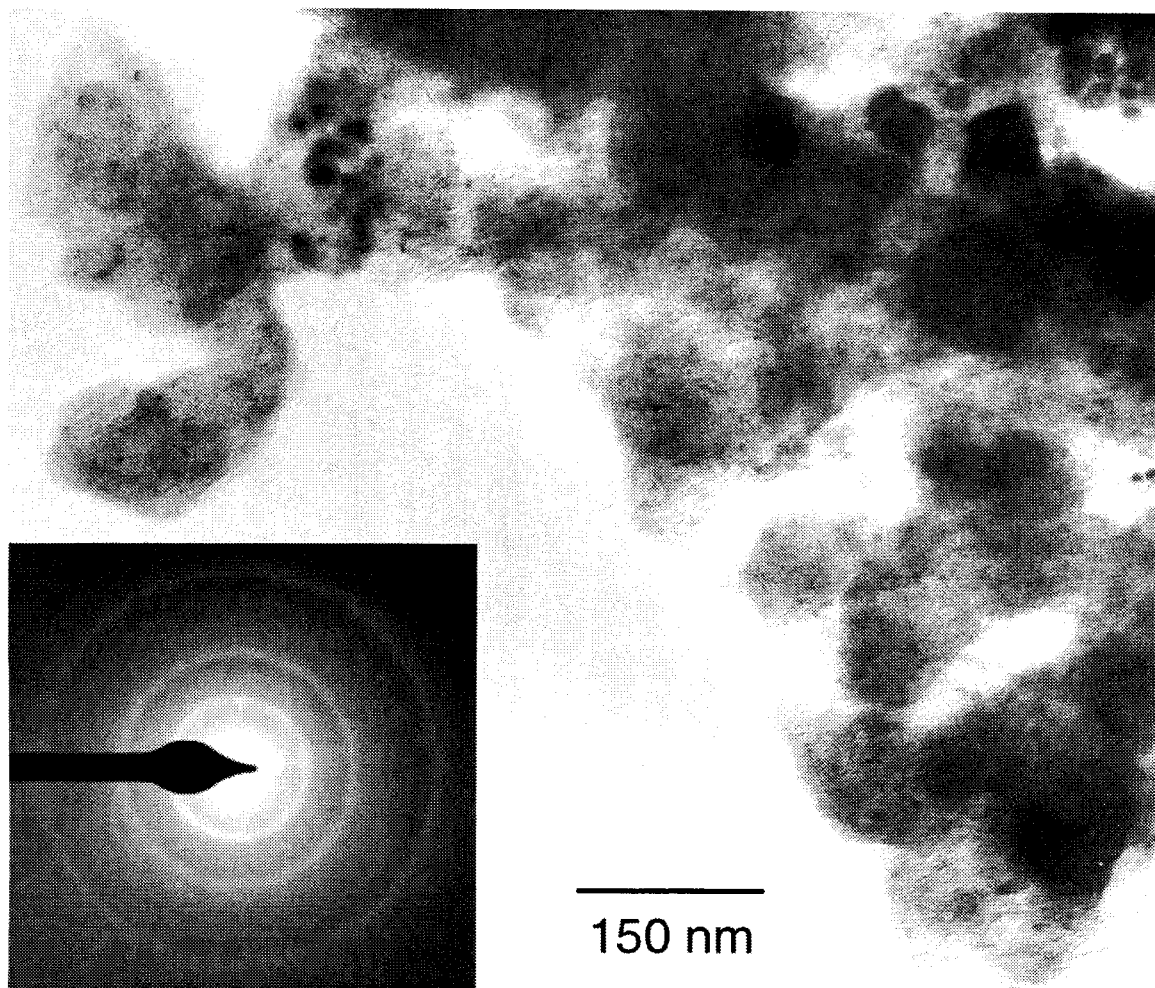


Figure 4.21. Bright field transmission electron micrograph of the Li_5SnO anode material.

within a few seconds after the region was moved into the electron beam. The diffraction pattern shows primarily β -Sn, although some diffraction spots from $\text{Li}_{22}\text{Sn}_5$ were visible in other diffraction patterns. On the other hand, this material was found to be primarily $\text{Li}_{22}\text{Sn}_5$ by XRD. The conversion to β -Sn suggests substantial oxidation of the thin TEM sample, as discussed below. The TEM image of Figure 4.21 shows many small regions that appear dark, likely because they are β -Sn particles that are diffracting or more absorbing. These regions range in size from a few nanometers to tens of nanometers. The lighter regions are probably Li oxide.

4.3.5 Mössbauer Spectrometry Results

4.3.5.1 Mössbauer Spectra of Control Samples

At the top of Figure 4.22 are transmission Mössbauer spectra from β -Sn, SnO_2 , and $\text{Li}_{22}\text{Sn}_5$ acquired at 300 K (RT). Deconvoluted spectra with higher resolution are shown below them. Also shown in Figure 4.22 are deconvoluted spectra acquired at 11 K. In general, the more oxidized the Sn, the larger the shift to negative velocities. The SnO_2 spectrum at RT comprises a doublet of equal intensity lines with $\text{IS}=0 \pm 0.03$ mm/s and a quadrupole splitting $\text{QS}=0.58 \pm 0.04$ mm/s. This is in good agreement with published values: ($\text{QS}=0.50$ mm/s [23], $\text{QS}=0.61$ mm/s [24], $\text{QS}=0.55$ or 0.56 mm/s [25], $\text{QS}=0.56$ mm/s [26], $\text{QS}=0.54$ mm/s [27]). The β -Sn spectrum at RT consists of a slightly-broadened single line ($\Gamma=0.95$ mm/s) with an isomer shift of 2.52 ± 0.03 mm/s at RT. It agrees with published values ($\text{IS}=2.56 \pm 0.02$ mm/s [24], 2.542 ± 0.005 mm/s [28]). It is important to note that the β -Sn isomer shift falls within the typical range (2.5-2.7

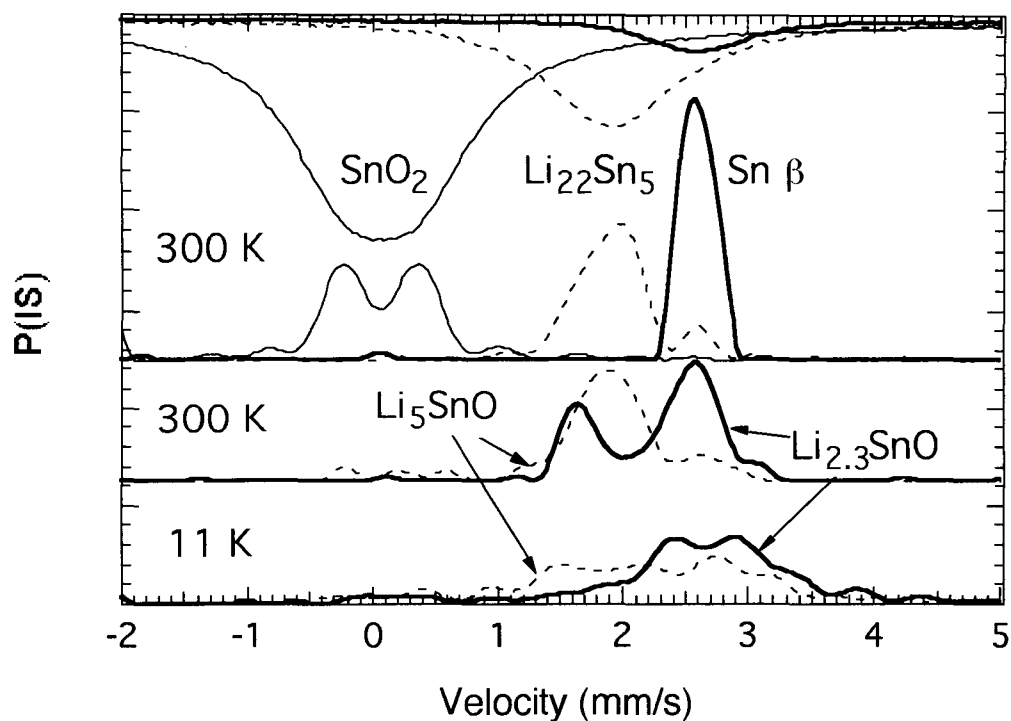


Figure 4.22. Top: transmission Mössbauer spectra of β -Sn, $\text{Li}_{22}\text{Sn}_5$, and SnO_2 (RT). Below them are deconvoluted Mössbauer spectra of β -Sn, $\text{Li}_{22}\text{Sn}_5$, and SnO_2 (RT). Middle: deconvoluted Mössbauer spectra from Sn oxide materials, Li_xSnO , charged to $x=2.3$ and $x=5$ (RT). Bottom: deconvoluted Mössbauer spectra from Sn oxide materials, Li_xSnO , charged to $x=2.3$ and $x=5$ (11 K).

mm/s) of isomer shifts of Sn^{2+} in SnO or in SnO_x ($x < 2$) (the precise values depend on x and on the actual oxide structures). The β -Sn can be distinguished, however, because the oxide spectra exhibit quadrupole splittings larger than 1 mm/s, and often close to 2 mm/s [23-30]. The isomer shift increases by about 0.04 mm/s when β -Sn is cooled to 77 K [31]. Theoretical calculations [32] shows that the isomer shift of β -Sn falls between the isomer shift of covalent β -Sn, 2.021 ± 0.012 mm/s at RT [28], and that of a hypothetical metallic fcc Sn structure. A quadrupole splitting $QS = 0.41 \pm 0.04$ mm/s is measured for β -Sn from the deconvoluted 11 K spectrum. Our data are in good agreement with results from recent theoretical calculations [33] of $QS = 0.37$ mm/s for α -Sn and $QS = 0.47$ mm/s for SnO_2 .

Three spectra were measured from the control sample of $\text{Li}_{22}\text{Sn}_5$: one at RT, one at 11 K, and one again at RT after recording the low-temperature spectrum. The spectrum of $\text{Li}_{22}\text{Sn}_5$ is mainly a single broadened line. After deconvolution, a main line with a maximum at 1.93 ± 0.03 mm/s is observed. This line is asymmetric and a high intensity shoulder at about 1.75 mm/s is also observed. A line with a relative area of 0.12 is also observed at 2.56 ± 0.03 mm/s. The deconvoluted RT spectrum in Fig. 4.21 also show a much smaller broad line at about 1.05 mm/s which may not be experimentally significant, and very small oscillations that are artifacts of the deconvolution procedure. (These oscillations are considerably stronger for the 11 K deconvoluted spectrum owing to poorer counting statistics.) The crystallographic structure of $\text{Li}_{22}\text{Sn}_5$ is of the $\text{Li}_{22}\text{Pb}_5$ type (fcc, $a = 1.978$ nm, with 16 formula units). This structure contains 432 atoms per unit cell and 80 Sn atoms in four different Sn sites with respective proportions 0.2, 0.2, 0.3, 0.3. In principle, these four chemical environments contribute up to eight independent

lines to the observed spectrum, but the resolution even of the deconvoluted spectra is inadequate to identify the eight independent peaks. We can say only that the broadening of the $\text{Li}_{22}\text{Sn}_5$ spectrum probably originates with the different crystallographic sites for Sn atoms in the $\text{Li}_{22}\text{Sn}_5$ structure. At 11 K, the spectrum is broadened significantly and rather symmetrically around 2.13 mm/s. This suggests an increase of the quadrupole splittings of the Sn sites when temperature is decreased. The isomer shift of approximately 2.0 mm/s for $\text{Li}_{22}\text{Sn}_5$ is consistent with α -Sn. We suggest, however, that the more negative isomer shift than that of β -Sn may have a chemical origin involving charge transfer between the Sn atoms and their Li neighbors.

The 300 K spectrum of $\text{Li}_{22}\text{Sn}_5$ measured subsequent to the 11 K spectrum is similar to the original 300 K spectrum, but shows some differences. The main line is still at 1.95 ± 0.03 mm/s, but the shoulder at 1.75 mm/s is relatively more intense than previously. The relative area of the line at 2.56 mm/s has increased to 0.19, and a smaller line is seen at 1.25 mm/s. We show below that these changes are consistent with an oxidation of the sample.

From these results on the control samples, we present a convenient summary of the velocity ranges in ^{119}Sn spectra:

-1.0 to 1.0 mm/s corresponds to Sn^{4+}

1.0 to 2.3 mm/s corresponds to Sn in a Li-Sn alloy

2.2 to 3.2 mm/s corresponds to β -Sn

Spectral areas were integrated over these three velocity ranges to prepare Tables 4.5 and 4.4 for the different anode materials. For the spectra measured at 11 K, however, the overlap of the spectral components from β -Sn and the Li-Sn alloy required that their spectral components were fit to a pair of overlapping Gaussian lines. This fitting procedure was more ambiguous than integrating the areas of well-resolved lines, so we present error bars in Table 4.5 to indicate uncertainties in the area fractions. These areas, normalized by the recoil-free-fractions, could be used to determine the fraction of Sn atoms in these three different chemical states.

4.3.5.2 Mössbauer Spectra of Anode Materials

Although the anode was prepared from SnO, Mössbauer spectrometry shows that the anode material of $\text{Li}_{2.3}\text{SnO}$ is a mixture of β -Sn plus a Li-Sn alloy, evidently $\text{Li}_{22}\text{Sn}_5$ from the XRD results. The fully-lithiated anode material, Li_5SnO , is primarily $\text{Li}_{22}\text{Sn}_5$ from XRD, and its Mössbauer spectrum is quite close to that of the standard sample of $\text{Li}_{22}\text{Sn}_5$. It is not surprising that no SnO is present after five charge/discharge cycles, because we expect the Li to reduce SnO. Evidently the α -Sn forms with lower Li stoichiometry, perhaps less than $\text{Li}_{2.3}\text{SnO}$, and the $\text{Li}_{22}\text{Sn}_5$ forms at higher Li concentrations, accounting for all the Sn in the sample of Li_5SnO . This is approximately consistent with trends reported for other Sn oxide anode materials [8-14]. Owing to the low recoil-free-fraction of β -Sn at RT, the fractions of spectral components in the spectrum acquired at 11 K are more representative of the actual phase fractions.

XRD (Figure 4.20) shows that the $\text{Li}_{22}\text{Sn}_5$ intermetallic compound forms over a broad range of Li insertions, at least from $\text{Li}_{2.3}\text{SnO}$ to Li_5SnO . It seems that there are some differences in this compound for low and high Li insertions, however. The coulometric titration of Fig. 4.17 shows a change of voltage from 0.7 to 0.25 V between $x=2.3$ and $x=5.0$, although a short plateau is observed at 380 mV near $x=4$, and can be associated with $\text{Li}_{22}\text{Sn}_5$ [34]. The Mössbauer spectrum from the $\text{Li}_{22}\text{Sn}_5$ in the anode material of composition $\text{Li}_{2.3}\text{SnO}$ seems to be shifted towards more negative velocities than that of the material of composition of Li_5SnO (Figure 4.22). Finally, the XRD peaks from the anode material of composition $\text{Li}_{2.3}\text{SnO}$ are broader than those from Li_5SnO (Figure 4.20). We suggest that the $\text{Li}_{22}\text{Sn}_5$ that forms initially is more defective crystallographically than the $\text{Li}_{22}\text{Sn}_5$ that forms after more Li insertion. The chemical potential for Li in this more defective material is evidently lower than that of the more perfect $\text{Li}_{22}\text{Sn}_5$. Perhaps the crystallographic defects originate with a sub-stoichiometry of Li, such as Li vacancies.

The change in the fractional contributions from the $\text{Li}_{22}\text{Sn}_5$ and the $\beta\text{-Sn}$ after the sample of Li_5SnO was cooled to 11 K is probably not significant, since there is strong overlap of these parts of the Mössbauer spectra. The sample of $\text{Li}_{2.3}\text{SnO}$ increased considerably its fraction of Sn^{4+} after cryogenic exposure, losing its alloy component and increasing the fraction of $\beta\text{-Sn}$. This is consistent with oxidation of the sample, since one of the windows on the sample package was not reliable upon cryogenic exposure. A detailed study of the oxidation behavior of these materials is presented below.

4.3.5.3 Recoil-Free Fractions: Standards

The recoil-free fraction (the efficiency of the Mössbauer effect for a ^{119}Sn nucleus in a given material at a specific temperature) is difficult to measure on an absolute basis. It is much easier to measure ratios of recoil-free fractions, which can be ratios of areas of spectral components of different phases, or ratios of areas of the same spectral component at different temperatures. For anode materials, we prefer the method of comparing the spectral areas of the same phase, since the phase fractions in a particular sample remain constant at different temperatures. Before using this method with anode materials, however, we first prepared four "standard" samples with known amounts of SnO_2 and $\beta\text{-Sn}$ powders. Standard No. 1 had an approximately equal amount of Sn in the two phases (24 mg SnO_2 plus 20 mg $\beta\text{-Sn}$). Standard No. 2 had more $\beta\text{-Sn}$ (8 mg SnO_2 plus 47 mg $\beta\text{-Sn}$), which ensured more comparable spectral areas at higher temperatures. The other two standards were mixtures of known amounts of $\text{Li}_{22}\text{Sn}_5$ with either $\beta\text{-Sn}$ or SnO_2 . Standard 3 was (26.52 mg $\text{Li}_{22}\text{Sn}_5$ plus 13.42 mg SnO_2) and Standard 4 was (15.44 mg $\text{Li}_{22}\text{Sn}_5$ plus 24.56 mg $\beta\text{-Sn}$).

The measured spectral intensities of the SnO_2 , $\beta\text{-Sn}$, and $\text{Li}_{22}\text{Sn}_5$ at temperature, T , are the product of the recoil-free-fractions, $f(T)$, and the atomic fractions, $x(T)$:

$$I_{\text{SnO}_2}(T) = x_{\text{SnO}_2} f_{\text{SnO}_2}(T) \quad (4.2)$$

$$I_{\beta\text{-Sn}}(T) = x_{\beta\text{-Sn}} f_{\beta\text{-Sn}}(T) \quad (4.3)$$

$$I_{\text{Li}_2\text{Sn}_5}(T) = x_{\text{Li}_2\text{Sn}_5} f_{\text{Li}_2\text{Sn}_5}(T) \quad (4.4)$$

For comparison to literature results on β -Sn and SnO_2 , we define the ratio, $R(T)$, as:

$$R_{\text{SnO}_2/\text{Sn}}(T) = \frac{f_{\text{SnO}_2}(T)}{f_{\beta\text{-Sn}}(T)} = \frac{x_{\beta\text{-Sn}} I_{\text{SnO}_2}(T)}{x_{\text{SnO}_2} I_{\beta\text{-Sn}}(T)} \quad (4.5)$$

We obtained $R_{\text{SnO}_2/\text{Sn}}(11\text{K}) = 1.74 \pm 0.30$ and $R_{\text{SnO}_2/\text{Sn}}(11\text{K}) = 1.40 \pm 0.30$ for Standards Nos. 1 and 2, respectively. With values in the literature of $f_{\text{SnO}_2}(11\text{K}) = 0.89$ at 11 K [35], and $f_{\beta\text{-Sn}}(10\text{K}) = 0.715 \pm 0.01$ [36], we expect $R_{\text{SnO}_2/\text{Sn}}(11\text{K}) = 1.24$, in reasonable agreement with our results. At room temperature we find $R_{\text{SnO}_2/\text{Sn}}(300\text{K}) = 8.4 \pm 0.8$. At room temperature, the Lamb-Mössbauer factors are reported to be: $f_{\text{SnO}_2}(300\text{K}) = 0.56$ [27], $f_{\text{SnO}_2}(300\text{K}) = 0.473$ [29], and $f_{\beta\text{-Sn}}(300\text{K}) = 0.04 \pm 0.01$ [36], $f(300\text{K}) = 0.060 \pm 0.002$ [37], although for 25 nm nanoparticles of Sn $f_{\beta\text{-Sn}}(300\text{K}) = 0.022 \pm 0.001$ [37]. These previously published values give a range of $R_{\text{SnO}_2/\text{Sn}}(300\text{K})$ from 8 to 14, again in reasonable agreement with the results on our standard samples.

The standard samples composed of Li_2Sn_5 plus β -Sn, and Li_2Sn_5 plus SnO_2 , were measured at RT, at 11 K, and again at RT. It was found that the sample was unstable over periods of weeks, forming some β -Sn when the Li reacted with the O. Nevertheless, from the spectra measured promptly at RT, we found:

$$R_{\text{Sn/LiSn}}(\text{RT}) = \frac{f_{\text{bSn}}(\text{RT})}{f_{\text{Li}_{22}\text{Sn}_5}(\text{RT})} = \frac{x_{\text{Li}_{22}\text{Sn}_5} I_{\text{bSn}}(\text{RT})}{x_{\text{bSn}} I_{\text{Li}_{22}\text{Sn}_5}(\text{RT})} = 0.50 \pm 0.10 \quad (4.6)$$

$$R_{\text{LiSn/SnO}_2}(\text{RT}) = \frac{f_{\text{Li}_{22}\text{Sn}_5}(\text{RT})}{f_{\text{SnO}_2}(\text{RT})} = \frac{x_{\text{SnO}_2} I_{\text{Li}_{22}\text{Sn}_5}(\text{RT})}{x_{\text{Li}_{22}\text{Sn}_5} I_{\text{SnO}_2}(\text{RT})} = 0.60 \pm 0.10 \quad (4.7)$$

Evidently the alloy $\text{Li}_{22}\text{Sn}_5$ has a larger effective Debye temperature than $\beta\text{-Sn}$, although smaller than SnO_2 . The sample of $\text{Li}_{22}\text{Sn}_5$ plus $\beta\text{-Sn}$, which was more stable against Li oxidation, showed as expected at 11 K that the RFF's of $\text{Li}_{22}\text{Sn}_5$ and $\beta\text{-Sn}$ were similar:

$$R_{\text{Sn/LiSn}}(11\text{K}) = \frac{f_{\text{bSn}}(11\text{K})}{f_{\text{Li}_{22}\text{Sn}_5}(11\text{K})} = \frac{x_{\text{Li}_{22}\text{Sn}_5} I_{\text{bSn}}(11\text{K})}{x_{\text{bSn}} I_{\text{Li}_{22}\text{Sn}_5}(11\text{K})} = 1.0 \pm 0.2 \quad (4.8)$$

We made an effort to obtain these Debye temperatures from our standards, which are: 277 K for SnO_2 , 212 K for $\text{Li}_{22}\text{Sn}_5$, and 134 K for $\beta\text{-Sn}$. Errors may be about ± 20 K.

4.3.5.4 Recoil-Free Fractions: Anode Materials

It might be expected that the phase fractions of the Li_5SnO anode material can be determined with the recoil-free fraction information from the standard samples. Qualitative phase fractions can be obtained from Tables 4.5 and 4.6, but we cannot quantify them further owing to the following interesting phenomenon.

Mössbauer spectra from the sample of Li_5SnO were measured at 11 K and 300 K. We can use Eqs. 1 and 2 to eliminate the phase fractions to compare the temperature dependencies of the recoil-free fractions:

$$R_{\text{SnO}_2/\text{Sn}} \equiv \frac{R_{\text{SnO}_2/\text{Sn}}(\text{RT})}{R_{\text{SnO}_2/\text{Sn}}(11\text{K})} = \frac{I_{\text{SnO}_2}(\text{RT}) I_{\beta\text{Sn}}(11\text{K})}{I_{\beta\text{Sn}}(\text{RT}) I_{\text{SnO}_2}(11\text{K})} \quad (4.9)$$

Using our own experimental results from the calibration standards, we obtain $R_{\text{SnO}_2/\text{Sn}} = 5.4$. From the data in Table 4.5 for the anode material of Li_5SnO , we obtain $R_{\text{SnO}_2/\text{Sn}} = 1.5 \pm 0.4$.

The unexpectedly different result for $R_{\text{SnO}_2/\text{Sn}}$ and $R_{\text{Sn}/\text{Li}_2\text{Sn}_5}$ for the standards and for the anode material is well beyond expected errors, and can have two explanations. When comparing the SnO_2 and the $\beta\text{-Sn}$, either the effective Debye temperature of the $\beta\text{-Sn}$ in the anode materials is higher than that of the $\beta\text{-Sn}$ in the control sample, or the Debye temperature of the Sn^{4+} in the anode material (nominally SnO_2) is lower than that of the Sn^{4+} in the control sample of SnO_2 . We cannot prove one case or the other from the measurements we have performed. One argument is that the Debye temperature of the SnO_2 in the anode material is lower than that of the control sample, because atomic-scale defects in oxide structure can suppress the Debye temperature. Assuming the $\beta\text{-Sn}$ in the anode material to have a Debye temperature of 134 K, we obtain a Debye temperature of 146 K for the Sn^{4+} in the anode material. Another argument is that electropositive Li neighbors may increase the phonon

frequencies of β -Sn. We expect that electropositive Li neighbors can alter one way or another the phonon frequencies of β -Sn [38], but it is not clear if the frequencies will increase when the small β -Sn particles are of 10 nm spatial dimensions. We consider it less likely that the anomalous behavior of $R_{\text{SnO}_2/\text{Sn}}$ originates with a stiffening of the vibrational frequencies in the β -Sn, which would need a Debye temperature close to that of SnO_2 . Either case, however, requires that the microstructure of the anode material contain disorder on nanometer or sub-nanometer dimensions.

In the same way, by comparing the RFF.'s of the $\text{Li}_{22}\text{Sn}_5$ alloy and β -Sn we find $R_{\text{Sn}/\text{Li}_{22}\text{Sn}_5} = 0.2$ for calibration standards, and $R_{\text{Sn}/\text{Li}_{22}\text{Sn}_5} = 0.35$ for the anode material of Li_5SnO . We consider this discrepancy insignificant, however, because of the difficulty of resolving the two overlapping contributions to the Mössbauer spectra at 11 K. We cannot reliably report an anomaly in the RFF. ratio of the β -Sn and the $\text{Li}_{22}\text{Sn}_5$ in the anode material. It is known, however, that the Debye temperature of nanoparticle Sn is low [37], so it is possible that the Debye temperature of the $\text{Li}_{22}\text{Sn}_5$ in the anode material is also suppressed.

One might expect to use the results from XRD to quantify the fractions of phases in the anode material, but we detected no SnO_2 in the XRD patterns. We offer the following interpretation of these results on the SnO_2 , in the anode material. First, the Mössbauer spectrometry tells us only that the Sn is Sn^{4+} , not necessarily the structure of crystalline bulk SnO_2 . The hyperfine parameters of the Sn^{4+} in the anode material differ from those reported in bulk SnO_2 . In the next section we describe how the Sn^{4+} spectrum of the anode materials evolved to that characteristic of SnO_2 when the anode

material was exposed to ambient air over a long period of time. The initial Sn^{4+} in the anode material is not in the expected local structure of SnO_2 . The absence of distinct XRD peaks indicates that the Sn^{4+} oxide is either present as extremely small particles, or as an amorphous phase (or both). The anomalous ratio of $R_{\text{SnO}_2/\text{Sn}}$ for Sn in the electrode material tends to support the interpretation of small particles, although an amorphous oxide could also have a low recoil free fraction, and would be less visible in an XRD pattern.

4.3.6 Oxidation in Ambient Air

Figures 4.23 and 4.24 present XRD patterns from the $\text{Li}_{2.3}\text{SnO}$ and Li_5SnO materials during long-term exposure to ambient air at 300 K. All samples show the same trends, and oxidation proceeds in two stages. The initial Li-Sn alloy undergoes a separation into β -Sn and Li oxide over a period of about 30 minutes for the $\text{Li}_{2.3}\text{SnO}$ and several hours for the Li_5SnO anode material. This process is followed by a much slower oxidation of the β -Sn by the formation of SnO_2 observed by Mössbauer spectrometry. Figures 4.25 – 4.26 present Mössbauer spectra from the $\text{Li}_{2.3}\text{SnO}$, Li_5SnO and $\text{Li}_{22}\text{Sn}_5$ materials, respectively, during long-term exposure to ambient atmosphere at 300 K. All samples show the same trends, and these trends are in good agreement with the results from XRD. The initial Li-Sn alloy^f undergoes a separation into β -Sn and Li oxide, without the formation of Sn^{4+} . This process is followed by a much slower oxidation of the β -Sn by the formation of Sn^{4+} , which approaches the spectrum of SnO_2 . In the early

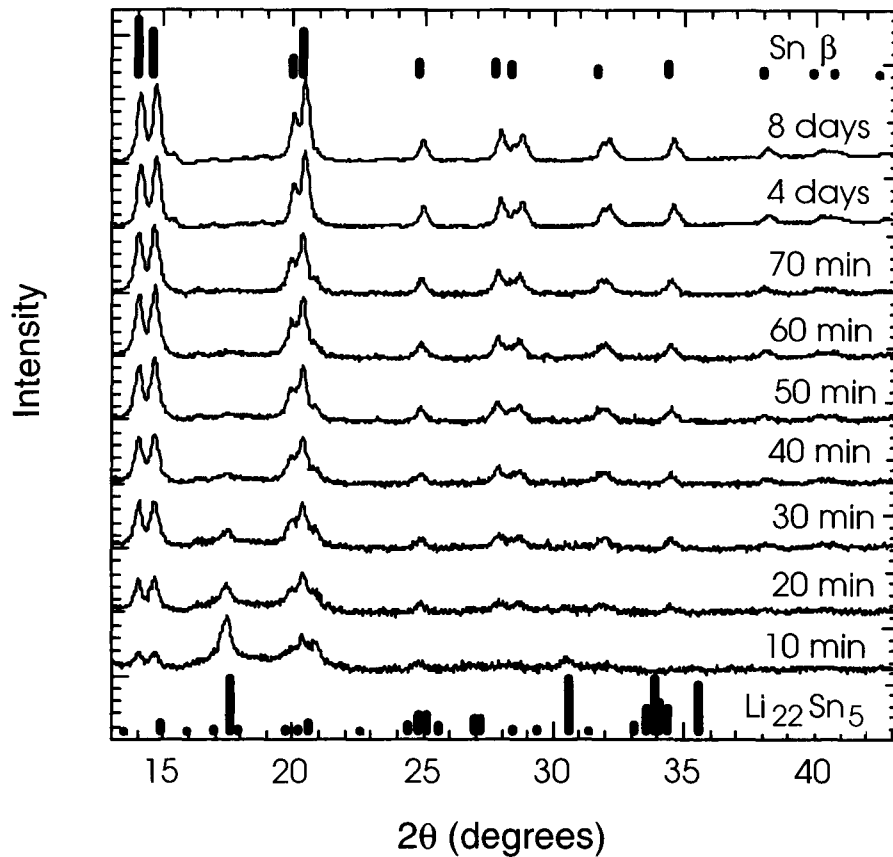


Figure 4.23. X-ray diffraction patterns from $\text{Li}_{2.3}\text{SnO}$ anode material exposed to ambient air for various times.

[†] The small amount of Sn^{4+} in the starting material could be associated with oxide regions kinetically inaccessible to Li, or a surface oxidation associated with inadvertent atmospheric exposure.

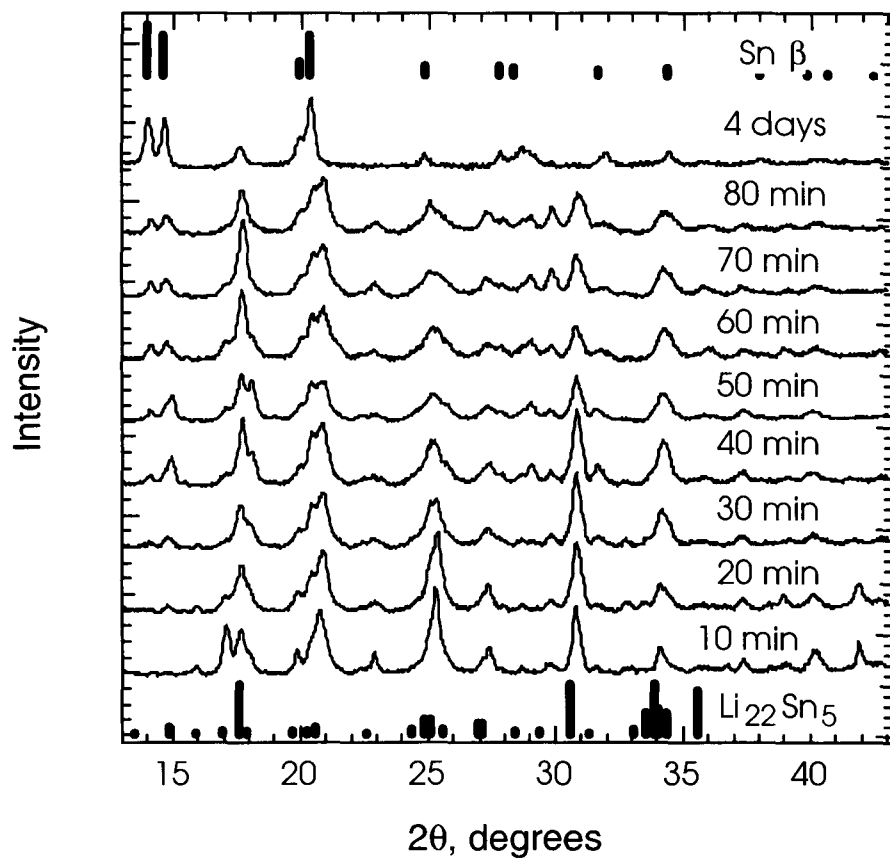


Figure 4.24. X-ray diffraction patterns from Li_5SnO anode material exposed to ambient air for various times.

stages of oxidation, for the three materials $\text{Li}_{2.3}\text{SnO}$, Li_5SnO , and $\text{Li}_{22}\text{Sn}_5$, the hyperfine parameters of the Sn^{4+} differ from those of crystalline SnO_2 , but both samples show a trend towards a symmetric quadrupole doublet, approaching it over 100 days or so. Since the SnO_2 formation was observed clearly by Mössbauer spectrometry, but not by XRD, we suggest that this oxide has an amorphous structure.

The spectra of $\text{Li}_{22}\text{Sn}_5$ exposed to air for more than 100 days show two small peaks at 1.89 mm/s and at 3.61 mm/s with $QS = 1.72 \pm 0.04$ mm/s and $IS = 2.75 \pm 0.04$ mm/s, which are typical of Sn^{2+} in SnO [23-26,30,39]. The hyperfine parameters depend on the structure, and the parameters found here agree with those of amorphous Sn^{2+}O [39] and of ultrafine oxidized Sn particles [25], but not with those of crystalline tetragonal SnO [40,41].

We observed a curious small peak at 4 mm/s in the anode material undergoing oxidation. This peak is probably real, but is not easy to understand. It could be one peak of a quadrupole doublet from an environment with a large electric field gradient, for instance surface SnO , Sn_2O_3 or amorphous SnO_x . Perhaps it originates with an unusual crystal structure of Sn such as electrochemically-prepared allotropic forms of Sn “ α_2 -Sn” [42-45], such as fcc diamond type [42] with lattice parameters of about 5.66 Å for IS about 4.10 mm/s. Ref [44] gives $QS=0$, $IS = 4.08 \pm 0.05$ mm/s.

4.3.7 Thermodynamics of Anode Reactions and Oxidation

The initial insertion reaction of Li into SnO is the energetically favorable reaction of Li oxidation, which occurs with a change in chemical potential of the Li atom of about 3 eV with respect to the Li metal reference electrode. The capacity of this reaction to consume

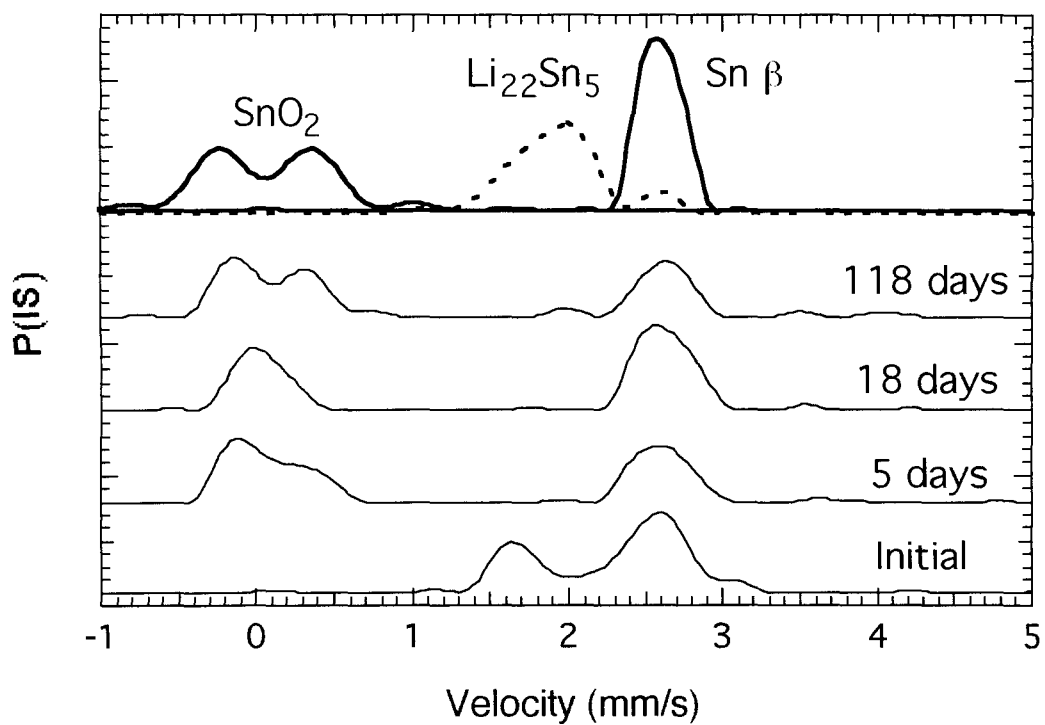
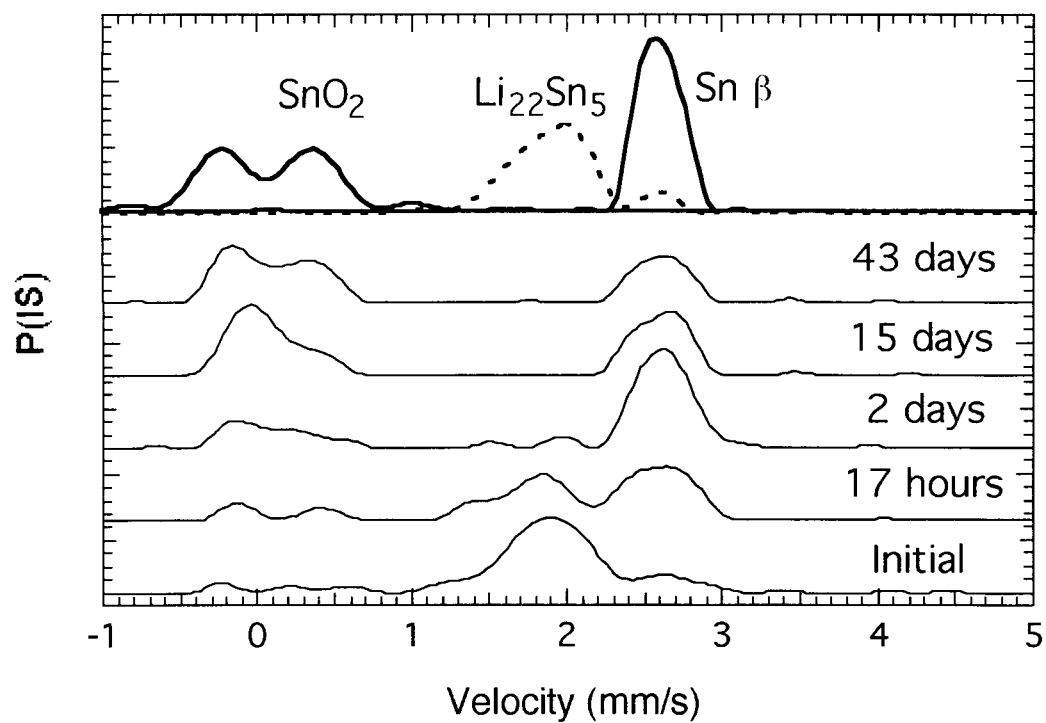


Figure 4.25. Deconvoluted room temperature Mössbauer spectra from $\text{Li}_{2.3}\text{SnO}$ anode material exposed to ambient air for various times.



Figures 4.26. Deconvoluted room temperature Mössbauer spectra from Li_5SnO anode material exposed to ambient air for various times.

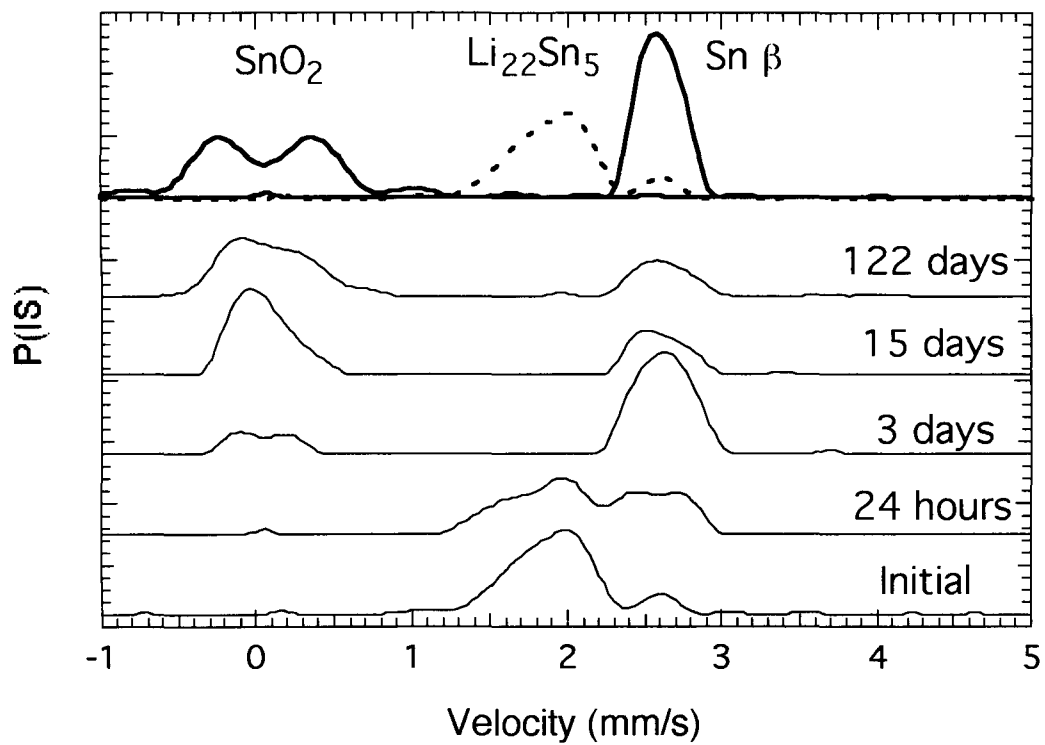


Figure 4.27. Deconvoluted room temperature Mössbauer spectra from $\text{Li}_{22}\text{Sn}_5$ alloy exposed to ambient air for various times.

Li is much smaller than the subsequent reaction at about 0.5 V, which involves the formation of a Li-rich Li-Sn alloy, evidently the compound $\text{Li}_{22}\text{Sn}_5$. Experimental evidence for these two reactions is seen in Fig. 4.17 at the voltages of 3 and 0.4 V. Note, however, that the first reaction of Li oxidation has a much larger capacity than expected from the formation of Li_2O or LiO . We attribute this excessive consumption of Li to the decomposition of electrolyte, as for example in the formation of the surface-electrolyte interphase (SEI). Neither the oxidation of Li in reacting with SnO , nor the oxidation of Li during electrolyte decomposition, are reversible reactions in normal cell operation. The second reaction below 0.8 V with respect to the Li reference electrode is reversible in normal cell operation. In some Sn oxide anode materials the formation of a Li-Sn alloy may occur in stages involving a number of intermediate alloy compounds [8-14, 41], but for our initial SnO anode we find evidence only for the formation of the $\text{Li}_{22}\text{Sn}_5$ intermetallic compound. From the data of Figure 4.18, it appears that when the Sn is fully utilized in this compound, the subsequent reaction is the deposition of Li metal on the anode. This is the third reaction shown at 0.0 V. This reaction is perhaps electrochemically reversible, but it is likely that the electroplating of Li will cause changes to the anode or SEI.

With the exposure of the anode material to oxygen in the ambient air, the system is opened and new reactions occur. The first reaction is the same as occurs in the first charging of an electrochemical cell, that is, more Li will oxidize. This reaction is favored thermodynamically more than the oxidation of the Sn, but oxidation of the Sn is expected once the Li is consumed. The data of Figure 4.23 – 4.27 show that the oxidation of the Li occurs in tens of minutes, whereas the Sn oxidation occurs over tens of days. The

oxidation of Li is strongly favored kinetically over the oxidation of Sn, suggesting that a higher diffusive mobility of Li atoms than Sn atoms may play a role in the kinetics of oxidation.

The total free energy change of each reaction must be favorable. In the first reaction of lithiation of SnO or oxidation of the anode material in air, for example, the Li oxides must be more stable than the Sn oxides if Li oxidation is to occur. This is true, with the difference in standard energies of formation of these compounds being about 30 kJ/mol. The chemical bonds involving Li are stronger than those involving Sn, and the electrode reactions can be understood by consideration of the Li alone. The exception is the final oxidation of Sn in ambient air, which does not involve further changes to any Li. It is interesting that per Sn atom, the standard free energies of formation of SnO and SnO₂ are not very different, being -252 and -258 kJ/mole, respectively. Mössbauer spectrometry showed that the formation of Sn⁴⁺ in a structure related to SnO₂ was the dominant reaction during the exposure of Li₂₂Sn₅ to ambient air. With increasing time, however, we found evidence for the formation of a small amount of Sn²⁺ (as in SnO) by the appearance of a weak Mössbauer peak at about 4 mm/s.

4.3.8 Conclusions

Mössbauer spectrometry and XRD measurements were performed on anode materials of SnO in which Li was inserted electrochemically. These measurements were interpreted with the aid of results on standard samples prepared from β -Sn, Li₂₂Sn₅, and SnO₂, measured at room temperature and 11 K. In anode materials, at low Li capacities the SnO is reduced to small particles of β -Sn. The Sn⁴⁺ in the anode material had an

anomalous temperature dependence of its recoil-free fraction, indicating a severely defective structure on the atomic scale. The lack of XRD peaks from a Sn oxide indicates that the Sn^{4+} is in an amorphous oxide, and may have small spatial features as well. With increasing Li concentration, there was first the formation of β -Sn as small particles of ~ 10 nm dimension, and Li oxide, which may have been amorphous. With more Li insertion, a Li-Sn alloy was formed. This alloy seems to have been exclusively the $\text{Li}_{22}\text{Sn}_5$ intermetallic compound. Although the $\text{Li}_{22}\text{Sn}_5$ develops over a range of Li concentrations in the anode material, from XRD it appears that at low Li insertions the $\text{Li}_{22}\text{Sn}_5$ is more defective than bulk $\text{Li}_{22}\text{Sn}_5$. From coulometric titrations, this crystallographically-defective $\text{Li}_{22}\text{Sn}_5$ appears to have a more favorable chemical potential for Li atoms.

Although the reactions in SnO-Li electrode materials involve all atom species, the thermodynamic tendencies for these reactions were dominated by the chemical preferences of the Li atoms. The voltages of these reactions show that the initial insertion of Li into SnO is accompanied by an additional oxidation of Li, which we interpret as electrolyte decomposition in the formation of a surface-electrolyte interphase (SEI), for example. The irreversible capacity for this initial insertion of Li is large, being 500 mAh/g. The remaining cycles are largely reversible, with Li atoms inserting into and de-inserting from metallic alloys that include $\text{Li}_{22}\text{Sn}_5$. While the early cycles showed an excellent reversible capacity of greater than 600 mAh/g, the material has an unfortunately short cycle life of perhaps 30 cycles.

We also studied the oxidation of Li-charged anode materials and Li-Sn alloys during long-term atmospheric exposure. The oxidation tendencies involved a quick

selective oxidation of Li that occurred over tens of minutes. Metallic β -Sn was observed during this separation of the Li-Sn alloy. The β -Sn then oxidized over longer times of weeks, forming primarily Sn^{4+} but later a small amount of Sn^{2+} . The hyperfine parameters of the Mössbauer spectra indicate that in the early stages of oxidation of the Sn, there is a formation of amorphous, small, or highly defective oxides with Sn^{4+} .

4.3.9 Acknowledgments

We thank Prof. B. Malaman (Universite Henri Poincare, Nancy I) for useful discussions.

Table 4.5. Relative spectral areas f_i ($i=1,2,3$) at 300 K and at 11 K for the Sn^{4+} , Li-Sn alloy and β -Sn contributions in Li_5SnO .

Sample	f_1 (Sn^{4+})	f_2 ($\text{Li}_{22}\text{Sn}_5$ alloy)	f_3 (β -Sn)
300 K as-prepared	0.09	0.80	0.11
at 11 K	0.13 ± 0.03	0.62 ∓ 0.12	0.25 ± 0.10
300 K after 11 K	0.10	0.59	0.31

Errors represent uncertainties in the fitting procedure, which arise in the case of strongly overlapping sub-spectral components.

Table 4.6. Relative spectral areas f_i ($i=1,2,3$) at 300 K and at 11 K for the Sn^{4+} , Li-Sn alloy and β -Sn contributions in $\text{Li}_{2,3}\text{SnO}$.

Sample	f_1 (Sn^{4+})	f_2 (alloy)	f_3 (β -Sn)
300 K as-prepared	0.01	0.36	0.63
at 11 K	0.07	0.10	0.83
300 K after 11 K	0.12	0.0	0.88

4.3.10 References

1. *Lithium Batteries, New Materials, Development and Perspectives*, G. Pistoia, Editor, Elsevier, New York, (1994).
2. *Lithium Batteries*, J.-P. Gabano, Editor, Academic Press, New York (1983).
3. D. H. Doughty, B. Vyas, T. Takamura, and J. R. Huff, eds., *Materials Research Society Symposium Proceedings 393*, MRS, Pittsburgh (1995).
4. B. A. Boukamp, G. C. Lesh, and R. A. Huggins, *J. Electrochem. Soc.* 128, 725 (1981).
5. R. A. Huggins and B. A. Boukamp, U. S. Patent 4,436,796 (1984).
6. Y. Idota, et al., European Patent 651,450A1 (1995). Y. Idota, et al., U. S. Patent 5,478,671 (1995).
7. Y. Idota, T. Kubota, A. Matsufuji, Y. Maekawa, T. Miyasaka, *Science* 276, 1395 (1997).
8. I.A. Courtney and J. R. Dahn, *J. Electrochem. Soc.* 144, 2943 (1997).
9. I.A. Courtney and J. R. Dahn, *J. Electrochem. Soc.* 144, 2045 (1997).
10. I. A. Courtney, W. R. McKinnon, and J. R. Dahn, *J. Electrochem. Soc.* 146, 59 (1999).
11. O. Mao, R. A. Dunlap, I. A. Courtney, and J. R. Dahn, *J. Electrochem. Soc.* 145, 4195 (1998).
12. O. Mao, R. A. Dunlap, and J. R. Dahn, *J. Electrochem. Soc.* 146, 405 (1999).
13. O. Mao and J. H. Dahn, *J. Electrochem. Soc.* 146, 414 (1999).
14. Y. Wang, J. Sakamoto, C. K. Huang, S. Surampudi, S. G. Greenbaum, *Solid State Ionics* 110, 167 (1998).

15. T. Brousse, R. Retoux, U. Herterich, and D. M. Schleich, *J. Electrochem. Soc.* 145, 1 (1998).
16. W. Liu, X. Huang, Z. Wang, H. Li, and L. Chen, *J. Electrochem. Soc.* 145, 59 (1998).
17. S. C. Nam, Y. H. Kim, W. I. Cho, B. W. Cho, H. S. Chun, and K. S. Yun, *Electrochemical and Solid-State Letters* 2, 9 (1999).
18. R. A. Dunlap, O. Mao and J. R. Dahn, *Phys. Rev. B* 59, 3494 (1999).
19. G. Le Caër and J. M. Dubois, *J. Phys. E : Sci. Instrum.* 12, 1083 (1979).
20. G. Le Caër and R. A. Brand, *J. Phys. Cond. Matter* 10, 10715 (1998)
21. S. J. Campbell and F. Aubertin in *Mössbauer Spectroscopy Applied to Inorganic Chemistry, Vol 3*, G. Long, Editor, Plenum Press, New York (1988).
22. D. Rancourt in *Mössbauer Spectroscopy Applied to Magnetism and Materials Science, Vol 2*, G. Long and F. Grandjean, Editors, Plenum, New York (1996) p. 105.
23. B. Stjerna, C. G. Granqvist, A. Seidel and L. Häggström, *J. Appl. Phys.* 68, 6241 (1990).
24. M. S. Moreno, R. C. Mercader and A. G. Bibiloni, *J. Phys. Cond. Matter* 4, 351 (1992).
25. C. H. Shek, J. K. L. Lai, G. M. Lin, Y. F. Zheng and W.H. Liu, *J. Phys. Chem. Solids* 58, 13 (1997).
26. J. Isidorsson, C. G. Granqvist, L. Häggström and E. Nordström, *J. Appl. Phys.* 80, 2367 (1996).
27. J. L. Solis, J. Frantti, V. Lantto, L. Häggström and M. Wikner, *Phys. Rev. B* 57, 13491 (1998).

28. J. G. Stevens and W. L. Gettis, *Isomer Shift Reference Scales*, Mössbauer Effect Data Center, University of North Carolina, Asheville, NC, USA (1981).
29. M. S. Moreno and R. C. Mercader, *Phys. Rev. B* 50, 9875 (1994).
30. H. G. Neumann, P. Zeggel and K. Melzer, *J. Non-Cryst. Sol.* 108, 128 (1989).
31. G. M. Rothberg, S. Guimard and N. Benczer-Koller, *Phys. Rev. B* 1, 136 (1970).
32. A. Svane, *Phys. Rev. Lett.* 60, 2693 (1988).
33. A. Svane, N. E. Christensen, C. O. Rodriguez and M. Methfessel, *Phys. Rev. B* 55, 12572 (1997).
34. J. Q. Wang, I. D. Raistrick, and R. A. Huggins, *J. Electrochem. Soc.* 133, 457 (1986).
35. M. S. Moreno and R. C. Mercader, *Hyperfine Interact.* 83, 415 (1994).
36. C. Hohenemser, *Phys. Rev.* 139, A185 (1965).
37. I. P. Suzdalev, M. Ya Gen, V. I. Gol'danskii and E. F. Makarov, *Soviet Phys. JETP* 24, 79 (1967).
38. V. Ozolins and A. Zunger, *Phys. Rev. Lett.* 82, 767 (1999).
39. G. S. Collins, T. Kachnowski, N. Benczer-Koller and M. Pasternak, *Phys. Rev. B* 19, 1369 (1979).
40. M. Renteria, A. G. Bibiloni, M. S. Moreno, J. Desimoni, R. C. Mercader, A. Bartos, M. Uhrmacher and K. P. Lieb, *J. Phys. Cond. Matter* 3, 3625 (1991).
41. J. Sangster and C.W. Bale, *J. of Phase Equilibria* 19, 70 (1998).
42. V. Rusanov, T.S. Bonchev, I. Mandjukov and M. Mihov, *J. Phys. F : Metal Phys.* 16, 515 (1986).
43. V. Rusanov, I. Mandjukov, T.S. Bonchev and K. Kantchev, *J. Phys. F: Metal Phys.* 18, 1311 (1988).

44. S.K. Peneva, N.S. Neykov and K.D. Djuneva, *Z. Kristall.* 202, 191 (1992).
45. S.K. Peneva, N.S. Neykov, V. Rusanov and D.D. Chakarov, *J. Phys.: Condens. Matter* 6, 2083 (1994).

Appendix A Mechanical Alloying of Fe and Mg

A.1 Introduction

Magnesium alloys are extremely attractive candidates for hydrogen storage applications since many can absorb between 3 and 8 wt.% hydrogen [1,2].

Unfortunately, all Mg alloys studied to date have been burdened with both an excessive hydrogen stability (i.e., inconveniently low equilibrium pressures), and sluggish reaction kinetics at service temperatures below 300 °C [1,2]. During electrochemical charge-discharge cycles, Mg₂Ni electrodes have exhibited disappointingly low capacities and cyclic lifetimes [3,4]. There are recent reports of improvements in the hydriding behavior of Mg-Ni alloys processed by mechanical alloying [5-8]. Practical Mg alloys for either hydrogen gas storage [6-8] or electrochemical cells [5] remain elusive, however.

The present investigation was designed to study Fe-Mg alloys prepared by mechanical alloying. We were interested in determining if mechanical alloying could extend the solid solubilities of either Mg in bcc Fe or Fe in hcp Mg, which in equilibrium are negligible at any temperature [9]. We chose this alloy system so that we could perform ⁵⁷Fe Mössbauer spectrometry measurements to obtain information about the first neighbor chemical environment of Fe atoms in bcc alloys [10]. To our knowledge there have been no previous studies of mechanically alloyed Fe-Mg. Didisheim, et al. [11] have prepared the ternary hydride Mg₂FeH₆ by sintering at about 500°C under 20 - 120 atm hydrogen pressure. While this hydride has an excellent 5.5 wt.% hydrogen content, it is too stable to desorb its hydrogen at practical temperatures. Hydrogen

desorption of Mg_2FeH_6 at elevated temperatures leads to disproportionation into elemental Mg and Fe, consistent with the very low mutual solubilities of Mg and Fe.

We found that for Mg concentrations up to about 20 at.%, mechanical alloying can produce single-phase bcc alloys. From density and diffractometry measurements, we found that the Mg atoms occupy substitutional sites on the bcc lattice. Mössbauer spectrometry shows, however, that rather few ^{57}Fe atoms have first-nearest-neighbor Mg atoms, indicating the formation of Mg-rich regions in the bcc lattice. Similarly, we deduce that the hcp Mg-rich alloys contain some Fe, but the Fe atoms are chistened. Interactions of hydrogen with these metastable alloys will be the subject of future studies.

A.2 Experimental

The Fe-Mg alloys were prepared from appropriate masses of pure metal powders of iron (99.9%, 6-9 micron) and magnesium (99.8%, -325 mesh), obtained from Johnson Matthey, MA, USA. Ball milling was performed for 24 h with a Spex 8000 mixer / mill using hardened steel vials and balls. Knife edges on the cap and the bodies of the vials were used to seal the vial with a copper gasket. The ball-to-powder weight ratio was 10:1. The vial was loaded and sealed in an argon atmosphere. X-ray diffractometry was performed on the as-milled powders with an INEL CPS-120 powder diffractometer using $\text{Co K}\alpha$ radiation ($\lambda = 1.7902 \text{ \AA}$). The fractions of bcc and hcp phases were determined by comparing the intensities of the bcc (110) and hcp (101) peaks. These peaks were reasonably immune to the effects of overlap with broadened neighboring peaks. Thus detection limits were determined primarily by the statistical quality of the data and we

estimated to be about 0.5%. The conversions of peak intensities into phase fractions were done with the expressions [12]:

$$f_{\text{bcc}} = \frac{0.0692I_{110}}{I_{101} + 0.0692I_{110}}, \quad f_{\text{hcp}} = \frac{I_{101}}{I_{101} + 0.0692I_{110}} \quad (1a,b)$$

Lattice parameters were determined using the Nelson-Riley extrapolation method [13].

Grain sizes were estimated with the Scherer approximation

$$L = \frac{0.89\lambda}{B(2\theta) \cdot \cos \theta} \quad (2)$$

where L is the crystal thickness, λ is the wavelength, and $B(2\theta)$ is the full width at half maximum for the (101) hcp peak and the (110) bcc peak.

Density measurements were performed with the Archimedes method using toluene and a Mettler digital balance. The density of toluene was calibrated by density measurements of V, Ti, and Cu ingots. These measurements were compared to models of alloy density by assuming that Mg atoms occupied either Fe sites or interstitial sites in the bcc matrix. The modeled densities of the substitutional, ρ_{sub} , and interstitial, ρ_{inter} , alloys are:

$$\rho_{\text{sub}} = (1-c) \frac{2m_{\text{Fe}}}{a^3} + c \frac{2m_{\text{Mg}}}{a^3}, \quad (3a)$$

$$\rho_{\text{inter}} = \frac{2m_{\text{Fe}}}{a^3} + \frac{c}{1-c} \frac{2m_{\text{Mg}}}{a^3}, \quad (3b)$$

where m_{Fe} is the atomic mass of Fe, m_{Mg} is the atomic mass of Mg, c is the Mg concentration in at.%, and a is the measured lattice parameter.

Mössbauer spectrometry was used for measuring the effects of Mg on the hyperfine magnetic fields (HMF) of Fe. Mössbauer spectra were obtained in transmission geometry at room temperature with a constant-acceleration spectrometer. The radiation source was 10 mCi of ^{57}Co in a Rh matrix. The method of Le Caër and Dubois [14] was used to extract hyperfine magnetic field (HMF) distributions from the broadened sextets of these spectra. Saturation magnetization measurements were performed on the samples at room temperature in an applied field of 4 kOe using a rotating sample magnetometer calibrated with different masses of Fe and Ni powders.

A.3 Results

A.3.1 X-ray Diffractometry

Figure A.1 shows X-ray diffraction patterns from the ball-milled Fe-Mg alloys. These diffraction patterns show predominantly bcc phase until the Mg composition exceeds 20 at.%. For Mg concentrations up to 20 at.%, there is an increased broadening and shift of the bcc diffraction peaks. This behavior suggests that Mg dissolves into the Fe bcc lattice for concentrations less than 20 at.%. To test this hypothesis, a sample of Fe - 15 at.% Mg was annealed at 500°C for three hours with the intent of unmixing the Mg from the Fe. The X-ray diffraction patterns of the as-milled and annealed samples are compared in Figure A.2. Compared to the annealed sample, the diffraction peaks from the as-milled sample are clearly broadened and shifted in position. The insert of Figure A.2 shows the emergence of an hcp phase in the annealed sample. The lattice parameters

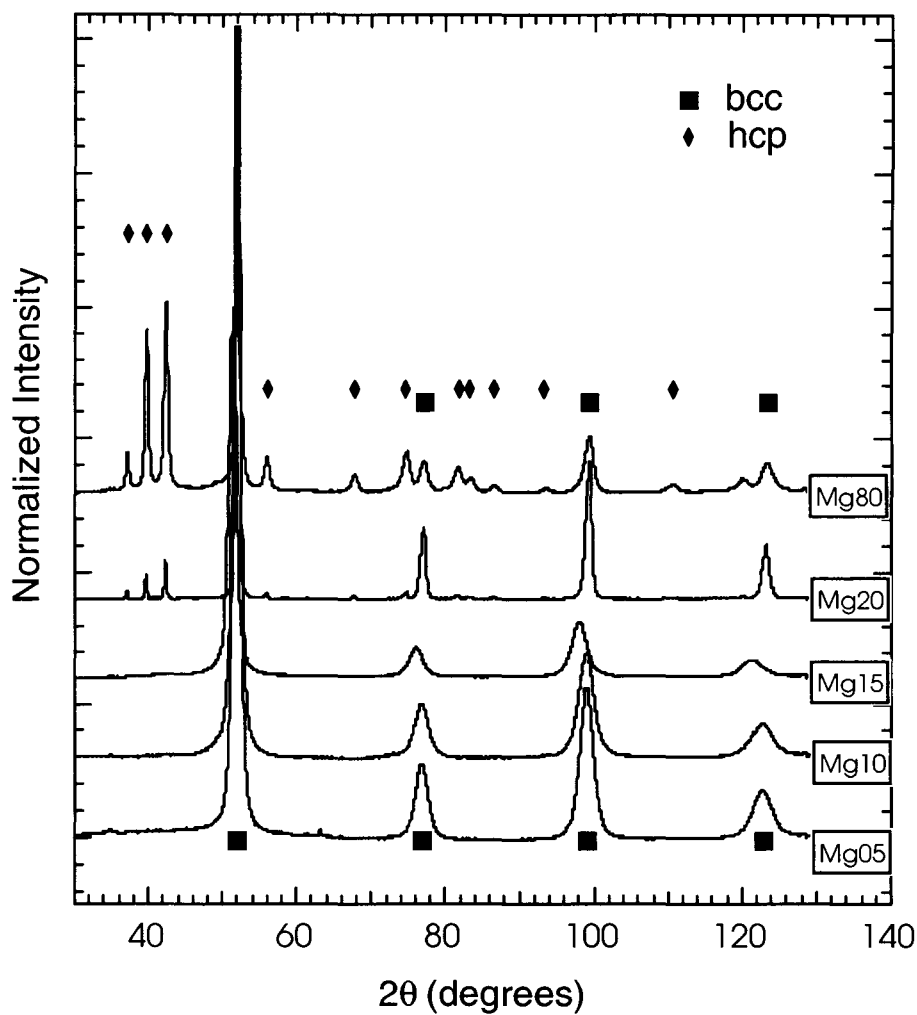


Figure A.1. X-ray diffraction patterns of Fe-Mg alloys. Diffraction peaks for Mg concentrations below 20 at.% are shifted to smaller angles. For alloys of higher Mg concentration, hcp peaks are observed and the bcc peaks shift back to the bcc Fe positions.

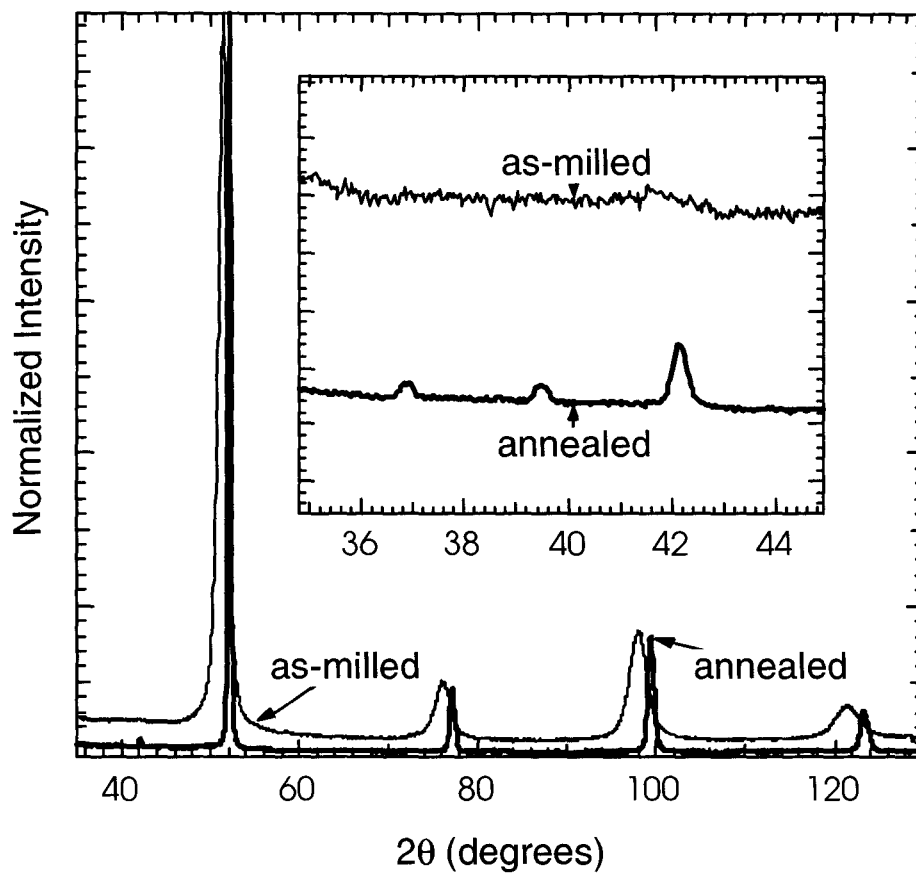


Figure A.2. X-ray diffraction patterns off as-milled Fe₈₅Mg₁₅, and same material after annealing at 500C for three hours. The insert is an enlargement of the low angle range.

of the as-milled Fe-Mg alloys are shown in Figure A.3. Alloys with Mg concentration below 20 at.% had X-ray peaks that were shifted to lower angles, corresponding to an increase in bcc lattice parameter. Figure A.3 shows how the lattice parameter of the pure bcc Fe (initially 2.8662 Å [15]) is increased with the addition of Mg, consistent with the larger metallic radius of Mg.

For higher Mg concentrations, a Mg-rich hcp phase coexists with the Fe-rich bcc phase. Beyond concentrations of 20 at.% Mg, the lattice parameters for the bcc phase relax to nearly that of pure iron. Analysis of the hcp lattice parameters assumed a close-packed structure and consistently gave values less than the literature value of 3.2094 Å for pure Mg [15]. This smaller lattice parameter suggests Fe substitution onto the hcp lattice. Figure A.4 compares the bcc and hcp phase fractions as calculated with Eqns. 1a,b as a function of the Mg concentration. The plot is nonlinear and shows a greater fraction of hcp phase than the Mg concentration in the alloy.

A.3.2 Density

Density measurements were used to determine the nature of the site occupancy of Mg in the bcc Fe-rich alloys. As demonstrated by Figure A.5, the experimental density data most resemble the model for Mg dissolving substitutionally into Fe. The experimental densities are systematically below the calculated values, possibly because of some residual porosity in the ball milled samples.

A.3.3 Mössbauer Spectrometry

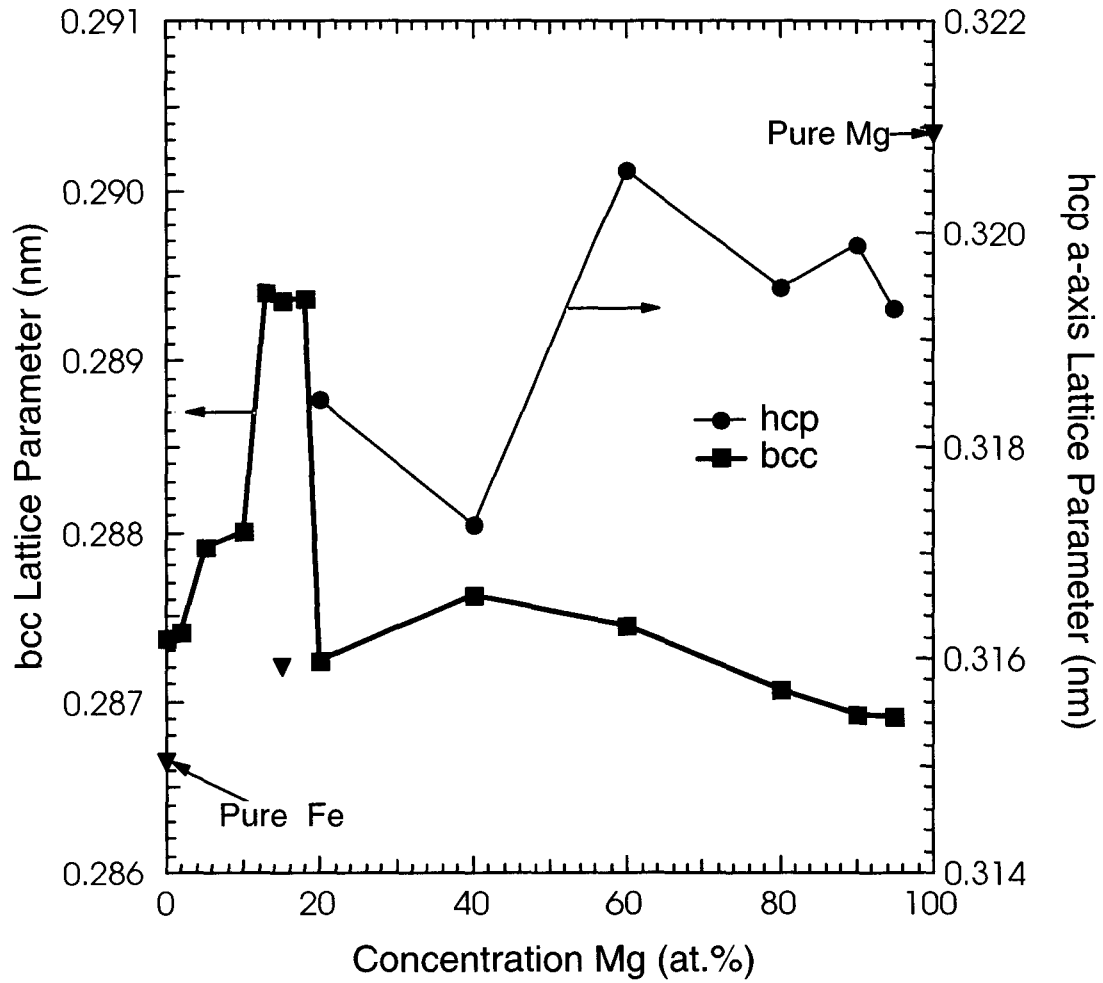


Figure A.3. Lattice parameters of the bcc and hcp phases, with reference data for pure bcc Fe and hcp Mg. Also shown with a triangle is the lattice parameter of the annealed Fe₈₅Mg₁₅ alloy.

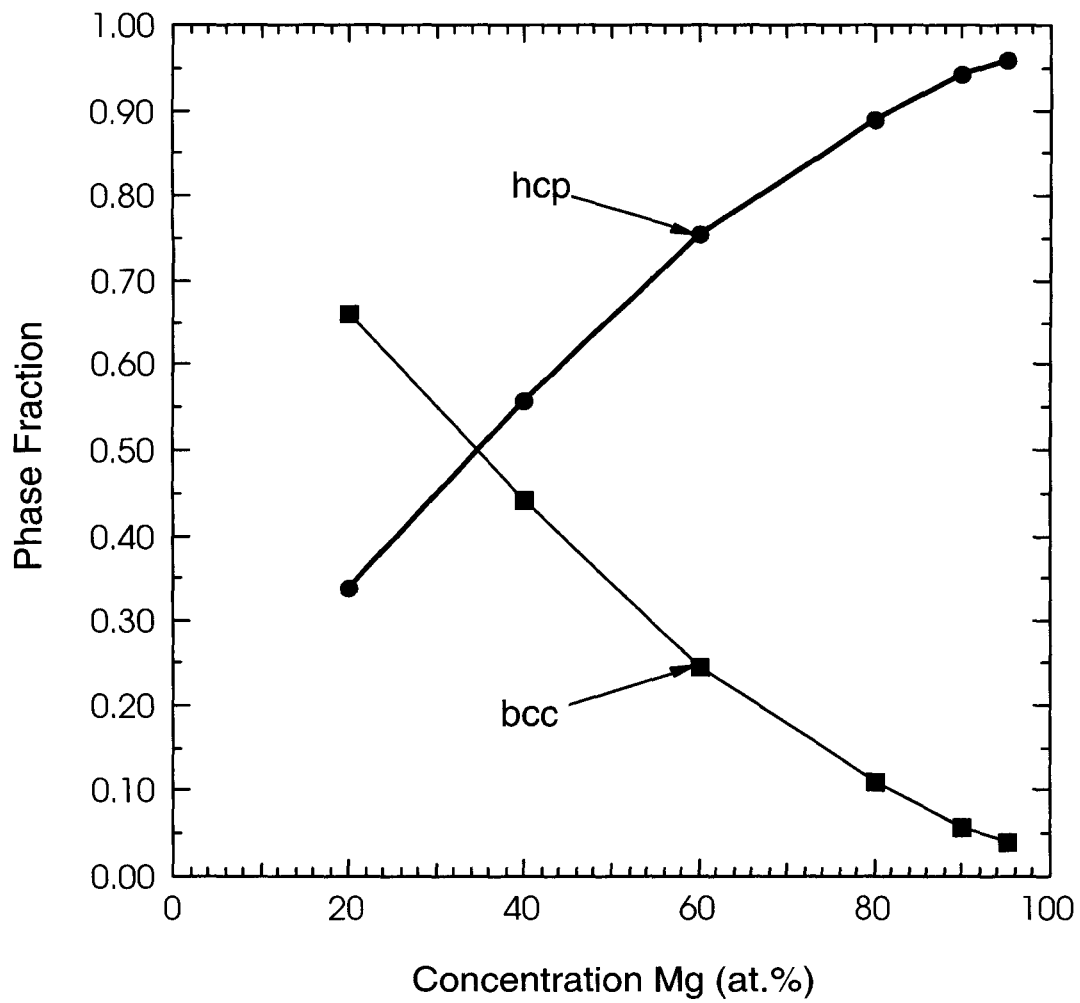


Figure A.4. Fractions of bcc and hcp phases determined from intensities of x-ray diffraction peaks and Eqs. 1a,b.

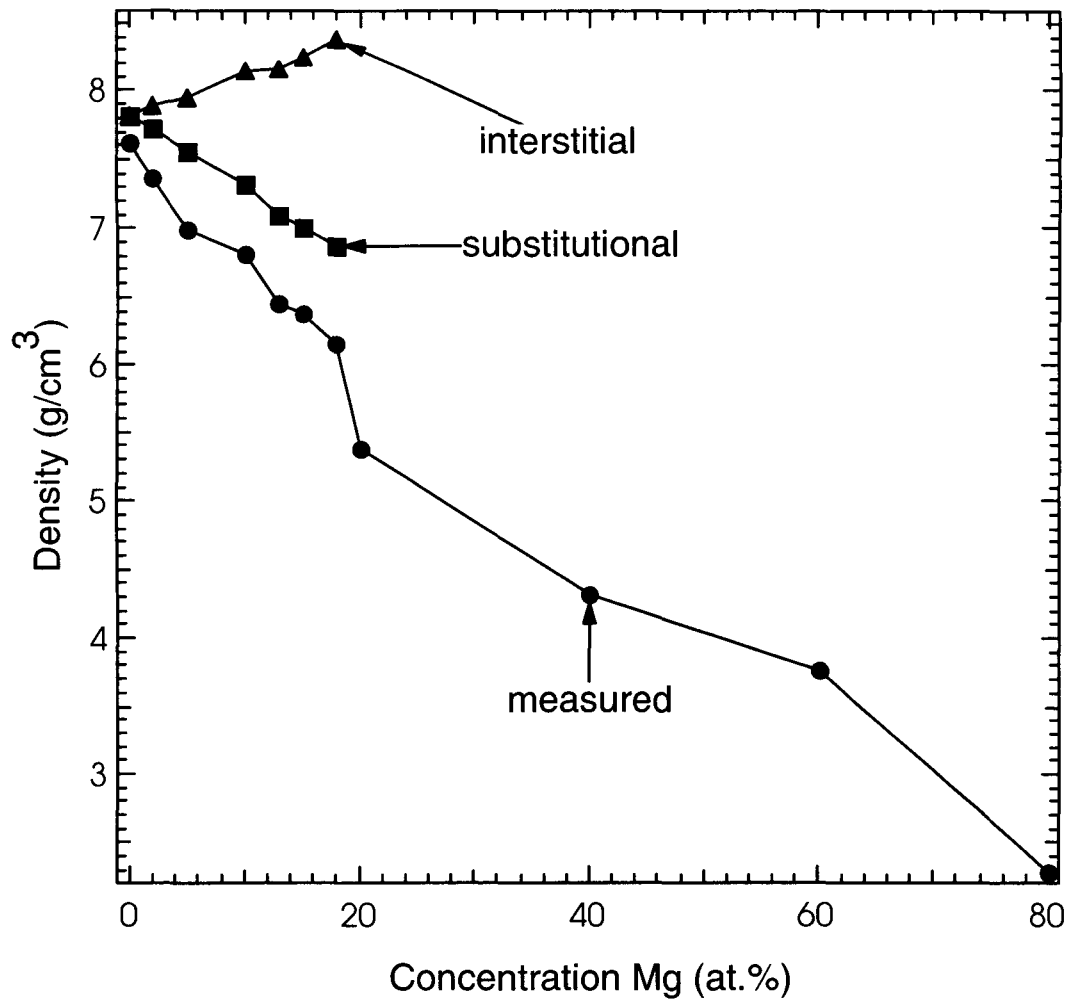


Figure A.5. Density measurements of as-milled alloys, and calculated curves using Eqs. 2a,b for models of interstitial and substitutional Mg sites.

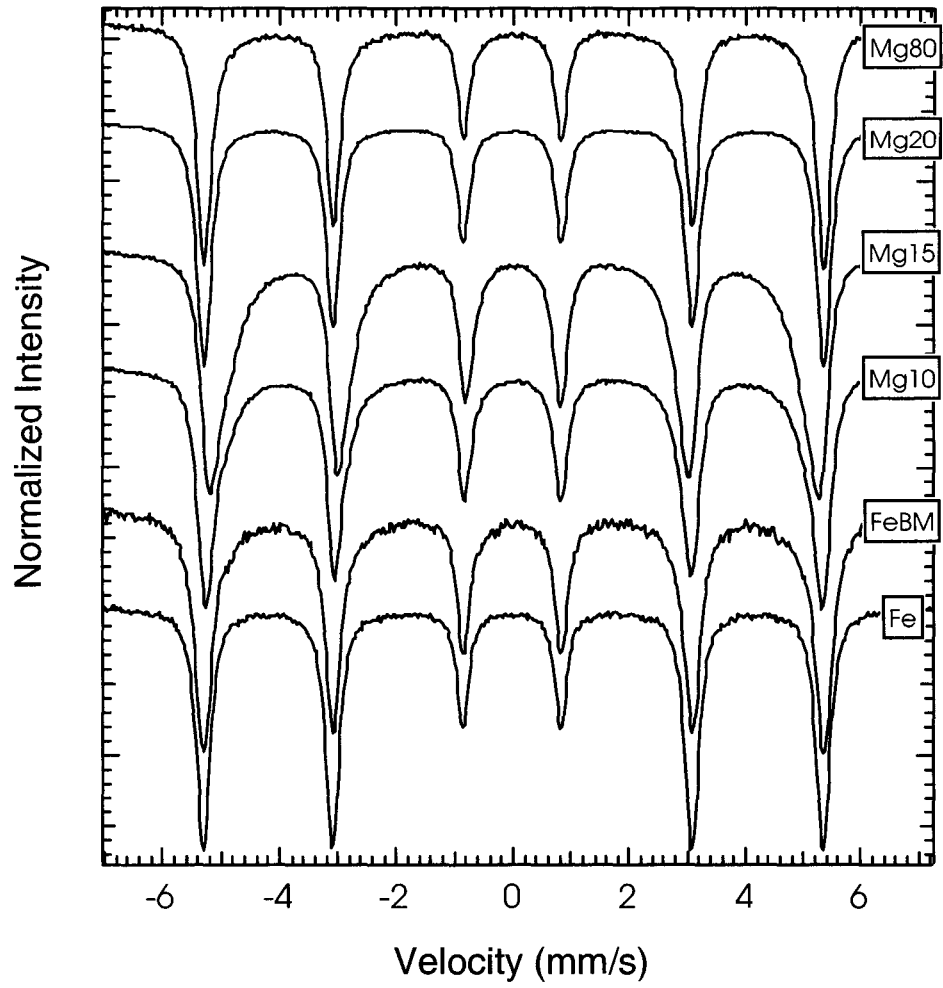


Figure A.6. Mössbauer spectra of as-milled Fe-Mg alloys.

Some Mössbauer spectra are presented in Figure A.6, and the corresponding HMF distributions are presented in Figure A.7. These HMF distributions were fit to two broadened gaussian functions, one centered at 325 kG and the other at 300 ± 2 kG. The areal ratio of these two gaussian functions is presented as a function of Mg concentration in Figure 8. For Mg concentrations less than 20%, the peak at 300 kG increases with greater Mg concentration. For higher Mg concentrations, this 300 kG peak decreases considerably. The data of Figure A.8 follow closely the trend in lattice parameter shown in Figure A.3. There is evidence by the peak at 300 kG in the ball milled Fe sample that there may be a small contamination from Mn in the milling media. The much stronger peaks at 300 kG observed from the Mg-containing alloys overshadow this contamination peak, however.

A.3.4 Rotating Magnetometry

The saturation magnetization values obtained with a 4 kOe applied field are presented in Figure A.9. For all Mg concentrations, the alloy magnetization per atom follows approximately a simple dilution with Mg concentration.

A.4 Discussion

A.4.1 Chemical Distributions in bcc Alloys

For Mg concentrations less than 20 %, X-ray diffractometry showed that the samples were entirely bcc phase. This suggests solubility of Mg in the bcc phase, as do the two observations that 1) the single phase bcc alloy shows an increase in lattice parameter with Mg concentration (Figure A.3), and 2) the measured density is more

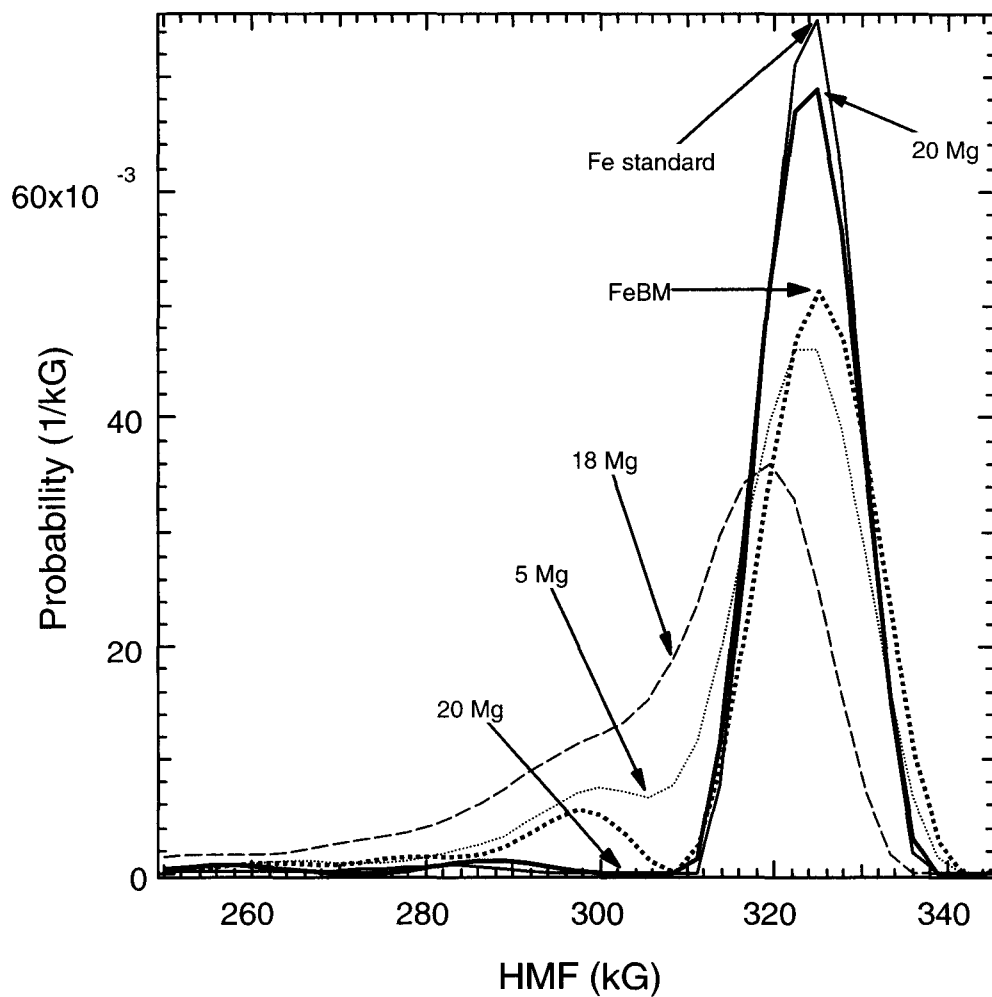


Figure A.7. Hyperfine magnetic field distributions obtained from experimental spectra.

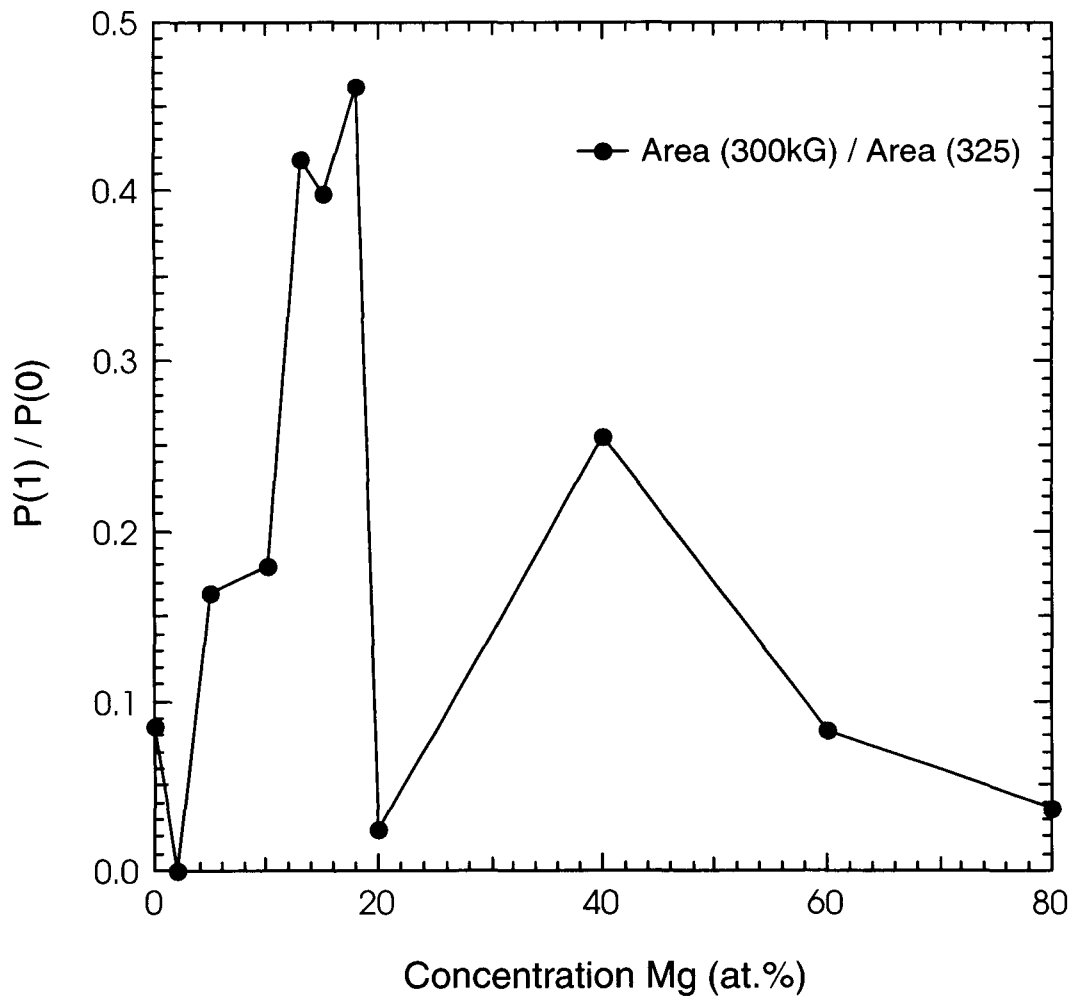


Figure A.8. Ratio $p(1)/p(0)$ (relative numbers of ^{57}Fe atoms with one Mg first-nearest-neighbor), obtained fitting to the HMF distributions of Fig. 7 Gaussian peaks at 300 kG and 330 kG. Note the resemblance to the composition trend of Fig. 3.

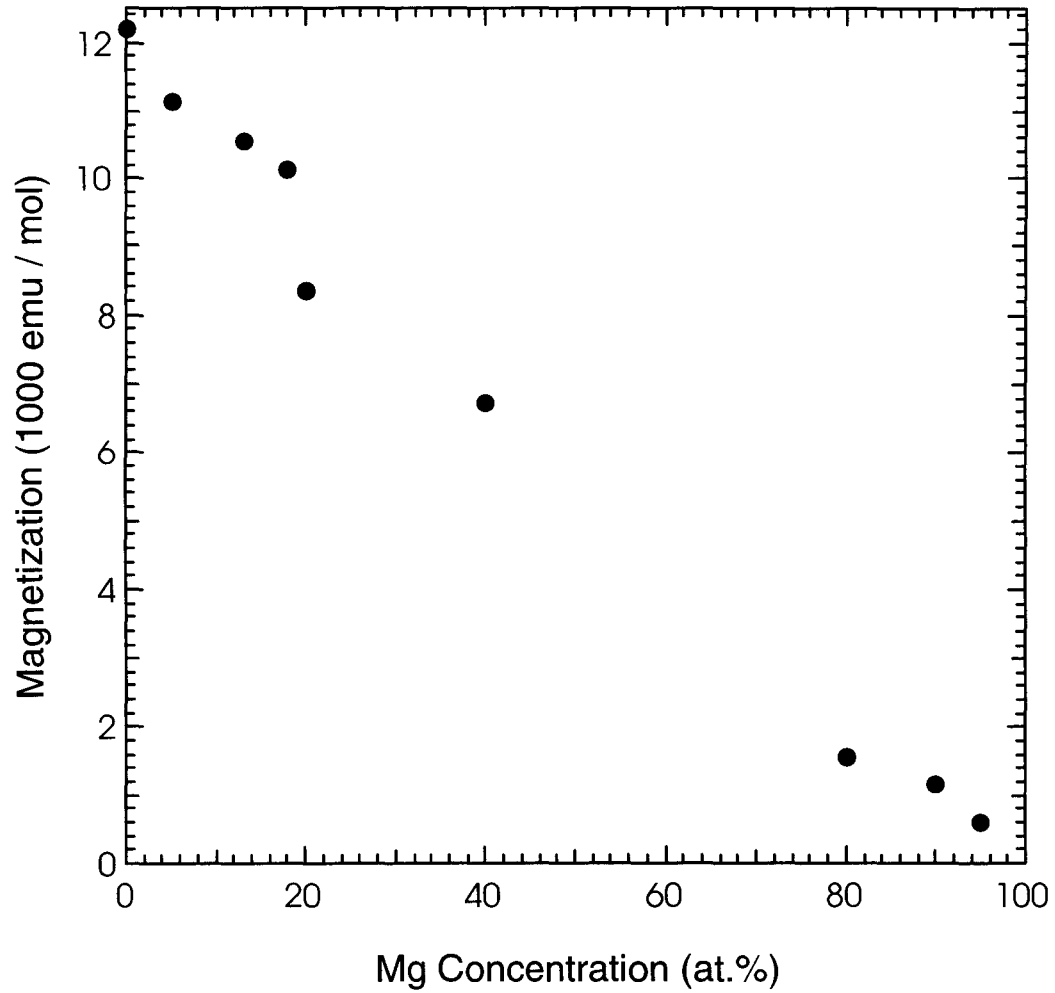


Figure A.9. Saturation magnetization data for as-milled Fe-Mg alloys at room temperature in a 4 kOe magnetic field.

consistent with a substitutional solid solution than an interstitial solid solution (Figure A.5).

On the other hand, Mössbauer spectrometry indicates that the bcc Fe-Mg samples are not disordered bcc solid solutions of Mg in Fe. The ^{57}Fe HMF distributions of Figure A.7 are typical of those from Fe alloys with nonmagnetic solutes that cause no disturbance of the magnetization of neighboring Fe atoms (i.e., magnetic holes in the bcc lattice). Each first-nearest-neighbor (1nn) non-magnetic solute atom causes a decrease in the magnitude of the ^{57}Fe HMF by about 25 kG [10]. For this reason we interpret the peak at 325 kG as originating with ^{57}Fe atoms with zero Mg neighbors, and the peak at 300 kG as originating with ^{57}Fe atoms with one Mg neighbor. For a truly random solid solution, the ratio of intensities of the two peaks should be the ratio of intensities of the binomial probability distributions, $P(N,m,c)$, where N is 8 for the 1nn shell, m is the number of 1nn Mg atoms (0 or 1), and c is the Mg concentration. The ratio $P(8,1,c)/P(8,0,c)$, is:

$$\frac{P(8,1,c)}{P(8,0,c)} = \frac{p(1)}{p(0)} \quad , \quad (4)$$

$$\frac{p(1)}{p(0)} = \frac{\frac{8!}{1! 7!} c(1-c)^7}{\frac{8!}{0! 8!} (1-c)^8} \quad , \quad (5)$$

$$\frac{p(1)}{p(0)} = \frac{8c}{(1-c)} \quad (6)$$

For a ratio, $p(1)/p(0) = 0.45$, the maximum value shown in Figure A.8, the Mg concentration must be 5.3 %. This calculated concentration is smaller by a factor of 3 than the actual alloy composition of 18 %.

This large discrepancy between Mg concentrations indicated by Mössbauer spectrometry and X-ray diffractometry led us to perform an ancillary experiment to validate our interpretation of the Mössbauer spectra. In particular, if Mg atoms do not act as magnetic holes in the bcc Fe lattice, we would not expect simple systematics for how Mg atoms affect the HMF at neighboring ^{57}Fe atoms. While it is improbable that the Mg atoms themselves hold a magnetic moment, we thought that perhaps the Fe neighbors of Mg atoms may have enhanced magnetic moments. Such a phenomenon occurs with Ni and Co neighbors of Fe, although these elements have little chemical resemblance to Mg. The magnetization results presented in Figure 9 are consistent with simple dilution, which implies no magnetic moments on the Mg atoms, and little change in the magnetic moments of those ^{57}Fe atoms having Mg neighbors. For this reason, the ^{57}Fe HMF caused by Mg atoms is best interpreted as a disturbance in the Fe 4s conduction electron polarization that is transferred from the Mg site to neighboring ^{57}Fe atoms [10].

For Mg concentrations as high as 18 %, Mössbauer spectrometry shows that there are few ^{57}Fe atoms with 1nn Mg neighbors. Nevertheless, density and diffractometry measurements show that the Mg atoms are within the bcc phase. We are led to the conclusion that the Mg atoms are in the bcc phase, but their distribution is heterogeneous. Specifically, we believe the Mg atoms cluster into zones on the bcc lattice, and these

zones have few Fe atoms in them. The ^{57}Fe Mössbauer spectra therefore show few Fe atoms with Mg neighbors. There has been a previous ^{57}Fe Mössbauer spectrometry study of Fe/Mg artificial multilayers, prepared in thin film form by molecular beam epitaxy [16, 17]. For thick Fe layers, the spectra reported in this previous study look much like those of Figure A.6. There is a strong main sextet of peaks characteristic of pure Fe, and a weaker satellite peak with an average hyperfine field that is about 90 % of the bulk value identified with Fe atoms near the Mg interface layer [17]. The secondary peak at 300 kG in Figure A.9 for the ball milled Fe-Mg alloys is 92% of the bulk value at 325 kG.

Chemical unmixing of Fe and Mg atoms in the bcc alloys could also involve some segregation of Mg atoms to grain boundaries. With a grain size range of 10-17 nm for the bcc crystallites, grain boundary segregation would require only short diffusion distances. The following experimental evidence shows that grain boundary segregation does not accommodate all Mg atoms, however: 1) in spite of a careful search, we did not find any variations in the backgrounds of the diffraction patterns between 20 - 50 degrees 2θ that would be consistent with diffuse scattering from a disordered Mg structure, 2) the density of the grain boundary would probably be more consistent with the density of Mg metal, leading to a simple linear slope across the entire graph of Figure A.55 (without a kink at 18%), and 3) the alloy lattice parameter is increased by 1.0 % for the 18 at.% Mg alloy.

A.4.2 Limits of Solubility

Unmixing of Fe and Mg atoms on the bcc lattice of the as-milled alloys is expected from the large difference in electronegativity and size of the Fe and Mg atoms. Hume-Rothery rules for solubility in mechanical alloying were proposed previously [18]. The rules for a Spex 8000 mixer/mill are that 25 at.% solid solubility occurs when the metallic radii of the elements differs by 15 %, and their electronegativities differ by less than 0.4. The metallic radii of Fe and Mg differ by 25 % (Mg is larger), and their electronegativities differ by 0.64 (Mg is smaller) [19]. The dissolution of Mg in our Fe-rich bcc alloys is therefore expected to be low.

For Mg concentrations of 20 at.% and higher, the as-milled alloys comprised two-phase (bcc plus hcp) mixtures (see Figure A.1). Simultaneously, the lattice parameter of the bcc phase decreased precipitously, although it remained larger than for pure bcc Fe. Meanwhile, the lattice parameter of the hcp phase was decreased somewhat below its value for pure hcp Mg. The intensity of the 1nn satellite peak in the ^{57}Fe HMF distribution (at 300 kG) decreased significantly for the alloys with Mg concentrations greater than 20 at.%. These changes at Mg concentrations near 20 at.% are reminiscent of a first-order phase transformation, such as one that occurs by nucleation and growth. We suggest that during ball milling of Fe-rich alloys there is a significant barrier, either energetic or kinetic, to the nucleation of the hcp phase. At a composition around 20 at.% Mg, however, some of the larger Mg-rich regions transform into the hcp structure. The sharpness of the hcp diffraction peaks indicate hcp crystallite sizes range from 15 - 22 nm, so these Mg-rich hcp crystallites appear to have grown in size by acquiring more Mg.

Without the benefit of Mössbauer spectrometry, we have less detailed information about the Mg-rich hcp phase. Since the lattice parameter of the hcp phase is smaller than

that of pure hcp Mg, we expect that there is some solubility of Fe in the hcp phase. The curvature of the phase fraction curves in Figure 4 suggests that at Mg concentrations above 20%, there is greater solubility of Fe in the hcp phase than there is for the Mg in the bcc, but features of these curves are difficult to interpret quantitatively. The Mössbauer spectra for Mg concentrations greater than 20% (Figure A.6) did not exhibit the singlet peak previously attributed to isolated Fe atoms in a Mg matrix [17]. This results indicates that ball milling does not produce isolated Fe atoms in the hcp Mg matrix

Data on the lattice parameter of the Mg-rich hcp phase leads us to conclude that Fe is dissolved in the hcp matrix. The lack of a paramagnetic peak in the Mössbauer spectra, however, implies that the Fe atoms are clustered on the hcp lattice.

A.5 Conclusion

We performed mechanical alloying of Fe and Mg powders with a wide range of compositions. Alloys with less than 20 at.% Mg were single phase bcc with an enlarged lattice parameter. For Mg concentrations from 20 - 95 at.%, the alloys were a mix of bcc and hcp phases. For the single-phase bcc alloys, density measurements indicated that the Mg substituted onto bcc sites. Magnetization measurements indicated that the alloy saturation magnetization followed an approximately linear dilution with the concentration of Mg. Mössbauer spectra of the Fe-Mg alloys showed relatively few Fe atoms with Mg first-nearest-neighbors, certainly far fewer than would be expected of disordered solid solutions with Mg concentrations of up to 20 at.%. We conclude that the Mg is

distributed heterogeneously on the bcc lattice in Mg-rich zones. Likewise, we found that some Fe was dissolved heterogeneously on the hcp lattice of Mg-rich alloys.

A.6 References

1. J. J. Reilly, *Z. Phys. Chem. NF* **117**, 155 (1979).
2. K. Yvon, in Encyclopedia of Inorganic Chemistry, edited by R. B. King (Wiley, New York, 1994), p.1401.
3. N. Cui, B. Luan, H. K. Liu, H. J. Zhao, and S. X. Dou, *J. Power Sources* **55**, 263 (1995).
4. N. Cui, B. Luan, H. J. Zhao, H. K. Liu, and S. X. Dou, *J. Alloys Compounds* **233**, 236 (1996).
5. Y.-Q. Lei, Y.-M. Wu, Q.-M. Yang, J. Wu, and Q.-D. Wang, *Z. Phys. Chem.* **183**, 379 (1996).
6. M. Y. Song, *J. Mater. Sci.* **30**, 1343 (1995).
7. L. Zaluski, A. Zaluska, J. O. Strom-Olsen, *J. Alloys Compounds* **217**, 245 (1995).
8. S. Orimo and H. Fujii, *J. Alloys Compounds* **232**, L16 (1996).
9. W. G. Moffatt, Handbook of Binary Phase Diagrams, Vol. 3, (Genium Publishing, Schenectady, New York, 1984).
10. H. H. Hamdeh, J. Okamoto, and B. Fultz, *Phys. Rev. B* **42**, 6694 (1990). Brent Fultz, in Mössbauer Spectroscopy Applied to Magnetism and Materials Science Vol. I, G. J. Long and Fernande Grandjean, eds., (Plenum Press, New York, 1993) p. 1-31.
11. J.-J. Didisheim, P. Zolliker, K. Yvon, P. Fischer, J. Schefer, M. Gubelmann, and A. F. Williams, *Inorg. Chem.* **23**, 1953 (1984).
12. L. B. Hong and B. Fultz, *J. Appl. Phys.* **79**, 3946 (1996).
13. H. P. Klug and L. E. Alexander, X-ray Diffraction Procedures (Wiley-Interscience, New York, 1974) p. 594

14. G. Le Caër and J. M. Dubois, *J. Phys. E: Sci. Instrum.* **12**, 1083 (1979).
15. P. Eckerlin, H. Kandler, Landolt-Börnstein Numerical Data and Functional Relationships in Science and Technology, Vol. 6 Structure Data of Elements and Intermetallic phases, Springer-Verlag, New York 1971
16. T. Shinjo and T. Takada in Industrial Applications of the Mössbauer Effect, G. J. Long and J. G. Stevens, eds., (Plenum, New York, 1986), p. 739.
17. K. Kawaguchi, R. Yamamoto, N. Hosoito, T. Shinjo, and T. Takada, *J. Phys. Soc. Japan* **55**, 2375 (1986).
18. C. Bansal, Z. Q. Gao, L. B. Hong, and B. Fultz, *J. Appl. Phys.* **76**, 5961 (1994).
19. E. T. Teatum, K. A. Gschneider, Jr., and J. T. Waber, Compilation of Calculated Data Useful in Predicting Metallurgical Behavior of the Elements in Binary Alloy Systems, Los Alamos Laboratory Report LA-4003 (1968).

Appendix B Kinetics of Hydrogen Diffusion in $\text{LaNi}_{5-x}\text{Sn}_x$ Alloys

B.1 Introduction

The durability of LaNi_5 -based electrodes during electrochemical cycling is generally improved by a partial substitution of La or Ni with suitable solutes. Various additives such as Nd [1], Ti [2], Zr [3] and Ce [4], for La and Co [1], Mn, Al [5] and Si [1] for Ni have been found to be successful substituents for lowering the absorption plateau pressures and/or improving the cycle life. Sakai et al. [5] performed a rigorous evaluation of several other elements as ternary solutes in $\text{LaNi}_{5-x}\text{M}_x$. The cycle life was found to increase in the order $\text{Mn} < \text{Ni} < \text{Cu} < \text{Cr} < \text{Al} < \text{Co}$. In all the above ternary alloys, the improvement in the cycle lifetime is unfortunately accompanied by a decrease in the hydrogen absorption capacity, long activation, or slow kinetics. The use of Sn as a partial substituent for Ni in LaNi_5 , on the other hand, was found to reduce the absorption plateau pressure and minimize the hysteresis, while retaining most of the high absorption capacity of the binary alloy [6]. Furthermore, the Sn substituent was found to result in a 20-fold increase in the cyclic lifetime in thermal cycling [7] and a charge-discharge cycle life comparable to a multi-component, misch metal based alloy [8]. Additionally, the kinetics of hydrogen absorption-desorption appear to be more facile upon Sn substitution, indicating that favorable surface conditions are prevalent on these alloys [9]. Similar beneficial effects were realized with Ge substituent also [10].

The mechanism of electrochemical hydriding-dehydriding contains a series of steps. For example, the charge transfer reaction produces adsorbed atomic hydrogen (H_{ad}) and OH on the electrode surface (Volmer process). The adsorbed hydrogen either diffuses through the surface layer and grain boundaries into the bulk of the alloy to form the hydride or combines with adjacent adsorbed hydrogen atom to form molecular

hydrogen (Tafel process) and thus hydrogen evolution. The performance of the metal hydride electrode is determined by the kinetics of the process occurring at the electrode/electrolyte interface as well as of hydrogen transport within the bulk of the alloy. The charge transfer process is the rate-determining step for electrodes containing small particles, while the hydrogen diffusion dominates for larger particles [11].

Reliable values for the hydrogen diffusion coefficients in the LaNi_5 hydride phases have been difficult to obtain due to complex microscopic diffusion processes [12, 13] in crystal structures where hydrogen simultaneously occupies several distinct types of interstitial sites. Furthermore, various physical properties of activated LaNi_5H_x powders often impeded analyses and interpretations of commonly employed techniques such as nuclear magnetic resonance (NMR) and quasielastic neutron scattering (QNS). Performing a critical assessment of NMR and QNS methods to characterize hydrogen diffusion in $\beta\text{-LaNi}_5\text{H}_x$ when $x > 6$, Richter, et al. [12] concluded that the long-range diffusion coefficient at 300 K is in the range $1 - 5 \times 10^{-8} \text{ cm}^2/\text{s}$. Züchner, et al. [14] applied the current pulse electrochemical method on single crystal $\alpha\text{-LaNi}_5\text{H}_x$ with $x < 0.07$ to obtain anisotropic diffusion coefficients of $2 - 3 \times 10^{-8} \text{ cm}^2/\text{s}$ at 298 K. Apparently, there is not a very large difference in hydrogen diffusion behavior between these two phases even though the hydrogen contents vary considerably.

There have been relatively few studies [12] of the effect of substitutional alloying on hydrogen diffusion in the AB_5 hydrides. Using NMR methods, Bowman, et al. [15] showed that Al substitution greatly decreased hydrogen motion in the $\beta\text{-LaNi}_{5-y}\text{Al}_y\text{H}_x$ with an accompanying increase in activation energy. Zheng, et al. [16] obtained with electrochemical methods a room temperature diffusion coefficient of $3 \times 10^{-11} \text{ cm}^2/\text{s}$ for an

LaNi_{4.25}Al_{0.75} hydride electrode which was much below the value of $7 \times 10^{-10} \text{ cm}^2/\text{s}$ reported for a LaNi₄Cu electrode by van Rijswijk [11]. More recently, Zheng, et al. [17] used a constant current discharge technique to derive a hydrogen diffusion constant of $7 \times 10^{-11} \text{ cm}^2/\text{s}$ from an LaNi_{4.27}Sn_{0.24} electrode. Disc-type electrodes made with MmNi_{4.2}Al_{0.5}M_{0.3} (M = Cr, Mn, Fe, Co, Ni) were used by Iwakura, et al. [18] to evaluate hydrogen diffusion coefficients in the a-phase by the electrochemical potential step method. The diffusion constants measured at 303 K ranged between $1.6 \times 10^{-8} \text{ cm}^2/\text{s}$ to $3.2 \times 10^{-8} \text{ cm}^2/\text{s}$. It should be noted that the hydrogen diffusion coefficients deduced using electrochemical methods on alloy powders are smaller by one-to-two orders-of-magnitude than values obtained from NMR, QNS, or electrochemical measurements on bulk samples. [14, 18]

In this work, we study the transport kinetics of hydrogen in LaNi_{5-x}Sn_x alloys electrochemical pulse techniques, i.e., chronoamperometry and chronocoulometry. Sn substitution results in improved interfacial conditions for electrochemical hydriding-dehydriding processes and in lower absorption pressures due to enlarged lattice volume. It is interesting to see if these features, especially the latter, also lead to enhanced transport of hydrogen within the bulk of the alloy. The results from these studies, combined with the extensive electrochemical and structural characterization already performed on LaNi_{5-x}Sn_x alloys, will help us better understand the role of the ternary solute on hydrogen diffusion.

B.2 Experimental

The $\text{LaNi}_{5-x}\text{Sn}_x$ alloys were prepared by induction - melting and were subsequently annealed in evacuated quartz ampuls at 950°C . The annealed ingots were subjected to five hydrogen decrepitation cycles to activate the alloys. Metal hydride disk electrodes were prepared by filling the BAS (Bioanalytical Systems) disk electrodes with the mixture of MH powders (with 20% Ni and 5 % PTFE), of equal quantities in each case to ensure equal surface area (0.07 cm^2), charge density (5.6 g/cm^3), and porosity in all the electrodes. A NiOOH electrode formed the counter-electrode, and a Hg/HgO (0.098 V vs. SHE) with a Luggin capillary served as the reference electrode in a three-electrode flooded cell with 31 w% KOH electrolyte.

The scheme of experimentation includes constant current charges at 40 mA/cm^2 (20 mA/g) to a capacity corresponding to 400 mAh/g , potentiodynamic polarization curves for estimating diffusion limiting currents, constant - current discharges at 64 mA/cm^2 (33 mA/g) to -0.5 V vs. Hg/HgO for calculating the absorbed hydrogen concentration in the alloy and chronoamperometric and chronocoulometric transient measurements for determining the diffusion coefficients. The polarization experiments were carried out with an EG&G 273 Potentiostat / Galvanostat using 352 corrosion software. Chronocoulometric response was, however, monitored with a Nicolet storage oscilloscope. Temperature measurements were conducted in a Tenney environmental chamber, $\pm 0.1^\circ\text{C}$.

It may be difficult to distinguish the hydriding and hydrogen evolution processes electrochemically. In a potentiodynamic polarization, for example, a smooth, almost unnoticeable transition occurs from the hydride formation to the hydrogen evolution [2]. The concurrent hydrogen evolution thus induces uncertainties in the analysis of cathodic polarization data, due to reduced current efficiency and changing surface conditions. In

order to alleviate such uncertainties, the present studies are restricted to the anodic regime, both for the transient and steady state experiments. Besides, the slow diffusing species during discharge is undoubtedly hydrogen within the bulk of the alloy, where as in the charging process, hydroxyl ions in the electrolyte phase could move more sluggishly, depending on the porosity and tortuosity of the electrode [17].

B.3 Results

B.3.1 Steady State Measurements

B.3.1.1 Potentiodynamic Polarization - Limiting currents

Figure B.1 shows the steady state polarization curves of $\text{LaNi}_{5-x}\text{Sn}_x$ alloys with different Sn contents (x from 0 to 0.5) at a slow scan rate (0.5 mV/s) approximating steady state conditions. The polarization curves show strong interference of mass transfer processes on the charge transfer kinetics, as evident from the current being invariant with an increase in the overpotential. At high overpotentials, ≥ 400 mV, the discharge reaction is limited by the rate of hydrogen transport within the bulk of the alloy. The corresponding current, termed as diffusion limiting current and estimated from Figure B.1 increases upon Sn substitution and decrease later at $x \geq 0.2$ (Figure B.2). The low-limiting current of the binary alloy is due to the difficulty associated with its charging in a partially-sealed cell. The limiting currents of the Sn-substituted alloys are ~ 500 mA/g as reported earlier for LaNi_5 .

B.3.1.2 Discharge Characteristics

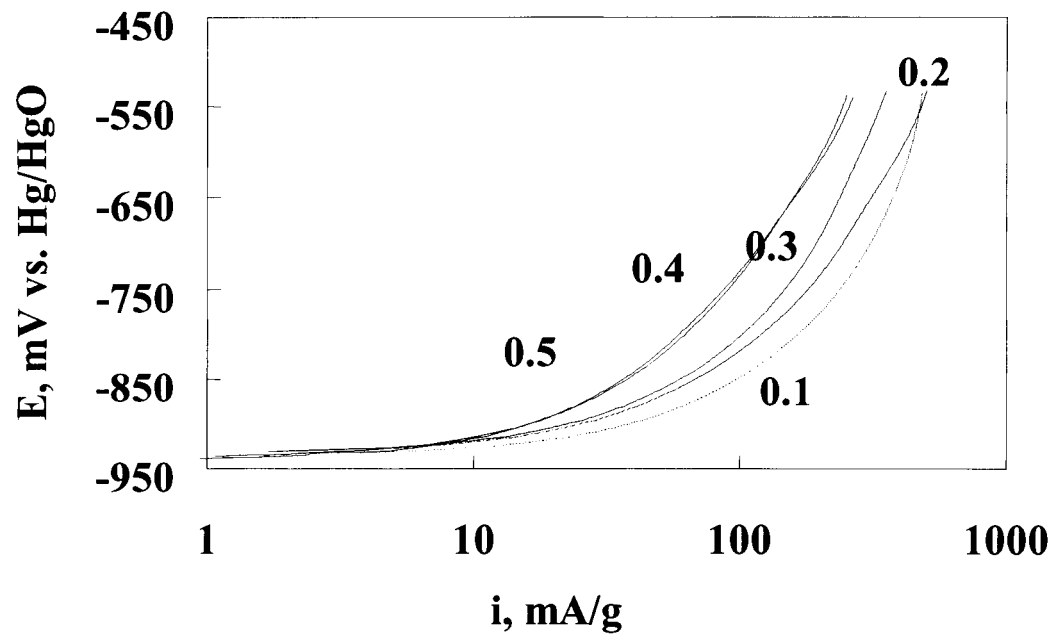


Figure B.1. Potentiodynamic polarization curves of $\text{LaNi}_{5-x}\text{Sn}_x$ alloys, illustrating diffusion-limited behavior.

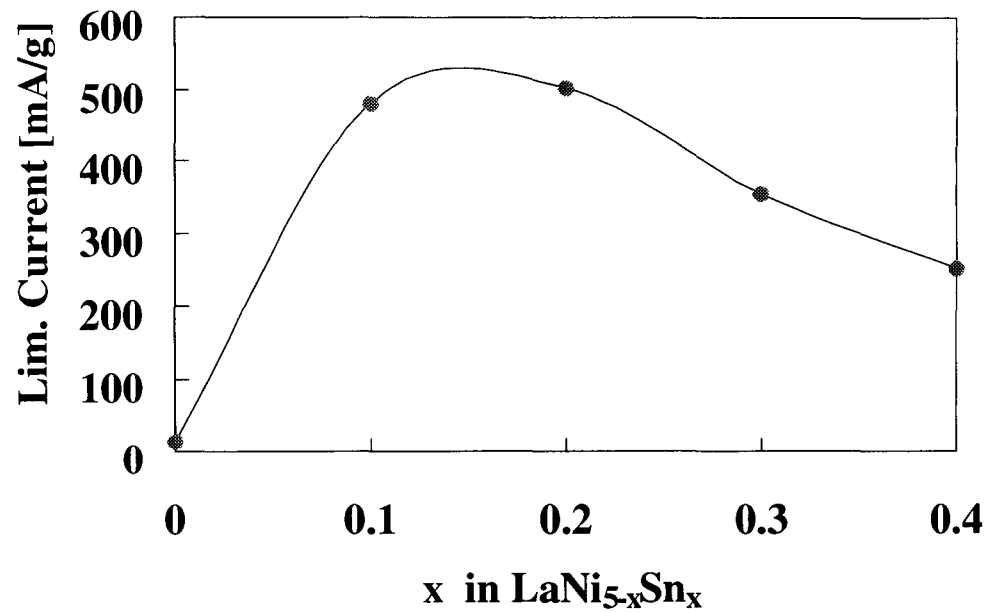


Figure B.2. Diffusion limiting currents of LaNi_{5-x}Sn_x alloys, estimated from potentiodynamic polarization curves.

In order to obtain the value of hydrogen concentration required for calculating the diffusion coefficients from the transient response below, the electrodes were discharged after a prior, complete charge. Figure B.3 shows the discharge curves of $\text{LaNi}_{5-x}\text{Sn}_x$ alloys. The discrepancy in the electrochemical capacity in these alloys is mainly due to the differences in their absorption plateau pressures [9]. MH alloys with high plateau pressures (> 1 atm.) are not efficiently charged in the open cell adopted for these studies. At high Sn contents, on the other hand, the discharge kinetics are relatively sluggish. The capacity is thus maximum with a Sn content of 0.2-0.3.

It should be realized that the degree of hydriding is such that the MH alloy exists in the two-phase region, i.e., in the α and β form. The measured diffusion coefficients therefore represent an average value of α and β phase hydrides.

B.3.2 Transient Measurements

B.3.2.1 Chronoamperometry

The transient methods involve the application of a potentiostatic pulse (corresponding to the mass transfer regime identified in the steady-state experiment) to the electrode and monitoring the amperometric and coulometric responses. From the dependence of the diffusion current and coulombic charge on time, it is possible to obtain values for the diffusion coefficients, by applying appropriate diffusional equations. The boundary conditions applicable to the present case for the outward diffusion of hydrogen within the bulk of the alloy are i) uniform initial concentration, i.e., at $t = 0$, the concentration of hydrogen is the same at any x , the distance from the interface ii) at $t > 0$, the concentration at large x approaches the bulk concentration and iii) the interfacial

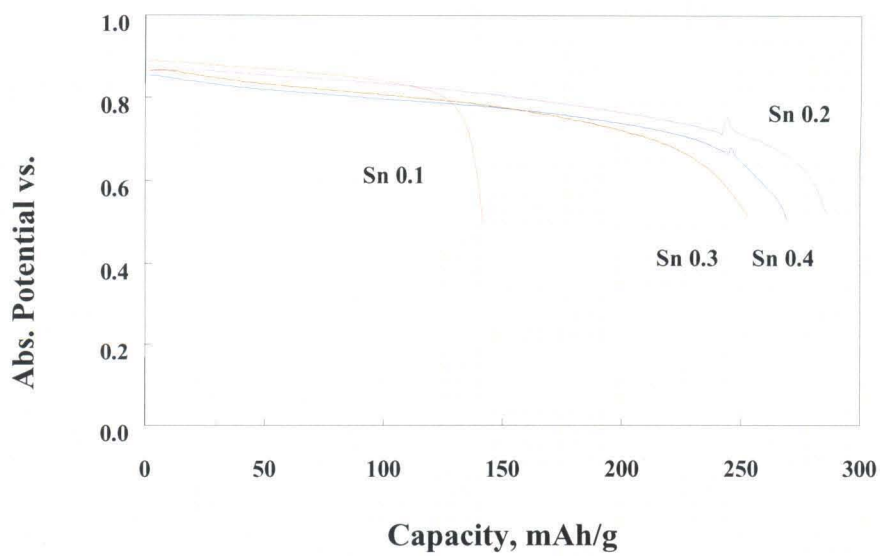


Figure B.3. Discharge curves of LaNi_{5-x}Sn_x alloys

hydrogen concentration is zero at $t > 0$, after the potential step. Assuming semi-infinite linear diffusion conditions, the instantaneous current in the diffusion-limited regime may be expressed by Cottrell's equation¹⁹ as

$$i = \frac{n F A D_H^{1/2} C^*}{\pi^{1/2} t^{1/2}} \quad (1)$$

where i is the instantaneous current at time t , D_H is the diffusion coefficient of hydrogen, C^* is the bulk concentration of the diffusing species, A is the area of the electrode and F is the Faraday constant.

Figure B.4 shows the chronoamperometric curves of $\text{LaNi}_{5-x}\text{Sn}_x$ alloys on applying a potentiostatic pulse of +400 mV vs. OCV, which corresponds to the diffusion-controlled regime. From the slope of these curves in Figure B.4 and the concentrations for the absorbed hydrogen obtained from the electrochemical discharge capacities using geometric volume of the electrode (Figure B.3 and Table B.1), the diffusion coefficients for hydrogen in $\text{LaNi}_{5-x}\text{Sn}_x$ alloys were calculated (Table B.1). The diffusion coefficients thus calculated are 6.69×10^{-9} , 8.38×10^{-9} , 7.53×10^{-9} and $9.36 \times 10^{-9} \text{ cm}^2/\text{s}$ for Sn contents of 0.1, 0.2, 0.3 and 0.4, respectively (Figure B.6, Table B.1).

B.3.2.2 Chronocoulometry

Here also, the electrode potential is shifted to a sufficiently positive value (for oxidation) to enforce diffusion-limited conditions. The coulometric output from the Potentiostat is recorded as a function of time. The coulometric response may be describes by the Cottrell equation integral form 19] such as

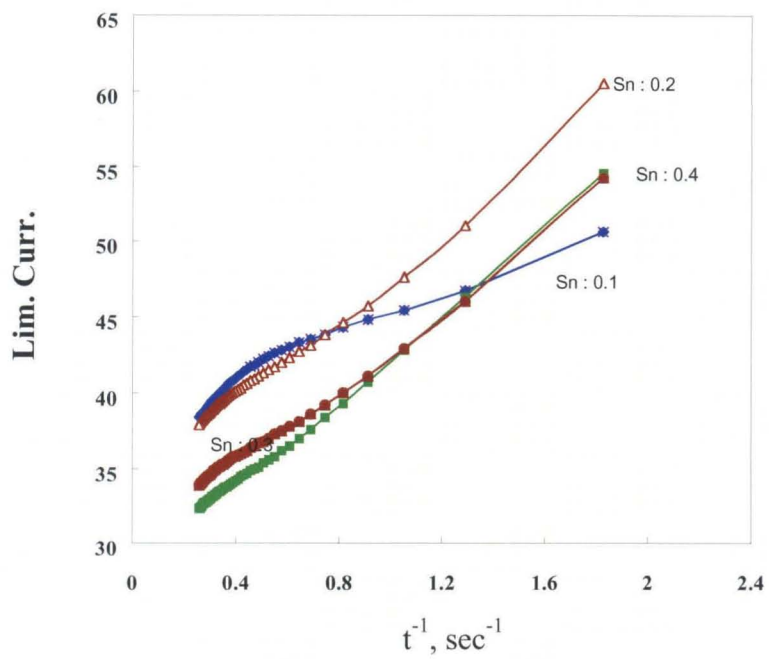


Figure B.4: Analyses of chronoamperometric curves of $\text{LaNi}_{5-x}\text{Sn}_x$ alloys.

$$Q = \frac{2 n F A D_H^{1/2} C t^{1/2}}{\pi^{1/2}} \quad (2)$$

where Q is the cumulative charge passed at any instant, t . A plot of Q vs. $t^{1/2}$ is thus linear, the slope of which yields the diffusion coefficient.

Chronocoulometric curves were obtained for $\text{LaNi}_{5-x}\text{Sn}_x$ alloys at a potentiostatic pulse corresponding to an anodic perturbation of 400 mV (Figure B.5). From the slope of these curves in Figure B.5 and the concentrations for the absorbed hydrogen obtained from the electrochemical discharge capacities using geometric volume of the electrode (Figure B.3 and Table B.1), the diffusion coefficients for hydrogen in $\text{LaNi}_{5-x}\text{Sn}_x$ alloys were calculated (Table B.1). The diffusion coefficients thus calculated are 3.49×10^{-9} , 3.86×10^{-9} and $3.77 \times 10^{-9} \text{ cm}^2/\text{s}$ for Sn contents of 0.2, 0.3 and 0.4, respectively (Figure B.6, Table B.1).

B.4 Temperature Studies

Temperature studies were performed on the $\text{LaNi}_{4.8}\text{Sn}_{0.2}$ alloy to determine its effective activation energy. The $\text{LaNi}_{4.8}\text{Sn}_{0.2}$ alloy was chosen for its superior cycle-life [9]. Figures B.7 and B.8 display the chronoamperometric and chronocoulometric curves respectively. Both figures show the expected decrease in kinetics with lower temperatures. The diffusion coefficients calculated from Figures B.7 and B.8 are displayed on an Arrhenius plot in Figure B.9. The activation energy of hydrogen in $\text{LaNi}_{4.8}\text{Sn}_{0.2}$ is calculated to be 0.19 eV by chronocoulometry and 0.29 eV by chronoamperometry. The disparity in activation energy between the two measurements is a result of the composite nature of the measured electrode (binder, conductive diluent,

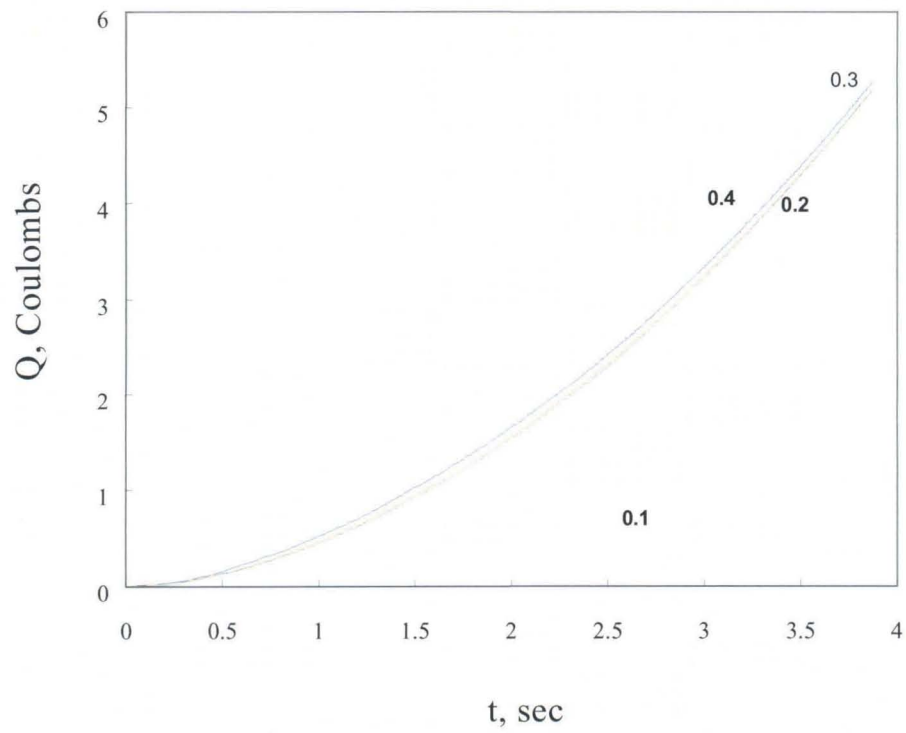


Figure B.5. Analyses of chronocoulometric response of LaNi_{5-x}Sn_x alloys.

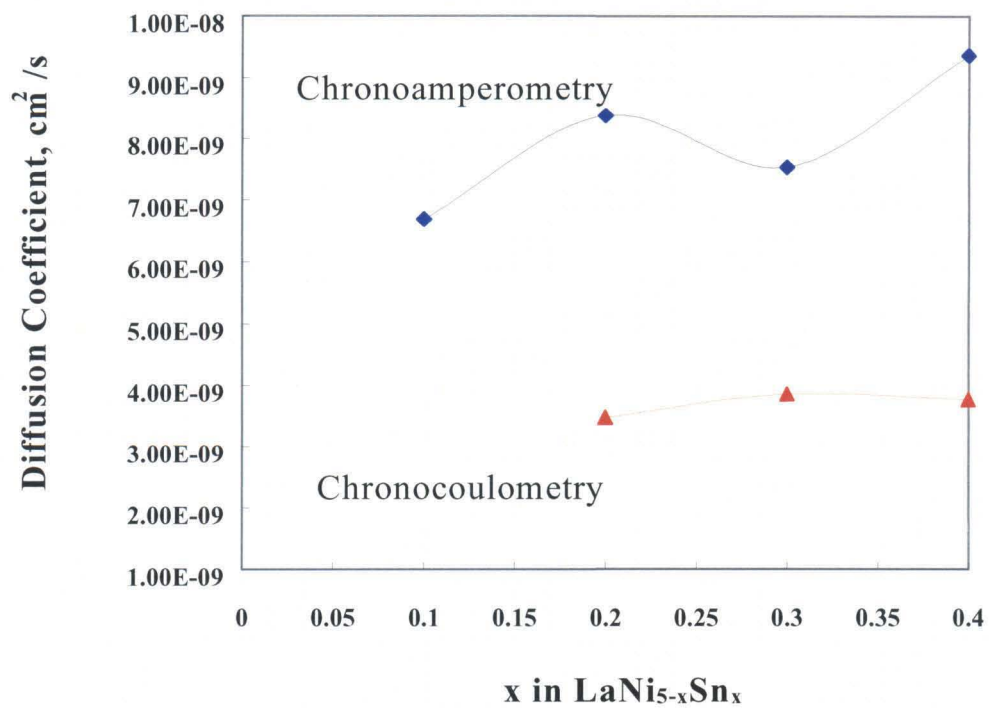


Figure B.6. Variation of diffusion coefficient of hydrogen in Sn-modified LaNi₅ alloys with the Sn content

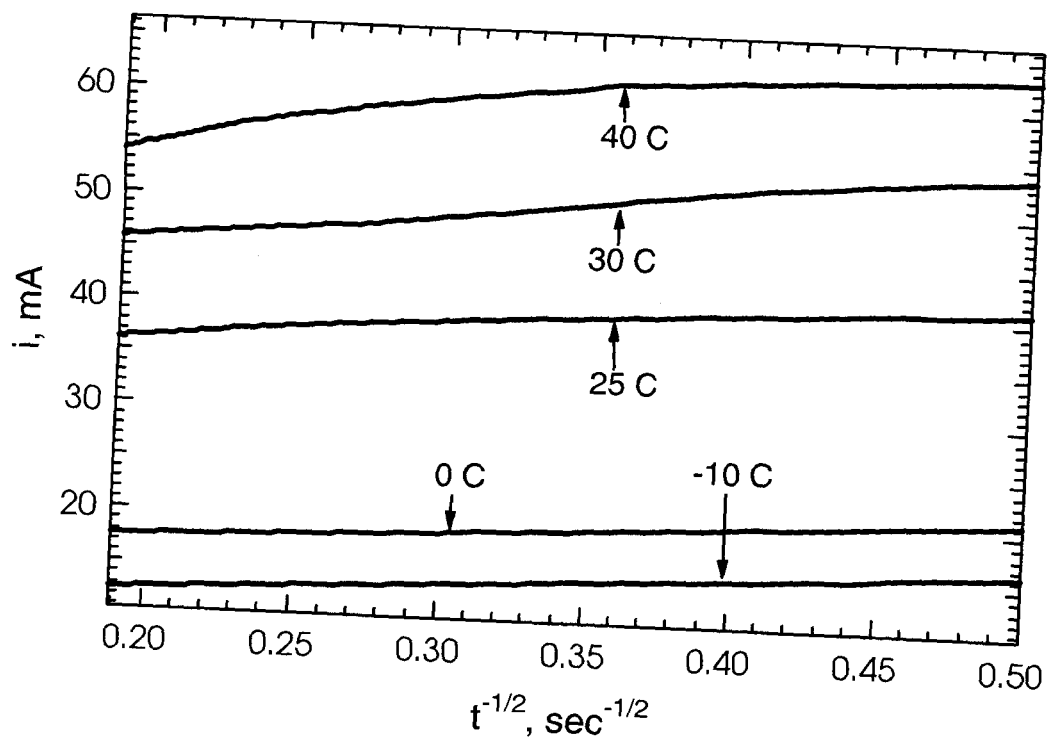


Figure B.7. Analyses of chronoamperometric curves of LaNi_{4.8}Sn_{0.2} alloy at various temperatures.

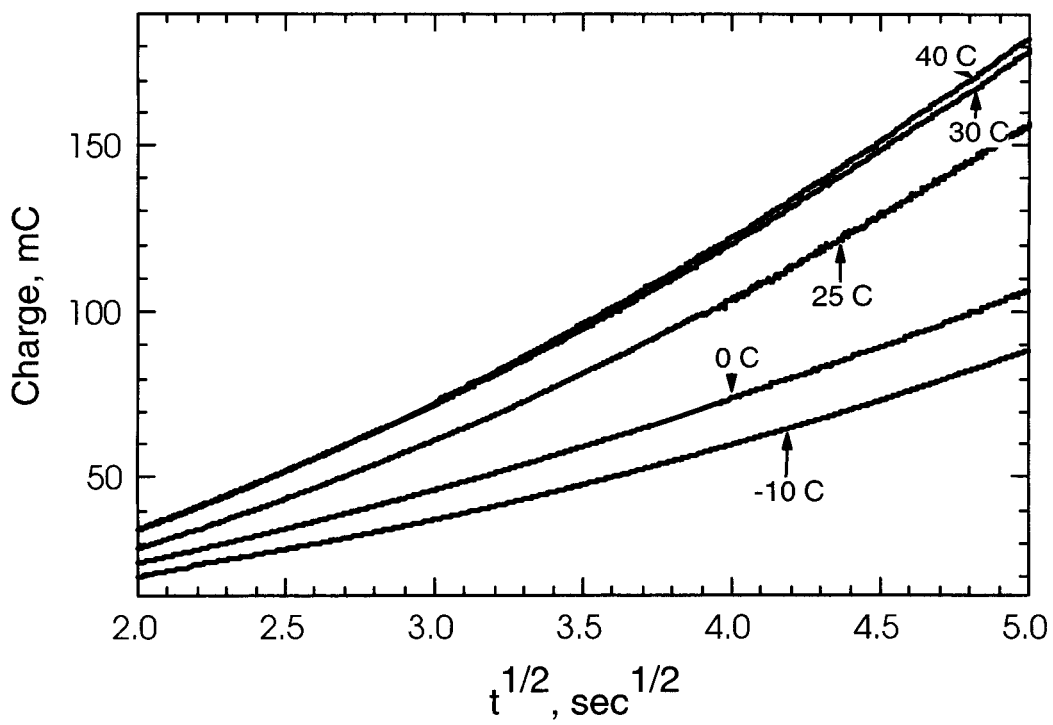


Figure B.8. Analyses of chronocoulmetric curves of $\text{LaNi}_{4.8}\text{Sn}_{0.2}$ alloy at various temperatures.

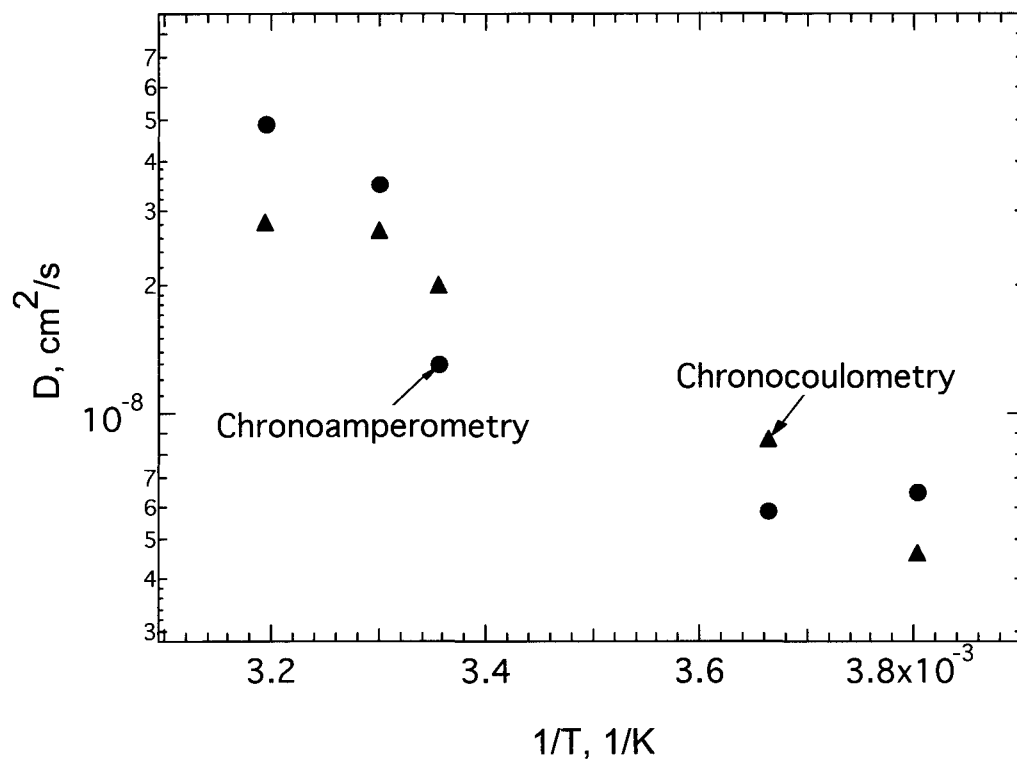


Figure B.9. Arrhenius plot of $\text{LaNi}_{4.8}\text{Sn}_{0.2}$ temperature. Activation energies calculated from plot slopes are 0.19 eV by chronocoulometry (▲) and 0.29 eV by chronoamperometry (●).

polycrystalline alloy). Thus an “effective” activation energy is measured which averages over the various crystal orientations and the non-Faradic impedances. These results are in good agreement with NMR studies by Bowman et al. [20].

B.5 Conclusion

The diffusion coefficients for the diffusion of hydrogen, obtained from the amperometric and coulometric outputs upon a potential pulse corresponding to the diffusion limiting conditions, are in close agreement with each other, suggesting that the analyses and the assumptions involved are reasonable. The actual values of the diffusion coefficients are marginally lower than those obtained from NMR and QNS techniques, but clearly larger than the values of Zheng et al, obtained from constant-current discharges.

Finally, with increasing Sn content in $\text{LaNi}_{5-x}\text{Sn}_x$ alloys, the diffusion of hydrogen is not hindered, whereas some sluggishness was observed in the charge transfer kinetics. On the other hand, the diffusion of hydrogen seems to be enhanced marginally upon the substitution of Sn for Ni. Measured “effective” activation energies correspond to published NMR studies

Table B.1 : Determination of diffusion coefficients by chronoamperometric and chronocoulometric methods

x in $\text{LaNi}_{5-x}\text{Sn}_x$	Capacity mAh/g	Concen., C_H m. moles/cc	Chronoamp. $\text{mA}\cdot\text{s}^{-1/2}$	Chronocoul. $\text{mCoul}\cdot\text{s}^{1/2}$	D_H (Chronamp) cm^2/s	D_H Chronocoul) cm^2/s
0.1	141	0.467	6.2		6.69×10^{-9}	$\times 10^{-9}$
0.2	285	0.978	14.5	18.8	8.38×10^{-9}	3.49×10^{-9}
0.3	253	0.846	11.9	18.6	7.53×10^{-9}	3.86×10^{-9}
0.4	271	0.913	14.4	18.2	9.36×10^{-9}	3.77×10^{-9}

B.7 References

1. G. G. Willems, *Philips J. Res.*, **39 (Suppl. 1)**, 1 (1984); J. G. G. Willems and K. H. J. Buschow, *J. Less Common Metals*, **129**, 13 (1987).
2. T. Sakai, H. Miyamura, N. Kuriyama, A. Kato, K. Oguru, and H. Ishikawa, *J. Less Common Metals*, **159**, 127 (1990).
3. T. Sakai, H. Miyamura, N. Kuriyama, A. Kato, K. Oguru, and H. Ishikawa, *J. Electrochemical Soc.*, **137**, 795 (1990).
4. T. Sakai, T. Hazama, H. Miyamura, N. Kuriyama, A. Kato, and H. Ishikawa, *J. Less Common Metals*, **172-174**, 1175 (1991).
5. T. Sakai, K. Oguru, H. Miyamura, N. Kuriyama, A. Kato, and H. Ishikawa, *J. Less Common Metals*, **161**, 193 (1990).
6. M. H. Mendelsohn, D. M. Gruen, and A. E. Dwight, *Mat. Res. Bull.*, **13**, 1221 (1979).
7. R. C. Bowman, Jr., C. H. Luo, C. C. Ahn, C. K. Witham, and B. Fultz, *J. Alloys and Compounds*, **217**, 185 (1995).
8. B. V. Ratnakumar, G. Halpert, C. Witham and B. Fultz, *J. Electrochem. Soc.*, 141, L89(1994); *Proc. ECS Symp. Hydrogen Batteries*, 94-27, 57(1994).
1. B. V. Ratnakumar, C. Witham, R. C. Bowman, Jr., A. Hightower, and B. Fultz, *J. Electrochem. Soc.* 143, 2578 (1996).
10. C. Witham, B. V. Ratnakumar, R. C. Bowman, Jr., A. Hightower, and B. Fultz, *J. Electrochem. Soc.* 144, (1996).
11. M. H. J. Van Rijswijk, in 'Hydrides for Energy Storage', Ed., A. F. Anderssen and A. J. Maeland, p. 261, Pergamon, Oxford (1978).
12. D. Richter, R. Hempelmann, and R. C. Bowman, Jr., in *Hydrogen in Intermetallic Compounds II*, Ed L. Schlapbach (Springer-Verlag, Berlin, 1992) p. 97.

13. C. Schönfeld, R. Hempelmann, D. Richter, T. Springer, A. J. Dianoux, J. J. Rush, T. J. Udovic, and S. M. Bennington, *Phys. Rev. B* **50**, 853 (1994).
14. H. Züchner, T. Rauf, and R. Hempelmann, *J. Less-Common Met.* **172-174**, 611 (1991).
15. R. C. Bowman, Jr., D. M. Gruen, and M. H. Mendelsohn, *Solid State Commun.* **32**, 501 (1979).
16. G. Zheng, B. N. Popov, and R. E. White, *J. Electrochem. Soc.* **142**, 2695 (1995).
17. G. Zheng, B. N. Popov, and R. E. White, *J. Electrochem. Soc.* **143**, 834 (1996).
18. C. Iwakura, T. Oura, H. Inoue, M. Matsuoka, Y. Yamamoto, *J. Electroanal. Chem.* **398**, 37 (1995).
19. A. J. Bard and L. R. Faulkner, “*Electrochemical Methods; Fundamentals and Applications*”, John Wiley & Sons, Inc., New York (1980).
20. G. Majer, U. Kaess, R. C. Bowman Jr., *Phys. Rev. B*, **57**, pp. 599, (1998)

Appendix C Performance of LaNi_{4.7}Sn_{0.3} Sealed Cells

C.1 Introduction

Since the mid-1980's, studies on metal hydrides as anodes in nickel metal hydride (NiMH) batteries have moved from fundamental scientific investigations to product-based industrial efforts. Metal hydrides (MH) now have widespread application as negative electrodes in rechargeable batteries for the consumer electronics industry. The present investigation focused on electrochemical properties of metal hydride alloys based on LaNi₅, denoted generically as "AB₅" alloys.

Commercial AB₅ metal hydride alloys in rechargeable batteries include substantial substitutions of other elements for La and for Ni. To reduce cost and improve cycle life, La is replaced with mischmetal (Mm) which is a reduced ore of a variety of rare earth elements. Sakai, et al. [1] studied various ternary substitutions for Ni in LaNi₅, and reported that the cycle life improves with the ternary substituents in the order Mn < Ni < Cu < Cr < Al < Co. The beneficial effects of Co have led to large Co substitutions for Ni in commercial AB₅ alloys. Higher costs and limited availability of the strategic element Co make it worthwhile to investigate alternate elements for substitution with Ni. Sn has proven itself as a viable candidate for promoting cycle life while retaining cell capacity in laboratory tests.

The characteristics of LaNi_{4.7}Sn_{0.3} have been well documented in laboratory cells. Previous studies by the Caltech /JPL group on LaNi₅ substituted with 0 - 8.3 at.% Sn for Ni revealed trends between alloy performance and Sn composition [2,3]. Kinetics, thermodynamics, and cycle life of LaNi_{5.0-x}Sn_x (x = 0 - 0.5) were determined by electrochemical and gas-phase studies. The microstructures of these alloys were determined by X-ray diffractometry and TEM [4-6]. Compared to other ternary alloys, LaNi_{5.0-x}M_x (M = Al, Ga, In, Si), Sn-containing alloys showed the longest cycle life. The optimal concentration of Sn, with respect to a balance among cycle life, capacity and

kinetics, was found to be in the range of $\text{LaNi}_{5.0-x}\text{Sn}_x$, $x = 0.25 - 0.3$. The reason for the improved cycle life may be related to the strong chemical bonding between La and Sn [7].

These previous results have prompted us to investigate the performance of Sn-substituted alloys in sealed cells. Here we report results of studies on the kinetics, capacity, and cycle life of sealed cells of $\text{LaNi}_{4.7}\text{Sn}_{0.3}$. The performance of these alloys, as-cast and after annealing, is compared to a standard commercial AB₅ alloy.

C.2 Experimental

The AB₅ alloys used in this study were produced by vacuum induction melting of elemental raw materials of commercial purity (99+%). The Sn-containing alloy was melted as a 6 kg heat. Half of the ingot was annealed for 72 hours at 950°C in an argon atmosphere. The partial ingots were then mechanically crushed to < 75 microns powder. The oxygen content of the powder obtained from the heat-treated ingot was 0.07 wt.%. The chemical composition as determined by Induction Coupled Plasma (ICP) Atomic Emission Spectroscopy was $\text{LaNi}_{4.58}\text{Sn}_{0.3}$, or just slightly sub-stoichiometric. The commercial AB₅ alloy used as the control has the nominal composition $\text{MmNi}_{3.6}\text{Co}_{0.7}\text{Al}_{0.4}\text{Mn}_{0.3}$, where Mm is La-rich mischmetal, a mixture of light rare earth elements, with the approximate atomic ratio of $\text{La}_{0.53}\text{Ce}_{0.32}\text{Pr}_{0.04}\text{Nd}_{0.11}$. The heat size was in excess of 300 kg and the ingots were mechanically crushed to < 75 microns powder. Chemical control is ± 0.2 wt. % for each of the B-side elements (Co, Al and Mn).

AA NiMH cells were assembled at Energizer by winding thin planar $\text{Ni}(\text{OH})_2$ sinter-type electrodes and pasted MH electrodes between a layer of battery-grade nylon separator. The MH electrodes used in this study were fabricated using pulverized, < 75 microns, MH alloy powder, admixed with a small (<2%) amount of binder and solvent, applied to thin nickel-plated perforated steel substrate, dried, calendared and sized. Approximately 7 g of MH alloy was used per electrode. The same alloy weight was used for all MH compositions. Electrolyte consisting of KOH with small additions of NaOH and LiOH was added prior to cell sealing. The cell capacity was set by the positive electrode at approximately 1000 mAh for all of the cells assembled.

Cycling of the AA NiMH cells at Energizer was performed on automated battery cycling equipment. Cycling conditions were 1C rate (1000 mA) charge to a negative change in voltage ("negative delta V") or until 38°C was reached (which ever comes first), followed by a C/10 charge rate (approximately 2 hours) to ensure complete cell charging and to fill a 3 hour test time window. Cells rested 2 minutes after charge and then discharged at 1C rate to 0.9 V. Following discharge, cells were given a 1 hour rest before recharge.

The cycling of cells at JPL was carried out with an automatic battery cycler made by Arbin Corp., College Station, TX. The cycling conditions included a discharge step at 1C rate to 0.9 V. After a two minute rest period, charging was done in two steps. Initial charging at 1C rate was performed for a maximum of one hour or to 1.6 V followed by charge step at C/10 rate for half an hour. This procedure gave a charge/discharge ratio of 1.25 or a cutoff voltage of 1.6 V, whichever came first.

Gas pressure and analysis were performed on laboratory equipment that punctures a cell, releases cell gases into a pre-measured volume, measures pressure using a Dynisco

pressure transducer, calculates internal cell pressure and sends a sample of the captured gas to a Gow-Mac Gas Chromatograph (Series 500) for analysis. Gas pressure and composition were measured immediately after removing the cells from charge.

Self discharge rates were carried out at JPL using the same charge and discharge conditions described above for cell cycling. Annealed $\text{LaNi}_{4.7}\text{Sn}_{0.3}$ and $\text{Mm}(\text{NiAlCoMn})_5$ cells were subjected to five cycles to establish a baseline capacity. The cells were then allowed to sit at 25°C and 45°C for several days. Their discharge capacities were then measured and normalized to initial capacity.

AC impedance measurements were carried out with the EG&G 273 Potentiostat and Solartron 1255 Frequency Response Analyzer, using EG&G Impedance software 388.

C.3 Results and Discussion

C.3.1 Isotherms

Figure C.1 displays isotherm data of gas-phase desorption at 45°C of a typical $\text{Mm}(\text{NiAlCoMn})_5$ and $\text{LaNi}_{4.7}\text{Sn}_{0.3}$ in the as-cast and annealed conditions. The isotherm of the annealed Sn alloy displays a flatter plateau and larger capacity relative to the $\text{Mm}(\text{NiAlCoMn})_5$. The upward slope of the isotherm for the as-cast Sn alloy can be attributed to the chemical inhomogeneity of the material. An inhomogeneous distribution

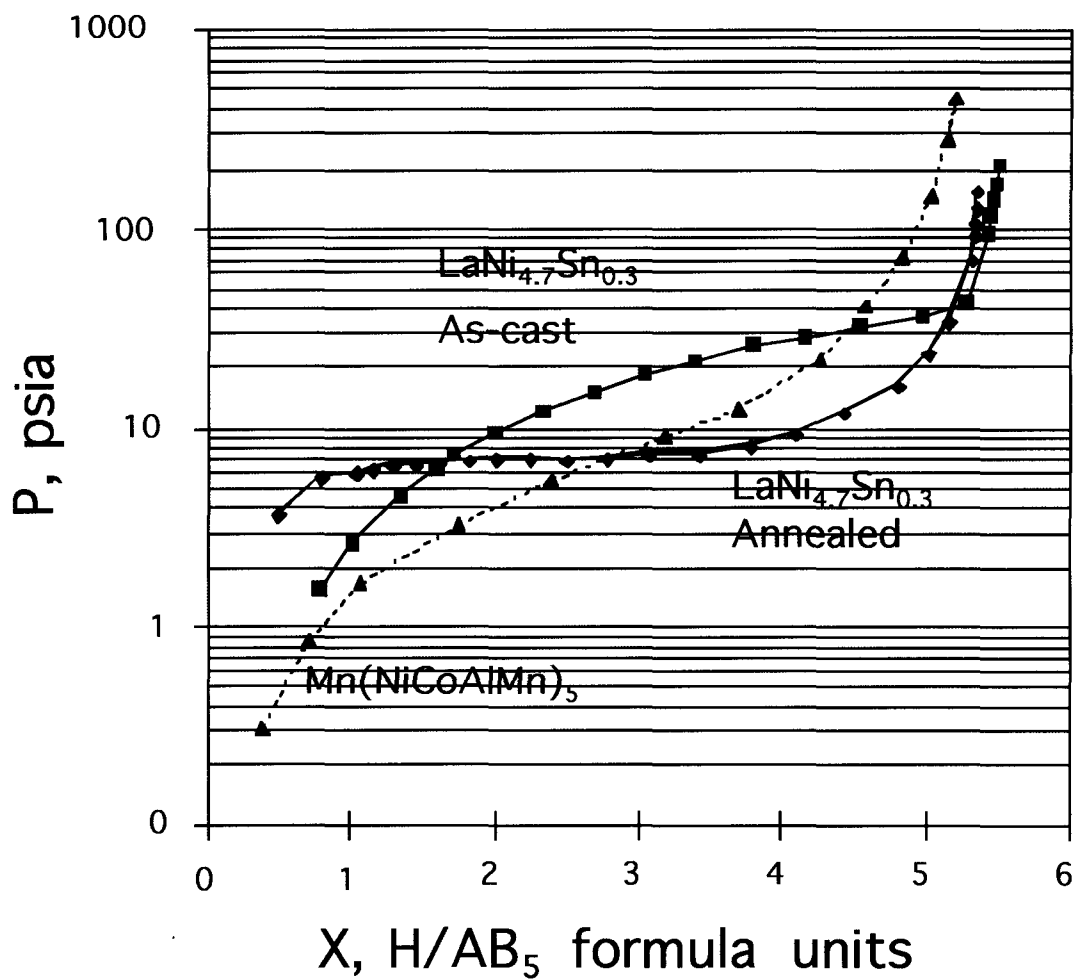


Figure C.1. Gas phase desorption isotherms of the as-cast $LaNi_{4.7}Sn_{0.3}$ alloy, annealed $LaNi_{4.7}Sn_{0.3}$, and the commercial alloy of typical $Mm(NiAlCoMn)_5$ composition measured at $45^\circ C$.

of Sn in the as-cast alloy will lead to some regions favorable for hydrogen occupancy but other regions less so.

C.3.2 Self Discharge

A correlation between hydride desorption pressure and self discharge ratios have been reported by Anani, et al [8]. A lower self-discharge for annealed $\text{LaNi}_{4.7}\text{Sn}_{0.3}$ alloys was suggested by the gas phase isotherms. The lower H_2 pressure at greater hydrogen to metal hydride ratios ($\text{H/f.u.} > 3$) indicates the greater stability of hydrogen in the $\text{LaNi}_{4.7}\text{Sn}_{0.3}$ alloys. The flat isotherms translate into smaller gradients in the hydrogen chemical potential and thus reduced hydrogen evolution. Results of self discharge tests are shown in Figure C.2 As expected, we consistently find lower self discharge in annealed $\text{LaNi}_{4.7}\text{Sn}_{0.3}$ sealed cells (AA - size) as compared to $\text{Mm}(\text{NiAlCoMn})_5$ cells. The degree of self discharge increases with temperature, with the $\text{LaNi}_{4.7}\text{Sn}_{0.3}$ being less sensitive to this effect. Self discharge can also be influenced by the by-products of nylon separator degradation and nitrates remaining in the positive Ni electrode. However, these cells were fabricated with identical procedures and thus the differences in self-discharge shown in Figure C.2 reflect the nature of the MH electrode material.

C.3.3 Rate Measurements

It is difficult to infer negative electrode kinetics from the performance measurements of commercial sealed cells. This is because the cells are purposely built with an excess of negative electrode (i.e., positive limited to reduce H_2 gassing

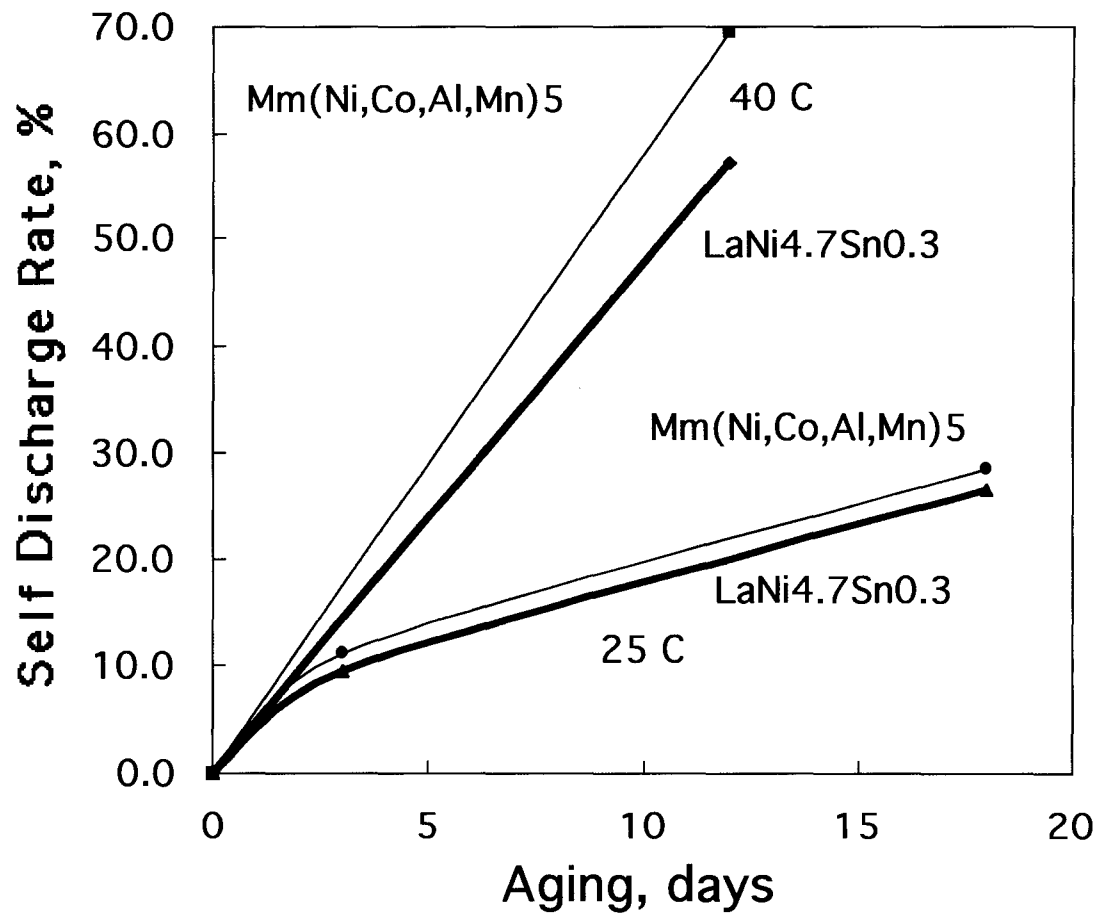


Figure C.2. Self discharge data showing loss in stored electrochemical capacity versus time for annealed $\text{LaNi}_{4.7}\text{Sn}_{0.3}$ alloy and commercial alloy of typical $\text{Mm}(\text{NiAlCoMn})_5$ composition measured at 25°C and 45°C.

problems). Cell capacity variations are shown in Figure C.3 as a function of discharge current up to 3C. Groups of 2 to 5 cells were tested to obtain these results. The higher capacity evidenced for the $\text{LaNi}_{4.7}\text{Sn}_{0.3}$ at all discharge rates, may be indicative of improved kinetics for this alloy. Nevertheless, the difference in rate capacity of the $\text{LaNi}_{4.7}\text{Sn}_{0.3}$ and $\text{Mm}(\text{NiAlCoMn})_5$ electrodes is not substantial.

C.3.4 Pressure Measurements

Pressures of gases evolved from the charging of the sealed cells at 1C rate were measured. There were similar amounts of total gases evolved from all cells. Figure C.4 shows that the amount of H_2 gas evolved from each cell increases with the time of charge. The reduced hydrogen emission of the annealed Sn alloy follows from the reduction in plateau pressure. The as-cast $\text{LaNi}_{4.7}\text{Sn}_{0.3}$, with its more inhomogeneous Sn distribution, showed greater hydrogen evolution.

C.3.5 Cycle Life

Cycle life tests on sealed cells of as-cast and annealed $\text{LaNi}_{4.7}\text{Sn}_{0.3}$ are compared to $\text{Mm}(\text{NiAlCoMn})_5$ control cells in Figure C.5 and C.6. These experiments were conducted at JPL and Energizer under different cycling conditions and provided the data for Figure C.5 and C.6, respectively. The as-cast and annealed $\text{LaNi}_{4.7}\text{Sn}_{0.3}$ cells exhibit shorter activation times and more rapid degradation compared to control cells in both series of measurements.

The $\text{Mm}(\text{NiAlCoMn})_5$ alloys display superior cycle life to the $\text{LaNi}_{4.7}\text{Sn}_{0.3}$ alloys. It is widely accepted [9] that the substitution of Co and Al for Ni inhibit volume

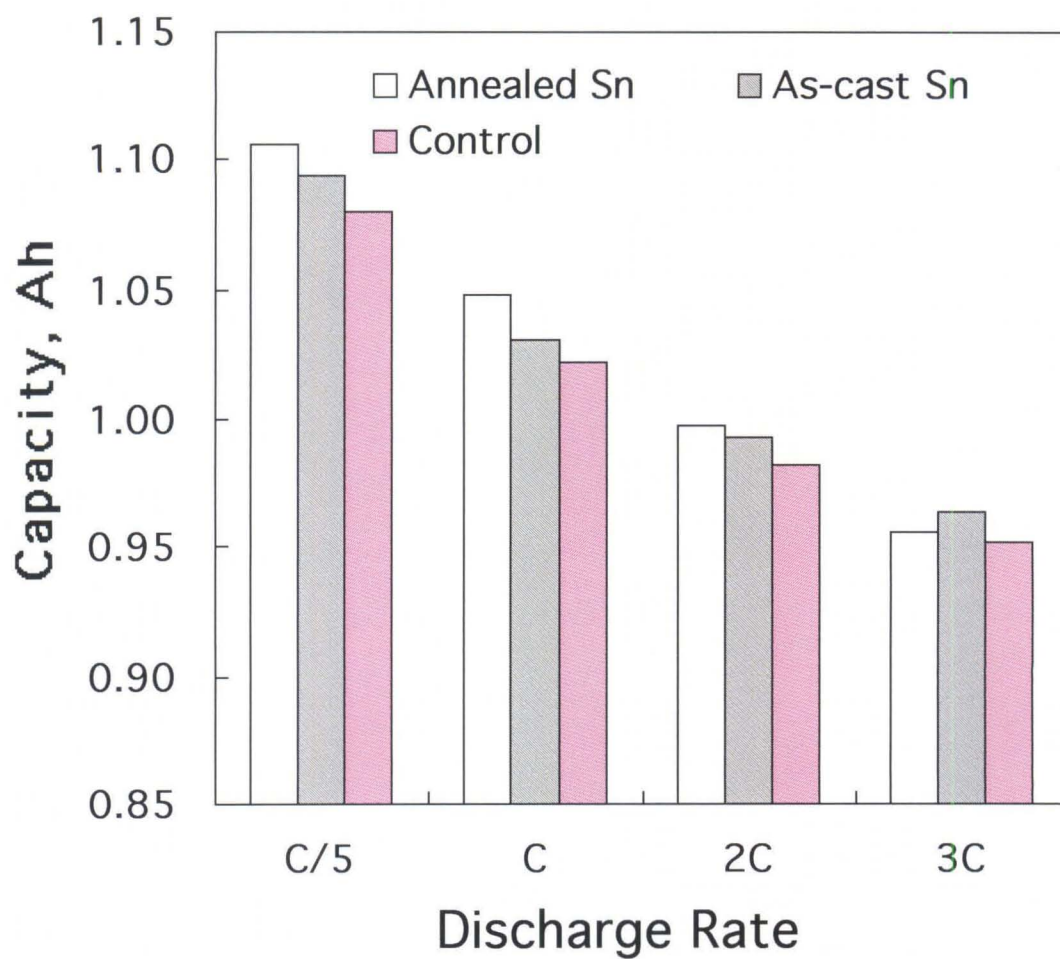


Figure C.3. Electrochemical capacities of AA cells measured at different rates of discharge.

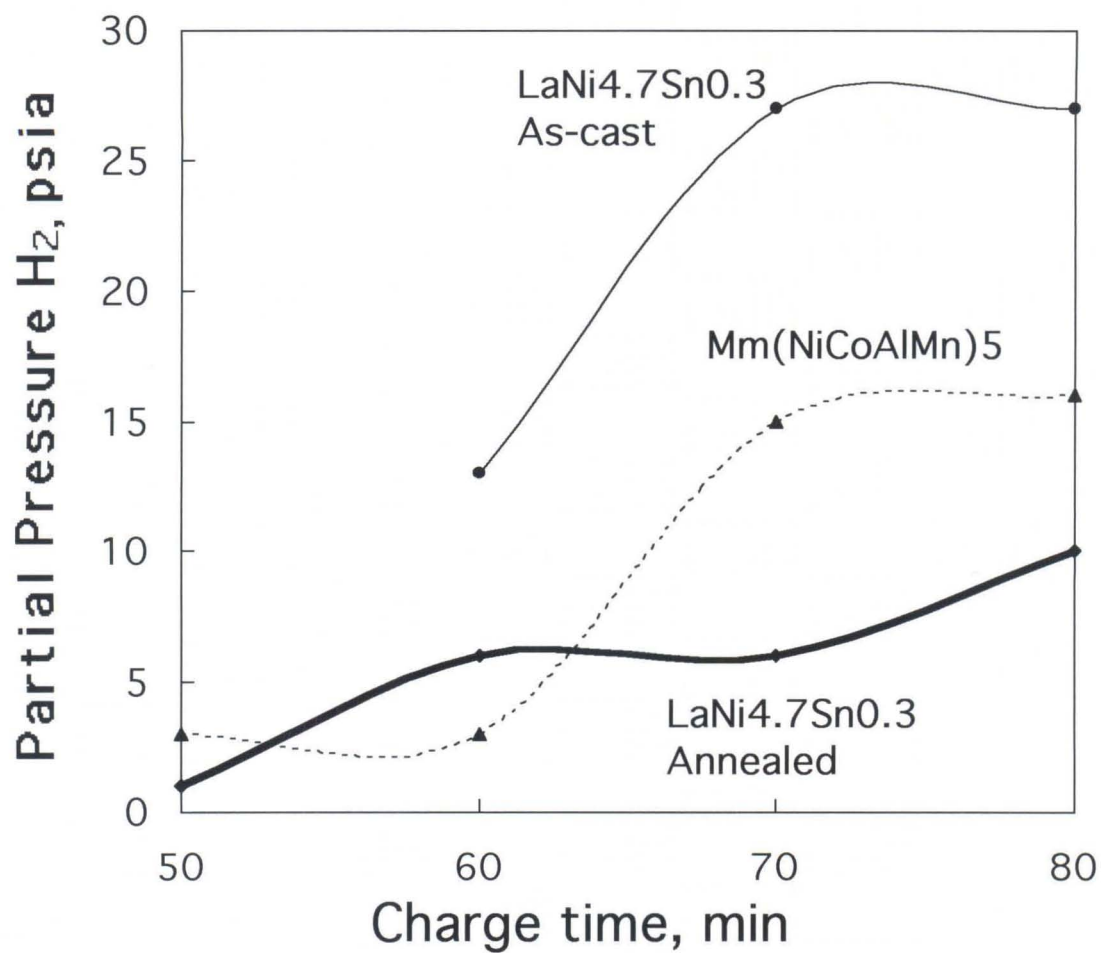


Figure C.4. Partial pressure of H₂ gas evolved from cells during different charging times at 1C rate.

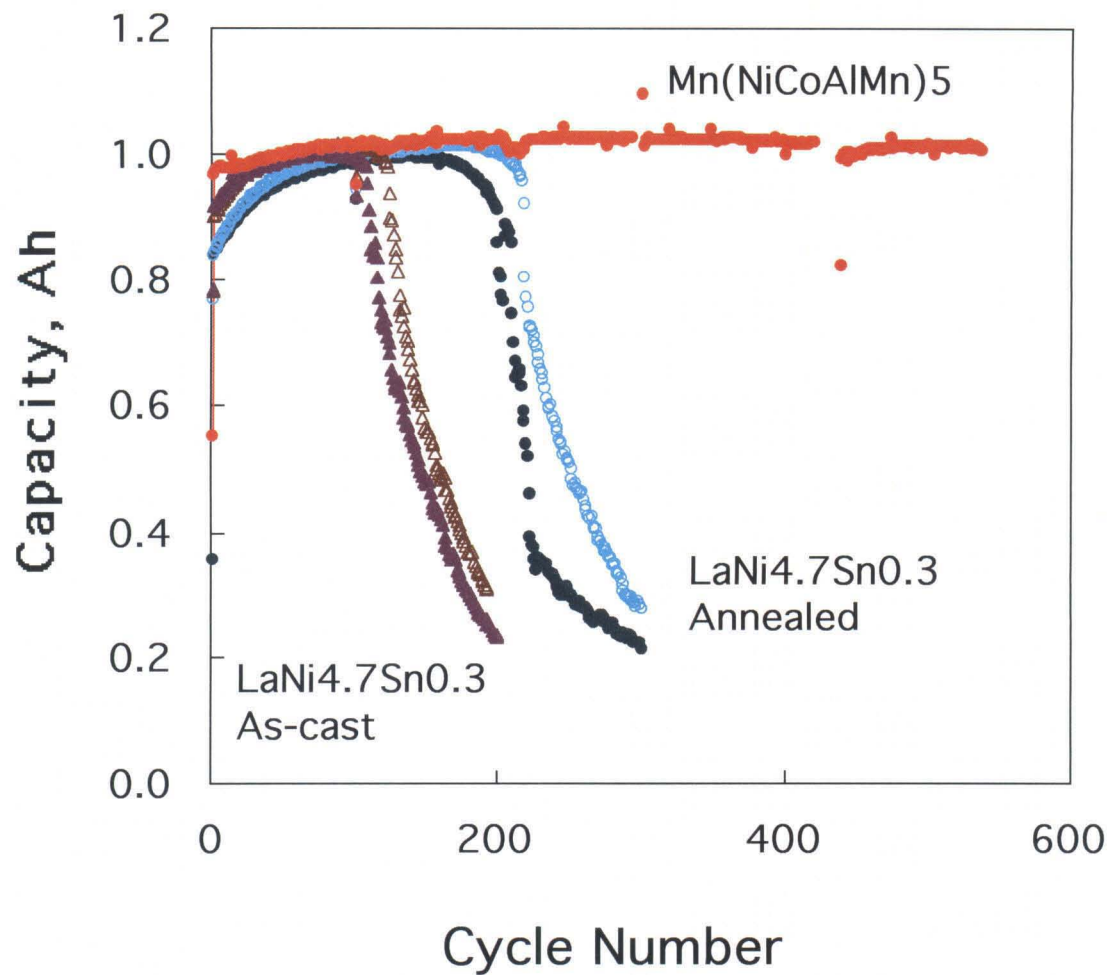


Figure C.5. Cycle life for sealed cells containing as-cast $\text{LaNi}_{4.7}\text{Sn}_{0.3}$ alloy, annealed $\text{LaNi}_{4.7}\text{Sn}_{0.3}$, and the commercial alloy of typical $\text{Mn}(\text{NiAlCoMn})_5$ composition measured at room temperature. Two cells of each were measured at JPL.

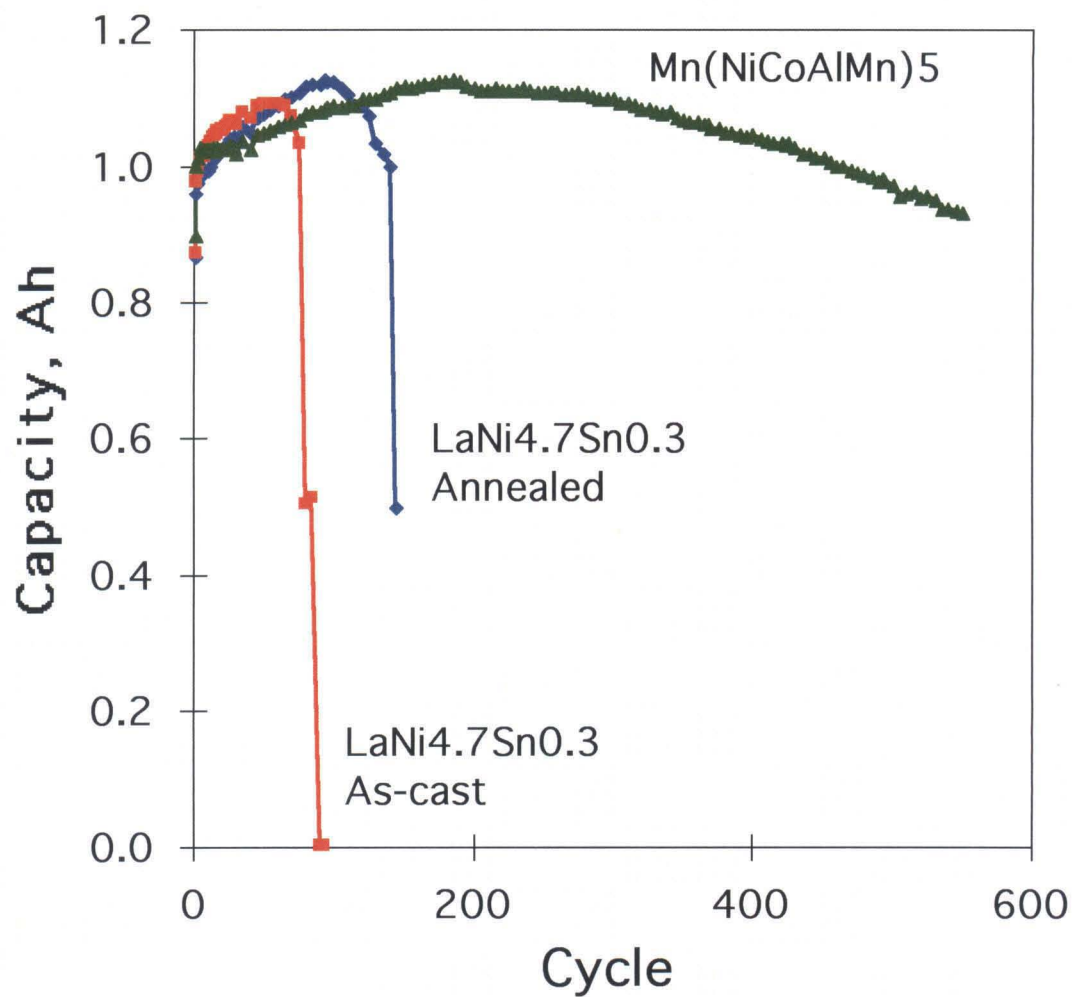


Figure C.6. Cycle life data for sealed cells containing as-cast $\text{LaNi}_{4.7}\text{Sn}_{0.3}$ alloy, annealed $\text{LaNi}_{4.7}\text{Sn}_{0.3}$, and the commercial alloy of typical $\text{Mm}(\text{NiAlCoMn})_5$ composition. Measurements were carried out at Energizer.

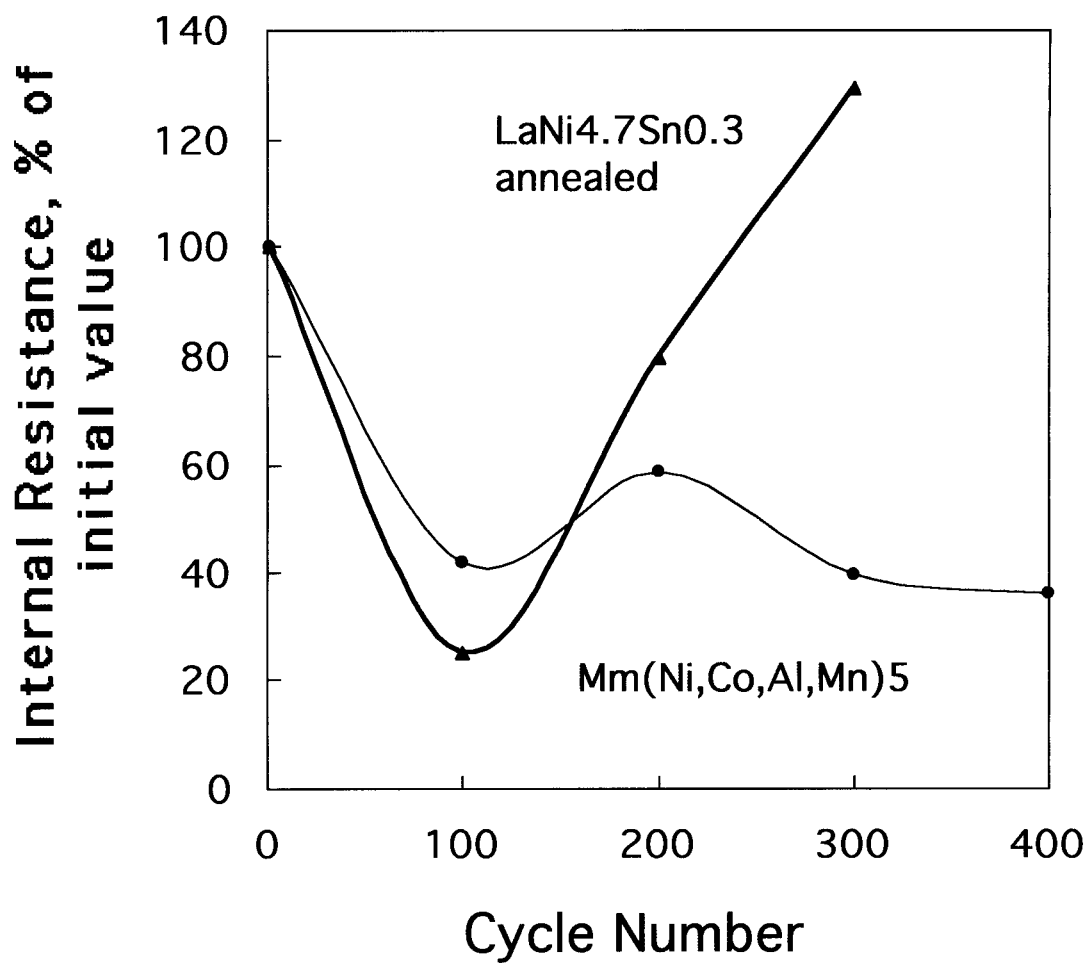


Figure C.7. Cell internal resistances vs. cycle number determined by AC impedance studies on annealed $\text{LaNi}_{4.7}\text{Sn}_{0.3}$ and the commercial $\text{Mm}(\text{NiAlCoMn})_5$.

dilatation during hydrogen absorption, and thereby improves cycle life. It has also been proposed that the Ce [10] and Nd [9] present in the mischmetal promotes beneficial passivating films. These passivating films protect the rare earth elements from the corrosive electrolyte. We suggest that the lifetimes of $\text{LaNi}_{4.7}\text{Sn}_{0.3}$ could be improved with the substitution of mischmetal for La. Encouraging results from Ce additions have been reported previously [11].

C.3.6 AC Impedance

The $\text{LaNi}_{4.7}\text{Sn}_{0.3}$ and $\text{Mm}(\text{NiAlCoMn})_5$ sealed cells differ considerably in their series Ohmic resistance during cycling, as shown in Figure C.7. The Ohmic resistance of sealed cells, generated from the interfaces between electrode, electrolyte, and leads, was measured by AC impedance spectrometry. The initial decrease seen in this parameter could be due to the decrepitation of the metal hydride alloy particles, which results in an enhanced surface area (and thus reduced resistance). The subsequent increase in the resistance may be an indication of the corrosion and passivation processes, which might be responsible for the shorter cycle life of the cells with Sn-based alloy.

C.4 Conclusions

Our studies have found $\text{LaNi}_{4.7}\text{Sn}_{0.3}$ alloys to possess limited utility in rechargeable nickel metal hydride batteries. The enhancements relative to $\text{Mm}(\text{NiAlCoMn})_5$ in kinetics and reduction in self discharge observed in laboratory cells have been demonstrated in sealed cells. The $\text{LaNi}_{4.7}\text{Sn}_{0.3}$ cells exhibited lower self discharge and greater capacities at higher rates of discharge compared to cells of the standard mischmetal composition $\text{Mm}(\text{NiAlCoMn})_5$. The $\text{LaNi}_{4.7}\text{Sn}_{0.3}$ cells did not

display cyclic lifetimes comparable to the $\text{Mm}(\text{NiAlCoMn})_5$ cells. Hence, the enhancements in lifetime from Sn substitution alone, which were clearly demonstrated in previous half-cell electrode studies [3,7] and attributed to the strong chemical bonding between La and Sn, was not found to be as effective as the combined contributions in commercial $\text{Mm}(\text{NiAlCoMn})_5$ alloys. The next logical step is to investigate improvements to the lifetimes of the $\text{LaNi}_{4.7}\text{Sn}_{0.3}$, by substituting Ce for a portion of the La. We expect that the surface effects from passivating films and changes to the alloy volume expansion on hydriding [11] will improve cycle life for reasons independent of the beneficial effects of Sn. However, substitution of Ce may reduce capacity through formation of other impurity phases. This behavior will be the subject of future studies.

C.5 References

- [1] T. Sakai, K. Oguru, H. Miyamura, N. Kuriyama, A. Kato and H. Ishikawa, *J. Less Common Metals*, 161, 193 (1990).
- [2] R.C. Bowman, Jr., C.H. Luo, C.C. Ahn, C.K. Witham and B. Fultz, *J. Alloys and Compounds*, 217, 185 (1995).
- [3] B.V. Ratnakumar, C. Witham, R. C. Bowman, Jr., A. Hightower, and B. Fultz, *J. of Electrochem. Soc.*, 143, 2578 (1996).
- [4] M. Mendelsohn, D. Gruen, A. Dwight, *Inorg. Chem.* 18, 3343 (1979).
- [5] J. S. Cantrell, T.A. Beiter and R.C. Bowman, Jr., *J. Alloys and Compounds*, 207/208, 372 (1994).
- [6] M. Wasz, R.B. Schwarz, S. Srinivasan and M.P.S. Kumar, in *Materials for Electrochemical Energy Storage and Conversion - Batteries, Capacitors, and Fuel Cells*, Symposium Proceedings of The Materials Research Society, San Fransico, CA Vol. 93, pp. 237-242, Spring (1995).
- [7] C. Witham, R. C. Bowman, Jr., B.V. Ratnakumar, and B. Fultz, in *AB₅ Metal Hydride Alloys for Alkaline Rechargeable Cells.*, Proceedings of The Eleventh Annual Battery Conference on Applications and Advances, Long Beach, CA (Inst. Electrical Electronic Eng., Piscataway, NJ), (1996), pp. 129-134.
- [8] A. Anani A. Visintin, S. Srinivasan, A. J. Appleby, J. J. Reilly, and J. R. Johnson *Electrochem. Soc. Proc.* 92-5, p. 105 (1992).
- [9] J. J. G. Willems, *Philips J. Res.*, 39 (Suppl. 1), 1 (1984); J.J.G. Willems and K.H. J. Buschow, *J. Less Common Metals*, 129, 13 (1987).
- [10] T. Sakai, T. Hazama, H. Miyamura, N. Kuriyama, A. Kato and H. Ishikawa, *J. Less Common Metals*, 172-174, 1175 (1991).

- [11] G. D. Adzic, J. R. Johnson, J. J. Reilly, J. McBreen, S Mukerjee, M. P. Sridlar Kumar, W Zhang, S. Srinivasan, *J. Electrochem. Soc.* 142, 3429 (1995).